uOttawa

L'Université canadienne
Canada's university

FACULTÉ DES ÉTUDES SUPÉRIEURES ET POSTOCTORALES

uOttawa

L'Université canadienne
Canada's university

FACULTY OF GRADUATE AND POSDOCTORAL STUDIES

Martin Kenward

AUTEUR DE LA THÈSE / AUTHOR OF THESIS

Ph.D. (Physics)

GRADE / DEGREE

Department of Physics

FACULTÉ, ÉCOLE, DÉPARTEMENT / FACULTY, SCHOOL, DEPARTMENT

On the stimulation and theory of polymer dynamics in sieving media: friction, molecular pulleys, Brownian ratchets and polymer scission

TITRE DE LA THÈSE / TITLE OF THESIS

Gary Slater

DIRECTEUR (DIRECTRICE) DE LA THÈSE / THESIS SUPERVISOR

CO-DIRECTEUR (CO-DIRECTRICE) DE LA THÈSE / THESIS CO-SUPERVISOR

EXAMINATEURS (EXAMINATRICES) DE LA THÈSE / THESIS EXAMINERS

Béla Joos	Andre Marziali
Mads Kaern	David Sinclair

Gary W. Slater

Le Doyen de la Faculté des études supérieures et postdoctorales / Dean of the Faculty of Graduate and Postdoctoral Studies

On the simulation and theory of polymer dynamics in sieving media: friction, molecular pulleys, Brownian ratchets and polymer scission.

Martin Kenward

B.Sc. Honours, M.Sc.
(Memorial University)

A thesis submitted in partial fulfillment of the requirements for the degree of

Doctor of Philosophy

Department of Physics

uOttawa

L'Université canadienne
Canada's university

University of Ottawa
Ottawa, Ontario
Canada
April 19, 2007

Your file Votre référence
ISBN: 978-0-494-49369-4
Our file Notre référence
ISBN: 978-0-494-49369-4

Summary

The study of single polymer dynamics has, in the past few years, undergone a resurgence. This has been spurred on by the emergence of the fields of micro- and nanofluidics and their associated applications, especially by their ability to promise revolutionary techniques to, for example: rapidly sequence DNA, analyze proteins, carry out large-scale laboratory techniques in centimeter sized devices (lab-on-a-chip) and test and verify fundamental concepts related to the statistical physics of single molecules in fluids.

In particular, the study of (typically single, isolated) polymers and the development of theoretical methods and computational tools to examine these polymers in microfluidic environments is a key challenge. In this thesis, we examine several different phenomena related to the dynamics of polymers in either microfluidic environments or related applications to DNA sequencing or separation. A recurrent theme throughout this work is the use of Molecular Dynamics (MD) simulations with an explicit solvent. Explicit solvent is an important aspect of our simulations and contrasts much work in the current literature which either artificially includes solvent or neglects it all together. This explicit inclusion of solvent allows us to explore phenomena (related to hydrodynamics) that is not observable with, for example, Brownian (or Langevin) Dynamics or Monte Carlo simulations.

Chapter 2 contains a primarily computational examination of the friction coefficients of uncharged polymers. We explore the effects of deforming polymer chains on their friction coefficients along with examining several fundamental concepts of polymer friction (including hydrodynamic permeability). A key result is a verification of the hydrodynamic coupling of polymer chains resulting from a net reduction in the friction of polymer chains in hairpin (or folded) conformations. We also show that polymers undergo frictional transitions as they are stretched by an external force applied to the middle of the molecules.

In chapter 3 we use some of the concepts and results from chapters 1 and 2 to explore

the problem of a polymer chain migrating under the influence of an external force (or fluid flow) through a molecular obstacle course. These polymers collide with either fixed obstacles (or other polymers) and can be trapped in meta-stable long-lived, pulley-like conformations. This method can be used to separate polymers by molecular weight. We use both MD simulations and a general classical theory for the collisions to explore several different collision regimes. We also show that a classic experimental result, the formation of so-called V-shaped states, can occur in single polymer collision events, contrary to the popular assumption that it was necessary for a polymer to collide with multiple polymers.

In chapter 4 we build on the results and ideas from the first three chapters and examine another phenomenon related to polymer transport, that of (Brownian) ratchets. A ratchet is essentially a method to rectify the thermal noise in a system in order to perform work, for example, to generate net transport. We use our MD simulations to examine the behaviour of polymers in the presence of an asymmetric saw tooth ratchet potential. We also show that existing ratchet models, where the ratchet widths are on the order of a polymer gyration radius, neglect an important effect of chain relaxation and thus underestimate optimal operating parameters. We propose and derive equations illustrating a new operational mode for a ratchet which inherently uses the deformation of polymer chains induced by the application of a ratcheting potential. We present a simple mathematical expression to incorporate time-dependent diffusion coefficients $D(t)$ into ratchets.

The final chapter presents work done in collaboration with Annelise Barron's group at Northwestern University and examines the breaking of polymer chains in extensional flow fields as a method to systematically and predictably reduce the polydispersity (PDI) of polymer solutions. The experimental investigation, carried out by the Barron group illustrated that a dilute polymer solution, when passed through a narrow constriction at high pressure can systematically reduce the PDI of the polymer solution. My contribution to this work was to develop a statistical model which calculates polymer molecular weight distributions and which can predict the resulting degraded polymer distribution. Two key things resulted from this investigation, the first is that polymers can break multiple times during a single scission event (i.e., one pass through the experimental system). Secondly we showed that it is possible to predictably reproduce polymer distributions after multiple scission events.

Statement of Originality

In accordance with the guidelines for a Ph.D. thesis in the Department of Physics, University of Ottawa this preamble provides a description of the originality of the work contained herein. The material in this thesis is in part based on a number of published (or submitted) articles and conference presentations made during the course of my Ph.D. program. The work is original to the extent that I have either extended existing work or have created new models and developed news ideas for study; in the former case references are given to previous studies on similar subjects. In all instances a detailed list of references is given to provide the interested reader sufficient background to further peruse any of the topics discussed. The contribution to collaborative works are clearly delineated in the text of this thesis. Any works not directly incorporated into the main body of the thesis are included in the appendix for completeness and the extent of my contribution is explained prior to each occurence.

Refereed Publications:

1. **M. Kenward** and G. W. Slater. *Molecular Dynamics Simulations with Explicit Hydrodynamics III: On the deformation of polymers in asymmetric ratchet potentials.* Euro. Phys. J. E., submitted 2007.

2. **M. Kenward** and G. W. Slater. *Molecular Dynamics Simulations with Explicit Hydrodynamics II: On the Collision of Polymers with Molecular Obstacles.* Euro. Phys. J. E., 20, (2), 125–141 2006.

3. **M. Kenward** and G. W. Slater. *Molecular Dynamics Simulations with Explicit Hydrodynamics I: On the Friction Coefficients of Deformed Polymers.* Euro. Phys. J. E., 14, (1), 55–66, 2004.

4. B. A. Buchholz, J. N. Zahn, **M. Kenward**, G. W. Slater, A. E. Barron. *Flow–Induced Chain Scission as a Physical Route to Narrowly Distributed, High Molar Mass Polymers.* Polymer, 45, (4), 1223–1234. 2004.

5. S. Casault, **M. Kenward** and G. W. Slater. *Combinatorial design of passive drug delivery platforms.* International Journal of Pharamaceutics. To appear, 2007.

Supplementary publications and/or conference preceedings:

1. G. W. Slater, Y. Gratton, **M. Kenward**, L. C. McCormick, F. Tessier. *Deformation, Stretching and Relaxation of Single Polymer Chains: Fundamentals and Examples.* A Chapter in the book: Soft Materials: Structure and Dynamics. Eds. J. R. Dutcher and A. G. Marangoni. Marcel Dekker, New York, 2004.

2. G. W. Slater, Y. Gratton, **M. Kenward**, L. C. McCormick, F. Tessier. (2003) *Deformation, Stretching and Relaxation of Single Polymer Chains: Fundamentals and Examples.* Soft Materials, 1, (3), 365–391, 2003.

3. G. W. Slater, **M. Kenward**, L. C. McCormick, M. G. Gauthier. *Theory of DNA Separation by Capillary Electrophoresis.* Current Opinion in Biotechnology, 14, (1), 58–64, 2003.

4. **M. Kenward**, F. Tessier, S. Guillouzic, Y. Tatek, Y. Gratton and G. W. Slater. *Molecular Dynamics Simulations of Polymers in Microenvironments.* Proceedings of the 17^{th} Annual International Symposium on High Performance Computing, Systems and Applications. Ed. D. Sénéchal. Sherbrooke, Quebec, NRC Press, pp. 47–55, 2003.

5. G. W. Slater, S. Guillouzic, M. G. Gauthier, J–F. Mercier, **M. Kenward**, L. C. McCormick, F. Tessier. *Theory of DNA Electrophoresis (1999–2002 $\frac{1}{2}$): A Review.* Electrophoresis, 23, (22-23), 3791–3816, 2002.

Conference presentations (oral and poster) and workshops attended:

1. **M. Kenward.** *Polymers In Silico: Aspects of computational (bio)–polymer physics and its applications.* Ottawa Carleton Institute of Physics (OCIP) graduate symposium. University of Ottawa, December, 2005.

2. **M. Kenward.** *Polymers In Silico: Aspects of computational (bio)–polymer physics and its applications.* (Invited speaker). 1st Annual HPCVL–SharcNet joint symposium on high performance and applications. Ryerson University, Toronto, Ontario, October, 2005.

3. **M. Kenward** and G. W. Slater. *Modelling polymer-obstacle collisions: Molecular Dynamics simulations and theory.* Annual March meeting of the American Physical Society (APS), Los Angeles, California, USA, March, 2005.

4. Sorin Nedelcu, **M. Kenward**, L. McCormick G. W. Slater. *Theory of End-Labeled Free Solution Electrophoresis: Using Branched Polymeric Labels with ssDNA.* Annual March meeting of the American Physical Society (APS), Los Angeles, California, USA, March, 2005.

5. **M. Kenward** and G. W. Slater. *Molecular Dynamics Simulations of Polymer Friction Coefficients and Polymer Obstacle Collisions.* Annual March meeting of the American Physical Society (APS), Montreal, Quebec, Canada, March, 2004.

6. **M. Kenward** and G. W. Slater. *Molecular Dynamics simulations of polymer friction coefficients and polymer obstacle collisions.* Poster. **Computational soft-matter: From synthetic polymers to proteins.** International winter school on computational soft-matter. Abstract published in conference proceedings. Gustav–Stressemann Institut, Bonn, Germany, March, 2004.

7. G. W. Slater and **M. Kenward.** *Molecular Dynamics simulations of polymer/post collisions.* American Institute of Chemical Engineers (AIChE), San Francisco, California, November, 2003.

8. G. W. Slater, B. A. Buchholz, J. M. Zahn, **M. Kenward**, A. E. Barron. *Exploiting a transient elongational flow field to prepare monodisperse polymer samples by midpoint chain scission.* American Institute of Chemical Engineers (AIChE), San Francisco, California, November, 2003.

9. **M. Kenward** and G. W. Slater. *Molecular Dynamics simulations of polymer obstacle collisions.* Poster. **Hairy Interfaces and Stringy Molecules.** International Summer

School and Workshop on Colloids and Biophysics, University of Southern Denmark, Odense, Denmark, August, 2003. Awarded Travel Grant.

10. **M. Kenward** on behalf of G. W. Slater. *Molecular Dynamics simulations of polymers in microfluidic environments.* 1st Annual Canadian Network for Computational Materials Science (CNCMS) Workshop, McMaster University, Hamilton, Ontario, May, 2003.

11. **M. Kenward**, F. Tessier, S. Guillouzic, Y. Tatek, Y. Gratton and G. W. Slater. *Molecular Dynamics Simulations of Polymers in Microenvironments.* 17th Annual International Symposium on High Performance Computing, Systems and Applications. Sherbrooke, Quebec, May, 2003.

12. **M. Kenward** and G. W. Slater. *Molecular Dynamics simulations of polymer obstacle collisions with explicit hydrodynamic interactions.* Annual March meeting of the American Physical Society (APS), Austin, Texas, USA, March 2003.

13. Selected to attend *Opportunities in Biology for Physicists.* Sponsored by the American Physical Society, Boston, Mass., USA, September 2002. Awarded Travel Grant.

14. G. W. Slater, **M. Kenward**, F. Tessier. *Computer simulations of polymers and polymer dynamics in confined environments and microfluidic devices.* Poster. Materials Management Ontario (MMO), Partnerships 2002. Toronto, Ontario, June, 2002.

15. **M. Kenward**, F. Tessier, J-F. Mercier, S. Guillouzic and G. W. Slater. *Computer Simulations of DNA in microfluidic devices.* Poster. Opening of the High Performance Computing Virtual Laboratory (HPCVL), Carleton University, May 2002.

16. **M. Kenward** and G. W. Slater. *Molecular Dynamics simulations of polymer obstacle collisions.* Annual March meeting of the APS, Indianapolis, Indiana, USA, March 2002.

Contents

Acknowledgements

I hope I shall not be thought ungracious
if I say at the outset that nothing on earth
could have induced me to (~~attend~~) read the kind of
(~~lecture~~) thesis that you may think
(~~I am about to give~~) you are about to read.

(Variation of Quote)
—— **Sir P. B. Medawar**
(1915–1987)

Gary, many thanks for: your enthusiam for science, patience, opportunities to attend numerous conferences, having a seemingly endless stream of new ideas and helping me refine all the concepts which resulted in the production of this thesis. It has been a great learning experience and a pleasure to work with you.

From friends in the physics department, I would like to thank the following people, if I have missed anyone please forgive me. Fred *gout de beau* (Tessier) for being a great friend, a sounding board for ideas, a mutual connoisseur of *geeky* things, artistic advice, countless cups of coffee, along with possesing a great font of knowledge (and a great knowledge of font – sorry I couldn't resist). Michel (Gauthier) (*pronounced* Mitchel Gothiere) for just being Michel and for putting up with the *mehhhhhhhhh's* and my inability to speak *la langue Française*. J-F (Mercier) for his JF-ness, monumental games of chess (by the way I haven't played since) and the refusal to accept his inner geek and franco-Ontarian heritage. Laurette (*always waiting for Laurette*) McCormick for always making us wait – again I couldn't resist — and a mutual appreciation for great tea. Yannick (YG) Gratton for his uncanny knack at *Franglais* and all of his questions. Seb (*Draknaar*) Casault for all of the good laughs, the beers and the 450 kilometer bike trip. Eric (ECJO) Oliver for the beer making sessions and for the Risk games. Bertrand for your epic rants about, well,

everything, use your unusual gift wisely. Tatek (Yergou) for the introduction to injera and Ethiopian cuisine and for tolerating my *click* language jokes (hopefully you never get to read that). Owen (I drink too much Coke for my own good) (Hickey) for all the tennis games. Katerina (and Ondrej) for their kindness and Ondrej's ability to drink entirely too much beer. Nabil *Mr. B.* (Bennabou) for tolerating my presence in the office for nearly five years. Christian (Jungreuthmayer) for a shared interest in all things Linux. Juergen (*I am not German*) (Zanghellini) for introducing me to the fine art of Bloomsday celebrations and the email about his going away "party". Lora (Canadian Research Chair in Computational Nanophotonics) (Ramunno) for the lunches and the laughs. Bela (Joos) and Ivan (L' Heureux) for many great conversations.

I would thank the greater OpenSource software community for developing the tools with which parts of this thesis were constructed.

To my immediate and extended family — the Kenward's, Spencer's, Foley's, Hadfield's, Hulan's, Gosse's and Husk's— many thanks for all of the great times together and the constant – *"When are you going to be finished?"*

A very special thanks to Fleur and Alexandria for both being a constant source of inspiration. Fleur, thank you for your help when I needed it most, I don't think I could have made it to this point without you.

To Lori Ann – thank you for everything, your: love, kindness, compassion and especially your patience and support throughout all of the trials and tribulations associated with the completion of this thesis.

Martin

December 14th 2006

1 Introduction

The future ain't what it used to be.
—— **Yogi Berra**
(1925–Present)

The aim of this introductory chapter is twofold: to give a summary of the material presented in the ensuing chapters which is suitable for both the expert and (more importantly) the non–expert, and to provide some historical context and motivation for the work presented in this thesis. Ample references are given to ensure that interested readers may easily peruse any related material and topics.

1.1 Prelude

A silent revolution is afoot! With the recent advent of micro- (μm) and nanofluidic (nm) devices and a host of experimental techniques for the manipulation of single isolated polymers and polyelectrolytes, such as deoxyribonucleicacid (DNA), the development of powerful analytical diagnostic equipment is just around the corner [1–5]. Unlike science fiction, equipment reminiscent of Dr. McCoy's *tricorder* (of Star Trek fame) will eventually become science fact. For example, future Lab-on-a-Chip technologies will provide complete and thorough bio-analytical diagnostic tools (essentially providing the capability of an entire laboratory) in palm sized devices. Immature precursors of these technologies are beginning to emerge on the market [6].

The emergence of these technologies and the science underlying their operation involves the conglomeration of a wide range of disciplines. The Human Genome Project, i.e., the sequencing of the human genome (see reference [7] for a complete list of the goals of this monumental endeavour) relied heavily on emerging technologies from the microfluidic world (e.g., automated capillary electrophoresis systems). This *tour-de-force* of human achievement was accomplished decades ahead of its predicted completion date due to the innovative development of new sequencing technologies [8–10]. However, this represents only a step in bringing to fruition the imaginative ideas which hold the potential to revolutionize those fields which lie on the boundaries between physics, chemistry, engineering, biochemistry and biology [11]. Although this sounds like rather heady banter it is merely meant to give the reader an appreciation for the great possibilities which lie ahead. After all, is it not a goal of research to look forward and attempt to see what we can offer to better the understanding of the world around us?

Granted, the preceding paragraph is rather daunting, so it is worth bearing in mind that goals such as the Human Genome Project rely on the work of thousands of individuals working on minutiae *seemingly* unconnected from the context of the original problem. Such is often the nature of science. On that note certainly any sane reader (outside the field) might ask what business a physicist has talking about the Human Genome. *Ah, there's the rub!* The great wheels of human ingenuity find a place for us all. Physicists are playing an enormously important role in these endeavours. Series of conferences (such as the one I attended in Boston (in 2002), *Opportunities for Physicists in Biology*) are even being held to help speed up this collaborative process as the forefront of these fields are pushed forward.

From the perspective of a physicist, this is an exciting time. The breadth and wealth of knowledge being generated at the confluence of the aforementioned fields is difficult to grasp in its entirety. Equally so are all of the inevitable consequences of this work. As scientists we are obliged to be aware of the direct (and indirect) implications of our work. In a conventional thesis, such as this, these are difficult issues to address, although at the very least we are responsible for being aware of them [12, 10].

At any event, we now turn our focus to the work at hand, providing an introduction to the material in the thesis. The work presented herein revolves around the physics of polymer molecules in a number of different environments. The main focus is related to

applications in micro- and nanofluidics and polymer separation methods. The following sections clarify the main goals of this thesis and the concepts used throughout.

1.2 From *mono* to *poly*: a tale of many *mers*

The world around us (and indeed inside us) is, in the most literal sense filled with polymers. Our fundamental building block as humans is a polymer, perhaps one of the most fascinating, deoxyribonucleicacid or its more well known moniker DNA[1]. The recipe for all things living is in fact *written* on a polymer (DNA). Not to typecast humans but we are essentially polymers and water! Every facet of our lives is affected by the presence of polymers, whether it be the soles of our shoes (or indeed the soles of our feet), the clothes on our backs or the tires on our bicycles, we simply cannot avoid them, they are an integral part of everyday life.

The term *polymer* is most often associated with plastics. Test this for yourself, ask someone on the street what a polymer is—besides them looking at you rather oddly—I bet that their answer will be a resounding "Plastic!" (not that I'm an *anti-plasticisite*; it's just that there are much more fascinating polymers). Instead, polymer is really a more general terminology to refer to an assemblage of repeated subunits or *monomers*. These collections of monomers can have a vast array of properties, hence their omnipresence and usefulness. Moreover, large numbers of these polymer molecules have fascinating collective properties.

As noted in the book *An Introduction to Polymer Science* by Elias [13], there are inherent problems with the common definition and usage of the words *polymer* and *polymer molecule*. In principle they are not synonymous with each other; however, in practice this is not necessarily the case. A polymer is usually defined as some substance composed of many individual polymer molecules (a polymeric material). In this thesis we don't strictly adhere to this usage and *polymer* and *polymer molecule* are used synonymously in many instances.

In a general sense a polymer (read polymer molecule) is simply a series of monomers, which we denote by A (of some particular chemical composition), which are covalently

[1] I will avoid TUOABTAD as much as possible in this thesis. For those unfamiliar with this, TUOABTAD is an acronym for "the use of acronyms before they are defined".

bonded to one another. Alternatively one can have several different types of monomers, A, B, C, ... connected in a variety of ways. Figure **1.1** shows a few of these polymers, both the linear variety and branched polymers (where monomers branch off from the main polymer chain). It is about here in every thesis on polymers that one of the simplest polymers, polyethelyene is introduced . This thesis is certainly no different. Polyethylene's monomer is simply CH_2 and a polyethylene polymer is constructed of many of these repeated monomer units connected by covalent bonds (with terminal CH_3 groups at the ends of the molecule, as shown in Figure **1.2**). This is done much in the same manner that one constructs, dimers, trimers, tetramers etc. The word polymer then is simply the N^{th} order equivalent of these expressions and means many–units (*poly–mer*).

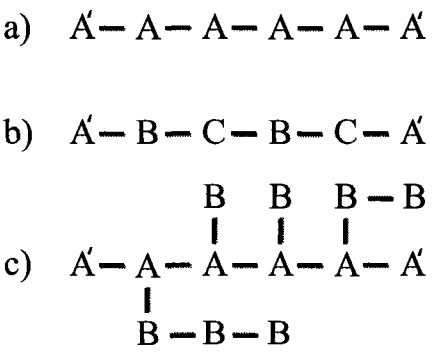

Figure 1.1: Schematic depictions of simple polymers. a) A linear homopolymer comprised solely a single monomer species A, with terminal A' monomers. b) A linear copolymer composed of three types of monomers, A, B and C c) A branched copolymer composed of two monomer types A and B.

Polymers have a large range of sizes. Here we talk about size in terms of the number of monomers N (referred to as the degree of polymerization). Equivalently one can talk about their actual molecular weight or any other measure of polymer size (e.g., number average molecular weight) some of which are discussed later. Typical polymers like polyethylene can range in size from hundreds to tens of thousands of monomers, $N \in [10^2, 10^5]$. However, there are truly gigantic polymers which can have on the order of millions to billions of monomers [14]!

Before delving further into polymers-present lets take a brief diversion into polymers-past and a few historical tidbits. It wasn't until the early 20^{th} century that the view of polymers as large distinct molecules was accepted. It was originally surmised that polymers were complex colloidal systems and the notion of polymers being long individual molecules was initially rejected by the scientific community [14].

To quote Grosberg and Khokhlov's book *Giant Molecules* [14], many great scientific ideas go through three stages,

— at the beginning people say, "It's impossible!" then, "There may be something in it!" and

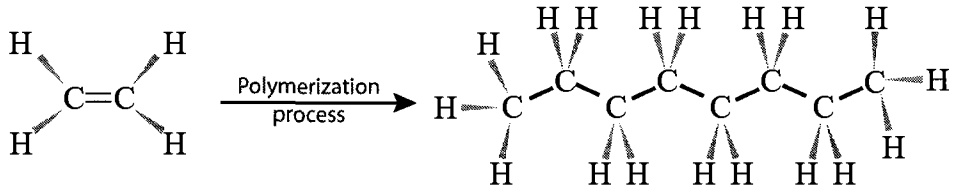

Figure 1.2: A typical polymer, polyethylene. Polyethylene is produced by a polymerization process involving ethylene molecules. The chemical formula for the polyethylene polymer molecule is $CH_3 - [CH_2]_n - CH_3$, where n is the number of monomers in the interior part of the chain, the total number of monomers would then be $n + 2$ taking into account the ends of the chain.

eventually, "Oh well, but that's a well known fact!" [14] —

Polymers are the prototypical example of this phenomena.

Hermann Staudinger[2] first proposed that polymers were indeed compound molecules and not complex colloidal systems (as was widely assumed). He also coined the German term *makromoleküls* (the English equivalent that is widely used today is *macromolecules*, *macro* being Greek for large). The difference between a *polymer* and a *macromolecule* is rather simple, most if not all macromolecules are polymers (since they are composed of many repeating subunits). However, not all polymers are macromolecules and the term is reserved for the special class of polymers which have thousands to tens of thousands of monomers (these are just semantics and no clear quantitative distinction exists).

Staudinger's concept had many stalwart opponents and he was known to have been jeered at during seminars while discussing this idea [14] — the "It's impossible!" phase. It took about 10 years from the time that Staudinger first proposed the concept (early 1920's) until enough experimental evidence was produced to substantiate this claim (mid 1930's)—the "There may be something in it!" phase. Finally, the notion of polymers being large covalently bonded molecules became the mainstay of polymer science and entire fields devoted to their research ensued. Staudinger later received the Nobel prize for "his

[2]The index contains both conventional index content and brief history bites for all names mentioned in the text of the thesis.

discoveries in the field of macromolecular chemistry" [15]. Thus the, "Oh well, but that's a well known fact!" phase.

Long before Staudinger's conceptual breakthrough polymers were used in many fascinating ways. For clarification I will define two general groups of polymers: naturally occurring polymers and synthetically produced polymers. Naturally occurring polymers are those created by or as a result of some natural process in nature. Synthetic polymers are artificially made by chemical means and do not otherwise occur in nature [14].

A particularly interesting example of polymer usage is that of natural latex, which is the sap (also known variously as resin or gum) from a number of types of trees, most notably the rubber tree (*Heveas brasiliensis*) not to be confused with the common household plant of the same name which is really a ficus (*Ficus elastica*) [16]. The ancient Mayans of early Mesoamerica are known to have extracted this sap (much in the same way as maple syrup is collected today) as early as 1600 BC. Through a stroke of good luck, the morning glory plant normally grows next to rubber trees and the Mayans eventually learned that mixing juices from the morning glory and the sap from the rubber tree yield an initially malleable substance which sets into a springy material much like the rubber in well known *Indian rubber balls* [14].

Incidentally, the term *rubber* is attributed to British chemist Joseph Priestly, who first noted its efficacy in removing pencil marks from paper if rubbed across them, he also coined the term *Indian rubber*. This material (known to the Mayans as *caa o-chu* (loosely meaning wood which weeps) was fashioned into various items, most notably a ball used in a traditional game (often resulting in sacrificial killing), idols and in various implements. The modern day word for rubber in French is caoutchouc, most likely deriving from the original *caa o-chu*. It wasn't until Europeans explored much of central America that rubber made its first appearance in Europe (rubber trees are only indigenous to South America) [16].

Another milestone in the history of polymers (or of rubber at least) was the discovery and popularization of the process of vulcanization of rubber (something undoubtedly mentioned in numerous other theses!) [14, 17]. The problem with the rubber material from the last paragraph is that it degrades rather quickly (often due to exposure to sunlight). Vulcanization is essentially a process to stabilize rubber (using heat and a stabilizing additive, for example sulphur). Most sources indicate that Charles Goodyear was the first

to successfully vulcanize rubber using sulphur. However, there is also evidence that early Mayans carried out a similar process to stabilize the rubber created from the rubber tree [16]. Vulcanized rubber solved many existing problems with commercial rubber (in particular it's stickiness) and spawned the modern industry of rubber production.

The first commercially successful synthetic polymer was that created by Leo Baekeland, the commercial name of which was Bakelite (it's chemical name is phenol formaldehyde resin polyoxybenzylmethylenglycolanhydride) [18]. Bakelite is a non-conducting and rather good heat resistant material, which made it ideal for use in electrical applications. In fact, there is a very good chance that there is still some Bakelite in your home today (probably in an old appliance or light fixture). As noted on Wikipedia [19], a search for Bakelite on eBay™ [20] will return with a number of products readily available, all of which contain Bakelite (for the really curious there is also an online Bakelite museum [18]).

Although commercial synthetic polymers and products resulting from them are common in our everyday lives and products that we buy (mostly in the form of plastics), the real champions of polymers are naturally occurring ones. Examples of naturally occurring polymers include: latex, surfactant molecules (found in cell membranes and the key ingredient in detergents), proteins, complex sugars, starches and DNA (to mention just a few). The stuff of life (so to speak) is polymers and certainly every single living thing is composed to a large extent of polymers. Of the naturally occurring polymers, the sub class that includes those occurring in biological entities are perhaps the most interesting as they are the molecules which control in great part the essential mechanisms for life as we know it. Understanding them is crucial to unravelling the mysteries of biological function. Certainly one of the most intriguing of these polymers is DNA.

1.3 DNA – a polymer in a class of its own

The previous section gave a flavour of some polymeric substances, where they occur, a few examples of their uses and a brief history of their study. Some passing mention has also been made of DNA. As a polymer, DNA is unique; it is truly a *macromolecule* and certainly in terms of relative importance it is pretty high on the list (I could not have written this thesis without it).

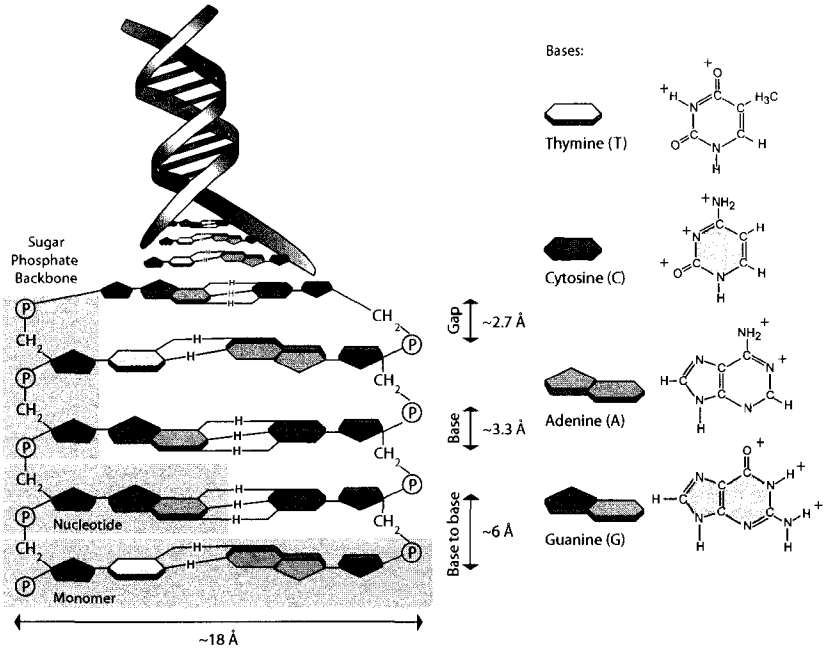

Figure 1.3: A double stranded DNA molecule and its monomer units, the so-called bases Adenine (A), Thymine (T), Cytosine (C), and Guanine (G) (with the associated sugar-phosphate backbone) in a schematic representation of the double helical structure of DNA. Also shown is the sizes of the components of DNA. *Adapted from Access Excellence @ the National Museum (original image online [21]) — with written permission.*

DNA is a giant among polymers. Figure **1.3** shows a schematic picture of a double stranded DNA molecule (dsDNA) (a single stranded DNA (ssDNA) is simply one strand of the DNA double helix). The monomeric units of DNA are its famous bases: Adenine (A), Thymine (T), Cytosine (C), and Guanine (G). One of these bases and the attached sugar phosphate group along the backbone of the dsDNA is referred to as a nucleotide. The bases are paired in such a manner that A is paired with T, and C paired with a G base.

Figure **1.3** also shows the chemical structure of these bases. It is worth noting that the AT pair is bound together with a double hydrogen bond while the CG pair is bound with a triple hydrogen bond. Deep sea creatures living near hydro-thermal vents thrive in an environment in which pressures exceed ten times that of the normal atmosphere

and temperatures are on the order of 400 °C [22]. These creatures have a proportionally higher number of CG bases. The CG bases are connected with triple bonds. This increases the effective stability of their DNA and allows them to endure the harsh conditions of the deep sea environment [22].

The human genome is essentially the sequence of AT and CG pairs which occur in an individual's DNA. This sequence is literally the recipe for life (this is of course a gross over-simplification and although the genetic information is directly encoded in an individual DNA many other components are need to rebuild an organism, e.g., proteins and other cellular components). The human genome contains roughly three billion base pairs. To put this amount of information into perspective, if this thesis were only text and had three billion characters (roughly, 32 lines per page, 80 characters per line, current font size) it would be approximately 1.2 million pages long! It is also rather surprising that the human genome is not nearly the longest, many other species have much larger genomes. Table **1.1** gives a listing of some values for the size of genomes of a number of different species. The common butterfly has a genome with 1.2×10^{11} bases [23]!

Species	Number of Chromosomes	Number of Genes	Size of Genome (millions of base pairs)
Butterfly	380	(Not Known)	124,900
Human	46	25,000	3,300
Corn	20	59,000	2,500
Chicken	78	23,000	1,000
Rice	24	45-56,000	441
Fruit Fly	8	14,000	165
Wall Cress	10	25,000	125

Table 1.1: Table of common species and a listing of their: number of chromosomes, number of genes and number of base pairs in their genome [23].

Evidently, it's not the size of the genome, it's how you use it (being tongue in cheek here). Clearly genomic size is not all that matters when it comes to the complexity and place in the hierarchy of the world (for example the size of the human and corn genome

are on the same order of magnitude!). Why some genomes are longer is certainly a very important question. It turns out that much of the content of DNA is non-coding (i.e., does not directly code for a gene or protein) but is thought to serve other purposes (related to structure and evolution. These non-coding regions used to be referred to as junk DNA [24].

To put the size (or length) of DNA in perspective, we (i.e., humans) have a genome with three billion bases, a quick back-of-the-envelope calculation using those values shown in Figure **1.3** gives an estimate of the effective length of a DNA. A single human genome (if you calculate the distance along the double helix) is an astounding 1 meter in length!! Although this seems like a lot of stuff to pack into a cell, nature has devised very efficient schemes of packaging DNA [14]. Figure **1.4** is a schematic illustration of the packaging of DNA inside a cell (the actual packing of DNA inside a cell is a very complex and highly efficient process [14]). Figure **1.5** shows a schematic representation of the relative lengths of DNA scaled by a factor of 10^6. The genome, i.e., the sequence of A, T, C and G's, *codes* for genes and subsequently the genes *code* for proteins. When you read *code,* it can be interpreted loosely as *provide a set of instructions to build* — much in the same way a computer code instructs a computer to do things in its language of binary. Genes and proteins (the workhorses of cellular machinery) are in turn polymers!

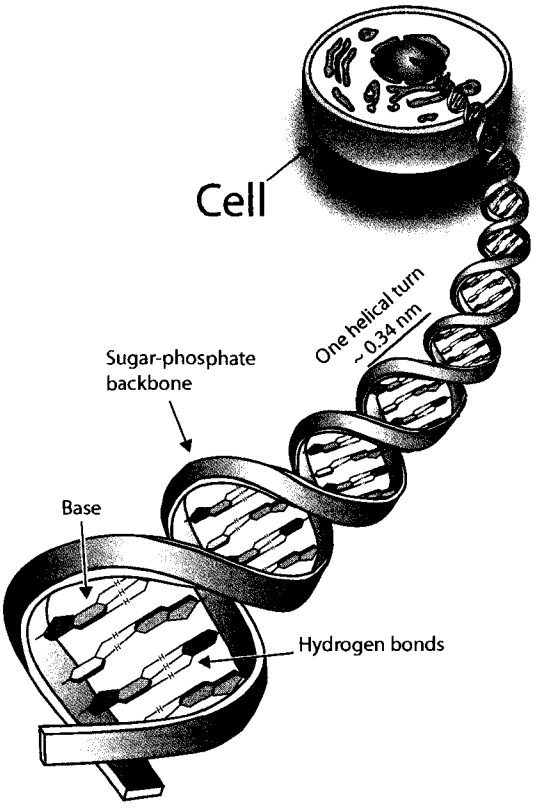

Figure 1.4: Schematic illustration of a DNA molecule and a cell. *Adapted from Access Excellence @ the National Museum (original image online [25]) — with written permission.*

Like synthetic polymers, DNA has a rather long history. To do full justice to the topic probably requires an entire book unto itself. The approach here is to just mention some of the important milestones in the history of DNA. This is done entirely in Figure **1.6**.

It is a light hearted approach to the chronology of DNA. (Caricatures in Figure **1.6** are reproduced and modified with written permission of Dr. Alfred Buchanan of Santa Monica College).

There are several particularly noteworthy episodes in the history of DNA. The first being "unravelling" of the DNA structure by James Watson, Francis Crick and Maurice Wilkins (not shown in Figure **1.6**), with credit later given to Rosalind Franklin [26]. There are numerous interesting accounts of these events including a book written by Watson himself [26]. The discovery of the structure of DNA was a milestone in scientific history. The other immediately notable event is the sequencing of the Human Genome [7]. The last picture (the large question mark) is what we can expect in the future.

In this section, I have given the mistaken impression everything is known about DNA; this is very much far from the truth. Although a generic sequence of the human genome has been carried out, it took nearly two decades to accomplish this task! Being able to sequence an individual's genome in a tractable amount of time (less than a day and for less than $1000) is a holy grail of science. Moreover, the fundamental physics of DNA (and indeed of polymers in general) in many situations are still not well understood.

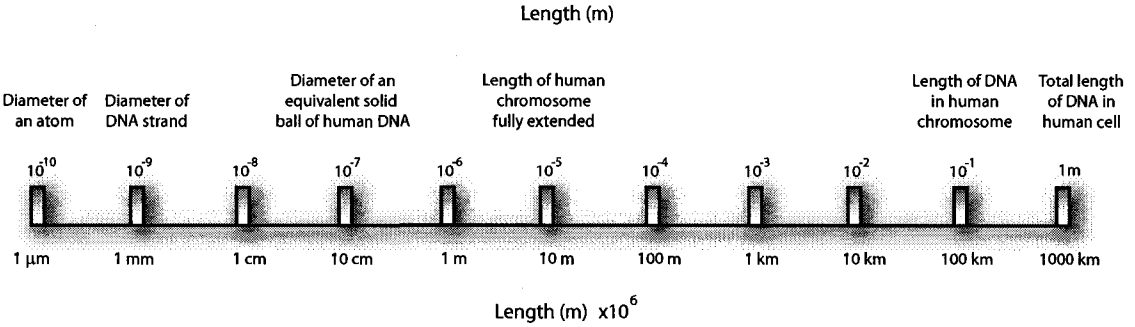

Figure 1.5: Relative lengths of DNA and distances scaled by a factor 10^6. The total length of DNA inside a human cell is on the order of 1 meter!

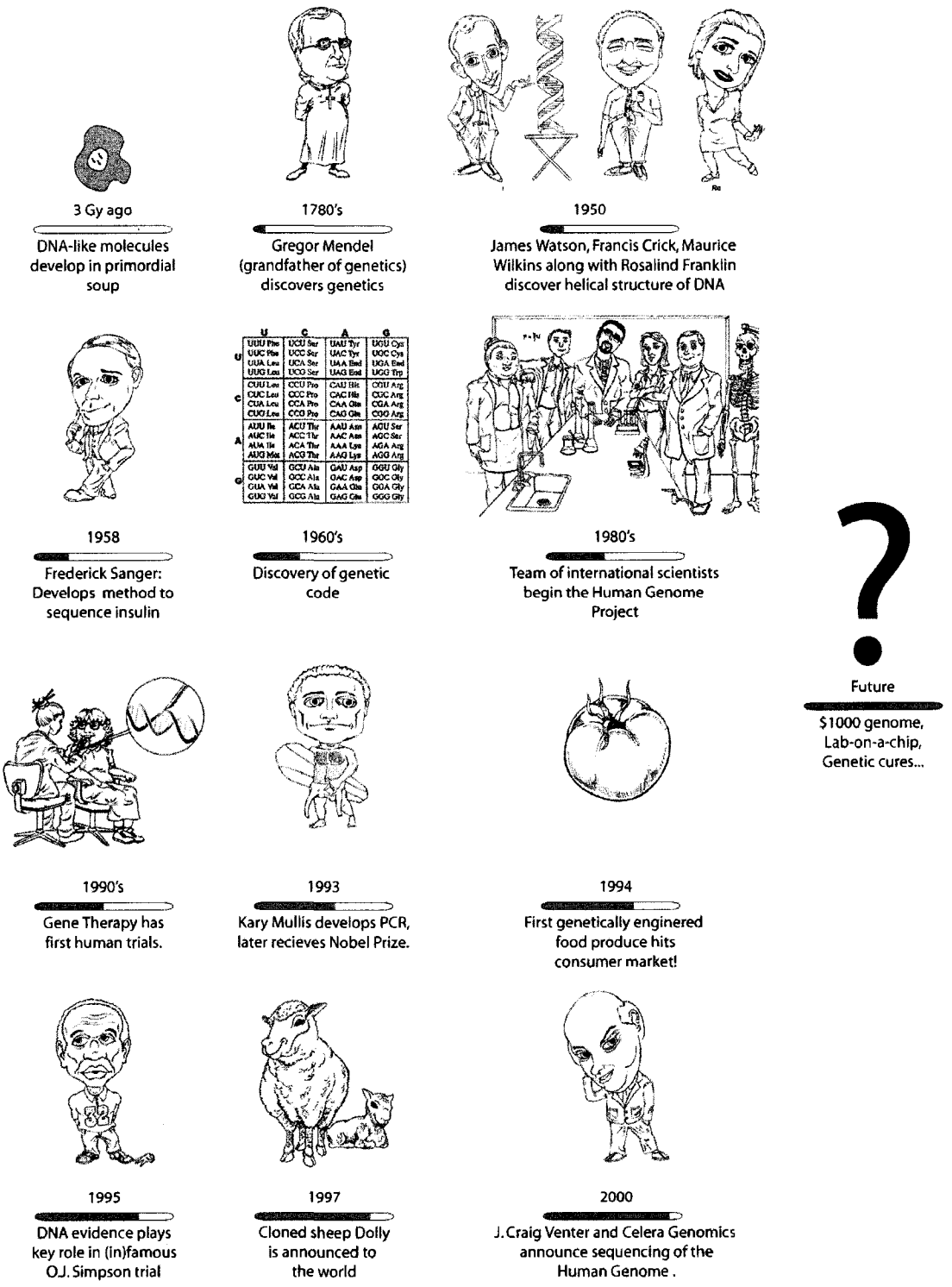

Figure 1.6: Chronology of DNA – a light hearted depiction. Caricatures reproduced (and modified) with written permission of Dr. Alfred Buchanan (Santa Monica College). Original images can be found on the website for Santa Monica College [27].

1.4 The wet computing revolution

You will recall that the first line of this Chapter stated that *A silent revolution is afoot!*. Indeed, this is the case. It can be thought of as a wet computing revolution, very much akin (in many regards) to the revolutions of solid state science (for example the development of the transistor and related integrated circuit technology) and the emergence of computers in the early 1960's [28]. This revolution is the development of micro- and nanofluidic devices and the associated components and technologies of which they are comprised [4].

The fields of micro- and nanofluidics can be loosely defined as the science of systems which contain, manipulate, detect, analyze or process fluid (and constituent components, polymers for example) at length scales on the order of micrometers (μm $\equiv$ 10^{-6}m) to nanometers (nm $\equiv$ 10^{-9}m) with associated fluid volumes on the order of nano– and picolitres [29]. To quote a recent review from George M. Whitesides [29]:

> — As a technology, microfluidics seems almost too good to be true: it offers so many advantages and so few disadvantages (at least in its major applications in analysis) ...The field of microfluidics is in early adolescence, and still lacks essential requirements (e.g., integration into complete functional systems), in addition to the integration of components into systems that can be used by non-experts. As a field, it is a combination of unlimited promise, pimples and incomplete commitment. This is a very exciting time for the field, but we still do not know exactly what it will become when it grows up. [29] —

Fluidic technologies have such wide spread applications that at first glance it is difficult to understand why they are not more pervasive. As Whitesides notes, the bated spread of microfluidics is certainly not a peculiarity, it is a phenomenon well known to the adoption of new technologies (as they struggle, as he puts it, to "make it into the big time" [29]). Applications include: sequencing technologies, molecular analyses (protein analysis for example), single molecule and single cell biophysics and related medical technologies (the real list is certainly much longer) [30]. There is some irony in the fact that many of us do not realize that the most widespread microfluidic technology is sitting right on our desktops in the form of inkjet printers; the print cartridges are in fact microfluidic devices [31].

In terms of an analogy between the computer revolution and that of microfluidics, the rabbit hole runs deep. Just as the microelectronics era heralded the development and wide spread use of computers, the microfluidic revolution will ultimately spawn entire industries of commercial products. In the early stages this will result in mostly industrial, diagnostic and research related technology and later consumer level [6, 29, 30]. The emergence of high performance bio-analytical technologies centers (e.g., for speedy sequencing) are even predicted, much in the same fashion that existing high performance computing centers are today an integral part of computational sciences. Much of this depends, implicitly, on the current technologies being developed and research being done, right now. Microfluidics (and its associated tools) offer unprecedented opportunities for applications. However, as importantly, it also allows us a unique opportunity to examine, model, develop theories for and do experiments on the fundamental physics of (for example) fluids in confined environments and single molecule (polymer) physics. As a result this will allow the direct testing of many theoretical notions of the behaviour of polymer chains, for example fundamental concepts from statistical mechanics.

One particular application of microfluidics, DNA sequencing, has an equivalent Moore's law (Intel co-founder Gordon Moore stated (1965) that computing power doubles every 18 months) [24]. If you look at the cost to sequence 1000 bases of DNA, as a function of time, it turns out that this is an equivalent of Moore's law and the price drops by a factor of 2 about every 12 months [24]. Microfluidics is now at the forefront of these changes. This year (2006) marks the 25th anniversary of the first sales of a PC for home usage (the IBM PC, on 12 August 1981 (25 years to the day of the writing of this sentence)). It is fascinating to think what microfluidics will look like in 25 years!!

How physics fits into the scheme of things is rather interesting. The naïve approach to building microfluidic devices would be to simply miniaturize existing bioanalytical laboratory equipment and shrink the dimensions of the apparatus. This is both wrong and myopic [29]. The problem is that the physics of normal laboratory-sized equipment is that of macroscopic physics (the pipette and petri dish regime). When the dimensions of the system components shrink to the micrometer scale, not only does the size of your sample decrease, but also the fundamental physics of the system itself changes (dramatically in many instances). This difference is amplified when dealing with nanofluidic systems, where system dimensions may be on the order of 10's of water molecules!

1.5 The conceptual toolkit

The goal, so far, has been to provide a general description of polymers and some of the tools used to study them (e.g., microfluidic devices). In the next two sections we outline the theoretical and computational methods and concepts used in the chapters which follow. To begin, there are three fundamental differences between the macroscopic world and that of polymers/fluids (and microfluidic devices). The realm we are dealing with (polymers in fluids) is one where diffusion is important, flow is laminar (non turbulent) and Reynolds numbers are low. For a refreshing discussion on the latter subject one should read E. M. Purcell's – *Life at low Reynolds number* [32].

1.5.1 Diffusion: micro *versus* macro

The microscopic world of polymers and liquids is a tempestuous one. Consider for example a single particle in a fluid. If one were to track it's position in space, it would appear erratic. This apparent behaviour is referred to as Brownian motion, named after botanist Robert Brown who first published an account of the effect while studying the detailed structure of pollen grains [33]. In actuality, Brown was not the first to observe this effect; Anton van Leeuwenhoek is known to have made similar observations [33]. However, Brown was the first to systematically characterize this phenomenon and unlike previous observations, he did not attribute its existence to an innate living essence and simply stated that it was ubiquitous, occurring in both dead and living material alike [33].

The path of a so-called Brownian particle is an unbiased random walk (or drunkard's walk) and is a result of the constant bombardment of surrounding particles. There are two descriptions of this diffusive behaviour: the macroscopic theory of diffusion which is derived from Fick's Law and diffusion theory (microscopic theory of diffusion). The later is evidently one of Einstein's greatest (albeit lesser known) achievements. In 1905 Einstein published a paper entitled – "*On the movement of small particles suspended in a stationary liquid demanded by the molecular kinetic theory of heat*" [34]. In it he put forward a theory of microscopic particles which undergo incessant motion in the absence of external forces. This paper described what we now refer to as Brownian motion or diffusion. Moreover, this paper prescribed a method to verify Ludwig Boltzmann's molecular kinetic theory

(which was not fully accepted at the time). It is a rather unfortunate loss to science that less than a year later, in 1906, Boltzmann, the undisputed father of statistical mechanics, killed himself in despair, never to see his grand achievement unquestionably verified.

In his paper, Einstein demonstrated two important things [34]. The first, that the mean squared displacement of a particle, $\langle \Delta x^2 \rangle$, with radius R, suspended in a quiescent fluid as a function of time t, with viscosity η at temperature T can be written as

$$\langle \Delta x^2 \rangle = 6Dt, \quad D = \frac{k_B T}{6\pi\eta R}. \tag{1.1}$$

This addressed the long standing issue of attempting to characterize Brownian motion in terms of particle velocities (which both varied rapidly and were rather difficult to measure). Instead one could simply observe the mean squared displacement of a particle over long time scales [33]. Einstein's original result is stated differently; although, only the form of the constants vary (evidently it also gave a novel method to calculate Avogadro's number, N_A). The constant D is now recognized as the so-called diffusion constant (or coefficient) and is the ratio of the thermal energy of a particle ($k_B T$) to its dissipative friction (ξ). For a spherical particle of a of *size* R in a fluid with viscosity η the friction coefficient is $\xi = 6\pi\eta R$. In Chapter 3 we explore in detail this friction coefficient for fluid particles and polymers.

The other major contribution of Einstein's work was a derivation of the diffusion equation

$$\frac{\partial P(x,t)}{\partial t} = D\frac{\partial^2 P(x,t)}{\partial x^2} \tag{1.2}$$

where $P(x,t)$ is the probability of finding a particle at position x, at time t. This version was purely of microscopic origin unlike previous derivations which began from a macroscopic standpoint. The solution of equation 1.2 subject to the initial condition $P(x,0) = \delta(x)$ is

$$P(x,t) = \frac{1}{\sqrt{4\pi Dt}} \exp\left[-\frac{x^2}{4Dt}\right]. \tag{1.3}$$

This theory (a phenomenal conceptual masterpiece) connected in an unambiguous manner the observed motion of particles to kinetic theory and also directly linked the thermal energy of a particle, $k_B T$, to its observed motion [34].

An equivalent approach (from a continuum perspective) to obtaining the diffusion equation begins with what is known as Fick's law. It can be stated mathematically as

$$j(x,t) = -D\frac{\partial c(x,t)}{\partial x} \tag{1.4}$$

where $c(x,t)$ is the concentration of material and $j(x,t)$ the flux at position x and time t. Equation 1.4 says that a macroscopic flux is both driven by a concentration gradient and is a linear function of $\partial_t c(x,t)$. One then combines equation 1.4 with the continuity equation

$$\frac{\partial c(x,t)}{\partial t} = -\frac{\partial j(x,t)}{\partial x} \tag{1.5}$$

which qualitatively says that material is neither created nor destroyed (in the absence of a source or sink) but moves from one place to another. Combining equations 1.4 and 1.5 leads to the macroscopic diffusion equation:

$$\frac{\partial c(x,t)}{\partial t} = D\frac{\partial^2 c(x,t)}{\partial x^2}. \tag{1.6}$$

Equations 1.2 and 1.6 are identical; however, equation 1.2 was derived purely on the basis of macroscopic observables and does not relate them to the microscopic world, whatsoever. In fact, $c(x,t) = C_0 P(x,t)$, where C_0 is the total concentration in the system.

Perhaps the most physically intuitive method to derive the time dependence of the diffusion of a particle, is that proposed by Langevin and is the one most often seen in text books [33]. In this method one simply equates the forces acting on a particle, including an appropriate stochastic force (both fluctuating and random) along with frictional terms [33]. The Langevin approach also provided direct calculation of the short time scale behaviour of a Brownian particle and he showed that the mean squared displacement of a particle can be written as

$$\langle \Delta x^2 \rangle = D\left[t - \gamma^{-1}\left(1 - e^{-\gamma t}\right)\right]. \tag{1.7}$$

For times $t \ll \gamma^{-1}$, the mean square displacement looks like

$$\langle \Delta x^2 \rangle \simeq \left(\frac{k_B T}{2M}\right) t^2 \tag{1.8}$$

while for $t \gg \gamma^{-1}$ we recover the Einstein expression of

$$\langle \Delta x^2 \rangle \simeq \left(\frac{k_B T}{\xi}\right) t. \tag{1.9}$$

For short time scales $t \ll \gamma^{-1}$ the motion of a particle appears ballistic while for long time scales $t \gg \gamma^{-1}$ we obtain the standard Brownian motion of a particle [33]. This addressed a long standing question about the effective velocity of a Brownian particle over various time scales.

1.5.2 Navier-Stokes and fluids

We now turn our attention to a description of fluids from macroscopic hydrodynamics. The equation which describes fluid behaviour (from a macroscopic perspective) is the classic Navier-Stokes equation given by

$$\frac{\partial \mathbf{u}}{\partial t} - \mathbf{u} \cdot \nabla \mathbf{u} = -\frac{1}{\rho}\nabla p + \eta \nabla^2 \mathbf{u} \tag{1.10}$$

where ρ is the fluid density, η is the viscosity, p is the pressure and $\mathbf{u} = \mathbf{u}(\mathbf{r}, t)$ is the velocity of a fluid element at position $\mathbf{r}$ at time t [35]. This represents the equation of motion for an incompressible fluid. Does anything change when we move to the microfluidic domain?

We can non-dimensionalize equation 1.10 using the following set of transformations:

$$\mathbf{r}' = \frac{\mathbf{r}}{d}, \quad \mathbf{u}' = \frac{\mathbf{u}}{v}, \quad t' = \frac{t}{vd^{-1}}, \quad p' = \frac{p}{\eta d v^{-1}}, \tag{1.11}$$

where v and d are characteristic velocities and length scales of the system. Using the above transformations we can rewrite equation 1.10 as

$$\mathrm{Re}\left(\frac{\partial \mathbf{u}'}{\partial t'} - \mathbf{u}' \cdot \nabla' \mathbf{u}'\right) = -\nabla' p' + \nabla'^2 \mathbf{u}' \tag{1.12}$$

where Re is the so-called Reynolds number [36]. Consider the flow of a fluid, at velocity v in a narrow constriction of dimension d or equivalently an object with dimension d moving in a fluid at velocity v. The Reynolds number in this case can be written as

$$\mathrm{Re} = \frac{dv\rho}{\eta}. \tag{1.13}$$

A more physical way of obtaining a measure of the Reynolds number is to consider the ratio of the inertial to viscous forces acting on a particle [37] and it can be written as

$$\mathrm{Re} \propto \frac{\mathrm{InertialForces}}{\mathrm{ViscousForces}} = \frac{\frac{1}{2}\rho v^2 d^3}{v\xi} \tag{1.14}$$

which will give an equivalent result to that of equation 1.13. To borrow some examples from Purcell [32], Table **1.2** summarizes some typical Reynolds numbers for various sized bodies.

For low Reynolds numbers the Navier-Stokes equation can be written as

$$\nabla'^2 \mathbf{u}' - \nabla' p' = 0. \tag{1.15}$$

What this means physically is that inertial terms are negligible for objects at low Reynolds number. As an example, if an external force is applied to an object in the low Reynolds number limit ($\mathrm{Re} < 1000$), when that force is switched off the object will stop immediately (i.e., it will not *coast*). In actuality the velocity relaxes exponentially fast [36]. This is very different from our everyday experience, where things *coast* due to inertial terms, for example when you swim [32].

As we have seen a natural consequence of a low Reynolds number is that the Navier-Stokes equation can be written in the form shown in equation 1.15. In this case it turns out that the fluid flow is always non-turbulent or smooth (i.e., there are no instabilities in flows at low Reynolds number). This has fascinating consequences in microfluidics. For example the mixing of two fluid streams in a microfluidic device occurs only by diffusion, since you cannot generate turbulence [36–38].

Object	Dimensions (d)	Velocity (v)	Reynolds number (Re)
Blue Whale Swimming	10m	20km/hr	10^8
Human Swimming	1m	1m/s	10^6
Goldfish Swimming	5cm	1m/s	10^5
Spermatozoa Swimming	10μm	1-3 mm/min	10^{-2}
Microfluidic device	10μm	1cm/s	1
Nanofluidic device	10nm	1mm/s	10^{-2}

Table 1.2: Table of common Reynolds numbers (Re) for different *objects* of varying length and velocity scales. As the dimension of the objects decreases the Reynolds number decrease significantly [32].

To summarize, the physics of fluids at the microscopic scale: i) molecules are in continual diffusive motion, ii) inertia doesn't matter and velocities relax instantaneously and iii) flow at low Reynolds number is smooth [36, 37]. In a nearly identical manner, similar ideas apply to polymers. There are however additional concepts needed to model polymers and their behaviour.

1.5.3 Polymers: simple approaches

The simplest model for a polymer is a series of N connected units [39]. If we forget about the detailed structure of the polymers we can (rather naïvely) model them as connected segments (of a fixed length b) in space. We will also remove the restriction that real polymer segments cannot overlap one another (i.e., no self-avoidance or excluded volume) [39]. This corresponds to a discrete random walk, i.e., connected segments that have random orientations with respect to one another as depicted in Figure **1.7** and is referred to as the freely jointed chain (FJC) model. To characterize the static properties of this

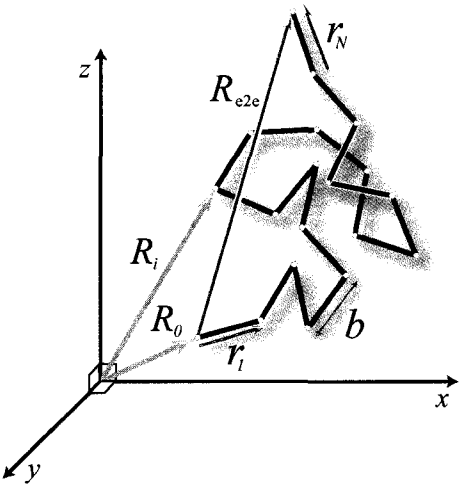

Figure 1.7: Illustration of a discrete (non self-avoiding) random walk polymer (freely jointed chain) with N segments of fixed unit length of b. The end-to-end vector of the polymer $\mathbf{R}_{e2e}$ is shown along with the individual segment vectors $\mathbf{r}_i$.

polymer lets examine the end-to-end vector, i.e., the vector connecting the terminal ends of the molecule. Denote the positions of the terminal ends of the chains by $\mathbf{R}_0$ and $\mathbf{R}_N$ respectively and the positions of the joints of the chain by $\mathbf{R}_i, i \in [1, N-1]$. Further denote the individual segment vectors as $\mathbf{r}_i, i \in [1, N]$. The end-to-end vector of the molecule $\mathbf{R}_{e2e}$ can then be written as

$$\mathbf{R}_{e2e} = \mathbf{R}_N - \mathbf{R}_0 = \sum_{i=1}^{N} \mathbf{r}_i \tag{1.16}$$

and where $|\mathbf{r}_i| = b$. It is straightforward to show that the average value of the end-to-end vector is actually zero ($\langle \mathbf{r}_i \rangle = 0$ since there is no preferential direction of the polymer segments), but the second moment, $\langle \mathbf{R}_{\text{e2e}}^2 \rangle$ is non-zero and is given by

$$\langle \mathbf{R}_{\text{e2e}}^2 \rangle = Nb^2. \tag{1.17}$$

In fact all odd moments of a random walk are zero and even moments are non-zero. An interesting method of deriving the properties of a polymer is using a path integral formulation [40].

The key thing to note is that the root mean square end-to-end distance of the molecule scales like

$$\langle \mathbf{R}_{\text{e2e}}^2 \rangle^{\frac{1}{2}} \propto N^{\nu} \quad \text{where} \quad \nu = \frac{1}{2}. \tag{1.18}$$

This is a universal property of random walks which ignore self-avoidance [39]. A variant of the FJC is the freely rotating chain (FRC). In the FRC model the angle, θ, between consecutive bond vectors, $\mathbf{r}_i$, is restricted. This leads to a similar scaling of the end-to-end distance of the chain [39].

The problem with the lack of self-avoidance in these models is that, physically, chain segments cannot overlap one another due to excluded volume (i.e., the finite size of units on a polymer chain). The first theory to successfully treat this excluded volume effect for polymers was that developed by Flory [39], although Kuhn was the first to note its qualitative importance for the properties of polymers [39].

The excluded volume effect causes a chain to *swell*; therefore, a chain with self-avoidance would naturally be larger than an equivalent chain which neglects self-avoidance. The inclusion of excluded volume does not allow for an analytical solution for the end-to-end distance. Flory's approach was to calculate the free energy of a chain which included this excluded volume (causing the chain to swell) and the chain connectivity (causing the chain to be more compact). The size of the polymer chain which minimizes this free energy is the effective size of the chain. The result obtained by Flory was

$$\langle \mathbf{R}_{\text{e2e}}^2 \rangle^{\frac{1}{2}} \propto N^{\nu} \quad \text{where} \quad \nu = \frac{3}{5}. \tag{1.19}$$

The exponent $\nu = 3/5$ is now referred to as the Flory exponent of the chain. Table **1.3** shows the results for several different regimes of a polymer chain including random walks and excluded volume chains. Although these simple models above prescribe a method

Model Type	Exponent (ν)
Random walk	$\frac{1}{2}$
Self-avoiding walk	$\frac{3}{5}$
Fully extended	1
Collapsed	$\frac{1}{3}$

Table 1.3: Table of Flory parameters for different chain types: random walk, self-avoiding walk, fully extended and collapsed (excluded volume) chain..

to examine the static properties of polymers, it does not give a description of dynamic properties of a polymer, for example, the diffusion coefficient. If one were to track the center-of-mass of a polymer it would diffuse in manner very much like that of a single particle undergoing Brownian motion [39]. The diffusion coefficient of a polymer molecule would naturally be written as

$$D = \frac{k_B T}{\xi_p} \tag{1.20}$$

where ξ_p is its friction coefficient. As a first guess, we might assume that $\xi_p = N\xi_1$, where ξ_1 is the friction of an individual polymer segment, i.e., that

$$D \propto N^{-1}. \tag{1.21}$$

This guess would be wrong. Experimentally, if one measures the diffusion coefficient of a polymer chain (in dilute polymer solutions) it scales with the molecular weight of the polymer (read the number of monomers) as

$$D \propto N^{-\frac{1}{2}}. \tag{1.22}$$

Our (albeit incorrect) guess in equation 1.21, can be obtained in a more robust manner from the so-called Rouse model for polymer dynamics [39]. The Rouse model portrays polymers as individual monomers connected via harmonic potentials; one then writes down the equations of motion for such a chain and an analytical solution yielding $D_{\text{Rouse}} \propto N^{-1}$ can be obtained.

The Rouse model completely neglects the effects of the hydrodynamic interactions between different parts of the polymer chain. These hydrodynamic interactions are the

source of the difference between our simple guess and experimentally observed diffusion coefficients [39]. These hydrodynamic interactions (i.e., non-local interactions between polymer segments mediated through a solvent) can be taken into account in the so-called Zimm model. In it, an effective hydrodynamic interaction is added to the equations of motion for the polymer chain. The result for the diffusion coefficient is then

$$D_{\text{Zimm}} \propto N^{-\nu} \tag{1.23}$$

This is in agreement with experimental results (again in dilute solutions). Qualitatively the Rouse model treats polymers as so-called hydrodynamically permeable molecules (in other words as a chain in which segmental motion is not correlated via the presence of a solvent). The Zimm model, however, correctly treats these hydrodynamic interactions. As a result a diffusing polymer really appears hydrodynamically impermeable and behaves as though it were a solid ball with a radius equivalent to that of the effective radius of a polymer ($R \sim N_{\text{p}}^{\nu}$) and equation 1.1 then applies.

These simple approaches are the fundamental starting point for much of polymer physics, though effects such as polymer stiffness and charged polymers bring with them additional concepts. Other natural things to include in these models are solvent properties and its effects on polymer size (poor solvent causes molecules to collapse, whilst good solvent causes molecules to swell) [39]. The variants of these models used in the following chapters are discussed in the context of each paper. Many features, including hydrodynamics, are difficult to model in a robust manner (especially for determining the dynamics of polymer chains). It should be noted that electrostatic effects have not been discussed in this work. In fact, many polymers are charged, including DNA. We do not treat the effects of electrostatic interactions. Instead we treat polymers as uncharged entities throughout the entirety of the chapters which follow. In order to model the dynamics of polymer chains, a natural approach is to attempt to extract properties of polymers and fluids by directly solving the equations of motion governing their behaviour.

1.6 Polymers and fluids *in Silico*

A key tool in the computational physicists arsenal is Molecular Dynamics (MD) simulations. Essentially these numerical simulations are the solution of the *classical* N-body

equations of motion for a particular system, subject to appropriate initial and boundary conditions [41]. These N-bodies can be any physical entity that one needs them to be, for example: liquids, polymers, solids, galaxies and stars. The potentials describing the physical interactions among components of a system (and external forces) are needed for our MD simulations (these potentials are implicitly dictated by the types of bodies used).

The N-body problem is, in general, intractable analytically (except for some special cases for small N) [42]. The only feasible route to a solution is then a numerical one. In the same vein as experimental techniques, computational methods to solve problems are now part and parcel of a theoretician's toolkit [41]. It is certainly worth bearing in mind that computational methods (such as MD) are not meant to replace theory and/or experiment but to complement them in the fullest fashion [43].

A MD simulation is then the numerical solution of the equations of motion for the N-body problem. These equations can be written in terms of a set of N generalized coordinates ($\mathbf{q}$) and momenta ($\mathbf{p}$) given by

$$\mathbf{q} = \{\mathbf{q}_1, \mathbf{q}_2 \dots \mathbf{q}_N\} \tag{1.24}$$

$$\mathbf{p} = \{\mathbf{p}_1, \mathbf{p}_2 \dots \mathbf{p}_N\}, \tag{1.25}$$

where $\mathbf{q}_i$ and $\mathbf{p}_i$ are the generalized position and momentum of the i^{th} body. Since we normally work with Cartesian coordinates we will change the notation from $\mathbf{q} \rightarrow \mathbf{r}$, herein. The Hamiltonian $\mathcal{H}(\mathbf{r}, \mathbf{p})$ for the system is then given by

$$\mathcal{H}(\mathbf{r}, \mathbf{p}) = \mathcal{T}(\mathbf{p}) + \mathcal{V}(\mathbf{r}) \tag{1.26}$$

where $\mathcal{T}(\mathbf{p})$ and $\mathcal{V}(\mathbf{r})$ are the kinetic and potential energies respectively. The kinetic energy $\mathcal{T}(\mathbf{p})$ can be written as

$$\mathcal{T}(\mathbf{p}) = \sum_{i=1}^{N} \sum_{\alpha=x,y,z} \frac{p_{i\alpha} \cdot p_{i\alpha}}{2m_i} \tag{1.27}$$

where $p_{i,\alpha}$ is the momentum of particle i in direction $\alpha = x, y, z$ and m_i is the mass of particle i. The potential energy $\mathcal{V}(\mathbf{r})$ can be rewritten as:

$$\mathcal{V}(\mathbf{r}) = \sum_{i=1}^{N} \phi_1(\mathbf{r}_i) + \sum_{i=1}^{N} \sum_{j>i}^{N} \phi_2(\mathbf{r}_i, \mathbf{r}_j) + \sum_{i=1}^{N} \sum_{j>i}^{N} \sum_{k>j>i}^{N} \phi_3(\mathbf{r}_i, \mathbf{r}_j, \mathbf{r}_k) + \dots \tag{1.28}$$

where the ϕ_n include: external potentials ($n = 1$), pair wise interactions ($n = 2$), three body terms ($n = 3$) and higher order terms ($n > 3$). The pair potential $\phi_2(\mathbf{r}_i, \mathbf{r}_j)$ is the

most important contribution to $\mathcal{V}(\mathbf{r})$. The pair potential usually suffices for liquids and gives excellent agreement with observable properties of liquids. Higher order terms are also very computationally expensive to calculate, which is another reason why they are normally not included [41, 43] for liquids. Higher order terms are often included for polymers since properties such as polymer stiffness arise from higher order interactions.

Let's assume that we do not know an analytical form of the pair potential, but we estimate it as $V_{\text{eff}}(r_{ij})$, where r_{ij} is the distance between two particles i and j. We can then rewrite the potential energy for the system as

$$\mathcal{V}(\mathbf{r}) = U_{\text{ext}} + \sum_{i=1}^{N} \sum_{j>i}^{N} V_{\text{eff}}(r_{ij}) \tag{1.29}$$

where $r_{ij} = |\mathbf{r}_i - \mathbf{r}_j|$ and U_{ext} is an external potential. Evidently this method requires $\mathcal{O}(N^2)$ computations to calculate the interactions between N particles; however, it is possible to reduce this to $\mathcal{O}(N \log(N))$ computations [41] for short range interactions.

What are the salient features of an effective pair potential, $V_{\text{eff}}(r_{ij})$, that would describe the pairwise interaction in a real liquid? The classic example is that of liquid argon [41], studies of which give a typical form for $V_{\text{eff}}(r_{ij})$. Since two particles cannot overlap one another a strong repulsive potential for small r_{ij} is required (the Pauli exclusion principle). While for large r_{ij} there is an attractive potential (van der Waals interactions) [41].

The choice of $V_{\text{eff}}(r_{ij})$ is clearly motivated by the potential obtained from experimental data [43]. Empirical expressions provide the simplest route to modelling the pair potential. The so-called Lennard-Jones potential (sometimes referred to as the 12–6 potential) provides such a description and is given by:

$$V_{\text{LJ}}(r_{ij}) = 4\epsilon \left(\left[\frac{\sigma}{r_{ij}} \right]^{12} - \left[\frac{\sigma}{r_{ij}} \right]^{6} \right) \tag{1.30}$$

where σ and ϵ are the length and energy scales, r_{ij} is the distance between two particles. For liquid argon values of $\epsilon/k_{\text{B}} = 120K$ and $\sigma = 0.34\text{nm}$ yield close approximation to measured experimental potentials [43]. Our simulations use a shifted and truncated Lennard-Jones potential which includes only the repulsive interaction in equation 1.30.

The potential is then

$$V_{\mathrm{LJ}}(r) = \begin{cases} 4\epsilon\left(\left[\frac{\sigma}{r}\right]^{12} - \left[\frac{\sigma}{r}\right]^{6}\right) + \epsilon, & r \leq r_{\mathrm{c}} \\ 0, & r \geq r_{\mathrm{c}} \end{cases} \tag{1.31}$$

where σ and ϵ are the length and energy scales, r is the center–to–center distance between two beads and $r_{\mathrm{c}} = \sqrt[6]{2}\sigma$ is the position of the minimum in the Lennard–Jones potential and corresponds to the cutoff for calculating forces [44, 45]. The fluid that we use in our simulations (in the ensuing chapters) is then composed of Lennard-Jones particles (i.e., particles that interact via this truncated Lennard-Jones potential). It has the expected properties of a fluid such as viscosity; the details of these properties are discussed in the context of the work presented in the chapters on Molecular Dynamics simulations.

Does the ability to reproduce liquid-like properties give us impetus to ignore a more detailed atomistic description of liquids (e.g., hydrogen bonding in water) or for that matter can we start straight from Quantum Mechanics? In fact, that is the wrong question to ask. At least in principle it is always desirable to begin with Quantum Mechanics (though seldom practical for large systems). Instead the question one should ask is, "What phenomena are we interested in studying and over what length and time scales are we interested in studying them?" This implicitly dictates the type of computational approach and model which will allow us to study a system in reasonable amounts of time (e.g., time to complete a Ph.D.). In principle, one can always start with a quantum mechanical description of the system; however, for systems that we study the computational times are simply intractable. Typically as one increases the level of complexity of the system the accessible length and time scales decrease. For example, in

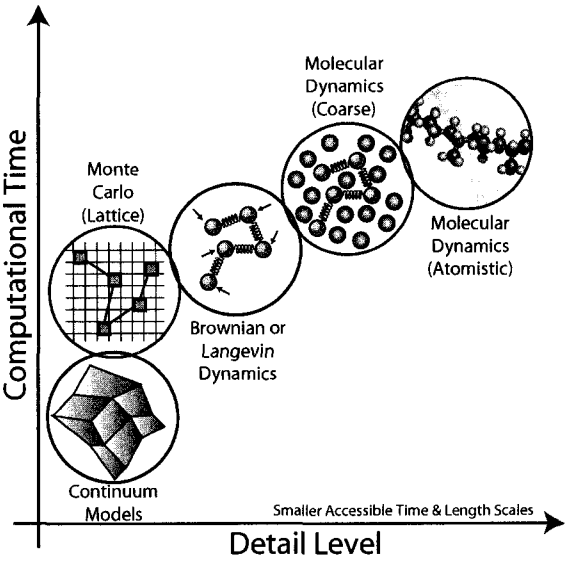

Figure 1.8: Schematic depiction of computational method and detail level versus algorithm type, starting with continuum models and tending towards atomistic (MD) simulations.

atomistic MD one deals with phenomena on length scales of nanometers and time scales on the order of picoseconds while in coarse grained MD one deals with microseconds and micrometers. Figure **1.8** shows a schematic picture of the way I envisage choosing an appropriate schema (i.e., finding the *sweet-spot* for a computational approach).

An approach which provides a good compromise between observable length/time scales and computational times (for the types of phenomena we are interested in) is referred to as coarse graining. This method involves stripping away some of the system details (or degrees of freedom) while preserving overall universal properties [44]. In a liquid, we must have those properties mentioned above, but our model may not explicitly include (for example) the hydrogen bonding of water. We use this coarse-graining ideology in our simulations and model the liquids as Lennard-Jones fluids [43]. The coarse-graining method has become a mainstay of the simulation community and is a valuable tool for examining a wide variety of phenomena [41].

Efforts are being made to reconcile coarse graining methods with atomistic and Quantum mechanical methodologies, using so called multi-scale modelling techniques and/or reverse mapping methods (fine grained inversion) [46, 47]. However, generalized systematic methods to go back and forth between continuum, coarse grained, atomistic and even Quantum level descriptions are currently lacking. One particularly difficult task is developing robust statistical mechanical descriptions appropriate to match boundaries between different domains, for example, matching the boundary between a coarse-grained MD simulation and an atomistic description of the system. One particularly successful example of such an approach is the work on crack propagation in solids. Near the apex of the crack (i.e., a local dislocation in the material) a full Quantum description is used, coupled to an atomistic description at its periphery, which in turn is coupled to coarse grained MD and finally to a continuum model [48, 47].

We apply a similar coarse graining idea to model polymers in our simulations. Figure **1.9** shows a schematic depiction of the idea of coarse graining a polymer. The polymer shown is a bead-spring representation of a real polymer. The key features we need to re-

cover are the excluded volume of two beads (i.e., they cannot occupy the same volume of space) and the connectivity of the polymer chain (i.e., the bonding of the monomers of a chain together). A polymer in our MD simulations is constructed as a series of contiguous Lennard-Jones beads connected via a bonding potential. The potential used to connect the monomers must satisfy two criterion: i) it must oscillate slightly about some mean value (since the distance between two beads will naturally fluctuate) and ii) there must be an upper bound on the maximum distance between two beads. A simple first guess for an appropriate potential might be a harmonic potential; however, this is not bounded and would allow infinite extension of the bonds along the polymer chain. A practical alternative is the so-called Finitely Extensible Non–linear Elastic (FENE) potential which satisfies both criteria and is given by:

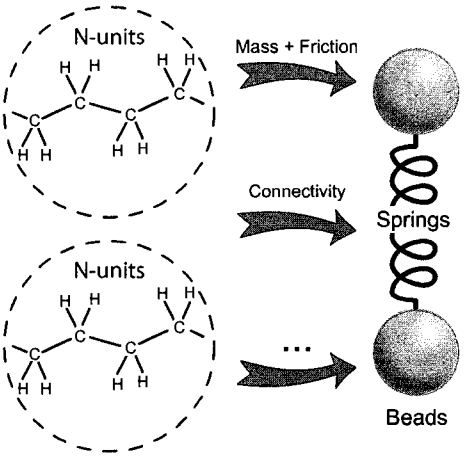

Figure 1.9: Schematic depictions of polymer coarse graining of a polyethylene molecule. Many monomers are *coarse grained* into a single bead, while the connectivity of the monomers are represented by a generalized spring.

$$V_{\text{bond}}(r) = -\frac{\kappa}{2} R_{\text{o}}^2 \ln\left(1 - \left[\frac{r}{R_{\text{o}}}\right]^2\right) \tag{1.32}$$

where R_{o} is the upper bound on the bond distance and κ is an effective spring constant. The linear polymers are modeled as N_{p} Lennard–Jones beads connected via $N_{\text{p}} - 1$ FENE bonds.

The above has given the prescription for the constituent components in our MD simulations (in particular, for polymers and liquids in a coarse-grained picture). Other components appear in the MD simulations presented in the following chapters and are explained in the context of the articles themselves. In order to obtain dynamic properties of the system we need to solve the equations of motion given by

$$\frac{\partial \mathbf{r}_i}{\partial t} = \frac{\mathbf{p}_i}{m_i} \tag{1.33}$$

$$\frac{\partial \mathbf{p}_i}{\partial t} = -\nabla_{\mathbf{r}_i} \mathcal{V}(\mathbf{r}_i). \tag{1.34}$$

The solution of these equations is obtained numerically, i.e., the equations of motion are

integrated using a numerical method. There are numerous methods of doing this, all of which involve discretizing the equations of motion and obtaining solutions using discrete time intervals δt, otherwise known as a finite difference scheme [43, 41]. The *gold standard* for MD simulations is the so-called velocity Verlet method, which is a second order finite difference scheme [42]. The velocity Verlet method is particularly efficient because it satisfies a number of important criteria for an effective integrator (in the context of MD): it is *time reversible* up to machine precision (i.e., the method is invariant under the transformation $t \to -t$) and it is *symplectic* (that is to say it conserves the invariant phase-space volume) meaning that the total energy of the system is conserved and the error on the energy is bounded [42].

Algorithm 1 Algorithm detailing the velocity Verlet method

Require: An integer $N > 1$ where N is the total number of particles in the system.

Require: Initial positions and velocities

for $t = 0$ to $t_{\max}$ **do**
  for $i = 1$ to N where N is the number of particles in the system. **do**
    $\mathbf{r}_i(t + \delta t) = \mathbf{r}_i(t) + \delta t \mathbf{v}_i(t) + \frac{1}{2}\delta t^2 \mathbf{a}_i(t) + \mathcal{O}(\delta t^3)$
    $\mathbf{v}_i(t + \delta t) = \mathbf{v}_i(t) + \frac{1}{2}\delta t \left[\mathbf{a}_i(t) + \mathbf{a}_i(t + \delta t)\right] + \mathcal{O}(\delta t^3)$
    Calculate velocities at $t + \frac{1}{2}\delta t$: $\mathbf{v}_i\left(t + \frac{1}{2}\delta t\right) = \mathbf{v}_i(t) + \frac{1}{2}\delta t \mathbf{a}_i(t) + \mathcal{O}(\delta t^3)$
    $\mathbf{v}_i(t + \delta t) = \mathbf{v}_i\left(t + \frac{1}{2}\delta t\right) + \frac{1}{2}\delta t \mathbf{a}_i(t + \delta t) + \mathcal{O}(\delta t^3)$
  end for
  $t = t + \delta t$
end for

The velocity Verlet finite difference scheme for integrating the equations of motion is summarized by Algorithm 1. One then implements this algorithm by writing a computer code to carry out the computations. The previous line appears trivial; however, the reader should bear in mind that this is an enormous task which can take many months to complete. For the Molecular Dynamics simulations presented in this thesis I wrote the computer programs to carry out these simulations, analyze data, visualize the systems (in 3D, written in OpenGL) and any other task that was needed to extract information from

the simulations. The book by Rapaport was used as a guide for the MD simulation method [41]. There exist many excellent references on the subject [41, 43].

In implementing a MD simulation there are numerous other issues: temperature thermostating, implementing flows and external forces, measuring thermodynamic observables and other quantities and many other implementation details [41, 43]. These details vary significantly from study to study. The remaining particulars of our implementation of MD is explained in each article along with ample references for relevant follow up material [41, 43].

1.7 Polymer dynamics and collisions

In the past few years the field of single molecule polymer physics has undergone a resurgence. This has been motivated both by the microfluidic revolution mentioned in the preceding text, and also by the development of tools such as single molecule fluorescence microscopy (which allows the realtime visualization of individual polymer chains and their dynamics). The combination of these tools provide methods to directly verify physical models of polymers.

The dynamics of single polymer chains are in part dictated by their friction coefficients, which for chains that are not hydrodynamically permeable, is a function of their conformation. If you deform a molecule you change its friction coefficient. If an external force is applied to a polymer chain (and we are neglecting electrostatic effects in this discussion) the velocity of the chain can simply be written as $v = F/\xi$, where F is the external force on the chain, ξ its friction coefficient and v its velocity. The friction coefficient ξ will be a function of the conformation of the polymer chain. This is one aspect we are able to capture in our MD simulations due to the inclusion of explicit solvent particles. If for example one were using Langevin Dynamics (were the fluid is replaced by an appropriate stochastic force, i.e., solving the Langevin equation) it would would not be possible to recover this phenomenon. However, there are artificial methods of introducing hydrodynamic interactions such as through the Oseen tensor. Thus the explicit solvent (and consequently hydrodynamics) is a key aspect of the MD model we present.

In Chapters 2 and 3 we use our MD simulation model to systematically examine the behaviour and dynamics of polymer chains in both free solution and in the presence of a

obstacles. The free polymer systems presented in Chapter 2 explore the friction of polymers in several different conformations. In Chapter 3 we then turn our attention to the examination of polymers colliding with molecular obstacles and develop a general model for these collisions and compare it with results from Molecular Dynamics simulations.

1.8 Ratchets – taming the tempest

Many molecular processes (e.g., all biological transport phenomena) operate in the realm where diffusion plays a role. Unlike our macroscopic world, in the microscopic domain diffusion is an integral part of transport processes and in many instances biological machinery cannot function correctly in its absence [49]. In this manner diffusion is used to the advantage of molecular entities, instead of trying to overcome it by brute force [49].

Using diffusion as part of transport processes is somewhat counterintuitive, mostly as a result of our bias towards using methods that are analogues of macroscopic manipulation techniques. In Chapter 4 we turn our attention to a particular variant of the methods which rectify the diffusion of molecules to generate net transport.

Consider for example a distribution of particles which have diffusion coefficient D, which is initially delta-distributed, i.e., that the distribution of these particles is a delta function $\delta(x - x')$ centered about some position x'. The well known result obtained from solving the diffusion equation is the probability distribution for the particles given by equation 1.3.

This probability distribution is for particles which freely diffuse and is a Gaussian whose width increases with time, as $\sqrt{t}$. The question then is: How can we rectify the diffusion of these particles to, for example, generate directed motion? There are several ways to do this. A simple yet effective method is the use of a series of asymmetric sawtooth potentials which are periodically switched off and on – this is often referred to as a flashing ratchet potential. Perhaps the definitive review article written on the subject of ratchets is that by Reimann [49].

Consider a distribution of particles localized at the minimum of an asymmetric potential like that depicted in Figure **1.10**. Assume for illustration that this potential is able to completely localize the particles and that their distribution is initially a delta function $\delta(x - x')$. Once the potential is subsequently switched off the particles diffuse away from the

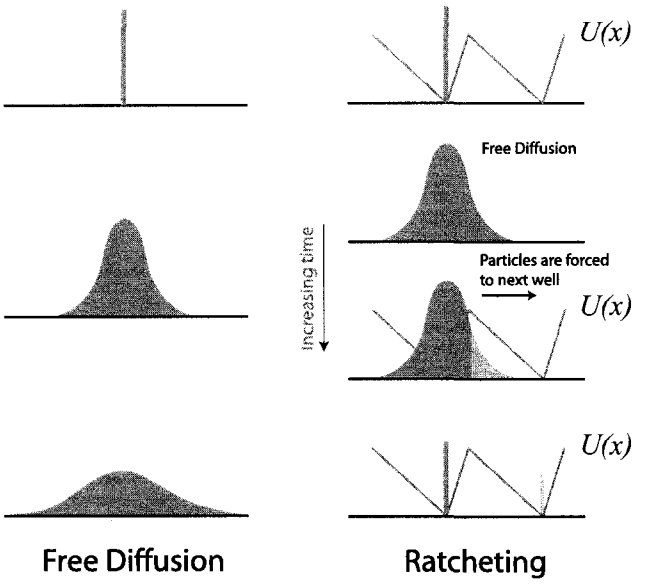

Figure 1.10: Schematic illustration of free diffusion (left) panel and ratcheting mechanism which employs an asymmetric sawtooth potential to generate net motion of particles (right panel). Those particles which traverse past the barrier to the right will be pushed forward to the next well once the ratchet is switched on again. The distribution of particles when the ratchet is on has been exaggerated and in general this distribution is rather broad and not delta distributed.

potential minimum. However, due to the asymmetry of the potential, once the potential is switched on again, some particles will have diffused past the barrier to the right (on the right of Figure **1.10**). These particles will be driven to the next potential minimum and a fraction of particles will be confined in the second of the potential minima while the remaining particles stay in the original ratchet well. Assume for example that the time the ratchet is kept off (for time t_{off}) is short enough that no particles have diffused backwards to the previous well of the ratchet. If this process of switching the ratchet off and on is continued, it is possible to generate net motion of the particles in the ratchet [49]. This may seem like a paradox since we have not applied any net force; however, there is no violation of the second law of thermodynamics since the ratcheting method is essentially biasing the diffusion of particles. A variant of this ratchet idea was discussed by Feynman

in his Lectures on Physics to illustrate the second law of thermodynamics [50].

Moreover if you have particles with different diffusion coefficients D it is possible to separate them from one another. This principle can be applied to polymers. The paper of Bader *et al.* [51] presents a simple model to describe the properties of polymers in ratchets. In Chapter 4 we turn our attention to the use of ratchets to induce net migration of polymer chains.

Our investigation of this phenomena centers around the idea of using polymer deformation to modulate the transport of polymer chains in ratchets. It is normally assumed that a polymer chain is undeformed by a ratchet potential, thus leaving its friction coefficient (and diffusion coefficient) unaltered. We show that in fact ratchets can deform polymers and alter their diffusion coefficients, thereby changing the polymer transport properties. We then apply our Molecular Dynamics algorithm to explore the effect of deformation on the behaviour of polymers in ratchet followed by the derivation of a modified Bader ratchet model which explicitly takes into account polymer deformation. The idea of using polymer deformation in ratchets represents a new concept for the operational mode of a ratchet and can in principle be used to modulate the net transport of polymers in ratchets.

1.9 Polymer scission

In chapter 5 we shift the focus of attention to a different problem from those discussed in the previous three chapters. We examine the degradation (or scission) of polymer chains in pressure driven extensional flows [52]. We also use a different conceptual toolkit to examine the problem. Unlike the previous chapters we do not use MD simulations; instead we use a purely statistical model (in the form of a master equation) to examine polymer degradation. The work in chapter 5 was done in collaboration with the Barron group at Northwestern University (Evanston, Illinois) and was motivated by experiments carried out on the breaking of polymers in extensional flows.

The topic of polymer scission, i.e., the degradation of polymers via some process, has a long history [53]. Some of the original theoretical work dates back to the 1930's, most notably the articles of Kuhn and Freudenberg [54, 55] (published in German), Hopf and the works of Mark and Meyer. Studies of polymer degradation were in part motivated by the ongoing research into the statistical nature of polymer growth and the production of high

polymers [*sic*] (i.e., high molar mass polymers). The degradation of polymers (essentially the reverse process of polymer growth) was of great interest since as it presumed that it would shed some light on the statistical nature of the polymer growth processes. The classic English publication on the matter was published in 1940, by Montroll and Simha [56] and gave a detailed statistical model for the degradation of chains of identical molecular weight which undergo random scission events (i.e., breaking at random positions on the chain) [57].

In living organisms the production of naturally occurring (bio)-polymers (e.g., DNA) is carried out by complex cellular machinery and is often referred to as biosynthesis [13]. For synthetic polymers there are two mechanisms that are used: polymerization and polycondensation. Polymerization is essentially the production of polymers by the monomer-wise growth of polymers to form successively longer chains. For example, the production of polyethylene is achieved by the joining of successive ethylene monomers. This growth process can be schematically represented by the following rule

$$R_{\mathrm{N}} + R \rightarrow R_{\mathrm{N}+1}, \tag{1.35}$$

where R_{N}, R are the inputs for a chemical reaction and $R_{\mathrm{N}+1}$ being the resulting product. This growth process is really a gross oversimplification but it contains the general rule of thumb for polymerization. In actuality there are a number of other factors that one needs to take into account such as the conditions necessary for the process to occur in the first place, and the conditions under which this process will terminate [14]. We don't go into the details of the chemistry of this process (doing such is no trivial task, but apologies are made in advance to any chemist reading this). Polycondensation is different from polymerization in that it normally has resulting byproducts where as polymerization does not [14].

Intuitively one immediate question would be: "What is the resulting distribution of polymers from a polymerization or polycondensation experiment?" Certainly it is difficult to imagine that such a procedure would produce polymers all of the same size. This would entail the Herculean task of having each chain acquire monomers at exactly the same rate. It would also require a method to ensure that the reaction terminating chain growth occurs at the same time for each molecule!

We can mathematically characterize the properties of polymer distributions. Denote the

normalized distribution of polymers by $p(N)$ (i.e., the probability of finding a polymer with N monomers), N being the degree of polymerization of the chains. If the synthesis method were able to produce polymers of a single size say N^*, the distribution of polymers $p(N)$ would then be a delta function $p(N) = \delta_{N,N^*}$. However, this is not the nature of polymer production. It is inherently a stochastic process and the distribution of polymer products $p(N)$ can be rather broad; this is termed polydispersity, that is to say a distribution of polymers as opposed to those of a single size. In order to characterize this broadness, we will define several commonly used metrics to determine the effective dispersion in a polymer sample.

The first measure is the so-called weight average molecular weight; it is defined as M_{w} and can be written as

$$M_{\mathrm{w}} = \frac{\sum_n n^2 p(n)}{\sum_n n p(n)}. \tag{1.36}$$

The second measure of the polymer distribution is the so-called number average molecular weight, which is defined as

$$M_{\mathrm{n}} = \frac{\sum_n n p(n)}{\sum_n p(n)}. \tag{1.37}$$

In the case of a truly monodisperse polymer solution all polymers have the same degree of polymerization (or molecular weight) and $M_{\mathrm{w}} = M_{\mathrm{n}}$. A common descriptor of the dispersion in the molecular weight distribution of a polymer solution is the so-called polydispersity index or PDI. It is defined as the ratio of the weight average molecular weight to the number average molecular weight of a polymer solution or

$$\mathrm{PDI} = \frac{M_{\mathrm{w}}}{M_{\mathrm{n}}}. \tag{1.38}$$

For a monodisperse distribution we have PDI $= 1$, all other systems are termed polydisperse. In general, synthetic polymer growth processes yield polydisperse distributions and one a holy grail of polymer chemistry is a chemical method for producing monodisperse polymer solutions!

The inverse process of polymer growth is polymer degradation (or chain scission). This inverse method of essentially breaking down the polymer chains can be done in a number of different ways:

- Depolymerization: polymer chains are systematically depolymerized by some process (e.g., exonucleases) targeting the ends of the chains and working backwards to the monomer level.
- Random scission: polymers are degraded at random sites on the polymer chains, this can be done using for example ultrasonic methods.
- Mid-point like scission: the chain is broken predominantly in the middle of a molecule using for example extensional flows, or mechanical milling methods.

The scission problem can be summarized as follows: we begin with a particular distribution of polymer sizes $p_0(n)$, which by its very nature is polydisperse and has a particular PDI. The question we then ask is, "What is the resulting polymer distribution after we break the molecules using some pre-defined technique (random, scission, mid-point scission etc.), i.e., what is $p_1(n)$, the distribution after the chains have been broken?"

The essential goal of chapter 5 is to present the experimental and model results which clearly indicate a systematic decrease in the polydispersity index of a polymer sample that is forced through a narrow constriction, thus creating an extensional flow. This is known to yield a situation where the maximum force on the chain is at its center, thus the scission mechanism is not random but centralized about the middle of the chains. It is this phenomenon that we is explored in Chapter 5.

2 Friction and polymers

There are no shortcuts to any place worth going.
—— **Beverly Sills**
(1929–Present)

Molecular Dynamics Simulations with Explicit Hydrodynamics I: On the Friction Coefficients of Deformed Polymers.
M. Kenward and G. W. Slater.
Euro. Phys. J. E., 14, (1), 55–66, 2004.

This chapter contains an article published in 2004 in the European Physical Journal E [58] and is the first in the series of three articles which used coarsed-grained MD simulations with explicit solvent. The article contains a systematic examination of the friction coefficients of short chain polymers in a variety of conformations. It examines a number of effects, including; hydrodynamic coupling, friction and the dependence of polymer friction on chain length and deformation. My contribution to this work was; writing the article in its entirety, carrying out all research (including development of simulation and analysis codes) and all other tasks related to the production of the article.

Eur. Phys. J. E **14**, 55–65 (2004)
DOI 10.1140/epje/i2004-10006-4

THE EUROPEAN PHYSICAL JOURNAL E

Molecular-dynamics simulations with explicit hydrodynamics I: On the friction coefficients of deformed polymers

M. Kenward[a] and G.W. Slater[b]

Department of Physics, University of Ottawa, 150 Louis-Pasteur, Ottawa, Ontario, K1N 6N5, Canada

Received 28 January 2004 and Received in final form 5 April 2004 /
Published online: 2 June 2004 –

Abstract. We implement large-scale Molecular-Dynamics (MD) simulations which incorporate hydrodynamic interactions via the inclusion of explicit Lennard-Jones solvent to examine the behaviour of polymer chains in sieving media. We begin by examining the friction coefficients of polymers in long-lived states responsible for inducing length-dependent mobility, *i.e.*, allowing separation of polymers (or polyelectrolytes) by molecular weight. In particular, the conformations we examine occur in devices which utilize arrays of molecular obstacles or dilute solutions of polymers. We compare the results from our MD simulations with expressions from macroscopic hydrodynamics for four specific cases: i) a random coil excluded-volume Zimm polymer, ii) a rigid polymer moving perpendicular to its major axis iii) a rigid polymer moving parallel to its major axis and iv) a rigid polymer, folded at different points along its contour. We also examine the behaviour of the friction coefficient of a fully flexible molecule pulled by its middle monomer as a function of an applied force F and show that there are several distinct frictional regimes.

PACS. 83.10.Mj Molecular dynamics, Brownian dynamics – 61.41.+e Polymers, elastomers, and plastics – 82.20.Wt Computational modeling; simulation

1 Introduction

Although the equilibrium dynamics of isolated polymer chains are relatively well understood, both theoretically and experimentally [1], a sound understanding of many phenomena involving the non-equilibrium dynamics and relaxation of polymers is still pending. In particular, the dynamics of polymers in environments native to separation media, including: gels, dilute solutions of polymers, microfluidic devices and the behaviour of polymers under a variety of rheological conditions, in many instances are still not well understood. Many experimental separation techniques rely heavily on polymer deformation and the induced length (molecular weight) dependent non-equilibrium dynamics to achieve separation [2,3]. In several of these systems, the separation mechanism involves the collision of a polymer chain with either a free and mobile isolated polymer or a fixed rigid microscopic obstacle [2–7].

In general, it is not possible to electrophoretically separate polyelectrolytes (such as DNA composed of more than a few hundred base pairs) in free solution. The presence of counterions surrounding the molecule effectively screens hydrodynamic interactions, resulting in a so-called free-draining polymer (a hydrodynamically permeable molecule) [8]. In the presence of an electric field the friction coefficient of the molecule is then a local property of the chain and the resulting induced velocity (and the mobility) is independent of the molecular weight, necessitating the use of a sieving media (*e.g.*, a gel or entangled polymer solution) to achieve any degree of separation.

Barron *et al.* [4] were the first to illustrate the use of ultra-dilute polymer solutions in capillary electrophoresis to separate DNA fragments. They also proposed a possible mechanism for separation, the so-called transient entanglement coupling mechanism, wherein a polymer collides with one or more neutral polymers in solution, thus impeding its motion. Doyle *et al.* [3] recently illustrated the use of self-assembled arrays of ferro-fluidic particles as sieving matrices. In both systems, the collision and entrapment of a polymer with an obstacle is in part responsible for its sieving properties. In order to model the *in situ* polymer dynamics, we require a better fundamental understanding of the underlying physical mechanisms which dictate polymer behaviour in these systems.

Several theoretical and/or computational examinations of various aspects of polymer obstacle collisions have been carried out [2,5,9,10]. Each of these approaches has its own merit; however, most investigations do not

[a] e-mail: mkenward@science.uottawa.ca
[b] e-mail: gslater@science.uottawa.ca (corresponding author).

explicitly include hydrodynamic interactions. As such we aim to provide a thorough investigation of the dynamics of polymers and polyelectrolytes undergoing collisions in separation media, with explicit hydrodynamic interactions. We do this in a series of three papers: we begin by examining the friction coefficients of polymers in conformations commonly occurring in sieving media. The second paper focuses on the collision dynamics of polymers with obstacles. These two papers focus entirely on systems with mechanical forces. The third paper will then examine polymer-obstacle collisions with explicit electrostatic interactions.

Hydrodynamics can play a number of roles in these systems, for example: it can be used as a transport mechanism (*e.g.*, pressure-driven flow), it serves to modulate the dynamic behaviour of polymers (*e.g.*, relaxation from non-equilibrium conformations) and it also implicitly dictates molecular friction. Moreover, stiff molecules such as short DNA fragments and rod-like proteins can be adequately described as rigid rods. The interpretation of experimental results for the dynamic behaviour of rigid molecules (from NMR for example) can also benefit from a better understanding of the hydrodynamic properties of these molecules; this has been the subject of intense experimental and theoretical investigations [11–14].

2 Molecular-dynamics simulations

In this paper classical molecular-dynamics simulations are used and we explicitly include a Lennard-Jones solvent. This inclusion brings with it a large computational burden; however, this method avoids commonly used implicit representations of hydrodynamics [15]. Hydrodynamic interactions emerge naturally as a consequence of the inclusion of explicit solvent in our simulations.

We implement a well-known version of MD (the so-called Kremer-Grest model), descriptions of which can be found in numerous publications [16–19]. We adopt a coarse-grained description of the solvent, which we represent by spherical particles (beads) of reduced mass m. All *non-bonded* pair interactions in the system are represented by the repulsive part of the Lennard-Jones (LJ) potential given by

$$\Phi_{\mathrm{LJ}}(r) = \begin{cases} 4\epsilon\left(\left(\frac{\sigma}{r}\right)^{12} - \left(\frac{\sigma}{r}\right)^{6}\right) + \epsilon, & r \le r_{\mathrm{c}}, \\ 0, & r \ge r_{\mathrm{c}}, \end{cases}$$

where σ and ϵ are length and energy scales, respectively, r is the center-to-center distance between two beads and $r_{\mathrm{c}} = 2^{1/6}\sigma \simeq 1.12\sigma$, corresponding to the minimum in the standard LJ potential.

All *bonded* interactions are modeled via the finitely extensible non-linear elastic (FENE) potential

$$\Phi_{\mathrm{FENE}}(r) = -\frac{\kappa}{2}R_0^2 \ln\left(1 - \left(\frac{r}{R_0}\right)^2\right), \qquad (1)$$

where R_0 is an upper bound on the bond distance and κ is a spring constant [16]. This approach ensures that the chain has only a finite range of extensions. We use standard values of $\kappa = 30.0\epsilon/\sigma^2$ and $R_0 = 1.5\sigma$. The polymers are constructed by connecting N contiguous solvent-like Lennard-Jones particles via $(N-1)$ FENE bonds. In our simulations, N ranges from as few as 2 monomers up to a maximum of 61. The contour length of the molecule is given by $L_{\mathrm{c}} \simeq (N-1)\langle b_{\mathrm{p}}\rangle + r_{\mathrm{c}}$; for $N \gg 2$ we can write $L_{\mathrm{c}} \simeq N\langle b_{\mathrm{p}}\rangle$, where $\langle b_{\mathrm{p}}\rangle$ is the average bond length. The extra factor of r_{c} comes from the physical extent of the polymer at its ends. From equilibrium MD simulations we obtain $\langle b_{\mathrm{p}}\rangle = (0.96 \pm 0.01)\sigma$ and note that to first order $\langle b_{\mathrm{p}}\rangle \simeq r_{\mathrm{c}} \simeq \sigma$.

The equations of motion are rewritten entirely in reduced units and are integrated using the second-order (symplectic) velocity Verlet integration scheme [19,20]. For a number of reasons —including numerical round-offs and heating due to the inclusion of external forces— the temperature is prone to drift. In order to thermostat the temperature to a constant value, we utilize a velocity rescaling method [19]. Moreover, due to the inclusion of external forces the mean velocity of the solvent tends to increase over time. To compensate for this, we remove the center-of-mass velocity of the solvent, sufficiently far from the polymer. Similar approaches have been utilized by Cheong *et al.* [21] and also by Motohiko and Grosberg [22].

Parallelepiped simulation cells are used with periodic boundary conditions in all three directions. The starting configurations of the particles are simple cubic lattice structures. Typical linear dimensions of the simulation cell range from 10σ to 200σ and our systems typically contain from $N_{\mathrm{s}} = 1000$ to $N_{\mathrm{s}} = 200000$ solvent particles. The density in the system is set to $\rho = 0.85\sigma^{-3}$ and the temperature to $T = 1.0\epsilon/k_{\mathrm{B}}$. In order reach equilibrium (or the steady state) we run the simulations for a sufficiently long time (typically on the order of 10^4 to 10^5 time steps) to erase memory of the initial configuration.

To characterize equilibrium solvent transport coefficients, we utilize the Green-Kubo approach [23]. This method is well suited for obtaining estimates of transport coefficients from equilibrium simulations. The expression for the shear viscosity, η, is

$$\eta = \frac{V}{k_{\mathrm{B}}T}\int_0^\infty \left\langle \sum_{\alpha<\beta} P_{\alpha\beta}(t)P_{\alpha\beta}(0)\right\rangle \mathrm{d}t, \qquad (2)$$

where V is the volume of the system [19,23] . This corresponds to the integrated autocorrelation function of the off diagonal elements of the pressure tensor $\mathsf{P}_{\alpha\beta}(t)$ in orthogonal directions, (α,β), at time t; these tensor elements are given by

$$\mathsf{P}_{\alpha\beta}(t) = \frac{1}{V}\left[m\sum_j v_{\alpha_j}v_{\beta_j} + \frac{1}{2}\sum_{i\neq j} r_{\alpha_{ij}}f_{\beta_{ij}}\right], \qquad (3)$$

where m is the mass of a solvent particle, v_{α_j} is the velocity of particle j in direction α, $r_{\alpha_{ij}}$ and $f_{\beta_{ij}}$ are the distance and force between particles i and j in direction α

Table 1. Table of common parameters and calculated observables for equilibrium MD simulations of our Lennard-Jones fluid.

	Time step	Temperature	Density	Shear viscosity	Diffusion coefficient	Friction coefficient	Bond length
Symbol	$\Delta\tau$	T	ρ	η	D_s	ξ_s	$\langle b_p \rangle$
Units	$\sigma\sqrt{m\epsilon^{-1}}$	ϵ/k_B	σ/V	$\sigma^{-2}\sqrt{m\epsilon}$	$\sigma\sqrt{\epsilon m^{-1}}$	$\sigma^{-1}\sqrt{\epsilon m}$	σ
Value	0.001–0.005	1.0	0.85	2.25 ± 0.05	0.0611 ± 0.0002	16.2 ± 0.2	0.96 ± 0.01

and β, respectively. The solvent diffusion coefficient, D_s, is also given by

$$D_s = \frac{1}{3N_s}\int_0^\infty \left\langle \sum_{j=1}^{N_s} \mathbf{v}_j(t)\cdot\mathbf{v}_j(0)\right\rangle \mathrm{d}t \qquad (4)$$

where $\mathbf{v}_j(t)$ is the velocity of particle j at time t.

Typical computation times (on a single processor) range from a few days to several weeks on SUN UltraSPARC III 900 MHz processors. Both serial and parallel calculations have been carried out, the later are implemented using OpenMP [24], a compiler directive based programming extension for parallelizing code on large-scale symmetric multi-processor machines. In the rest of this article, all physical quantities will be reported in dimensionless MD units.

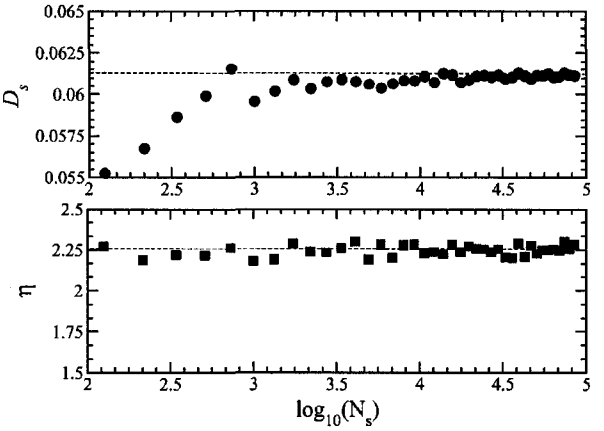

Fig. 1. Semi-log plot of the solvent diffusion coefficient D_s and the shear viscosity η as a function of the number of solvent particles in the system, N_s. The estimated asymptotic values for these transport coefficients are illustrated by dashed lines.

3 Molecular dynamics and fluids

Although the properties of Lennard-Jones fluids and the equilibrium dynamics of polymers in explicit solvent (including transport coefficients) have been studied elsewhere [20,25–32], we require estimates for the solvent viscosity in the calculation of the polymer friction coefficients. Consequently, we first examine the solvent shear viscosity η as well as the single solvent diffusion coefficient D_s [25,26]. The calculated values from our equilibrium MD simulations are $\eta = 2.25 \pm 0.05$ and $D_s = 0.0611 \pm 0.0002$, in agreement with previous calculations [20,25,26]. Both the value for the shear viscosity and the diffusion coefficient were obtained from equilibrium simulations of a Lennard-Jones fluid with a time step of $\Delta\tau = 0.005$. Table 1 illustrates values for some of the parameters and observables in the model.

Although the inclusion of explicit solvent particles to obtain hydrodynamic interactions is certainly not a novel method it is not widely used due (in part) to the prohibitive computational times which result from such an inclusion [27–32]. Figure 1 shows the evolution of the diffusion constant D_s and the viscosity η as a function of the number of solvent particles N_s. Even with as few as 20000 particles both D_s and η appear to have reached their asymptotic values. This is used as a metric in order to choose an appropriate system size that minimizes effects due to both finite system size and periodic boundary conditions. The hydrodynamic radius r_H of a hard-sphere fluid particle is simply given by its radius; however, since we are dealing with a soft-core potential, r_H is not easily defined. There are several pertinent length scales in our system: σ, r_c and the average inter-particle solvent distance. Thus r_H can be estimated from the position of the first peak in the radial distribution function, $g(r)$, given by

$$g(r) = \frac{2V}{N_s^2}\left\langle \sum_{i<j}\delta(\mathbf{r}-\mathbf{r}_{ij})\right\rangle, \qquad (5)$$

where $\sum_{i<j}$ corresponds to the sum over particle pairs. For simplicity the calculation is truncated at $r = 4$. A plot of the calculated $g(r)$ is shown in Figure 2. The first peak in $g(r)$, corresponding to the average center-to-center solvent spacing, is located at $r_{peak} \approx 1.08 \pm 0.01$, slightly below the cutoff radius $r_c \approx 1.12$. We thus estimate the hydrodynamic radius to be $r_H \simeq r_{peak}/2 \simeq 0.54 \pm 0.01$. This is equivalent to approximating the hydrodynamic radius of the solvent as an effective hard-sphere particle of size r_H. In the case of a true hard-sphere fluid the hydrodynamic radius then tends to the radius $r_{peak}/2$ of a LJ bead. The solvent friction coefficient ξ_s for a particle with hydrodynamic radius r_H is given by

$$\xi_s = C\pi\eta r_H, \qquad (6)$$

where the constant C depends on the boundary conditions at the surface of the particle. For particles less than about 10 times the size of the solvent (the so-called slip regime), it is predicted that $C = 4$ [8]. For larger particles (the

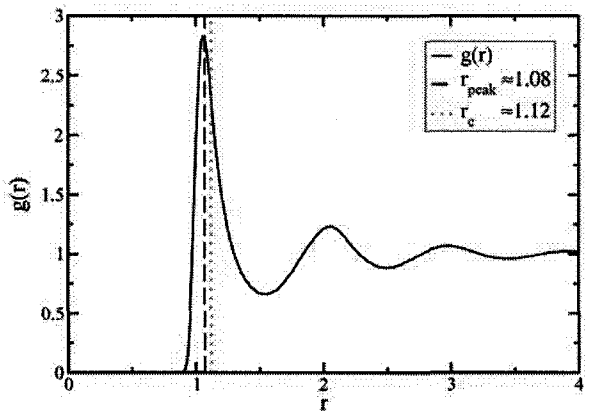

Fig. 2. Calculated radial distribution function $g(r)$ for our Lennard-Jones fluid ($\rho = 0.85$ and $T = 1$) as a function of r. The first peak in $g(r)$ is located at $r_{\text{peak}} \approx 1.08 \pm 0.01$. The corresponding value of the hydrodynamic radius is $r_{\text{H}} \simeq 0.54 \pm 0.01$.

so-called stick regime), we expect that $C = 6$. There is also a transitory regime, where the value of C changes continuously from $C = 4$ to $C = 6$.

The calculated friction coefficient from the simulations is $\xi_{\text{s}} = 16.2 \pm 0.2$. This was obtained from a non-equilibrium MD simulation by applying an external force of $F_{\text{ex}} = 50$ to a single solvent particle (the calculated value of ξ_{s} is independent of the force —not shown). We then measure its average velocity $\langle v \rangle$ and since $\xi_{\text{s}} = F_{\text{ex}}/\langle v \rangle$ we directly obtain ξ_{s}.

We can compare the expression in equation (6) with our MD results in two ways: i) calculate the friction coefficient in both the slip and stick regimes (using our value for the hydrodynamic radius obtained from the radial distribution function) and ii) calculate the hydrodynamic radius using the friction coefficient obtained from the MD simulations. Using method i) we obtain the following estimates for the friction coefficient:

$$\begin{aligned} \xi_{\text{s}}^{\text{slip}} &= 4\pi\eta r_{\text{H}} \rightarrow 14.9 \pm 0.7\,, \\ \xi_{\text{s}}^{\text{stick}} &= 6\pi\eta r_{\text{H}} \rightarrow 22.4 \pm 1.1\,, \\ \xi_{\text{s}} &= 16.2 \pm 0.2\,, \end{aligned} \tag{7}$$

with $\eta = 2.25 \pm 0.05$ and $r_{\text{H}} = 0.54 \pm 0.01$. The calculated values of ξ_{s} differ from the predicted values for the slip and stick regimes by 5% and 35%, respectively.

Alternatively, if we calculate r_{H} from equation (6), we obtain

$$\begin{aligned} r_{\text{H}}^{\text{slip}} &\rightarrow 0.58 \pm 0.02\,, \\ r_{\text{H}}^{\text{stick}} &\rightarrow 0.38 \pm 0.01\,, \\ r_{\text{H}} &\rightarrow 0.54 \pm 0.01\,. \end{aligned} \tag{8}$$

It would appear that, using the value for the hydrodynamic radius from $g(r)$, the slip regime better describes the single solvent friction coefficient.

The Stokes-Einstein expression for the diffusion coefficient D_{s} is given by

$$D_{\text{s}} = \frac{k_{\text{B}}T}{\xi_{\text{s}}} = \frac{k_{\text{B}}T}{C\pi\eta r_{\text{H}}}\,. \tag{9}$$

We can check the validity of this expression in the context of our MD simulations. The calculated single-particle diffusion and friction coefficient are $D_{\text{s}} = 0.0611 \pm 0.0002$ and $\xi_{\text{s}} = 16.2 \pm 0.2$, respectively. Solving for the temperature in the system, we obtain $T = 0.0611 \times 16.2 \approx 0.98 \pm 0.02$ fully consistent with the value of $T = 1$ as defined by our simulations.

We can also provide an estimate for the Reynolds number in our simulations using the calculated viscosity η, the density ρ, and estimates for the relevant length scales in the system. For a solvent particle with an applied force the typical average velocities are in the range $v \in [0, 5]$. The Reynolds number can be calculated as $R_e = \rho v d/\eta$, where d is either the dimension of a solvent particle or a polymer coil and we choose a maximum value of $v = 5$ in both cases. For the case of a solvent particle we estimate the Reynolds number to be

$$R_e^{\text{solvent}} \approx 2. \tag{10}$$

For a polymer chain, its dimensions are given $d \simeq N^{3/5}$, where $N \leq 61$ in our simulations. Consequently $d \approx 12$, again we choose the upper bound on the average velocity of $v = 5$ and obtain a Reynolds number of approximately

$$R_e^{\text{polymer}} \approx 25\,. \tag{11}$$

These values for the Reynolds number ensure that we are not dealing with turbulent fluid motion.

4 Hydrodynamics and friction

Macroscopic continuum descriptions of fluids (*e.g.*, Navier-Stokes) are often assumed *a priori* to remain valid even at the length scale of the fluid itself. Discrete representations of hydrodynamics which incorporate explicit solvent particles are the method of choice at the microscopic scale. This is increasingly becoming a practical alternative as the power and availability of high-performance computing resources increase, allowing us to examine larger and more complex systems.

Considering the rapid emergence of micro- and even nanofluidic devices, whose dimensions can be on the order of hundreds of solvent molecules [33–38], it is important to accurately model the components (polymers, fluid, surfaces...) in these systems. Further it is crucial to have a representation of the solvent which interacts with its surroundings in order to correctly reproduce dynamical effects, including correlated motions of polymers and the fluid.

When a polymer collides with an obstacle in a sieving system it is subject to deformation. This deformation, in turn, modifies the friction coefficient, and in feedback the

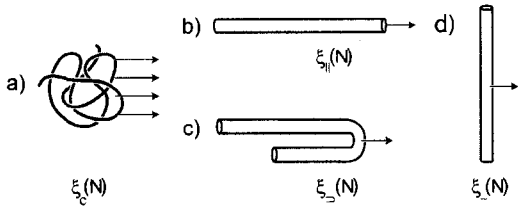

Fig. 3. Schematic illustration of a) a random coil polymer; b) a rigid polymer moving parallel (||) to its major axis; c) a folded rigid polymer (⊃) moving parallel to its major axis; and d) a rigid polymer moving perpendicular (⊥) to its major axis.

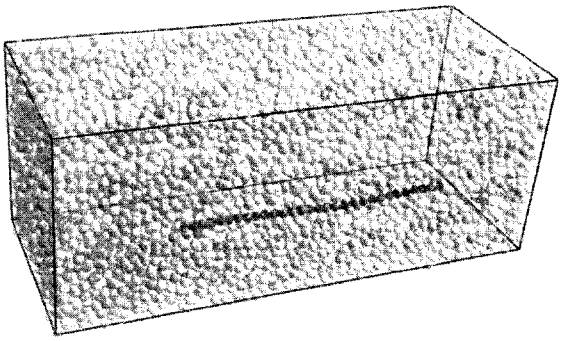

Fig. 4. Illustrative snapshot from molecular-dynamics simulations of a rigid-rod molecule with $N = 30$ monomers with the surrounding Lennard-Jones solvent (shown in slightly transparent colour).

dynamics of the molecule, a process which is modulated by the existence of hydrodynamics. In particular, during a collision event in the high-field regime (or high-velocity) the polymers form pulley-like conformations in the field direction [3,10,38].

There are several conformations which commonly occur. We examine four of these conformations, as depicted in Figure 3: a) a random coil polymer, b) a rigid polymer moving parallel to its major axis, c) a polymer folded at position $l_0 \leq L_c/2$, of effective length $L_c - l_0$ moving parallel to an applied force and d) a rigid polymer moving perpendicular to its major axis. Figure 4 shows a snapshot from the molecular-dynamics simulations of a single rigid polymer with the background Lennard-Jones solvent.

4.1 Friction coefficients of random polymer coils

The equilibrium static and dynamic properties of polymer chains are very well understood phenomena and constitute some of the fundamental physical concepts in polymer physics [1]. The hydrodynamic radius $R_H(N)$ of an equilibrium excluded-volume polymer chain with N monomers scales like

$$R_H(N) = N^{\nu}\alpha\,, \tag{12}$$

where $\nu = 3/5$ is the Flory exponent and α is a length scale. The corresponding friction coefficient of an equilibrium chain, $\xi_c(N)$ depends on the regime we consider, *i.e.*, whether the chain is hydrodynamically permeable or impermeable. For a hydrodynamically impermeable chain the mean friction coefficient is written as

$$\xi_c(N) = 6\pi\eta R_H(N). \tag{13}$$

The equation of motion for a polymer in bulk solution under the influence of an external force F_{ex} is then given by

$$F_{ex} = \xi_c(N)\cdot\langle v\rangle\,, \tag{14}$$

where $\langle v\rangle$ is the induced average velocity. The application of an external force (distributed evenly among all monomers) does not deform the polymer. The polymer still behaves as an ideal non-hydrodynamically permeable excluded-volume chain.

4.2 Friction coefficients of deformed polymer chains

Slender-body theory [39] makes predictions for the friction coefficients of a rigid rod of length L (corresponding to the contour length, $L \simeq L_c$) and diameter d moving either parallel (||) or perpendicular (⊥) to an applied force, in the $L/d \gg 1$ limit. The friction coefficients are often expressed in terms of the parameter $p = L/d$, *i.e.*, the ratio of length of the object to its diameter; however, it is more convenient to rewrite this directly as a function of N:

$$\frac{L}{d} = \frac{(N-1)\langle b_p\rangle + r_c}{r_c} \approx N\,, \tag{15}$$

where we utilize the fact that $\langle b_p\rangle/r_c \simeq 1$. As noted by Pecora *et al.* [12], the expressions from hydrodynamics are not strictly valid for $p < 30$ due to end effects; therefore, we restrict our analysis to $p \geq 30$. The friction coefficients for a rigid rod moving either parallel or perpendicular to its major axis can be written as

$$\xi_{||}(N) = \frac{C_{||}\pi\eta N\sigma}{\ln(2N) + \gamma_{||}}, \quad \xi_{\perp}(N) = \frac{C_{\perp}\pi\eta N\sigma}{\ln(2N) + \gamma_{\perp}}\,, \tag{16}$$

where $C_{\perp}, C_{||}, \gamma_{||}$ and $\gamma_{\perp}$ are numerical constants constants.

In the $p \gg 1$ limit these constants are $C_{\perp} = 4, C_{||} = 2, \gamma_{\perp} \simeq 0.5, \gamma_{||} \simeq -0.5$. This theory thus predicts that the ratio of these two friction coefficients is $\xi_{\perp}(N)/\xi_{||}(N) \approx 2$, for large N. It should be noted that this applies to the no-slip (or stick) regime, where the fluid at the surface of the object is assumed to move with the object, a reasonable assumption for macroscopic objects [39].

In each case we apply a constant external force $F_{ex} = 100$ to the polymer. The choice of F_{ex} does not affect the resulting value of the friction coefficient. The particular value of F_{ex} will affect the length of time necessary to calculate the friction coefficient (not shown). For small forces the orientation of the molecule will have large fluctuations and for very large forces the simulation will require increasingly smaller time steps. For both the random

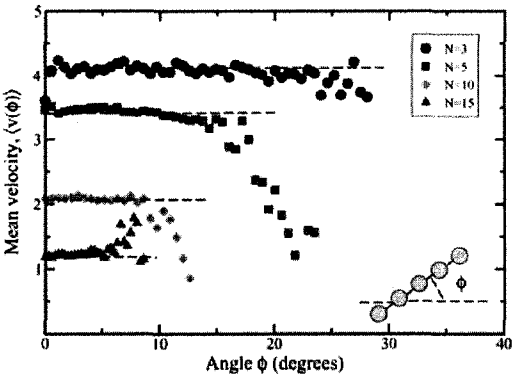

Fig. 5. Block averaged mean velocity $\langle v(\phi)\rangle$ as a function of the angle ϕ (in degrees) between the end-to-end vector and the field direction for several different polymers. This corresponds to the polymer moving parallel to the applied force.

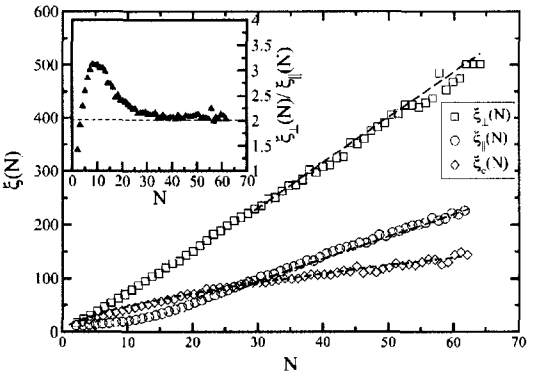

Fig. 6. Friction coefficients for a random coil polymer, a rigid rod polymer moving either perpendicular or parallel to its long axis denoted by $\xi_c(N)$, $\xi_\perp(N)$ and $\xi_{||}(N)$, respectively. The fitted curves are shown superimposed with the data. Inset figure is the ratio of $\xi_\perp(N)$ to $\xi_{||}(N)$ as a function of N. The ratio tends asymptotically to a value of 2, as predicted by slender-body theory.

coil and the perpendicular case, the force is evenly distributed among each monomer, while for the parallel case this force is applied only to the end of the chain. In order to ensure rigidity of the polymer, we utilize a standard dihedral bending potential $U_b(\theta)$ of the form,

$$U_b(\theta) = \frac{\Theta}{2}(\cos\theta + 1)^2 , \tag{17}$$

where Θ is a constant which defines the effective stiffness of the dihedral potential. We utilize a value of $\Theta = 10000$, ensuring an extremely rigid chain. A small force $f_{end} = 5.0$ is applied at both ends of the molecule to keep it oriented either parallel or perpendicular to the field direction. Though somewhat artificial this does not provide any net force on the molecule.

We monitor $v(\phi)$, the velocity of the chain as a function of the angle ϕ of the polymer end-to-end vector with respect to the direction of the applied force. A plot of $v(\phi)$ is shown in Figure 5 for the parallel case. We utilize $\langle v(\phi \to 0)\rangle$ in our calculations. The maximum deviation from the direction of net motion is less for longer molecules. For ($N < 10$) this angle is such that $\phi < 30°$. We then obtain the friction coefficient from the expression $\xi_c(N) = F_{eq}/\langle v(N)\rangle$. A plot of this data is shown in Figure 6. The inset shows a plot of $\xi_\perp(N)/\xi_{||}(N)$ as a function of N. As N increases we expect that $\xi_\perp(N)/\xi_{||}(N)$ will tend asymptotically to a value of 2; indeed, we observe this in the MD simulations. We can also directly compare results for both cases with the expression from hydrodynamics by fitting the expressions in equation (16) to the data in Figure 6. We choose $N \geq 30$, since there appears to be an inflection point for short lengths for the case of the parallel motion of the molecule and as noted above these expressions are presumed valid for this regime. We fit the data in Figure 6 utilizing $C_\perp$ and $C_{||}$ as the fitting parameter and using the accepted values of $\gamma_\perp \simeq 0.5, \gamma_{||} \simeq -0.5$; this procedure yields fits of the form

$$\xi_\perp(N) \simeq \frac{31.30N}{\ln(2N) + 0.5} , \tag{18}$$

$$\xi_{||}(N) \simeq \frac{17.61N}{\ln(2N) - 0.5} . \tag{19}$$

We expect that $C_\perp = 4$ and $C_{||} = 2$, while we obtain values of $C_\perp^{MD} = 4.42$ and $C_{||}^{MD} = 2.48$ with differences of 10–20%. The molecules in the MD simulations have inherent surface roughness due to their construction by discrete Lennard-Jones particles; this may account for some of the quantitative differences in the comparison [40].

For $N > 30$, the friction coefficient is to first order linear in N. Qualitatively, we have a friction coefficient that is a local property of the chain and can be written as

$$\xi_\perp \simeq 2\xi_{||} \sim N . \tag{20}$$

While for the random coil we always have sub-linear behaviour, and the friction coefficient is given by $\xi_c(N) \sim N^{3/5}$. When we deform a Zimm coil to an elongated rod-like conformation, we have a transition from a Zimm regime ($\xi \sim N^{3/5}$) to a regime where $\xi \sim N$ (or vice versa). Such transitions from linear to sub-linear friction coefficients can lead to very rich dynamical behaviour in a sieving system.

Figure 6 also shows the calculated friction coefficient for a random coil using non-equilibrium MD simulations. The friction coefficient for the random coil chain is expected to be $\xi_c(N) = 6\pi\eta R_H(N)$. We fit the data for the random coil with an expression of the form $\xi_c = \beta N^\nu$; we obtain $\beta = 12.05$ and $\nu = 0.598$. The correlation coefficient for this least-squares fit is $r = 0.994$. We also note that $\beta = 6\pi\eta\alpha$, where α is related to the Kuhn length: here we find $\alpha \simeq 0.28$.

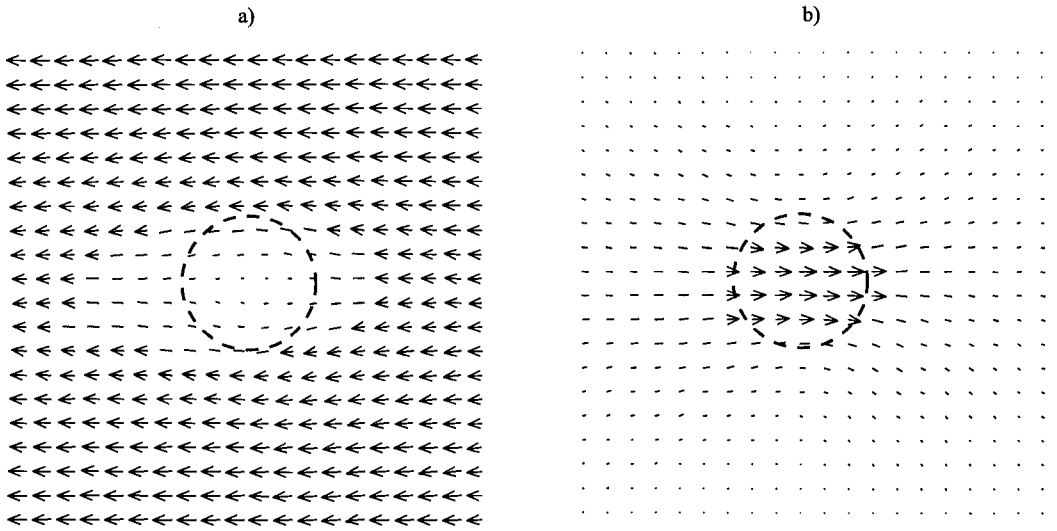

Fig. 7. a) Flow field in the reference frame of a random coil polymer with $N = 50$ monomers. b) Interior flow field in the reference frame of the fluid with $N = 50$ monomers. The fluid interior to the coil is moving at approximately the same velocity as the coil itself. The superimposed dashed circle corresponds to the effective hydrodynamic radius of the polymer $R_H(N = 50) \simeq 6.6$. This clearly illustrates the hydrodynamic impermeability of the polymer.

It is usually assumed *a priori* that a random coil is hydrodynamically impermeable. Under this assumption the polymer must drag a substantial amount of fluid with it, interior to the coil. Figure 7 shows the calculated exterior and interior vector *flow* fields of the solvent from a fixed reference frame of a polymer with $N = 50$ monomers. This is obtained by calculating the vector field in the reference frame of a moving polymer, and subtracting the average velocity, from the interior flow. The shown dashed circle in Figure 7 corresponds to the hydrodynamic radius, which we obtain from the friction coefficient, $R_H(N) = 6\pi\eta/\xi_c(N)$; for $N = 50$ we obtain $R_H(N = 50) \simeq 6.6$. From Figure 7 it is clear that the assumption of hydrodynamic impermeability is accurate in this context.

Figure 6 also exhibits a distinct crossover point at $N = N^* \simeq 28$, where the friction coefficient of a rigid rod (moving parallel to its long axis) and a coil are equivalent, *i.e.*, $\xi_c(N^*) = \xi_{||}(N^*)$, after which $\xi_c(N^*) < \xi_{||}(N^*)$. This is quite a remarkable observation, since it implies that the friction coefficient of a fully extended molecule of N^* monomers is entirely equivalent to that of a random coil composed of the same number of monomers. In fact, this can have a significant effect on the behaviour of short chains in a sieving process. For $N < N^*$, deformation can cause the molecules to speed up (under a fixed driving force), while for $N > N^*$ the molecules tend to slow down. As far we know, this point has not been considered before in the analysis of the physics of sieving systems. It is possible to vary the location of this crossover by altering the Kuhn or statistical segment length b_K (*i.e.*, the stiffness) of the polymer. An increase in b_K will increase R_H and therefore the coil friction coefficient. This implicitly increases the value of the crossover point N^*.

4.3 Friction coefficients and hydrodynamic coupling

According to equation (16) we expect that by folding a rigid rod in two (about its center) its friction coefficient will decrease by a factor of roughly two. Alternatively, by changing the fold position from $L/2 \rightarrow L$ the friction coefficient will tend from $\xi(L/2) \rightarrow \xi(L)$. This can be thought of as a hydrodynamic coupling between different parts of the molecule. André *et al.* [5] pointed out that this hydrodynamic coupling effect can be greatly pronounced in the context of a polymer-obstacle collision (in a solvent flow) where the polymer may take a multi-loop conformation (folding upon itself multiple times). In this case, the drag forces which dictate the escape of the polymer (due to the solvent flow) can be significantly modified.

In order to investigate this friction reduction mechanism, we carry out systematic MD simulations which examine the friction coefficient of a hydrodynamically coupled molecule. Two cases are considered: i) a polymer pulled by its middle monomer as a function of the number of monomers and ii) a polymer with a fixed number of monomers, $N = 61$, pulled at different locations along the molecule.

The methodology for these calculations is the following: we apply the bending potential as in equation (17) to all monomers except monomer n_0. So the polymer is composed of two stiff segments (of $N - n_0$ and n_0 monomers) joined together by a flexible joint. We then apply an external force $F_{ex} = 100$ to the freely jointed monomer: this

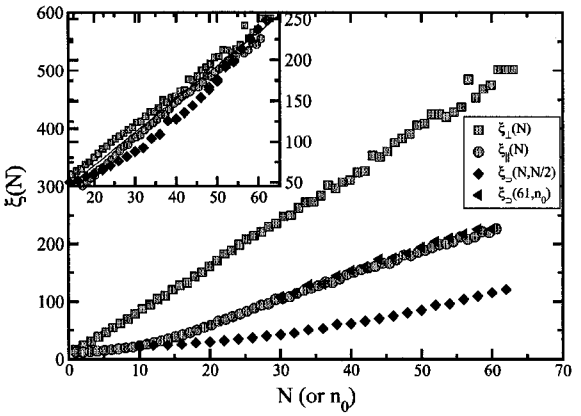

Fig. 8. Friction coefficients for a chain of monomers moving perpendicular $\xi_\perp(N)$ or parallel $\xi_{||}(N)$ to an applied field along with the friction coefficient of a polymer folded in the center $\xi_\supset(N, N/2)$ and a polymer folded at varying positions, n_0, along the chain $\xi_\supset(61, n_0)$ for a fixed number of monomers $N = 61$. The inset figure shows a reduced plot of these curves obtained by multiplying $\xi_\supset(61, n_0)$ and $\xi_\perp(N)$ by a factor of 2 and 1/2, respectively.

causes the polymer to rapidly fold upon itself. If the polymer originally had a diameter d and length $L \simeq L_c$ when fully elongated, after the application of the above procedure, the polymer has effective length L', where $L' < L$, and effective diameter $d' \simeq 2d$.

We can examine this effective hydrodynamic coupling quantitatively, in terms of the resulting friction coefficient. We denote the friction coefficient of a folded polymer as $\xi_\supset(L, l_0)$, where l_0 is the length of the shorter arm of the folded molecule. Using equation (16) it immediately follows that

$$\xi_\supset(L, l_0) \simeq \xi_{||}(L - l_0). \tag{21}$$

It is more convenient to write the friction coefficient in terms of the total number of monomers, N, and n_0 the monomer at which the chain is folded; this leads to $\xi_\supset(L, l_0) \equiv \xi_\supset(N, n_0)$.

Figure 8 shows data from the MD simulations for $\xi_\perp(N)$, $\xi_{||}(N)$, $\xi_\supset(N, N/2)$ and $\xi_\supset(N, n_0)$, for the later friction coefficient we only consider a single chain length $N = 61$. The inset figure contains a reduced plot of this data obtained by multiplying $\xi_\supset(N, n_0)$ and $\xi_\perp(N)$ by factors of 2 and 1/2, respectively. This illustrates that the data essentially collapses to a quasi-universal curve. For the case of $\xi_\supset(N, n_0)$ we vary n_0 from $n_0 = 31 \ldots 61$ corresponding to the filled triangles in Figure 8; the x-axis then gives n_0 instead of N. As n_0 decreases there is a reduction in the friction coefficient. In fact we map out almost exactly the friction coefficient for a polymer moving parallel to an applied field. Hydrodynamic coupling between the two parallel arms of the polymer significantly modifies the friction coefficient of a folded chain. For example, if we apply a constant (fixed) force to a polymer, with increasing coupling its velocity increases. Alternatively, this coupling mechanism reduces the force necessary to maintain a constant velocity for a given object. Although only the case of a single fold is examined here, it is relatively straight forward to extend these calculations to polymers with multiple folds.

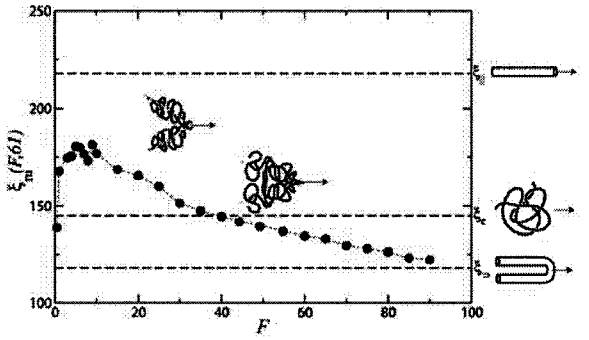

Fig. 9. Friction coefficient, $\xi_m(F, N)$, for a flexible polymer (with $N = 61$) pulled by its middle monomer as a function of an applied force F. This illustrates a frictional transition, from a random coil friction coefficient $\xi_c(N)$ through a maximum, then decreasing through $\xi_c(N)$ and finally tending asymptotically towards a lower value of $\xi_\supset(N, N/2)$. Also schematically illustrated are the conformations which typically occur.

5 Frictional transitions

In this section we consider a freely jointed chain (FJC) pulled by its middle monomer as a function of an applied force, F. We denote this friction coefficient by $\xi_m(F, N)$ (the subscript "m" denotes pulling by the middle monomer). Our analysis is restricted to a single chain with $N = 61$. Unlike the case of applying a force to each monomer, applying a force to a single monomer does deform the molecule. As F is increased the friction coefficient will tend to that of a hydrodynamically coupled polymer, *i.e.*, $\lim_{F\to\infty} \xi_m(F, N) \to \xi_\supset(N, N/2)$. While as F tends to zero we expect that $\lim_{F\to 0} \xi_m(F, N) \to \xi_c(N)$, *i.e.*, the friction coefficient will tend to that of a random coil in the low force limit.

Figure 9 shows a plot of $\xi_m(F, 61)$ as a function of F. In the low and high F limits, we do indeed recover the random coil and hydrodynamically coupled friction coefficients, respectively. Note however that as $F \to 0$ the computational time necessary to calculate the average velocity (and consequently the average friction coefficient) increases. As F is increased two striking features are observed. The first is that $\xi_m(F, N)$ initially increases to a maximum at around $F \simeq 5$. At this point $\xi_m(F, N)$ is nearly 20% larger than $\xi_c(N)$. With further increase in F, $\xi_m(F, N)$ decreases monotonically. At $F \simeq 40$, $\xi_m(F, N)$ has the same value as the equilibrium coil. The second remarkable thing to note is that $\xi_m(F, N)$ then decreases further and is bounded below by $\xi_\supset(N, N/2)$ where $\xi_c(N) > \xi_\supset(N, N/2)$ in this example. This transition depends on the values for the coil friction coefficient and the

associated upper and lower bounds. For example, it is even possible that the low and high force limits have the same value, *i.e.*, $\xi_{\rm m}(F \to 0, N) \equiv \xi_{\rm c}(N) = \xi_{\rm m}(F \to \infty, N)$. Although this falls outside of the range of N considered here, we estimate this value using the fitted functions of Section 4.2. Solving numerically for the value of N at which $\xi_{\supset}(N, N/2) \simeq \xi_{||}(N)/2 = \xi_{\rm c}(N)$ we obtain $N \simeq 116$.

Another interesting characteristic is the effective size and/or shape of the molecule, which is also a function of the applied force. Figure 10 shows the principal moments of the radius-of-gyration tensor in directions i, j, k, $\langle R_i^2 \rangle$, $\langle R_j^2 \rangle$ and $\langle R_k^2 \rangle$ (Note: $\langle R_{\rm g}^2 \rangle = \langle R_i^2 \rangle + \langle R_j^2 \rangle + \langle R_k^2 \rangle$ and $\langle R_i^2 \rangle > \langle R_j^2 \rangle > \langle R_k^2 \rangle$). These principal moments are the eigenvalues of the radius-of-gyration tensor given by

$$\mathsf{R}_{\rm g}^2 = \begin{bmatrix} R_{xx}^2 & R_{xy}^2 & R_{xz}^2 \\ R_{yx}^2 & R_{yy}^2 & R_{yz}^2 \\ R_{zx}^2 & R_{zy}^2 & R_{zz}^2 \end{bmatrix} . \tag{22}$$

The individual tensor elements $R_{\alpha\beta}^2$ are defined as

$$R_{\alpha\beta}^2 = \frac{1}{N} \sum_{k=1}^{N} (r_k^\alpha - r_{\rm cm}^\alpha)(r_k^\beta - r_{\rm cm}^\beta) , \tag{23}$$

where r_k^α and $r_{\rm cm}^\alpha$ are the position of the k-th monomer and the position of the center of mass of the molecule in direction α, respectively. The three directions i, j, k (corresponding to the principal axes of the molecule) do not necessarily correspond to the directions x, y, z of the simulation cell; however, at large F the direction of the applied force x and direction i are essentially the same. The dotted line in this figure corresponds to the radius of gyration of a cylinder with $N/2$ monomers and represents the upper bound on $R_{\rm g}^2$. Figure 10 illustrates that as we increase F the polymer initially decreases in size by about 10%, hence the minimum in $\langle R_i^2 \rangle$. This effect is possibly equivalent to that observed for a confined polymer, where the chain dimensions initially decrease with increasing confinement after which the chain increases in size monotonically [41]. The largest dimension $\langle R_i^2 \rangle$ appears to increase according to the power law

$$\langle R_i^2 \rangle \propto F^{0.5}. \tag{24}$$

A similar type of power law behaviour is observed for chains that are confined in harmonic potentials [41]. It may be possible to draw parallels between the middle pulled polymer and that of a confined polymer.

Figure 10 (inset) shows the lateral dimensions of the chain, which we define to be the sum of the two smallest principal radii $\langle R_\perp^2 \rangle = \langle R_j^2 \rangle + \langle R_k^2 \rangle$ as a function of F. In this case, the chain size initially increases with F after which it decreases monotonically. It would appear that the lateral chain dimension decreases inversely with the applied force, that is to say

$$\langle R_\perp^2 \rangle \propto F^{-1.0}. \tag{25}$$

This transitional behaviour between frictional regimes can play an important role in the manipulation of single polymer chains. For example, having an accurate model of the friction coefficient as a function of an applied force can aid in providing more robust methods of transporting molecules in micro-fluidic devices.

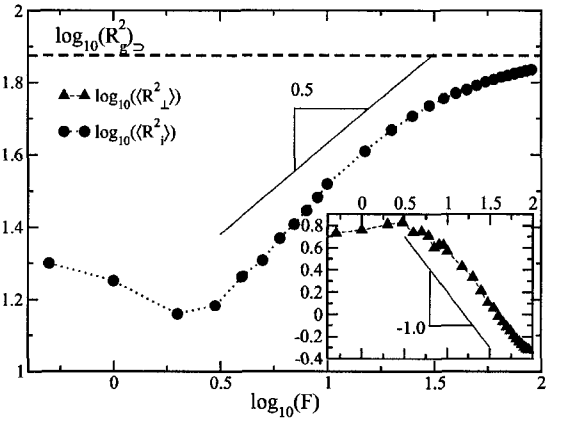

Fig. 10. Log-log plot of the largest principal moment on the radius-of-gyration tensor $\langle R_i^2 \rangle$ as function of the force applied to the middle monomer of the molecule. The inset shows a log-log plot of the sum of the two smaller principal radii $\langle R_\perp^2 \rangle = \langle R_j^2 \rangle + \langle R_k^2 \rangle$. The upper bound $(R_{\rm g}^2)_\supset$ corresponding to the radius of gyration of a cylinder of length $N/2$ is also shown as a guide to the eye.

6 Conclusions

With the use of molecular dynamics we have provided a systematic examination of the friction coefficients of polymers in conformations which are commonly observed in sieving media. A crucial aspect of our model is that we have an explicit representation of hydrodynamic interactions which emerge naturally from the presence of a molecular solvent. It is worth noting that, although we have only discussed *translation* friction coefficients, in principle it is also possible to examine *rotational* friction coefficients using a similar model. This represents a natural extension of these calculations.

We have shown that we can recover the known relationship between the single solvent particle friction coefficients and the expressions from macroscopic hydrodynamics along with the expression relating the diffusion and the single solvent friction coefficient. This verified that for the single solvent particles we are indeed in the slip regime.

Using our simulations we have been able to map out the friction coefficients for polymers in five specific cases: i) a random coil excluded-volume Zimm polymer, ii) a rigid polymer moving perpendicular to its major axis, iii) a rigid polymer moving parallel to its major axis, iv) a rigid polymer, folded at different points along its contour and v) the friction coefficient of a freely jointed chain folded as a function of an applied external force. We have also compared both quantitatively and qualitatively the expressions from macroscopic hydrodynamics with the calculated friction

coefficients with good agreement. Our results also illustrated very succinctly that a random coil polymer is hydrodynamically impermeable in the presence of an external force in the context of molecular dynamics.

The study of friction coefficients *versus* molecular weight (number of monomers) revealed several striking characteristics. The first is that the friction coefficient of the random coil is initially larger than that of a rigid rod moving parallel to its major axis, *i.e.*, $\xi_c(N) > \xi_{||}(N)$, below some critical value $N = N^*$ and $\xi_c(N^*) = \xi_{||}(N^*)$. The value of this crossover point N^* is a tunable system parameter and can be modified by changing the effective stiffness of a molecule. This be can advantageous in single molecule manipulation techniques.

For the case of polymers folded in the middle, as we increase N we essentially map out the friction coefficient of a molecule of $N/2$ monomers, *i.e.*, $\xi(N, N/2) = \xi_{||}(N/2)$. Moreover, if we vary the position of the fold, n_0, from the middle of the chain towards the end of the chain we recover the friction coefficient for a molecule of effective number of monomers $N-n_0$. Both results are crucial when examining polymer obstacle collisions.

We have also illustrated that for a fully flexible molecule pulled by its middle monomer, the friction coefficient $\xi_m(F, N)$, is a sensitive function of the applied force F. There are two remarkable observations to be made here. The first is that $\xi_m(F, N)$ initially increases and one can indeed have $\xi_m(F \to \infty, N) < \xi_m(F \to 0, N)$. The later point depends on the particular value of N. The second observation is that in principle it is possible to shift the upper and lower bounds on the friction coefficients by altering this value of N. So it is possible as we vary N that initially $\xi_m(F \to \infty, N) < \xi_m(F \to 0, N)$ then at a particular value of N, $\xi_m(F \to \infty, N) = \xi_m(F \to 0, N)$. Finally, with further increase in N, $\xi_m(F \to \infty, N) > \xi_m(F \to 0, N)$. This type of frictional transitions can have important consequences when manipulating polymers in sieving media. Although we only examine a single chain length, these calculations can be extended to examine a variety of chain lengths.

In our subsequent paper, we examine the collision dynamics of polymers with obstacles with similar molecular dynamics simulations and explicitly make use of the results obtained in this paper. In particular, we will utilize the expressions for the friction coefficients of rigid polymers moving parallel to an applied force.

Our investigation provides impetus to utilize MD simulations which include explicit solvent, and illustrates that such simulations are well within reasonable bounds on computational time. The methodology presented in this paper is easily applied to any number of problems. In particular, we can use it to examine a variety of problems related to microfluidic systems including those related to wall coating and electro-osmotic flow.

The authors acknowledge the financial support in the form of a post-graduate scholarship to MK and a Discovery Grant to GWS both from the Natural Sciences and Engineering Research Council of Canada (NSERC). MK also thanks the University of Ottawa for a National Excellence Scholarship. We also acknowledge the use of computational resources made available by the High-Performance Computing Virtual Laboratory (HPCVL) (`www.hpcvl.org`) and C3.ca (`www.c3.ca`). The authors thank Frédéric Tessier for many useful discussions.

References

1. M. Doi, S.F. Edwards, *The Theory of Polymer Dynamics* (Oxford University Press, 1986).
2. M.E. Starkweather, D.A. Hoagland, M. Muthukumar, Macromolecules **33**, 1245 (2000).
3. P.S. Doyle, J. Bibette, A. Bancaud, J. Viovy, Science **295**, 2237 (2002).
4. A.E. Barron, H.W. Blanch, D.S. Soane, Electrophoresis **15**, 597 (1994).
5. P. Andre, D. Long, A. Ajdari, Eur. Phys. J. B **4**, 307 (1998).
6. S. Hubert, G.W. Slater, J. Viovy, Macromolecules **29**, 1006 (1996).
7. H. Noguchi, M. Takasu, J. Phys. Soc. Jpn. **69**, 3729 (2000).
8. P. Munk, *Introduction to Macromolecular Science* (Wiley Interscience, Oxford, 1989).
9. G.I. Nixon, G.W. Slater, Phys. Rev. E **50**, 5033 (1994).
10. E.M. Sevick, D.R.M. Williams, Europhys. Lett. **56**, 529 (2001).
11. A. Ortega, G. de la Torre, J. Chem. Phys. **119**, 9914 (2003).
12. W. Eimer, R. Pecora, J. Chem. Phys. **94**, 2324 (1991).
13. B.U. Felderhof, J.M. Deutch, J. Chem. Phys. **62**, 2391 (1975).
14. J.M. Deutch, B.U. Felderhof, J. Chem. Phys. **62**, 2398 (1975).
15. B. Carrasco, J.G. de la Torre, J. Chem. Phys. **111**, 4817 (1999).
16. K. Kremer, G.S. Grest, I. Carmesian, Phys. Rev. Lett. **61**, 566 (1988).
17. K. Kremer, G.S. Grest, J. Chem. Phys. **92**, 5057 (1990).
18. M.P. Allen, D.J. Tildesley, *Computer Simulations of Liquids*, fourth edition (Oxford Science Publications, Oxford, 1987).
19. D.C. Rapaport, *The Art of Molecular Dynamics Simulation* (Cambridge University Press, 1995).
20. D. Levesque, L. Verlet, Phys. Rev. A **2**, 2514 (1970).
21. M. Cheong, J. Chang, J. Koplik, J.R. Banavar, Europhys. Lett. **58**, 215 (2002).
22. M. Tanaka, A.Y. Grosberg, Eur. Phys. J. E **7**, 371 (2002).
23. D.M. Heyes, *The Liquid State: Application of Molecular Simulations* (John Wiley and Sons, 1988).
24. Openmp, `http://www.openmp.org/`.
25. K. Meier, A. Laesecke, S. Kabelac, Int. J. Thermophys. **22**, 161 (2001).
26. A.M. Bazhenov, D.M. Heyes, J. Chem. Phys. **92**, 1106 (1990).
27. B. Dunweg, J. Chem. Phys. **99**, 6977 (1993).
28. B. Dunweg, K. Kremer, J. Chem. Phys. **99**, 6983 (1993).
29. B. Dunweg, K. Kremer, Phys. Rev. Lett. **66**, 2996 (1991).
30. C. Pierleoni, J.P. Ryckaert, J. Chem. Phys. **96**, 8539 (1992).
31. C. Pierleoni, J.P. Ryckaert, Phys. Rev. Lett. **66**, 2992 (1991).

32. C.F. Abrams, N.K. Lee, S.P. Obukhov, Europhys. Lett. **59**, 391 (2002).
33. M.L. Adams, M. Enzelberger, S. Quake, A. Scherer, Sens. Actuator A-Phys. **104**, 25 (2003).
34. B. Ilic, D. Czaplewski, M. Zalalutdinov, B. Schmidt, H.G. Craighead, J. Vac. Sci. Technol. B **20**, 2459 (2002).
35. H. Cao, J.O. Tegenfeldt, R.H. Austin, S.Y. Chou, Appl. Phys. Lett. **81**, 3058 (2002).
36. H.G. Craighead, Abstr. pap. - Am. Chem. Soc., **222**, 160-ANYL (2001).
37. S.R. Quake, A. Scherer, Science **290**, 1536 (2000).
38. C.F. Chou, R.H. Austin, O. Bakajin, J.O. Tegenfeldt, J.A. Castelino, S.S. Chan, E.C. Cox, H. Craighead, N. Darnton, T. Duke, J.Y. Han, S. Turner, Electrophoresis **21**, 81 (2000).
39. G.K. Batchelor, J. Fluid Mech. **44**, 410 (1970).
40. A. Meunier, J. Phys. II **4**, 561 (1994).
41. C.-Y. Shew, J. Chem. Phys. **119**, 10428 (2003).

3 Molecular Plinko

In all affairs it's a healthy thing now and then to hang a question mark on the things you have long taken for granted.
— **Bertrand Russell**
(1872–1970)

Molecular Dynamics Simulations with Explicit Hydrodynamics II: On the Collision of Polymers with Molecular Obstacles.
M. Kenward and G. W. Slater.
Euro. Phys. J. E., 20, (2), 125–141 2006.

This chapter contains an article published in 2006 in the European Physical Journal E [59]. This article presents a systematic study of the collision of polymer chains in three separate regimes; polymer-fixed obstacle collisions (driven by an external force), polymer-fixed obstacle collisions (driven by a fluid flow) and polymer-polymer collisions (driven by an external force). The article describes both the results from our Molecular Dynamics simulations and a theory which encompasses all three regimes. My contribution to this work was; writing the article in its entirety, carrying out all research (including development of simulation and analysis codes), derivation of all theoretical expression and all other tasks related to the production of the article.

Eur. Phys. J. E **20**, 125–141 (2006)
DOI 10.1140/epje/i2006-10008-2

THE EUROPEAN PHYSICAL JOURNAL E

Molecular-dynamics simulations with explicit hydrodynamics II: On the collision of polymers with molecular obstacles

M. Kenward[a] and G.W. Slater[b]

Department of Physics, University of Ottawa, 150 Louis-Pasteur Ottawa, Ontario, K1N 6N5 Canada

Received 27 February 2006 /
Published online: 16 June 2006 –

Abstract. We present a study of the dynamics of single polymers colliding with molecular obstacles using Molecular-dynamics simulations. In concert with these simulations we present a generalized polymer-obstacle collision model which is applicable to a number of collision scenarios. The work focusses on three specific problems: i) a polymer driven by an external force colliding with a fixed microscopic post; ii) a polymer driven by a (plug-like) fluid flow colliding with a fixed microscopic post; and iii) a polymer driven by an external force colliding with a free polymer. In all three cases, we present a study of the length-dependent dynamics of the polymers involved. The simulation results are compared with calculations based on our generalized collision model. The generalized model yields analytical results in the first two instances (cases i) and ii)), while in the polymer-polymer collision example (case iii)) we obtain a series solution for the system dynamics. For the case of a polymer-polymer collision we find that a distinct V-shaped state exists as seen in experimental systems, though normally associated with collisions with multiple polymers. We suggest that this V-shaped state occurs due to an effective hydrodynamic counter flow generated by a net translational motion of the two-chain system.

PACS. 83.10.Mj Molecular dynamics, Brownian dynamics – 61.41.+e Polymers, elastomers, and plastics – 82.20.Wt Computational modeling; simulation

1 Introduction

As emerging micro- and even nano-fluidic systems for manipulating polymers and biopolymers become ubiquitous, understanding the factors which dictate the behaviour of their various components at a variety of length and time scales is increasingly important. The classic example of such a manipulation technique is electrophoresis, in its many guises. The use of sieving media (*e.g.*, a cross-linked gel) is necessitated by the inability to separate polyelectrolytes by molecular weight in free solution (typically beyond a few hundred base pairs for double-stranded DNA (dsDNA)) [1]. This is a direct consequence of the screening of hydrodynamic interactions and results in an electrophoretic mobility, μ, which is independent of molecular weight. Therefore, in order to effectively fractionate polyelectrolytes a sieving mechanism (or media) is generally required.

A host of sieving media exists, examples of which include: i) ultra-dilute polymer solutions [2]; ii) rigid obstacles constructed using, *e.g.*, self-assembled arrays of ferrofluid particles or microlithographically etched arrays [3–7]; iii) entangled networks of polymers; and iv) cross-linked polymer gels [8,9]. It has been known for some time that, in these systems, a polymer can collide with non-stationary obstacles (cases i) and iii)) or a fixed molecular obstacle (cases ii) and iv)) [9]. These obstacles can deform and constrain the polymers in long-lived pulley-like conformations. The resulting dynamics is often molecular-weight dependent, thereby providing a fractionation method. Understanding how these collisions affect the molecules dynamics can ultimately lead to more robust sieving systems.

Several experimental, theoretical and computational studies have elucidated some of the physical mechanisms present in these systems [4–6,10–15]. Volkmuth *et al.* carried out some of the pioneering experimental work on single-polymer collisions [5]. There has recently been a renewed interested in single-polymer systems including the work of Doyle *et al.* [4,12] and numerous other groups [4–6,10–15]. Several simulation studies have primarily used Brownian dynamics (BD) to explore these systems [10,16,17] and a number of theoretical treatments have been put forward [18,11,15,17,19] which discuss various aspects of the collisions.

The majority of computational examinations of the systems neglect the effects of hydrodynamic interactions, mostly due to the exceedingly time-consuming nature

[a] e-mail: mkenward@science.uOttawa.ca
[b] e-mail: gary.slater@uOttawa.ca

of such calculations. The presence of hydrodynamics affects nearly all facets of polymer *deformo-dynamics* (non-equilibrium dynamics induced by the deformation of polymers due to some external perturbation, *e.g.*, externally applied field or fluid flow). Hydrodynamics is also partly responsible for the complex behaviour (stretching, relaxation) of polymers under a variety of rheological conditions [12,20–23].

Existing studies have mainly focused on the collision of a polymer with a fixed rigid microscopic object. In this paper we present a generalized model in which the obstacle is given a translational degree of freedom. The fixed-obstacle case is a natural asymptotic limit of our model. Incorporating a free obstacle allows us to model a wider range of systems including dilute polymer solutions. The single-polymer–obstacle collision system effectively represents the basic *quantum* of separation and a sound physical model describing its dynamics is required for a better understanding of the behaviour of polymers in sieving media.

In order to examine these systems we have implemented large-scale Molecular-dynamics (MD) simulations which explicitly include a Lennard-Jones solvent and, consequently, a self-consistent description of hydrodynamics. In this paper we restrict ourselves to purely mechanical driving forces: a sedimentation-like force and a (plug-like) fluid flow.

2 Molecular-dynamics simulations

We utilize the same Molecular-dynamics approach as outlined in numerous previous studies [24–28], sometimes referred to as the Kremer-Grest model [24–27]. It is a standard coarse-grained method where solvent molecules are represented by spherical particles, of reduced mass m. All *non-bonded* interactions in the system are represented by the repulsive part of the pairwise Lennard-Jones (LJ) potential given by

$$V_{\mathrm{LJ}}(r_{ij}) = \begin{cases} 4\epsilon\left(\left[\frac{\sigma}{r_{ij}}\right]^{12} - \left[\frac{\sigma}{r_{ij}}\right]^{6}\right) + \epsilon, & r_{ij} \le r_{\mathrm{c}}, \\ 0, & r_{ij} \ge r_{\mathrm{c}}, \end{cases} \quad (1)$$

where σ and ϵ are the length and energy scales, r_{ij} is the center-to-center distance between particles i and j and $r_{\mathrm{c}} = \sqrt[6]{2}\sigma$ is the minimum in the Lennard-Jones potential and corresponds to the cutoff for calculating forces.

The *bonded* interactions (providing polymer connectivity) are modeled using the finitely extensible non-linear elastic (FENE) potential [24]

$$V_{\mathrm{bond}}(r_{ij}) = -\frac{\kappa}{2}R_0^2 \ln\left(1 - \left[\frac{r_{ij}}{R_0}\right]^2\right) \quad (2)$$

where R_0 is maximum bond length and κ is an effective spring constant. The linear polymers are modeled as N_{p} Lennard-Jones beads connected via $N_{\mathrm{p}} - 1$ FENE bonds. We use the standard values, $\kappa = 30.0\epsilon/\sigma^2$ and $R_0 = 1.5\sigma$ [24,25]. The temperature in all of the simulations is chosen to be $T = \epsilon$.

The total number of solvent particles in the system, N_{s}, is typically in the range $10000 \le N_{\mathrm{s}} \le 500000$. The solvent density is selected to be the standard value of $0.85\sigma^{-3}$ [24,25]. The reduced viscosity of the Lennard-Jones solvent corresponding to the above parameters is $\eta = 2.25 \pm 0.05$ and the corresponding single bead friction coefficient (*i.e.*, the friction of an individual solvent bead or particle) is given by $\xi_{\mathrm{s}} = 16.2 \pm 0.2$ [28]. The contour length of the molecules is approximately given by $L_{\mathrm{c}} = (N_{\mathrm{p}} - 1)\langle b_{\mathrm{p}}\rangle + r_{\mathrm{c}} \simeq N_{\mathrm{p}}\langle b_{\mathrm{p}}\rangle$ for $N_{\mathrm{p}} \gg 2$, where $\langle b_{\mathrm{p}}\rangle$ is the average bond length. The extra factor of r_{c} comes from the physical extent of the chain at its ends. The value obtained from equilibrium MD simulations is $\langle b_{\mathrm{p}}\rangle = 0.96 \pm 0.01\sigma$ [28].

The equations of motion are written in reduced units and the integration is performed using the velocity Verlet algorithm [26], with a time step in the range $\Delta t = (0.001\text{–}0.005)$. For further descriptions and implementation details, the reader can consult references [24–27]. In addition to the polymers and solvent, our simulations also contain fixed obstacles which are composed of tightly packed columns of Lennard-Jones beads. The inter-bead spacing, r_{b}, for the obstacles is chosen so that an integer number of beads span the simulation cell under the condition that $r_{\mathrm{b}} \le \langle b_{\mathrm{p}}\rangle$. This method ensures that a polymer molecule is unable to cross the axis of a post (obstacle) and indeed no polymer-obstacle crossings were observed in the simulations.

Our non-equilibrium simulations implement either an external force on the polymer or a fluid flow. In the external force problems we apply a constant force per unit length f_0; the total force on the molecule is then $F_{\mathrm{ex}} = f_0 N_{\mathrm{p}}\langle b_{\mathrm{p}}\rangle$. This external force causes the temperature in the system and the net velocity of the center of mass of the solvent to slowly drift from their equilibrium values. In these instances a simple velocity-rescaling technique is used to thermostat the temperature [28–30]. To correct for the drift in the center-of-mass velocity, we remove the center-of-mass velocity in a narrow shell near the edge of the simulation cell relative to the center of mass of the polymer. A similar approach has been utilized in previous investigations [29,30,28].

In the case of a fluid flow, we implement a method suggested by Rapaport [27,31] for so-called open systems. The flow used in the simulations is a plug flow with no shear. Since we are using an *open* system, *i.e.*, one in which there are no walls to carry out thermalization, we need an alternative method to both implement a fluid flow and control the temperature in the system. The method used here randomizes the velocities and thermostats the particles as they cross the boundary of the simulation cell; a velocity bias is then added to ensure that we have a flow [29]. Parallelepiped simulation cells are used with periodic boundary conditions in all three Cartesian directions. Typical linear dimensions of the simulation cell range from 30σ to 200σ depending on the particular simulation.

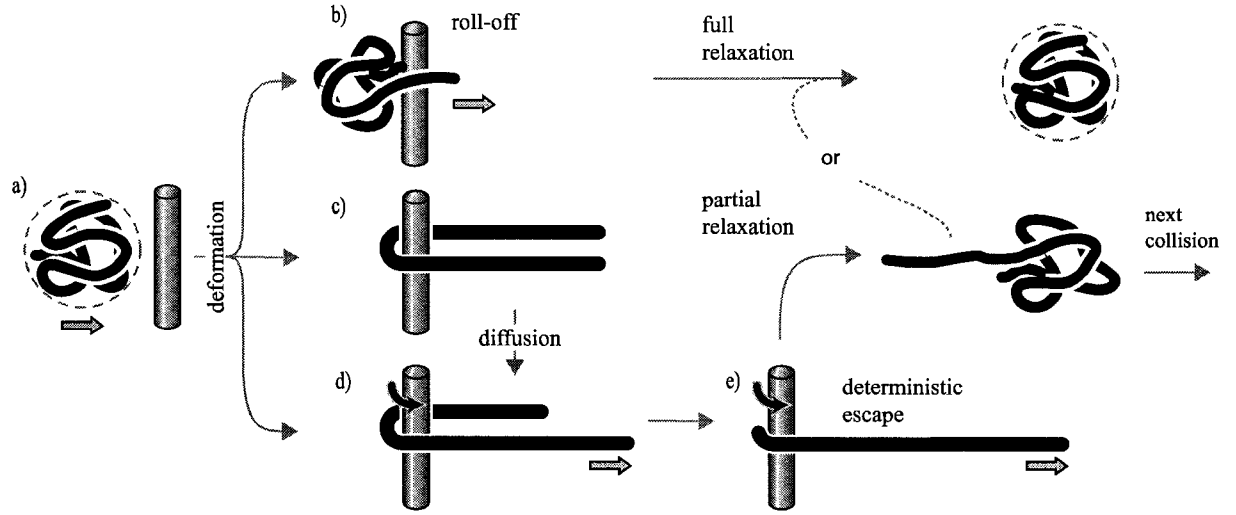

Fig. 1. Schematic illustration of the various polymer conformations commonly occurring in the polymer-obstacle collision problem. There are typically 5 unique conformations: a) the random coil O-shaped state, b) the roll-off collision with little deformation, c) the diffusion dominated U-shaped state (this state can be long lived but occurs very infrequently), d) the J-shaped state and e) the fully extended I-shaped state which occurs just prior to complete escape. The final state of the polymer before the next collision is *either* relaxation to an equilibrium coil *or* partial relaxation [7].

3 Generalized polymer-obstacle collision model

Experimentally it is observed that a polymer, migrating in the presence of obstacles, will undergo collisions which perturb its free flow migration [5,7,4,12,20]. Many of these collisions are glancing blows (roll-off events) in which there is a small to negligible deformation of the molecule [12]. However, some collisions result in long-lived states, where the polymer hooks around the obstacle. In these instances the polymer is deformed significantly and elongates in the field direction, subsequently forming a pulley-like conformation. The magnitude of the externally applied force (or flow) must be sufficient to deform the polymer. This is essentially almost always the case in experiments where deformation in part dictates the molecules dynamics.

The polymer-obstacle collision and escape sequence is comprised of a number of distinct chain conformations (or states). These states are depicted in Figure 1 (for the case of a fixed obstacle): a) the random coil O-shaped state; b) a roll-off event; c) the U-shaped state; d) the J-shaped state; and e) the fully extended I-shaped state. The U- and J-shaped states correspond to the long-lived states in the system. The passage from state to state is also schematically depicted in Figure 1. A description of polymer migration can be made in terms of these states (along with transitions between them) assuming multiple loop conformations do not occur.

During a collision for sufficiently large applied forces, $F_{\rm ex}$, the polymer will fully extend and its length in the field direction $L_{\rm p}$ will be on the order of the contour length $L_{\rm c}$, *i.e.*, $L_{\rm p} = L_{\rm c} \simeq N_{\rm p}\langle b_{\rm p}\rangle$. As noted by André *et al.* [11] this occurs when $F_{\rm ex} \gg k_{\rm B}T/\langle b_{\rm p}\rangle$ (in our case, the polymer

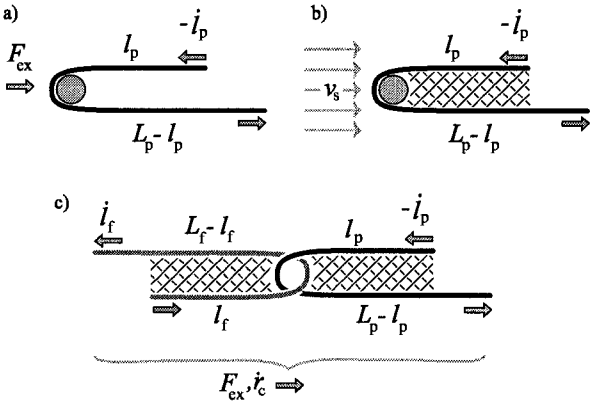

Fig. 2. Schematic illustration of the three collision problems: a) a polymer in the presence of an external force $F_{\rm ex}$ colliding with a fixed post; b) a polymer in the presence of a fluid flow at velocity $v_{\rm s}$ colliding with a fixed post; and c) a *test* polymer under external force $F_{\rm ex}$ colliding with a *free* polymer in solution. The hash marks between the opposites arms of the chain are meant to denote hydrodynamic coupling of the adjacent arms of the molecule.

Kuhn length is comparable to the bond length). We focus on three specific collision problems as depicted schematically in Figure 2: a) a polymer (driven by an external force) colliding with a fixed obstacle (or post); b) a polymer (driven by a fluid flow) colliding with a post; and c) a polymer (driven by an external force) colliding with a free polymer in solution. All examples correspond to purely mechanical systems, with no electrostatics. In each of the three cases we carry out MD simulations and make

comparisons with calculations from our generalized collision model.

3.1 Model description

In this section we describe a general model for a *test* polymer (acted on by an external force) colliding with a *free* polymer in solution as schematically depicted in Figure 2c. Our approach is a generalization of a similar method used by Sevick and Williams [18]. In various asymptotic limits the equations of motion can yield closed-form analytical solutions while the general case leads to a series solution.

In the general case, the molecules have total contour lengths L_x, friction per unit length ξ_x and linear mass densities ρ_x. In the hooked state the length of the shortest arm of the molecule is denoted by $l_x(t)$. The subscripts $x = p$ and $x = f$ denote the *test* and *free* chains, respectively. The entire system is allowed to translate; the position and velocity of the point of contact between the two chains are given by $r_c(t)$ and $\dot{r}_c(t)$, respectively. All time derivatives are denoted using superscript dot notation throughout; *e.g.*, $\dot{l}_x(t) = \mathrm{d}l_x(t)/\mathrm{d}t$.

We proceed by calculating the total potential and kinetic energies, $\mathcal{T}$ and $\mathcal{V}$, respectively. Moreover, since the system is dissipative we need to account for the frictional energy dissipated, denoted by $\mathcal{F}$. This is obtained from the so-called Rayleigh dissipation function [32]. We then calculate the Lagrangian, $\mathcal{L} = \mathcal{T} - \mathcal{V}$ and the associated equations of motion are obtained from the Lagrange equation

$$\frac{\mathrm{d}}{\mathrm{d}t}\left(\frac{\partial \mathcal{L}}{\partial \dot{q}_j}\right) - \frac{\partial \mathcal{L}}{\partial q_j} + \frac{\partial \mathcal{F}}{\partial \dot{q}_j} = 0, \tag{3}$$

where the $\{q_j, \dot{q}_j\}$ represent conjugate coordinate-momenta pairs. In our system there are three such pairs corresponding to $q_j = \{l_p(t), l_f(t), r_c(t)\}$. We thus obtain three differential equations. Although we only consider the two-chain system, a generalization to multi-chain systems is possible, although tedious.

The total potential energy of the system, $\mathcal{V}$, can be written as

$$\begin{aligned}\mathcal{V} = {} & f_0\left(r_c(t) - \frac{1}{2}l_p(t)\right) l_p(t) \\ & + f_0\left(r_c(t) - \frac{1}{2}[L_p - l_p(t)]\right)[L_p - l_p(t)],\end{aligned} \tag{4}$$

where the factors of 1/2 arise from the integration along the chain. The total kinetic energy contains contributions from the *free* and *test* chains, given by $\mathcal{T}_p$ and $\mathcal{T}_f$, respectively, such that $\mathcal{T} = \mathcal{T}_p + \mathcal{T}_f$:

$$\begin{aligned}\mathcal{T}_p = {} & \frac{1}{2}\rho_p l_p(t)\left(\dot{l}_p(t) - \dot{r}_c(t)\right)^2 \\ & + \frac{1}{2}\rho_p\Big(L_p - l_p(t)\Big)\left(\dot{l}_p(t) + \dot{r}_c(t)\right)^2, \\ \mathcal{T}_f = {} & \frac{1}{2}\rho_f l_f(t)\left(\dot{l}_f(t) - \dot{r}_c(t)\right)^2 \\ & + \frac{1}{2}\rho_f\Big(L_f - l_f(t)\Big)\left(\dot{l}_f(t) + \dot{r}_c(t)\right)^2.\end{aligned} \tag{5}$$

Similarly the total frictional energy dissipated, $\mathcal{F} = \mathcal{F}_p + \mathcal{F}_f$, is written in terms of contributions from the *test* and *free* chains, $\mathcal{F}_p$ and $\mathcal{F}_f$, respectively:

$$\begin{aligned}\mathcal{F}_p = {} & \frac{\xi_p}{2}\Big(L_p - 2l_p(t)\Big)\left(\dot{l}_p(t) + \dot{r}_c(t)\right)^2 \\ & + \frac{\xi_p}{2}l_p(t)\dot{r}_c(t)^2 + \xi_p l_p(t)\dot{l}_p(t)^2, \\ \mathcal{F}_f = {} & \frac{\xi_f}{2}\Big(L_f - 2l_f(t)\Big)\left(\dot{l}_f(t) + \dot{r}_c(t)\right)^2 \\ & + \frac{\xi_f}{2}l_f(t)\dot{r}_c(t)^2 + \xi_f l_f(t)\dot{l}_f(t)^2.\end{aligned} \tag{6}$$

Equation (6) includes hydrodynamic coupling of the adjacent sections of length $l_x(t)$ (when $\dot{r}_c(t) \neq 0$), resulting in a friction coefficient that is reduced by a factor of two [11,28]. These equations contain three contributions: i) the unbalanced length $L_x - 2l_x(t)$ moving at velocity $(\dot{l}_x(t) + \dot{r}_c(t))$; ii) the coupled sections $(l_x(t))$ moving at velocity $\dot{r}_c(t)$; and iii) the sliding of the short sections $l_x(t)$ at velocity $\dot{l}_x(t)$. Since hydrodynamic coupling exists only for small obstacles; a minor modification may be required for large inter-arm separations.

For consistency we examine asymptotic expressions for $\mathcal{F}$. When $\dot{r}_c(t) \to 0$, the only contribution to $\mathcal{F}_x$ is from sliding and it reduces to the expected expression

$$\lim_{\dot{r}_c(t)\to 0} \mathcal{F}_x = \frac{\xi_x}{2}L_x\dot{l}_x(t)^2. \tag{7}$$

Alternatively, if $\dot{l}_x(t) \to 0$, sliding ceases and there is only net translation of the system; this yields

$$\lim_{\dot{l}_x(t)\to 0} \mathcal{F}_x = \frac{\xi_x}{2}\Big(L_x - l_x(t)\Big)\dot{r}_c(t)^2 \tag{8}$$

which is the expected result for a folded (coupled) segment of effective length $L_x - l_x(t)$ moving at velocity $\dot{r}_c(t)$.

The equations of motion for the system are obtained from equation (3) for each of the coordinate pairs. For the test polymer corresponding to the $(l_p(t), \dot{l}_p(t))$ pair we obtain

$$\begin{aligned}-\rho_p L_p\ddot{l}_p(t) = {} & \Big(L_p - 2l_p(t)\Big)\Big(f_0 + \rho_p\ddot{r}_c(t) + \xi_p\dot{r}_c(t)\Big) \\ & + \xi_p L_p\dot{l}_p(t),\end{aligned} \tag{9}$$

while for the free polymer corresponding to the $(l_f(t), \dot{l}_f(t))$ pair we obtain

$$\begin{aligned}-\rho_f L_f\ddot{l}_f(t) = {} & \Big(L_f - 2l_f(t)\Big)\Big(\rho_f\ddot{r}_c(t) + \xi_f\dot{r}_c(t)\Big) \\ & + \xi_f L_f\dot{l}_f(t).\end{aligned} \tag{10}$$

Equations (9) and (10) are coupled via $\dot{r}_c(t)$ and $\ddot{r}_c(t)$. When the contact point is immobile ($\dot{r}_c(t) = \ddot{r}_c(t) = 0$), the equations of motion fully decouple.

The final equation of motion corresponding to the $(r_c(t), \dot{r}_c(t))$ coordinate pair yields

$$f_0 L_p + \Big(L_p - 2l_p(t)\Big)\Big(\xi_p \dot{l}_p(t) + \rho_p \ddot{l}_p(t)\Big) + \xi_p\Big(L_p - l_p(t)\Big)\dot{r}_c(t) + \rho_p\Big(L_p \ddot{r}_c(t) - \dot{l}_p(t)^2\Big) + \Big(L_f - 2l_f(t)\Big)\Big(\xi_f \dot{l}_f(t) + \rho_f \ddot{l}_f(t)\Big) + \xi_f\Big(L_f - l_f(t)\Big)\dot{r}_c(t) + \rho_f\Big(L_f \ddot{r}_c(t) - \dot{l}_f(t)^2\Big) = 0. \quad (11)$$

This equation serves to couple equations (9) and (10), and when combined, all three equations yield a complete description of the collision problem under investigation. In several instances analytical solutions can be obtained.

3.2 Polymer–(fixed)-obstacle collision: external force

We begin our analysis with a simple limiting example of the general problem, a single polymer colliding with a fixed obstacle. In terms of the model from Section 3.1, we require a static object, *i.e.*, $\xi_f \to \infty$. In this case, the contact point velocity and acceleration are both zero: $\dot{r}_c(t) = \ddot{r}_c(t) = 0$.

The escape dynamics of the molecules are obtained by solving equation (9), with $\dot{r}_c(t) = \ddot{r}_c(t) = 0$ (subject to the appropriate initial conditions):

$$-\rho_p L_p \ddot{l}_p(t) = f_0\left(L_p - 2l_p(t)\right) + \xi_p L_p \dot{l}_p(t), \qquad l_p(t=0) = l_p^0, \qquad \dot{l}_p(t=0) = 0. \quad (12)$$

The general solution of equation (12) is

$$l_p(t) = \frac{L_p}{2} - \left(L_p/2 - l_p^0\right) e^{-\frac{t}{\tau_\rho}} \cdot \left[\sinh\left(\frac{\Delta \cdot t}{2\tau_\rho \tau_\xi}\right) + \frac{\tau_\xi}{\Delta}\cosh\left(\frac{\Delta \cdot t}{2\tau_\rho \tau_\xi}\right)\right],$$

where

$$\Delta = \sqrt{\tau_\xi^2 + 4\tau_\rho \tau_\xi}, \quad (13)$$

where the two time scales corresponding to drift and inertial effects are respectively given by

$$\tau_\xi = \frac{\xi_p L_p}{2 f_0} \quad \text{and} \quad \tau_\rho = \frac{\rho_p}{\xi_p}. \quad (14)$$

In a viscous liquid $\tau_\xi \gg \tau_\rho$ and inertial effects are negligible (the term involving $\rho_p \ddot{l}_p(t)$ in (12) disappears), since we are in the overdamped limit where velocities relax exponentially fast. In all cases we therefore consider $\tau_\xi \gg \tau_\rho$. The molecular friction coefficient $\xi_p L_p$ is treated as that corresponding to a molecule of length L_p moving along its major axis for this problem. We utilize our previous numerical result [28] for this friction coefficient,

$$\xi_p L_p \simeq \xi^{\mathrm{md}}(L_p) = \frac{17.61 L_p/\langle b_p\rangle}{\ln(2L_p/\langle b_p\rangle) - 0.5}. \quad (15)$$

As an example, consider a molecule with $N_p = 40$ monomers: its total friction coefficient is $\xi_p L_p \simeq 180$ in reduced units [28]. A typical external force in our simulations would be $f_0 = 4$ and $\rho_p = 1$ which yields $\tau_\xi \approx 22.5$ and $\tau_\rho \approx 0.2$, such that $\tau_\xi > 100\tau_\rho$.

Neglecting inertial effects our solution becomes

$$l_p(t) = \frac{L_p}{2}\left(1 - \exp\left[\frac{t - \tau_{\mathrm{esc}}}{\tau_\xi}\right]\right), \quad (16)$$

where $\tau_{\mathrm{esc}}(l_p^0)$ is the time required for the molecule to unhook, *i.e.*, $l_p(\tau_{\mathrm{esc}}) = 0$, and $\alpha_p^0 = l_p^0/\frac{1}{2}L_p \in [0,1]$ is the initial fractional offset in the chain length. This escape time is given by

$$\tau_{\mathrm{esc}}(l_p^0) = \tau_\xi \ln\left(\frac{1}{1-\alpha_p^0}\right). \quad (17)$$

Although mathematically $\tau_{\mathrm{esc}}(l_p^0)$ diverges as $l_p^0 \to L_p/2$ (the net escape force is zero while the force on the obstacle is maximized), in actuality $\tau_{\mathrm{esc}}(l_p^0)$ is finite because the U-shaped state is mechanically unstable [15]. Transitions from U- to J-shaped states are driven by Brownian motion. Relative to the U-shaped state the molecule must diffuse a minimum critical distance δ_c before deterministic escape dominates. In other words, the deterministic motion becomes the faster mode of transport when $l_p^0 = L_p/2 - 2\delta_c$; before this the chain diffuses. As noted by Volkmuth *et al.* [5], the most rigorous approach requires the solution of a first-passage time problem. Our simple approach leads to an equivalent set of results.

We can estimate δ_c by comparing the time required to diffuse a distance δ ($\delta = 0$ corresponds to the U-shaped state) with the time required to move a distance δ deterministically (*i.e.*, to go from an offset of δ to 2δ or, in terms of the initial conditions, to go from $l_p^0 = L_p/2 - 2\delta$ to $l_p^1 = L_p/2 - 4\delta$). Moreover, if $\delta < \delta_c$, it is possible for the chain to diffuse backward towards the U-shaped state. This implicitly assumes that the deterministic and diffusive motions are decoupled, which suffices for the purposes of our calculation. The time required to diffuse a distance δ is simply

$$\tau_D = \frac{\delta^2}{2D_\cap}, \quad (18)$$

where $D_\cap = k_B T/\xi_p L_p$ is the curvilinear-diffusion coefficient of the molecule in the hooked state (denoted by the symbol $\cap$). The time to move from l_p^0 to l_p^1 deterministically, τ_d, is calculated from the expression for the escape time:

$$\tau_d = \tau_{\mathrm{esc}}\left(l_p^0\right) - \tau_{\mathrm{esc}}\left(l_p^1\right) = \tau_\xi \ln(2). \quad (19)$$

It is worth noting that τ_d does not depend on δ. The value of δ at which $\tau_d = \tau_D$ defines the critical distance δ_c;

$$\delta_c = \sqrt{2D_\cap \tau_\xi \ln(2)} = \sqrt{\frac{k_B T \ln(2)}{f_0}} \sim f_0^{-1/2}. \quad (20)$$

In essence, δ_c represents the critical distance over which the chain must move (relative to the U-shaped state) in

order for deterministic escape to be a faster mode of transport than thermal diffusion. In other words, if $\delta \gg \delta_c$, we can effectively ignore the Brownian-motion contribution to the escape dynamics. The critical distance δ_c is independent of the polymer length L_p. The corresponding time, τ_c, before deterministic escape dominates is

$$\tau_c = \frac{(\delta_c)^2}{2D_\cap} = \tau_\xi \ln(2) \sim L_p f_0^{-1}. \quad (21)$$

As soon as $\delta \geq \delta_c$, deterministic escape ensues. Although δ_c is small, τ_c is rather large: in fact $\tau_c = \tau_{esc}(l_p^0 = L_p/4)$! However, τ_{esc} is still finite and since collisions which trap polymers at their midpoint are relatively improbable, they contribute little to the overall dynamics.

For any distribution of l_p^0, $\Gamma(l_p^0)$, we can calculate the average escape time $\langle \tau_{esc} \rangle_\Gamma$ as

$$\langle \tau_{esc} \rangle_\Gamma = \frac{1}{L_p/2} \int_0^{\frac{L_p}{2}} \Gamma(l_p^0) \tau_{esc}(l_p^0) dl_p^0, \quad (22)$$

where $\tau_{esc}(l_p^0)$ will include contributions from both the diffusion-dominated and the deterministic regimes. For simplicity, we assume a uniform distribution of the initial conditions, $\Gamma(l_p^0) = 1$. In order to accurately estimate the escape time we need to split the integral in equation (22) into contributions from the diffusion and deterministic regimes. However, if we neglect contributions from U-shaped states (*i.e.*, $\delta_c \cong 0$) to the overall average escape time of the polymer, we obtain the following first-order average escape time from the J-shaped state:

$$\langle \tau_{esc} \rangle \simeq \tau_\xi = \frac{L_p}{2} \left(N_p \langle b_p \rangle \frac{f_0}{\xi_p L_p} \right)^{-1} = \frac{L_p}{2} / v_0^\cap. \quad (23)$$

Qualitatively, this first-order escape time $\langle \tau_{esc} \rangle$ is the time for the molecule to move a distance $L_p/2$ with effective velocity $v_0^\cap = N_p f_0 \langle b_p \rangle / (\xi_p L_p)$, which is independent of N_p. Even if the distribution of l_p^0 is not uniform (*e.g.*, Gaussian or Poisson) the average escape time can still be calculated. The escape time from the U-shaped state contains a logarithmic correction factor (when diffusion is taken into account), as first noted by Volkmuth *et al.* [5].

Our MD simulations consist of chains with $N_p \in [20, 70]$. In our model we have assumed that the chain is fully extended (Sect. 3.1) *i.e.*, $L_p \simeq N_p \langle b_p \rangle$. As a result, our choice of f_0 must provide sufficient stretching of the chain. Figure 3 shows $\langle L_p \rangle$ (in the hooked state) as a function of f_0 for $N_p = 20$. Increasing f_0 leads to an increase in $\langle L_p \rangle$ and reduces the fluctuations in $L_p(t)$ (not shown). For $f_0 = 4$ the chain is stretched to $\approx 85\%$ of its contour length, L_c.

An appropriate f_0 is one which simultaneously provides sufficient stretching and does not require an inordinately small integration time step Δt (for large N_p). In other words, f_0 implicitly dictates an appropriate Δt —an overtly small Δt yields prohibitively long simulations, whereas a large Δt can produce large discretization errors in the integration scheme. A choice of $f_0 = 4$ provides a good compromise. Although a detailed examination of $\langle L_p \rangle$ *vs.* f_0 is of fundamental interest, it is not the primary focus of our investigation and Figure 3 is simply included for completeness.

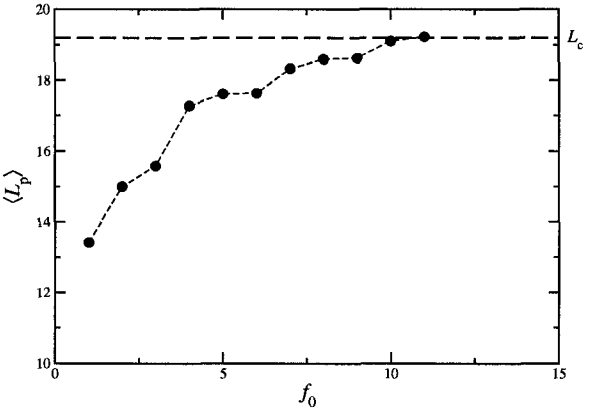

Fig. 3. Plot of $\langle L_p \rangle$ as a function of the force per monomer f_0 for a molecule with $N_p = 20$ beads during the initial part of the escape sequence where $\langle L_p \rangle$ remains relatively constant and does not exhibit chain compression. As f_0 increases the molecule becomes more elongated and $\langle L_p \rangle$ tends towards its contour length, $\langle L_p \rangle \to L_c$.

Figure 4 shows a typical collision and escape sequence of a chain with $N_p = 70$ from our MD simulations. At t_0 the molecule is an equilibrium coil, while at t_1 it collides with the obstacle and begins to deform, subsequently forming a J-shaped pulley conformation ($t_2 \to t_3$). The molecule then follows the deterministic-escape sequence ($t_4 \to t_7$) to the I-shaped state and finally begins relaxing to an equilibrium state ($t_8 \to t_9$).

From the simulations we extract $l_p(t)$, which we define as the distance from the last monomer on the shortest arm to the first bead on the trailing edge of the obstacle. To facilitate our comparison we write equation (16) as a universal curve using the transformation $t_\cap \to t - \tau_{esc}$. This yields $l_p(t_\cap) = L_p/2(1 - \exp(t_\cap/\tau_\xi))$. In effect, this synchronizes escape *clocks* and the dynamics are examined by beginning at τ_{esc} and moving backwards in time $t_\cap$. By writing the left-hand side of equation (16) as $\phi(t_\cap) \equiv 1 - l_p(t_\cap)/(L_p/2)$ and using $\exp(t_\cap/\tau_\xi)$ as the variable along the abscissa, we should obtain universal curves (*i.e.*, we plot $1 - l_p(t_\cap)/(L_p/2)$ *vs.* $\exp(t_\cap/\tau_\xi)$). A plot of the original data for $l_p(t)$ *vs.* $t_\cap$ from the simulations and the collapsed data are both shown in Figure 5 along with the expected universal function. The data follows the universal curve; however, there is some deviation. One contribution may be the implicit assumption that $L_p(t)$ is constant during the entire escape process. As $t \to \tau_{esc}$, $L_p(t)$ decreases by a non-negligible amount near the end of the escape, a phenomenon that is observed experimentally [33]. It is also noteworthy that for small $\exp(t_\cap/\tau_\xi)$ we tend toward the diffusion-dominated regime.

Chain compression alters the molecule's friction coefficient and can affect the escape process. To quantify the compression of the chain we monitor $L_p(t)$ during escape and rewrite $L_p(t)$ as a universal curve. Figure 6

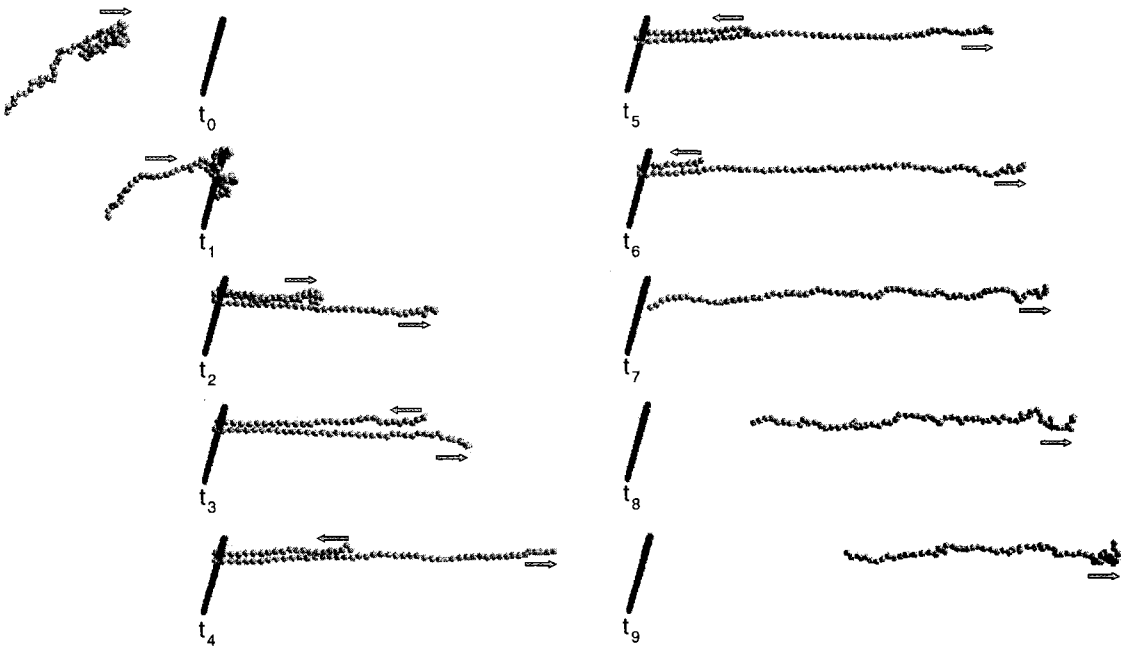

Fig. 4. Snapshots from a Molecular-dynamics simulation illustrating a polymer-post collision and escape sequence. This corresponds to a molecule with $N_p = 70$ monomers. Increasing time is shown from t_0 to t_9. The remainder of the simulation cell (of size $50\sigma \times 50\sigma \times 140\sigma$) is filled with solvent (not shown).

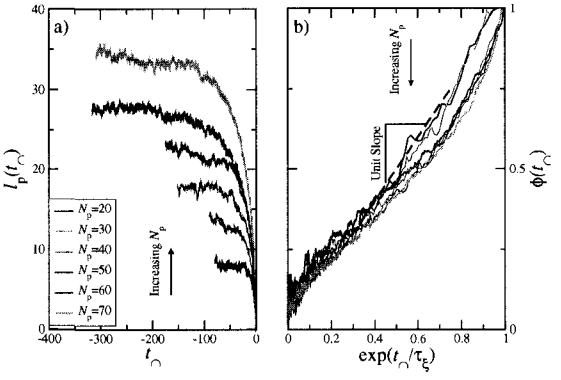

Fig. 5. a) Plot of escape curves $l_p(t_\cap)$ *vs.* time $t_\cap$. b) Plot of scaled escape curves $\phi(t_\cap) \equiv 1 - l_p(t_\cap)/(L_p/2)$ *vs.* $\exp(t_\cap/\tau_\xi)$. Both panels correspond to polymer-obstacle collisions with $f_0 = 4$ for various molecular sizes $N_p \in [20, 70]$. Panel b) illustrates that the molecules exhibit universal escape dynamics. The line of unit slope corresponds to the predicted universal curve.

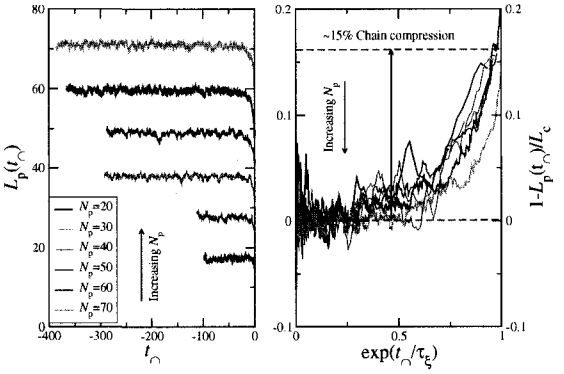

Fig. 6. Plots of $L_p(t_\cap)$ *vs.* $t_\cap$ and $1 - L_p(t_\cap)/L_c$ *vs.* $\exp(t_\cap/\tau_\xi)$ for several chain lengths. All chains appear to exhibit a compression of approximately 15% near the end of the escape sequence.

shows a plot of $L_p(t_\cap)$ *vs.* $t_\cap$ along with $1 - L_p(t_\cap)/L_c$ *vs.* $\exp(t_\cap/\tau_\xi)$. From Figure 6 it is clear that the molecule begins to relax back to its equilibrium conformation during the final part of the escape sequence. This compression is limited to approximately 15% of L_c, where L_c is the contour length of the chain (as previously defined). If $L_p(t_\cap)$ were constant up to the point of escape, we would expect Figure 5 to follow the expected universal curve more closely.

We now turn our attention to the forces on the obstacle given by F_{obs}, an expression for which is obtained from equation (11). We treat the post as a free polymer with friction coefficient ξ_f and the resulting force on the obstacle is $F_{obs} = \xi_f \dot{r}_c(t)$. We require $\xi_f \to \infty$ and $\dot{r}_c(t) \to 0$ while the product remains finite and is equal

to the remaining terms of equation (11). This calculation gives

$$f_0 L_p + (L_p - 2l_p(t))\xi_p \dot{l}_p(t) + F_{obs} = 0. \quad (24)$$

Substituting the expression for $l_p(t)$ into equation (24) and simplifying we obtain

$$-F_{obs} = f_0 L_p \left(1 - \exp\left[2\left(\frac{t-\tau_{esc}}{\tau_\xi}\right)\right]\right). \quad (25)$$

The maximum and minimum values of F_{obs} correspond to

$$\begin{aligned} l_p^0 &= \tfrac{L_p}{2} \Rightarrow |F_{obs}| = f_0 L_p, \\ l_p^0 &= 0 \Rightarrow |F_{obs}| = 0 \end{aligned} \quad (26)$$

and are associated with the U- and I-shaped states, respectively.

It is easy to conceive of a method to test this experimentally using optical tweezers. One can trap an obstacle in place and introduce polymers which collide with the obstacle, thus providing a direct method to measure the force on the obstacle. Although for a fixed obstacle F_{obs} does not alter the escape dynamics, it will play a role when the obstacle is allowed to translate.

The polymer-obstacle collision model agrees well with the data from the MD simulations. It is prohibitively difficult to test all aspects of the model, in particular obtaining a good measure of the force on the post due to the polymer is computationally challenging since the collisions are rather short lived and the instantaneous force on the obstacle has large fluctuations.

3.3 Polymer–(fixed)-obstacle collision: fluid flow

We now focus on a problem analogous to that of the previous section, a single polymer in a (plug-like) flow with velocity v_s which collides with a fixed obstacle. Although nearly a direct analog of the previous problem, replacing the external force by a flow introduces a few subtle differences.

In this example the force on the molecule is conformationally dependent and directly proportional to the magnitude of the flow, v_s. In contrast to the external-force example, the molecule will now experience hydrodynamic coupling (during a collision) thus reducing its friction coefficient [11,28]. The model of Section 3.1 incorporates this effect.

A schematic illustration of a fluid-flow–driven polymer-obstacle collision is shown in Figure 2b. In the absence of obstacles, the molecules are hydrodynamically impermeable (non–free-draining equilibrium coils with velocity v_s). In the context of our original equations of motion, during a collision the flow is equivalent to pulling the obstacle at constant velocity through the solvent. In terms of equation (9), $\dot{r}_c(t)$ is replaced by v_s and the resulting equation of motion is

$$-\rho_p L_p \ddot{l}_p(t) = v_s \xi_p \Big(L_p - 2l_p(t)\Big) + \xi_p L_p \dot{l}_p(t). \quad (27)$$

Equation (27) is identical to equation (9) except that f_0 is replaced by $v_s\xi_p$. The solution to equation (27) subject to the initial condition $l_p(0) = l_p^0$ and neglecting inertial terms is thus

$$l_p(t) = \frac{L_p}{2}\left(1 - \exp\left[\frac{t-\tau_{esc}^v}{\tau_\xi^v}\right]\right), \quad (28)$$

where $\alpha_p^0 = l_p^0/\frac{1}{2}L_p$ is the fractional offset in chain lengths and $\tau_{esc}^v(l_p^0)$ corresponds to the escape time of the molecule and is given by

$$\tau_{esc}^v(l_p^0) = \tau_\xi^v \ln\left(\frac{1}{1-\alpha_p^0}\right). \quad (29)$$

Equations (28) and (16) are also essentially the same except that τ_ξ is replaced by τ_ξ^v:

$$\tau_\xi^v = \frac{L_p}{2v_s}. \quad (30)$$

Although the fluid-flow and external-force regimes represent fundamentally different transport mechanisms, the resulting escape dynamics are essentially the same. The ratio of escape times for the two regimes is $\tau_{esc}(l_p^0)/\tau_{esc}^v(l_p^0) = \xi_p v_s/f_0$. In other words, to achieve equivalent escape dynamics in both regimes we require either a flow with velocity $v_s = f_0/\xi_p$ or an external force with magnitude $f_0 = \xi_p v_s$. Even though the escape dynamics in both cases are equivalent, the free velocities of the molecules (in the absence of obstacles) are quite different in each case. In a fluid flow the free velocity for all molecular sizes is v_s, whereas in the case of an external force the free velocity is $v_f = f_0 L_p/6\pi\eta R_H \propto N_p^{-2/5}$ (since the molecules are impermeable or non–free-draining).

Similar to the external-force method, we can estimate the length and time scales required for the molecule to make the transition from a U- to a J-shaped state. The critical length required for the molecule to move (relative to the U-shaped state) before deterministic escape ensues is

$$\delta_c^v = \sqrt{\frac{k_B T \ln(2)}{v_s \xi_p}} \sim v_s^{-1/2}. \quad (31)$$

The corresponding transit time from the U- to J-shaped state is

$$\tau_c^v = \frac{L_p}{2v_s} \sim N_p/v_s. \quad (32)$$

If the difference in arm lengths exceeds the critical value of δ_c^v (*i.e.*, if $l_p^0 \le L_p/2 - 2\delta_c^v$), it is reasonable to assume that deterministic escape ensues. In general, the U-shaped state contributes very little to overall dynamics in the system (as in the external-force regime).

The average escape time for a molecule assuming a uniform distribution of l_p^0 for the fluid-flow collisions is

$$\langle \tau_{esc}^v \rangle = \frac{L_p}{2}/v_s. \quad (33)$$

Qualitatively, $\langle \tau_{esc}^v \rangle$ represents the time for a molecule to move over a distance $L_p/2$ with an effective velocity v_s.

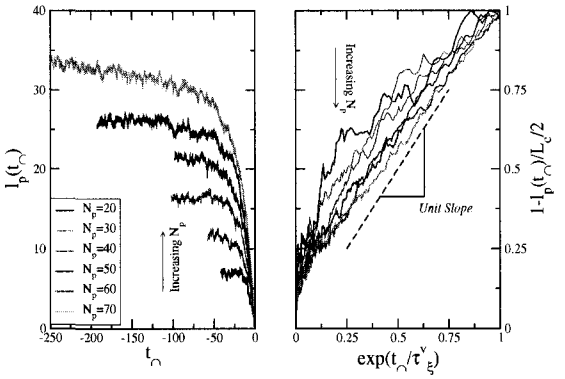

Fig. 7. Plot of $l_p(t_\cap)$ *vs.* $t_\cap$ and $\phi(t_\cap)$ *vs.* $\exp(t_\cap/\tau^v_\xi)$ for various molecular sizes N_p in a flow with a velocity $v_s = 2$. In this case the curves lie above the expected universal behaviour, a line of unit slope.

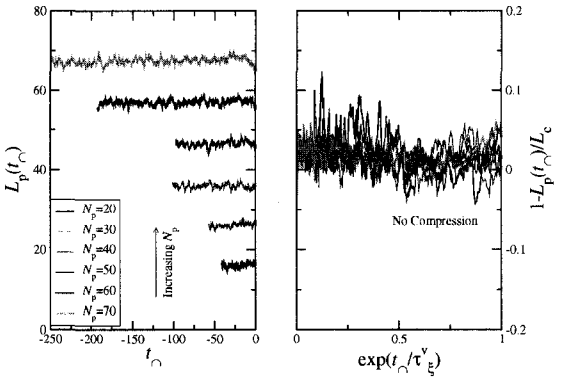

Fig. 8. Plots of $L_p(t_\cap)$ *vs.* $t_\cap$ and $1-L_p(t)/\langle L_p\rangle$ *vs.* $\exp(t_\cap/\tau^v_\xi)$ for several different chain lengths. Unlike the case of the external-force regime the molecules do not appear to undergo chain compression near the end of the escape sequence.

In our simulations the magnitude of the flow is chosen to be $v_s = 2$, while the other MD parameters remain unchanged. Figure 7 shows a plot of $l_p(t_\cap)$ as a function of $t_\cap = t - \tau^v_{esc}$ and the universal curves $\phi_s(t_\cap)$ (previously defined) as a function of $\exp(t_\cap/\tau^v_\xi)$. Plotted this way the data should fall on a straight line through the origin. Figure 7 shows the data for the escape curves for $N_p \in [20, 70]$. The MD data follow the expected trend and as N_p is increased the curves tend toward unit slope. Shorter chains experience larger fluctuations since the total force causing their elongation is directly proportional to their length. The presence of the polymer and the obstacle naturally deform the flow around the obstacle and, as a consequence, alter the forces on the polymer.

We can also examine the validity of the assumption that the molecule remains fully extended during the entire escape process. Figure 8 shows $L_p(t_\cap)$ as a function of $t_\cap$ along with a set of universal curves similar to the previous section. Unlike the external-force regime, we do not observe a chain compression at the end of the escape sequence. The molecules remain at nearly full extension up to the point at which they escape from the obstacle, $l_p(t) = 0$. The fluid flow keeps the molecule elongated during the entire escape process.

In a flow and during a collision, adjacent sections of a molecule are coupled (hydrodynamically) thus reducing the friction coefficient of the molecule. Although this effect does not alter the escape dynamics, the force on the obstacle is directly impacted (we neglect the force on the obstacle due to the flow, it is simply an additive constant proportional to the flow strength). In a manner similar to the external-force case, the force on the obstacle is obtained from equation (11) and can be written as

$$F^v_{obs} = v_s \frac{\xi_p L_p}{2}\left[1+\exp\left(\frac{t-\tau^v_{esc}}{\tau^v_\xi}\right)-2\exp\left(2\frac{t-\tau^v_{esc}}{\tau^v_\xi}\right)\right]. \tag{34}$$

The two limiting cases of F^v_{obs} are

$$\begin{aligned} l^0_p = \frac{L_p}{2} &\Rightarrow |F^v_{obs}| = v_s\frac{\xi_p L_p}{2}, \\ l^0_p = 0 &\Rightarrow |F^v_{obs}| = 0, \end{aligned} \tag{35}$$

corresponding to the U- and I-shaped states, respectively. The important thing to note is that unlike the external-force case, the maximum force on the obstacle does *not* occur for $l^0_p = L_p/2$. Instead, the maximum force on the obstacle occurs for $\alpha^0_p = \frac{3}{4}$, or $l^0_p = \frac{3}{4}\frac{L_p}{2}$:

$$\max|F^v_{obs}| = \frac{9}{16} v_s \xi_p L_p, \tag{36}$$

and is a direct result of hydrodynamic coupling.

We can compare the obstacle force in the external-force and fluid-flow examples by plotting the force on the obstacle (rescaled by $f_0 L_p$ and $v_s \xi_p L_p$, respectively) as a function of α^0_p. Figure 9 shows these reduced forces along with schematic depictions of the various conformations for which the extrema occur. As we expect, $F_{obs}/F^v_{obs} = 2$ for $\alpha^0_p = 1$ due to the hydrodynamic coupling of the molecule in the fluid flow (the U-shaped state), while $F_{obs} = F^v_{obs} = 0$ for $\alpha^0_p = 0$ (the I-shaped state). The key difference (and a very striking result at that) is that in the fluid-flow regime the maximum force on the obstacle occurs for $\alpha^0_p = 3/4$. This difference does *not* affect the escape dynamics since there is no overall translation of the system but such an effect may alter the dynamics in the polymer-polymer collision regime.

The presence of an obstacle naturally deforms our flow profile; moreover, the addition of a molecule will further alter the flow pattern. The effect that the presence of a polymer and an obstacle has on the flow is also of fundamental importance as it may contribute (non-trivially) to the chain dynamics, especially in more complex systems. By examining the streamlines, which are obtained by calculating the stream function

$$\Phi(\mathbf{r}) = \int \rho(v_j \mathrm{d}l_i - v_i \mathrm{d}l_j) \tag{37}$$

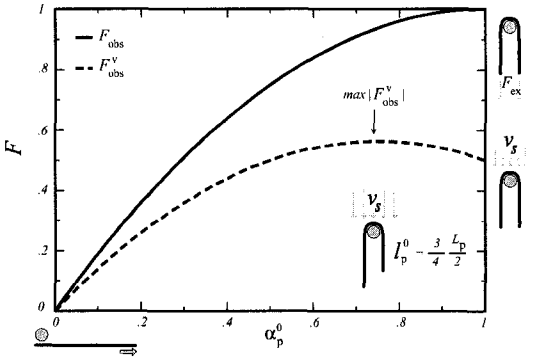

Fig. 9. Plot of the scaled force on the obstacle at $t = 0$ as a function of α_p^0, the fractional offset in chain lengths for both the external-force and fluid-flow regimes. Also schematically depicted are the conformations corresponding to the various regimes: I-shaped, J-shaped and U-shaped states.

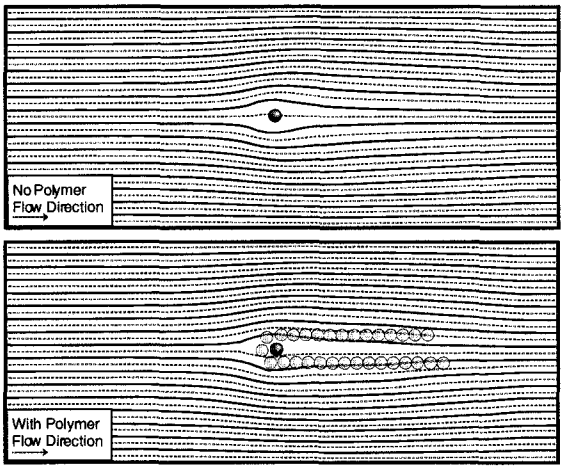

Fig. 10. Top: fluid streamlines around an isolated obstacle. The streamlines are symmetric about the x-axis and are (qualitatively) in the expected form for low Reynolds-number flow around an obstacle. Bottom: this panel illustrates the effects on the flow pattern due to the presence of a single polymer attached at one side of the obstacle. The polymer perturbs the flow field and, consequently, affects the resulting forces on the chain.

on a regular grid (in the simulation cell) and along the path $\mathbf{r}$, we can examine qualitatively the effects of the flow profile when we introduce the obstacle and the polymer [27]. In the above equation v_i are the average velocities of fluid particles in direction i.

The steady state equilibrium streamlines around the obstacle are shown in the top panel of Figure 10, while the bottom panel further includes a polymer with $N_p = 30$ (tethered in place on the left side of the obstacle). Qualitatively, the polymer disrupts the flow profile around the obstacle and, consequently, changes the resulting forces on the molecule. From Figure 10 (with polymer), the flow flattens locally near the polymer although the magnitude of the flow is not affected significantly along the chain. For large chains this effect will be more pronounced. In principle, one can incorporate directly the shape of the flow profile in analytical calculations and more accurately model the effects of the fluid flow in the presence of the polymer and obstacle [12]. Such a self-consistent approach can be very useful for systems with more complex geometries, for example in examining transient mixing of binary fluids.

3.4 Polymer-polymer collision

We now focus on the general polymer-polymer collision problem as outlined in Section 3.1. The system is composed of two molecules: a *test* molecule (on which an external force is applied) and a *free* molecule to which no force is applied. In the large free-polymer limit (*i.e.*, when $L_f, \xi_f \to \infty$ and $l_f(0) = L_f/2$) this case reduces to the polymer–fixed-obstacle collision example.

A polymer-polymer collision is similar to that of its fixed-obstacle counterparts, except for an overall translation of the system at velocity $\dot{r}_c(t)$ (as measured by the movement of the contact point between the two chains). It is in some senses a superposition of the external-force and fluid-flow regimes. A typical collision event involves the migration of the *test* chain in the direction of the applied force. When this chain collides with the *free* chain both molecules deform. The degree of deformation will depend on the initial collision parameters, *e.g.*, the external force and/or the initial conditions $l_p(0)$ and $l_f(0)$. Mid-point collisions ($l_p(0) = L_p/2, l_f(0) = L_f/2$) lead to the longest collision events and dynamics are initially dominated by Brownian motion.

The dynamics of the two-polymer collision are given by the following equations: the first governs the *test* polymer motion,

$$\Big(L_p - 2l_p(t)\Big)\Big(f_0 + \xi_p \dot{r}_c(t)\Big) + \xi_p L_p \dot{l}_p(t) = 0, \qquad (38)$$

while the equation for the *free*-polymer motion is

$$\Big(L_f - 2l_f(t)\Big)\xi_f \dot{r}_c(t) + \xi_f L_f \dot{l}_f(t) = 0. \qquad (39)$$

The final equation provides the connection between equations (38) and (39),

$$-f_0 L_p = \Big(L_p - 2l_p(t)\Big)\xi_p \dot{l}_p(t) + \Big(L_f - 2l_f(t)\Big)\xi_f \dot{l}_f(t) + \Big[\Big(L_p - l_p(t)\Big)\xi_p + \Big(L_f - l_f(t)\Big)\xi_f\Big]\dot{r}_c(t). \qquad (40)$$

These equations implicitly assume near complete extension of the chains as outlined in Section 3.1.

In terms of the MD model, the fixed-obstacle is replaced by a *free* chain whose monomers are physically identical to those of the *test* chain. In our simulations

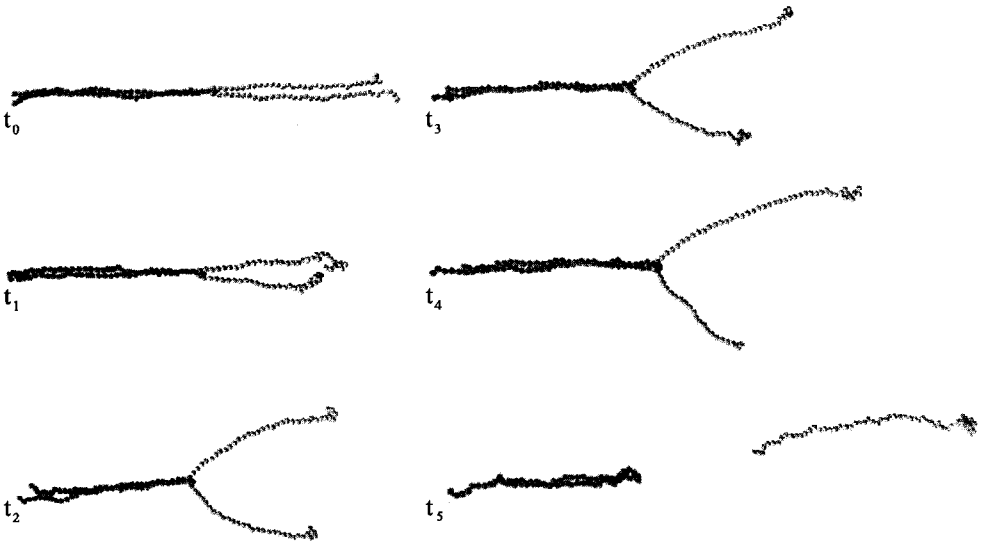

Fig. 11. Snapshots from a MD simulation of a polymer-polymer collision of chains with $N_p = 70$ and $N_f = 70$ monomers. The *test* chain has a force per monomer of $f_0 = 4$ applied to it while the *free* chain does not. The snapshots are taken in the reference frame of the point of contact between the two chains (in actuality the entire system is translating). The evolution of the escape dynamics can be clearly seen. The chains first form a double-hairpin conformation. The arms of the *test* chain then begin to open into the V-shaped conformation and escape occurs with the upper (longer) arm of the molecule cannibalizing the lower (shorter) arm ($t_2 \rightarrow t_4$). The last frame (t_5) shows the molecules beginning to relax. This simulation is carried out in a simulation box of size $50\sigma \times 50\sigma \times 140\sigma$.

the external force per monomer on the *test* chain is chosen to be $f_0 = 4$. A detailed statistical analysis of the polymer-polymer collisions using MD is an arduous computational task; we therefore restrict our examination to collisions where the *test* chain escapes first (in principle, this represents the physically interesting cases that lead to fractionation). More specifically, we focus on the case where the *free* chain is initially dragged by (or near) its middle monomer (*i.e.*, $l_f(0) \simeq L_f/2$). We use the largest chains that are computationally feasible, $N_f = 70$ and $N_p \in [20, 70]$. Larger systems result in prohibitively long simulation times given the need for large simulation cells.

Figure 11 shows a typical collision of two chains from our MD simulations with $N_p = 70$ and $N_f = 70$. It illustrates several striking features. The *free* chain is both hydrodynamically coupled and significantly extended. However, the *test* molecule is not fully elongated and it forms an open V-shaped state resulting from the mechanical instability associated with the two arms of the *test* chain being aligned in the direction of the overall translation. In other words, the V-shaped state is a result of the effective hydrodynamic counter flow on the chain due to its net motion (at velocity $\dot{r}_c(t)$). As we increase N_f this effect is reduced and as $N_f \rightarrow \infty, l_f(0) \rightarrow L_f/2$ it is completely nullified. The inclusion of explicit solvent allows us to observe this effect. Brownian dynamics would be unable to reproduce such an effect due to its purely stochastic nature (*i.e.*, the friction of the molecules is independent of their conformations).

These types of collisions do occur in experiments and similar V-shaped states have been observed [34,2]. In such experiments there are numerous *free* chains although the concentration of chains is still well below the entanglement threshold c^*. While this open state is seen in multi-chain systems, our simulations illustrate that a single *free* chain is also able to deform the *test* molecule and induce this V-shaped state. Therefore, an open V-shaped state is not evidence that a drifting DNA molecule is necessarily dragging along several free polymers (as is generally assumed in the literature).

It is evident from Figure 11 that the observed collision sequence differs from that assumed in our model due to the existence of the V-shaped state thus complicating a comparison with our model. The degree to which the dynamics differ is difficult to estimate. In light of these differences we qualitatively examine the escape curves from the polymer-polymer collision simulations and provide a detailed analysis of our equations in the next section.

Figure 12 shows plots of $l_p(t)$ for a series of N_p from the MD simulations along with the angle between the two arms of the molecule as a function of time. The time axis has also been translated so that all chains escape at $t \rightarrow t - \tau_{esc} = 0$. In this case $l_p(t)$ is the distance from the contact point to the terminal monomer on the short arm of the molecule. The length in the field direction (parallel to the net motion of the system) is $l_p^{||}(t)$ and is obtained from $l_p^{||}(t) = l_p(t)\cos[\theta(t)]$.

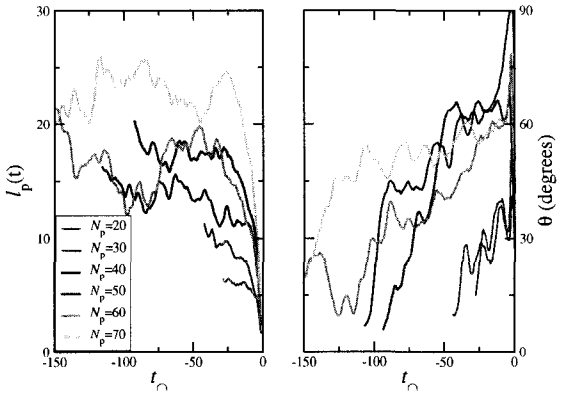

Fig. 12. Left panel: plots of the length of the shortest arm of the chain $l_p(t)$ for the *test* polymer during a polymer-polymer collision with a *free* chain of length $N_f = 70$. In these instances the *test* chain escapes first, *i.e.*, before $l_f(t) = 0$. Right panel: plot of the angle between the two arms of the test molecule $\theta(t)$ as a function of time. This angle $\theta(t)$ increases as the chain escapes since the shorter arm must eventually orient itself along the longer arm as it approaches complete escape. The time axis is translated so all chains escape at $t = 0$.

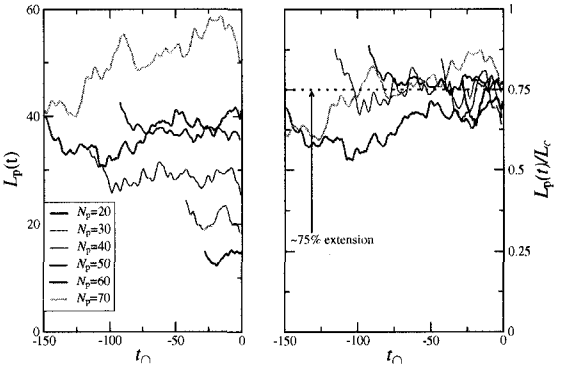

Fig. 13. Left panel: plot of the length of the *test* molecule, $L_p(t)$, during a polymer-polymer collision, calculated as the sum of the distances between the leading ends of the chain and the contact point between the chains. Right panel: plot of $L_p(t)$ for the individual chains scaled by the expected fully stretched length of the molecule $L_c^p \approx N_p\langle b_p\rangle$. The molecules tend to exhibit a compression of approximately 75%.

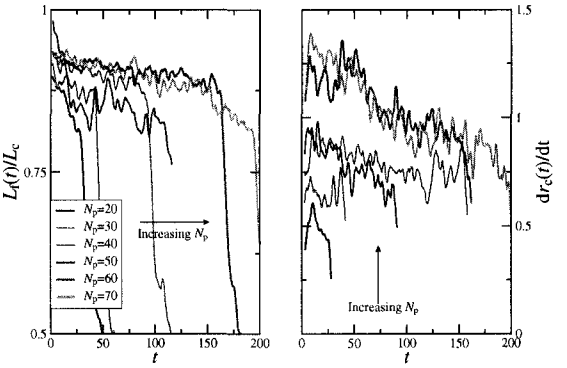

Fig. 14. Plot of the length of the *free* chain, $L_f(t)$, scaled by its contour length, L_c^f, as a function of time (left panel) along with a plot of the velocity of the contact point $\dot{r}_c(t)$ between the *free* and *test* chains as a function of time (right panel). The velocity of the contact point appears to vary roughly linearly in time during the escape process. The rapid drop in the $L_f(t)$ and $\dot{r}_c(t)$ corresponds to the escape of the *test* chain. The *free* chain has $N_f = 70$ monomers.

The $l_p(t)$ curves are qualitatively similar to those of the fixed-post example. However, there are much larger fluctuations in $l_p(t)$ due to the reduction in the overall force providing stretching of the chain (since the *free* chain has a finite friction) and the angle between the two arms of the chain as it escapes may also vary. As N_p is decreased, the retarding force required to achieve full extension of the *test* chain is lessened. The angle between the arms of the molecule is also reduced and fluctuates less. Another consequence of a smaller N_p is a resulting decrease in the net force on the *free* chain; this may lead to an incomplete extension of the *free* chain and larger fluctuations in the drag force. For the cases depicted in Figure 12 the *free* chain is relatively extended for the majority of the escape sequences. The angle between the two arms of the molecule $\theta(t)$ is an increasing function of time up to the point of escape. This is a result of the shorter arm tending to become oriented perpendicular to the field direction since the force keeping the shorter arm aligned in the field direction is decreasing as the chain escapes.

In order to quantitatively examine the extension of the *test* molecule we monitor its length, $L_p(t)$, along the line connecting the ends of the molecule and the point of contact between the chains. Figure 13, left panel, shows a plot of $L_p(t)$ for several N_p and Figure 13, right panel, shows a plot of $L_p(t)$ scaled by the contour length of the chain L_c. For the chosen parameters the molecule tends to extend by about 75% during the escape process. As noted, if we increase N_f the overall extension of the *test* chain will increase due to a larger retarding force on the *test* chain. The extension of either chain is a balance between the length of both chains and the applied external force. It is feasible to modify our model to include this inter-arm opening; however, it requires some non-trivial modifications and a number of simplifying assumptions.

In the examples we have chosen the *free* chain does not escape. The most important aspect of the *free* chain is the extent to which it remains stretched during the escape and what effect the variation of L_p has on this stretching. Figure 14 shows a plot of the length of the *free* chain, $L_f(t)$ along the direction of motion divided by the contour length of the molecule $L_c^f \simeq N_f\langle b_p\rangle$. The chains are stretched in the field direction within about 70–80% of their contour length. The data are shown up to the point of escape of the *test* chain. For our purposes the *free* chain can be considered to be near full extension. We note a very

fast relaxation of the *test* chain after the chains cease to be in contact.

The velocity of the contact point also plays an important role in the dynamics. Figure 14 (right panel) shows a plot of the velocity of the contact point between the two molecules. Interestingly enough, it would appear that $\dot{r}_c(t)$ decreases almost linearly as a function of time (we examine this in the next section). This decrease in the velocity is due to the escape of the test chain and the resultant decrease in the force driving escape. We will explore this aspect from our general set of equations in the next section.

3.5 Model polymer-polymer collision calculations

In this section we examine the dynamics of the two-chain collision system as dictated by equations (38–40). Although a V-shaped state is not directly included in the model it still provides a good first-order approximation to the system dynamics, especially in the limit of $N_f \gg N_p$.

We rewrite the equations of motion using the following transformations:

$$\Lambda_x(t) = 1 - \frac{l_x(t)}{L_x/2}, \qquad \Gamma_c(t) = \frac{r_c(t)}{L_p/2},$$
$$\mathcal{L}_{pf} = \frac{L_p}{L_f}, \quad \xi_{pf} = \frac{\xi_p}{\xi_f}, \quad \text{and} \quad \tilde{t} \to t/\tau_\xi, \tag{41}$$

where $\tau_\xi = 2f_0/(L_p\xi_p)$ and where $x = (p, f)$ denotes the *test* and *free* chains, respectively. We then obtain an expression for $\dot{\Gamma}_c(t) = (\mathcal{L}_{pf}{}^{-1})\dot{\Lambda}_f(t)/\Lambda_f(t)$ from equation (39) and insert it into equations (38) and (40). With some algebraic manipulation these equations become

$$\frac{d}{d\tilde{t}} \ln\left(\frac{\Lambda_f(\tilde{t})}{\Lambda_p^{\mathcal{L}_{pf}}(\tilde{t})}\right) + \mathcal{L}_{pf} = 0 \tag{42}$$

and

$$2 - \left[\frac{d}{d\tilde{t}}\Lambda_p^2(\tilde{t}) + \mathcal{L}_{pf}^{-1}\left(1+\Lambda_p(\tilde{t})\right)\frac{d}{d\tilde{t}}\ln(\Lambda_f(\tilde{t}))\right] - \frac{1}{\mathcal{L}_{pf}^2\xi_{pf}}\left[\frac{d}{d\tilde{t}}\Lambda_f^2(\tilde{t}) + \left(1+\Lambda_f(\tilde{t})\right)\frac{d}{d\tilde{t}}\ln(\Lambda_f(\tilde{t}))\right] = 0. \tag{43}$$

Equations (42) and (43) provide a compact version of the general polymer-polymer collision problem. We assume a solution of the form

$$\Lambda_x(\tilde{t}) = \exp(\lambda_x(\tilde{t})). \tag{44}$$

This allows us to obtain a series solution for $\lambda_x(\tilde{t})$ and, consequently, for the original problem (transformed equations not shown). The general series for $l_p(t)$ and $l_f(t)$ have the form shown in equations (45) and (46):

$$l_p(t) = \frac{L_p}{2}\left(1 - \exp\left[\frac{\Theta_0^f}{\Theta_0^f + \Theta_0^p\mathcal{L}_{pf}^{-1}}\frac{t}{\tau_\xi} + \sum_{n=1}^{\infty}\frac{\mathcal{L}_{pf}^{-1}\Theta_n}{\left(\Theta_0^f + \Theta_0^p\mathcal{L}_{pf}^{-1}\right)^{2n+1}}\left(\frac{t}{\tau_\xi}\right)^{n+1} - \frac{\tau_0^p}{\tau_\xi}\right]\right), \tag{45}$$

$$l_f(t) = \frac{L_f}{2}\left(1 - \exp\left[\frac{\Theta_0^p}{\Theta_0^f + \Theta_0^p\mathcal{L}_{pf}^{-1}}\frac{t}{\tau_\xi} - \sum_{n=1}^{\infty}\frac{\Theta_n}{\left(\Theta_0^f + \Theta_0^p\mathcal{L}_{pf}^{-1}\right)^{2n+1}}\left(\frac{t}{\tau_\xi}\right)^{n+1} - \frac{\tau_0^f}{\tau_\xi}\right]\right). \tag{46}$$

The Θ_0^f and Θ_0^p are constants and the Θ_n are n-th–order constant prefactors in the series, expressions for Θ_0^f, Θ_0^p and Θ_1 are given:

$$\Theta_0^f = 2((1-\alpha_f^0)^2 + 1) - (\mathcal{L}_{pf}\xi_{pf}\alpha_p^0 + \alpha_f^0), \tag{47}$$

$$\Theta_0^p = 2\mathcal{L}_{pf}^2\xi_{pf}(1 - (1-\alpha_p^0)^2), \tag{48}$$

$$\Theta_1 = \mathcal{L}_{pf}^2\xi_{pf}\Big(3\mathcal{L}_{pf}\xi_{pf}\Theta_0^f(1-\alpha_p^0)^3 + \Big[2 - 4\mathcal{L}_{pf}\xi_{pf} + 8(1-\alpha_f^0)^4 + 8(1-\alpha_f^0)^3 + (10 - 4\Theta_0^p - 8\mathcal{L}_{pf}\xi_{pf})(1-\alpha_f^0)^2 + (-\Theta_0^p + 4 - 4\mathcal{L}_{pf}\xi_{pf})(1-\alpha_f^0) + \xi_{pf}\Theta_0^p\Big](1-\alpha_f^0)^2 + \Theta_0^p(1-\alpha_f^0)(3-4\alpha_f^0) + \mathcal{L}_{pf}\xi_{pf}(1-\alpha_p^0)\Theta_0^f\Big). \tag{49}$$

The Θ_n are complicated functions of $\mathcal{L}_{pf}, \xi_{pf}, \alpha_f^0, \alpha_p^0$ and although a general formula for Θ_n is not known they can be calculated by brute force. The first two terms in the series solution yield the prefactors of the form shown in equation (49).

The two characteristic time scales τ_0^p and τ_0^f are

$$\tau_0^p = \tau_\xi \ln\left(\frac{1}{1-\alpha_p^0}\right) \quad \text{and} \quad \tau_0^f = \tau_\xi \ln\left(\frac{1}{1-\alpha_f^0}\right), \tag{50}$$

where $\alpha_p^0 = l_p^0/L_p/2$ and $\alpha_f^0 = l_f^0/L_f/2$ are initial offsets in chain lengths. The time scale τ_0^p clearly corresponds to the fixed-post limit escape time of the polymer, *i.e.*, when $\mathcal{L}_{pf} \to 0$ and $\xi_{pf} \to 0$. The first-order molecular escape times are obtained by solving equations (45) and (46) for the times at which the chains escape,

$$\tau_{esc}^p \simeq \tau_0^p\left[1 + \mathcal{L}_{pf}^{-1}\frac{\Theta_0^p}{\Theta_0^f}\right], \tag{51}$$

where τ_{esc}^p is the *test* chain escape time,

$$\tau_{esc}^f \simeq \tau_0^f\left[\mathcal{L}_{pf}^{-1} + \frac{\Theta_0^f}{\Theta_0^p}\right], \tag{52}$$

and where τ_{esc}^f is the *free*-chain escape time. We have compared the results for this series solution with numerical calculations and both agree within a few percent provided $\mathcal{O}(t^4)$ are included in the series expansion.

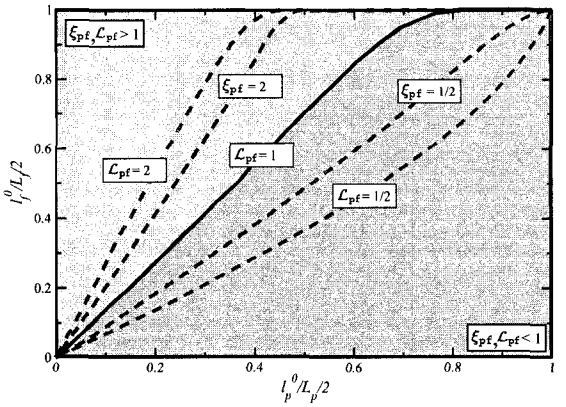

Fig. 15. (Colour on-line) Escape phase diagram in the (α_p^0, α_f^0) phase space for a number of values of the parameters $\mathcal{L}_{pf}$ and ξ_{pf}. The figure denotes regions where either the *free* or *test* chain escapes first; above each line the region corresponds to the *free* chain escape domain and vice versa for the *test* chain. The base case corresponds to that where $\mathcal{L}_{pf} = \xi_{pf} = 1$ and corresponds to two identical chains colliding with one another. Increasing $\mathcal{L}_{pf}$ or ξ_{pf} shifts the line to the left, while decreasing $\mathcal{L}_{pf}$ or ξ_{pf} shifts the line to right (asymptotically approaching the x-axis corresponding to the fixed-post regime). The upper shaded region (light pink) corresponds to $\xi_{pf}, \mathcal{L}_{pf} > 1$ and the remaining (lower, shaded) region corresponds to $\xi_{pf}, \mathcal{L}_{pf} < 1$.

The set of initial conditions α_p^0 and α_f^0 for which both chains escape at the same time (for particular $\mathcal{L}_{pf}$ and ξ_{pf}, τ_ξ will not alter the shape of this line) will provide us with an effective escape phase diagram for the chains. This line in the (α_p^0, α_f^0) phase space will denote the regions where either chain escapes first. We use $\mathcal{L}_{pf} = 1$ and $\xi_{pf} = 1$ as our reference case. Physically this corresponds to two chains colliding with the same contour lengths and the same friction coefficients per unit length. Intuitively, as we decrease $\mathcal{L}_{pf} < 1$ or $\xi_{pf} < 1$ we expect that this line will shift so as to increase the fraction of escapes where the *test* chain escapes first and vice versa for increasing $\mathcal{L}_{pf} > 1$ or $\xi_{pf} > 1$.

Figure 15 shows plots of several different escape scenarios obtained from numerical solutions of our equations, although the series approximation yields an essentially identical escape diagram. The case for $\mathcal{L}_{pf} = \xi_{pf} = 1$ is that shown by the solid line. The area under each curve yields the fraction of escapes which result from the *free* polymer escaping first, while the remaining area represents the fraction of escapes in which the *test* chain escapes first. For $\mathcal{L}_{pf} = \xi_{pf} = 1$ the *free* polymer is the one which predominantly escapes first. Varying either $\mathcal{L}_{pf}$ or ξ_{pf} shifts the line (and changes its overall shape) in the direction specified above. It turns out that $\xi_{pf} \simeq 1/2$ (or alternatively $\mathcal{L}_{pf} \simeq 1/2$) nearly corresponds to the regime where both chains escape with equal probabilities. Qualitatively, the asymmetry in the *test-free* polymer collision times arises from the competing forces which act on the *test* chain, it feels both the influence of the external force (which drives the escape process) but also the effective hydrodynamic counter flow which inhibits escape. On the other hand, the *free* polymer is driven purely by the overall translation of the system. As a result, for two chains of equal length the *free* chain would escape first in most instances; hence the need for a $\xi_{pf} < 1$ or $\mathcal{L}_{pf} < 1$ to achieve equal domains on the escape phase diagram. This argument is a gross simplification since (presumably) the escape dynamics are modulated by a complicated feedback mechanism depending on $\dot{l}_f(t), \dot{l}_f(t)$ $\dot{v}_c(t)$ and the particular values of $\xi_{pf} < 1$ and $\mathcal{L}_{pf} < 1$.

The case of a fixed post corresponds to the entire escape phase space, since only the *test* chain would escape. As we increase $L_{pf} > 1$ and $\xi_{pf} > 1$ the physical validity of the equations comes into question since we assumed *a priori* that the *free* polymer is large enough to provide sufficient retarding force on the *test* chain. Essentially Figure 15 provides a method of determining an optimal ratio of lengths and friction coefficients to obtain the desired fraction of escapes where either chain escapes first. One can imagine a parallel to decreasing the $L_{pf} < 1$ and $\xi_{pf} < 1$ with the effects in a multi-chain system, where the *test* chain collides with more than one *free* chain and results in an increase in the retarding force on the *test* chain. It is possible to modify the model to include the effects of multiple chains.

Using this form for the series solution of the general polymer-polymer collision problem we can also calculate the velocity of the contact point of the chain. The expression for the contact point velocity then has the form

$$\dot{r}_c(t) = \frac{L_p}{2}\frac{1}{\mathcal{L}_{pf}}\left(\frac{\Theta_0^p}{\Theta_0^f + \Theta_0^p \mathcal{L}_{pf}^{-1}}\frac{1}{\tau_\xi} - \frac{2\Theta_1}{\left(\Theta_0^f + \Theta_0^p \mathcal{L}_{pf}^{-1}\right)^3}\frac{t}{\tau_\xi^2}\right). \tag{53}$$

The above equation can be written in a more instructive form in the following manner:

$$\dot{r}_c(t) = \dot{r}_c(0)\left(1 - \frac{t}{T}\right), \qquad \forall\ t \in [0, \tau_{esc}],$$

$$\dot{r}_c(0) = \frac{L_f}{2\tau_\xi}\left(\frac{\Theta_0^p}{\Theta_0^f + \Theta_0^p \mathcal{L}_{pf}^{-1}}\right),$$

$$T = \tau_\xi \Theta_0^p \frac{\left(\Theta_0^f + \Theta_0^p \mathcal{L}_{pf}^{-1}\right)^2}{2\Theta_1} > \tau_{esc}. \tag{54}$$

For large T (for example a large *free* chain pinned in the middle) the system has essentially constant center-of-mass velocity. For the asymptotic case of two molecules colliding with $\alpha_f^0 = \alpha_p^0 = 1$, *i.e.*, corresponding to two middle pinned chains, neither of the molecules escape according to our equations. In actuality the chains will escape, driven by Brownian motion, and the escape time is finite. In this case Θ_1 is zero and the contact point velocity is simply given by

$$\dot{r}_c(t) = \frac{f_0 L_p}{\frac{L_p}{2}\xi_p + \frac{L_f}{2}\xi_f} \tag{55}$$

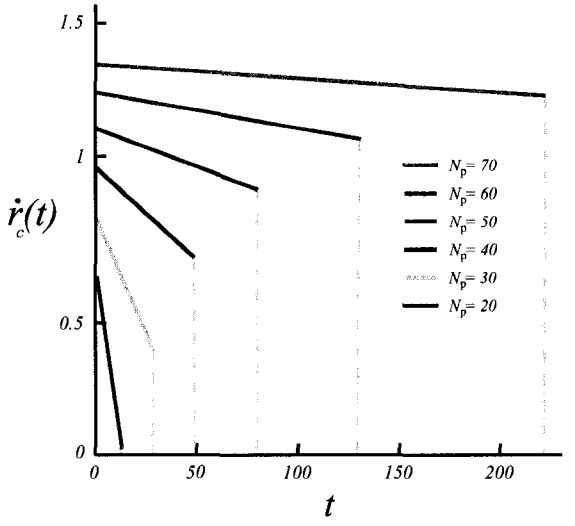

Fig. 16. Plot of the contact point velocity $\dot{r}_c(t)$ *vs.* time, for $N_p \in [20, 70]$. The *free* chain has $N_f = 70$. The dropdown lines are included to denote the point of escape of the chain and all chains are the initial conditions $\alpha_f^0 = 1$ and $\alpha_p^0 = 0.8$. The contact point velocity is a linearly varying function of t.

which is the expected result for two hydrodynamically coupled middle pinned chains colliding. Equation (53) is a decreasing function of t in the region where the equations are valid, that being $t < \tau_{esc}$.

Figure 16 shows a plot of the velocity of the contact point between the chains as a function of time for a *free* chain with $N_f = 70$ and for a number of different *test* chains as calculated directly from equation (54). The initial conditions are chosen to be in the same range as those for the MD simulations of the previous section, $\alpha_f^0 = 1$ and $\alpha_p^0 \simeq 0.8$, which corresponds to a non-escaping *free* chain.

Qualitatively the behaviour of $\dot{r}_c(t)$ is strikingly similar to that shown in Figure 14. The existence of the V-shaped state complicates a direct comparison but the values of T (slope of the line describing $\dot{r}_c(t)$) are close, for example for $N_p = 70$ the expression for $\dot{r}_c^{sim}(t) \simeq 1.29 - 0.0028t$ and that from our calculations yields $\dot{r}_c^{calc}(t) \simeq 1.35 - 0.00091t$. The discrepancy can be attributed to the V-shaped state, since in the model the chains are implicitly assumed to be fully elongated for the duration of the escape process. It is worth noting that the slope of the line $\dot{r}_c(t)$ is a constant and is given by the following expression:

$$\frac{d\dot{r}_c(t)}{dt} = -\frac{\dot{r}_c(0)}{T} = -\frac{L_f}{2\tau_\xi^2} \frac{2\Theta_1}{\left(\Theta_0^f + \Theta_0^p \mathcal{L}_{pf}^{-1}\right)^3}. \quad (56)$$

It turns out that this expression yields the following scaling law

$$\frac{d\dot{r}_c(t)}{dt} \propto N_p^{-1}. \quad (57)$$

Which is reflected in Figure 16, since for $N_p \gg 1$ the line tends to become horizontal.

Although the existence of the V-shaped state in the simulations does complicate a comparison of our model with simulations, the general equations can be used as a *rule of thumb* for predicting the behaviour in polymer-polymer collision systems. In our simulations, we looked at the cases where $\mathcal{L}_{pf} \approx 1$. In experiments it is often (though not always) the case that not only are the *free* polymers rather large, there are also a number of them and an individual *test* chain is more likely to be in collision with several free chains at the same time.

4 Conclusions

In this paper we have utilized large-scale Molecular-dynamics simulations with explicit solvent to examine the collision dynamics of polymers with molecular scale obstacles. We have also presented a simple but general model which can be applied to a number of different collision regimes, though we restrict our analysis to both the high-field and/or high-deformation limit. In particular, we have examined three distinct collision scenarios: the fixed-post (external-force) regime, the fixed-post (fluid-flow) regime and the polymer-polymer collision regime.

The case of a fixed-obstacle (external-force) collision is perhaps the simplest scenario which has a physical analogue in microfluidic systems. The dynamics of polymers colliding with these fixed obstacles contain important physical information which can be used to understand single-chain dynamics in media where these types of collisions occur. We have illustrated that chain dynamics can be described by a universal curve and our model and MD simulations agree well with each other in terms of these predicted dynamics. The inclusion of electrostatic forces may significantly modify the problem, typically non-conducting obstacles are used resulting in electric-field gradients that can significantly deform the chains in the presence of the posts as illustrated by Doyle *et al.* [4]. Electrostatics will also affect the dynamics of the chains between collisions since the molecules will be free-draining. The inclusion of electrostatic effects is certainly a useful extension of this work but is computationally quite challenging.

The fixed-obstacle (fluid-flow) regime, although nearly a perfect analogue of the external-force regime contained one important difference. During a collision in this regime the molecules are hydrodynamically coupled in the presence of the flow thus reducing the overall force on the obstacle. We have illustrated that although this hydrodynamic coupling mechanism does not qualitatively affect the escape dynamics and the two models can be mapped onto each other, there are quantitative differences in terms of the forces dictating the escape dynamics. We obtained expressions for the forces on the obstacles in both the external-force and fluid-flow regime. These expressions showed that the force on the obstacle in the fluid-flow regime is different from the external-force regime in a non-trivial manner.

We also examined the more general polymer-polymer collision problem. We illustrated that a V-shaped state

exists (for the *test* chain) where the molecule opens and a non-zero angle exists between the two arms of the molecule. This open state and the fact that we are limited to relatively small *free* chains which are unable to fully deform the *test* chain result in some minor differences in the overall escape dynamics. As we mentioned, for large *free* chains or numerous free chains we will asymptotically tend toward the fixed-post regime.

The investigation of the polymer-polymer collision problem provided a number of interesting results. For the chosen parameters the *test* chains compress by approximately 25% of the contour length of the molecule. Nonetheless, the escape dynamics look qualitatively similar to those observed in the fixed-post regimes except for an overall translation of the entire system. We also showed that the *free* chain, although slightly compressed, does extend to about 80% of its contour length and the assumption of hydrodynamic coupling of the *free* chain remains valid.

Although a closed-form analytical solution to the general problem is not obtained, we did present a series solution which hopefully will serve as a useful tool for exploring these systems. We have provided some insight into the escape behaviour and clearly illustrated that only two free parameters govern the relative escape of the two chains: the ratios of the lengths and the ratios of the friction coefficients per unit length given by $\mathcal{L}_{\rm pf}$ and $\xi_{\rm pf}$, respectively. Variations in $\mathcal{L}_{\rm pf}$ and $\xi_{\rm pf}$ have significant impact on the shape of the escape phase diagram in the $(\alpha_{\rm p}^0/L_{\rm p}/2, \alpha_{\rm f}^0/L_{\rm f}/2)$ space. In principle, it is possible to control these parameters experimentally. With more powerful computational resources we could examine in detail the statistical properties of the polymer-polymer collision problem and map out a phase diagram similar to that obtained from the model calculations. Ideally, our model will serve as a useful starting point for gaining a more robust understanding of both single polymer-polymer collisions and those occurring in multi-chain systems.

We also demonstrated that the contact point velocity is a linearly varying function of time during the escape process, both from the simulations and from the model calculations. Moreover, we have provided a relatively simple compact solution (up to order $\mathcal{O}(t^2)$) of the general polymer-polymer collision system, thus providing impetus for future theoretical work on multi-polymer collision systems. The appearance of the V-shaped state in the simulations is rather remarkable and we have offered a simple qualitative explanation for its existence. The V-shaped state simply results from the effective hydrodynamic counter flow on the chain due to the overall motion of the two-chain system at velocity $\dot{r}_{\rm c}(t)$, which causes the arms of the *test* chain to open and form the V-shaped state. The asymptotic limit of a fixed post completely nullifies this effect. In principle, it is possible to include the V-shaped state in our calculations although it would require a number of assumptions and may not be a trivial task.

There are several future studies which will make nice extensions to the model and the simulations. The inclusion of multiple free chains and modifications to include the non-zero angle between the two arms of the molecule would make the model more amenable to comparison with data for the regime where the chains are roughly of the same size $\mathcal{L}_{\rm pf} \simeq 1$, while for decreasing $\mathcal{L}_{\rm pf}$ we expect better agreement and the problem to collapse to the fixed-post regime in the asymptotic limit. The inclusion of electrostatic interactions in both the model calculations and the simulations themselves would be a rather difficult but highly instructive exercise. In principle, including the incomplete stretching of the chains and the inclusion of low-field limits for our expressions is also a valuable modification.

The authors would like to acknowledge the support of the Natural Sciences and Engineering Research Council of Canada (NSERC) for financial support in the form a research grant to G.W.S. and a post-graduate scholarship to M.K. The latter would also like to thank the Ontario Ministry of Training, Colleges and Universities for an Ontario Graduate Scholarship and the University of Ottawa for a National Excellence Scholarship. The authors also thank Dr Frédéric Tessier for many useful discussions. We also acknowledge the use of computational resources made available through both the High Performance Computing Virtual Laboratory (HPCVL) (`www.hpcvl.org`) and C3.ca (`www.c3.ca`).

References

1. J.-L. Viovy, Rev. Mod. Phys. **72**, 813 (2000).
2. A.E. Barron, H.W. Blanch, D.S. Soane, Electrophoresis **15**, 597 (1994).
3. C.F. Chou, R.H. Austin, O. Bakajin, J.O. Tegenfeldt, J.A. Castelino, S.S. Chan, E.C. Cox, H. Craighead, N. Darnton, T. Duke, J.Y. Han, S. Turner, Electrophoresis **21**, 81 (2000).
4. G.C. Randall, P.S. Doyle, Phys. Lett. Rev. **93**, 1 (2004).
5. W.D. Volkmuth, T. Duke, M.C. Wu, R.H. Austin, A. Szabo, Phys. Rev. Lett. **72**, 2117 (1994).
6. W.D. Volkmuth, R.H. Austin, Nature **358**, 600 (1992).
7. N. Minc, C. Futterer, K. Dorfman, A. Bancaud, C. Gosse, C. Goubault, J.L. Viovy, Anal. Chem. **76**, 3770 (2004).
8. L. Song, M.F. Maestre, J. Biomol. Struct. Dyn. **9**, 87 (1991).
9. J.M. Deutsch, J. Chem. Phys. **90**, 7436 (1989).
10. G.I. Nixon, G.W. Slater, Phys. Rev. E **50**, 5033 (1994).
11. P. Andre, D. Long, A. Ajdari, Eur. Phys. J. B **4**, 307 (1998).
12. P.S. Doyle, J. Bibette, A. Bancaud, J. Viovy, Science **295**, 2237 (2002).
13. M.E. Starkweather, M. Muthukumar, D.A. Hoagland, Macromolecules **31**, 5495 (1998).
14. M.E. Starkweather, M. Muthukumar, D.A. Hoagland, Macromolecules **33**, 1245 (2000).
15. E.M. Sevick, D.R.M. Williams, Eur. Phys. Lett. **56**, 529 (2001).
16. P.D. Patel, E.S.G. Shaqfeh, J. Chem. Phys. **118**, 2941 (2003).
17. P.M. Saville, E.M. Sevick, Macromolecules **32**, 892 (1999).
18. E.M. Sevick, D.R.M. Williams, Phys. Rev. Lett. **76**, 2595 (1996).

19. E.M. Sevick, D.R.M. Williams, Phys. Rev. E **50**, 3357 (1994).
20. J.S. Hur, E.S.G. Shaqfeh, J. Rheol. **45**, 421 (2001).
21. U.S. Agarwal, J. Chem. Phys. **113**, 3397 (2000).
22. B. Ladoux, P.S. Doyle, Europhys. Lett. **52**, 511 (2000).
23. R. Rzehak, D. Kienle, T. Kawakatsu, W. Zimmerman, Eur. Phys. Lett. **46**, 821 (1999).
24. K. Kremer, G.S. Grest, I. Carmesian, Phys. Rev. Lett. **61**, 566 (1988).
25. K. Kremer, G.S. Grest, J. Chem. Phys. **92**, 5057 (1990).
26. M.P. Allen, D.J. Tildesley, *Computer Simulations of Liquids*, 4th ed. (Oxford Science Publications, Oxford, 1987).
27. D.C. Rapaport, *The Art of Molecular Dynamics Simulation* (Cambridge University Press, 1995).
28. M. Kenward, G.W. Slater, J. Eur. Phys. E **14**, 55 (2004).
29. M. Cheon, J. Chang, J. Koplik, J.R. Banavar, Europhys. Lett. **58**, 215 (2002).
30. M. Tanaka, A.Y. Grosberg, Eur. Phys. J. E **7**, 371 (2002).
31. D.C. Rapaport, Phys. Rev. A **36**, 3288 (1987).
32. H. Goldstein, *Classical Mechaincs* (Addison-Wesley, 1980).
33. O.B. Bakajin, T.A.J. Duke, C.F. Chou, S.S. Chan, R.H. Austin, E.C. Cox, Phys. Rev. Lett. **80**, 2737 (1998).
34. O. de Carmejane, Y. Yamaguchi, T.I. Todorov, M.D. Morris, Electrophoresis **22**, 2433 (2001).

4 Polymer deformation in ratchets

Think from outside the box.
—— **Banksy**
(1974–Present)

Molecular Dynamics Simulations with Explicit Hydrodynamics III: Brownian ratchets and polymer deformation.
M. Kenward and G. W. Slater.
To be submitted to Euro. Phys. J. E., 2006.

This chapter contains a manuscript to be submitted to the European Physical Journal E and is third in the series of articles using coarsed grained MD simulations with explicit solvent. This manuscript provides a systematic examination of the deformation of polymer chains in ratchet potentials and the implications on the transport of polymers. We present a modification to the standard Bader ratchet model which takes into account the deformation of polymer chains induced by the application of the ratchet potential. and We also show that polymer deformation can be used to modulate the behaviour of polymers in ratchets. My contribution to this work was; writing the article in its entirety, carrying out all research (including development of simulation and analysis codes), derivation of all theoretical expression and all other tasks related to the production of the article.

EPJ manuscript No.
(will be inserted by the editor)

Molecular Dynamics simulations with explicit hydrodynamics III: Brownian ratchets and polymer deformation.

Martin Kenward[2] and Gary W. Slater[1]

[1] Department of Physics
University of Ottawa
150 Louis-Pasteur
Ottawa, Ontario, Canada
K1N 6N5
e-mail: gary.slater@uOttawa.ca
[2] e-mail: mkenward@science.uOttawa.ca

Received: date / Revised version: date

Abstract. We examine polymers in the presence of an applied asymmetric saw-tooth (ratchet) potential using molecular dynamics (MD) simulations with an explicit Lennard-Jones solvent. We show that the distribution of the center of mass for a polymer in a ratchet is relatively wide for potential well depths U_0 on the order of several k_BT. The application of the ratchet potential also deforms the polymer chains. With increasing U_0 the Flory exponent varies from that for a free 3d chain, $\nu = 3/5$ ($U_0 = 0$) to that corresponding to a 2d compressed (pancaked) polymer with a value of $\nu = 3/4$ for moderate U_0. This has the added effect of decreasing a polymer's diffusion coefficient from its 3d value D_{3d} to that of a *pancaked* polymer moving parallel to its minor axis D_{2d}. The result is that a polymer then has a time dependent diffusion coefficient, $D(t)$. We further show that this introduces a new idea for the operational mode of a ratchet, where the off time of the ratchet, t_{off} is defined in terms of the relaxation time of the polymer, τ_R. We also derive a modified version of the Bader ratchet model [1] which accounts for this deformation and we present a simple expression to describe the time dependent diffusion coefficient $D(t)$. Using this model we then illustrate that polymer deformation can be used to modulate polymer migration in a ratchet.

PACS. 83.10.Mj Molecular Dynamics, Brownian Dynamics – 61.41.+e Polymers, elastomers, and plastics – 82.20.Wt Computational modeling; simulation

1 Introduction

The environment in which biological macromolecules are found is a tempestuous one. The constant bombardment (i.e., Brownian motion) felt by entities at the molecular scale (nm–μm) is the source of diffusion and is directly related to molecular transport. It is a seemingly impossible task to generate deterministic motion against the forces to which a molecule is subject at these length scales (with typical energies on the order of k_BT). Borrowing an analogy from Bier, directed motion at the molecular level is akin to humans attempting to swim in molasses [2]. In spite of this, molecular processes work almost unimaginably well!

A key element of this success is a *molecular toolkit* which has evolved to inherently use diffusion in transport processes as opposed to it being a detriment. This is counterintuitive as diffusion is sometimes the bane of directed transport, often as a result of myopic attempts to scale down macroscopic manipulation techniques. Instead, diffusion plays an enormously important role in transport and we are only now beginning to fully appreciate its consequences [3–7].

The crucial question is then: How does a system (e.g., a piece of cellular machinery) extract useful work from the random fluctuations affecting a diffusing molecule? The second law of thermodynamics strictly forbids a periodic system at thermal equilibrium from performing any work. Therefore, in order to extract work the general *modus operandi* are to drive the system out of thermal equilibrium and to break its spatial inversion symmetry although other operational modes are possible [4]. These techniques are referred to as ratcheting effects and the mechanism itself as a ratchet. The classic illustrative example of this phenomena is the Feynman-Schmoluchowski ratchet, consisting of a ratchet and pawl system at thermal equilibrium, no directed motion is then possible [8–10]. The variant of this system in which the ratchet and pawl are thermally isolated from one another at different temperatures (broken thermal equilibrium) is able to perform useful work. The review of Reimann [4] gives a detailed historical development of ratchets.

In this paper we focus on the use of broken spatial inversion symmetry, manifested by the application of an asymmetric spatially periodic potential to generate directed transport. Numerous analogues of this method exist in biological systems,

including: the pumping mechanism in ion channels [7] and the movement of myosin along an actin filament [7]. These ratchets operate in one of two modes: a flashing mode (in which the ratchet is periodically switched on and off) [4–6, 11] or a tilted mode in which an external force is applied in addition to the periodic switching of the ratchet [2, 4]. We restrict our work to a discussion of flashing ratchets.

Within the rapidly growing fields of micro- and nanofluidics, methods which can effectively (and efficiently) manipulate material in environments where Brownian motion has non-negligible effects are increasingly important [7]. Ratchets (in their various forms) are one set of techniques which are on the forefront of this technological revolution [7]. A particular application, the manipulation of biological macromolecules (DNA for example) whether it be for separation purposes or purely transport methodologies is the intrinsic motivation for our work.

In this article we carry out a systematic examination of the behaviour of polymers in (flashing) asymmetric saw tooth (ratchet) potentials using Molecular Dynamics in which we explicitly include solvent particles and thus a self-consistent representation of hydrodynamics. We restrict our examination to regimes where the width of the ratchet is on the order of the polymer radius of gyration, R_g.

We provide an examination of the role of polymer deformation induced by the application of the ratchet. This deformation alters the equilibrium steady state friction coefficient of the molecules ξ and consequently the diffusion coefficient D both of which are functions of the effective size and shape of the molecules. This deformation plays a role in ratchet operation; however, it has not been included in current ratchet models. Downton et al. [5] and Craig et al. [6] have examined a number of aspects of polymer dynamics in ratchets using Brownian dynamics simulations (with no hydrodynamics) and in particular they have examined the role of the internal degrees of freedom of the polymer chains on the transport of polymers in ratchets and the effects of mechanical coupling of objects in ratchets. An explicit solvent allows us to directly examine the effects of deformation (for hydrodynamically impermeable coils) and associated effects on polymer dynamics in ratchets resulting from hydrodynamic interactions.

2 Simulation Model

We use a similar Molecular Dynamics model as described in the previous papers of this series [12, 13] and found in numerous other publications [14, 15]. The model is a variant of the classic Kremer-Grest model for coarse grained polymer systems. We have 2 constituent components in the system, the first are *soft* fluid particles which interact solely via the repulsive part of the Lennard-Jones (LJ) potential given by

$$V_{\mathrm{LJ}}(r) = \begin{cases} 4\epsilon\left(\left[\frac{\sigma}{r}\right]^{12} - \left[\frac{\sigma}{r}\right]^{6}\right) + \epsilon, & r \le r_{\mathrm{c}} \\ 0, & r \ge r_{\mathrm{c}} \end{cases} \quad (1)$$

where σ and ϵ are the length and energy scales, r is the center–to–center distance between two beads and $r_{\mathrm{c}} = \sqrt[6]{2}\sigma$ is the minimum in the Lennard–Jones potential and corresponds to the cutoff for calculating forces [14, 15].

The second component in our systems are polymers constructed via a series of contiguous LJ particles which are effectively *bonded* together using the Finitely Extensible Non–linear Elastic (FENE) potential [14]

$$V_{\mathrm{bond}}(r) = -\frac{\kappa}{2}R_{\circ}^2 \ln\left(1 - \left[\frac{r}{R_{\circ}}\right]^2\right) \quad (2)$$

where R_0 is the upper bound on the bond distance and κ is an effective spring constant. The linear polymers are modeled as N_{p} Lennard–Jones beads connected via $N_{\mathrm{p}} - 1$ FENE bonds. The use of the FENE potential ensures that the chains have a finite range of extensions. We use the standard values, $\kappa = 30.0\epsilon/\sigma^2$ and $R_0 = 1.5\sigma$ [14, 16]. The temperature in all of the simulations is chosen to be $k_{\mathrm{B}}T = 1$.

Our simulations typically have $10^4 \le N_{\mathrm{s}} \le 10^7$ solvent particles. The reduced density of the systems is set at a value of $\rho = 0.85\sigma^{-3}$ [14, 12]. The viscosity of the solvent (as calculated previously) is $\eta = 2.25 \pm 0.05$ and the corresponding single bead friction coefficient is $\xi_{\mathrm{s}} = 16.2 \pm 0.2$ [12] in MD units.

The equations of motion for the system are written in reduced units and integration is carried out using the standard velocity Verlet algorithm [14, 17] with a integration time step of $\delta t = 0.01$. More thorough descriptions of the entire MD simulation method can be found throughout the literature [14, 17].

In order to control to the temperature in our systems we use a dissipative particle dynamics (DPD) thermostat. The crux of the DPD method involves damping differences in particle pair velocities. The DPD thermostat has been shown to preserve hydrodynamic interactions and is becoming the method of choice for many practitioners of MD [18]. Detailed descriptions of the DPD method and its derivation abound in the literature [19]

2.1 Ratchet Potential

We use an asymmetric saw-tooth potential for our ratchet (see figure 1), which is given by the following piecewise continuous function:

$$U_{\mathrm{R}}(x') = U_0 \times \begin{cases} \frac{\alpha L_{\mathrm{R}} - x'}{\alpha L_{\mathrm{R}}}, & 0 \le x' < \alpha L_{\mathrm{R}} \\ \frac{\alpha L_{\mathrm{R}} + x'}{(1-\alpha) L_{\mathrm{R}}}, & \alpha L_{\mathrm{R}} \le x' \le L_{\mathrm{R}} \end{cases} \quad (3)$$

where L_{R} is the width of the unit ratchet cell, $x' = x \bmod L_{\mathrm{R}}$ is the position inside the potential. The parameter α is the effective asymmetry parameter of the ratchet ($\alpha = 0.5$ implies a symmetric potential). The depth of the well is U_0 and is kept in the range $U_0 \in [0, 10]$ (in units of $k_{\mathrm{B}}T$) which corresponds to the normal operational range for experimental ratchet systems [1, 5]. Figure 1 shows a schematic depiction of a polymer confined in this ratchet potential. The polymer is shown in a compressed *pancake* state and the effective dimensions of the chain are shown (discussed later).

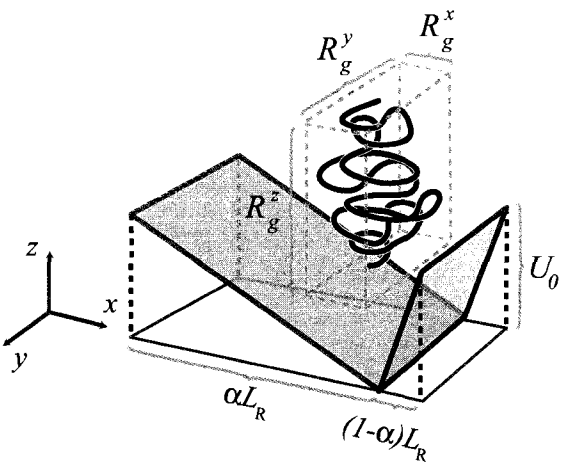

Fig. 1. *Schematic illustration of a polymer confined within an asymmetric saw-tooth potential with an asymmetry parameter* $0.5 \leq \alpha \leq 1$. *The length of the ratchet unit cell is* L_R. *The polymer is compressed in the* x*-direction as a result of the application of the ratchet potential of depth* U_0.

The ratchet is either on or off (i.e., either the potential is applied or it is not). The times over which the ratchet is either on or off are denoted by $t_{\rm on}$ and $t_{\rm off}$ respectively. For $t_{\rm on} = \infty, t_{\rm off} = 0$ the ratchet is purely in the on state, while for $t_{\rm on} = 0, t_{\rm off} = \infty$ the ratchet potential is off and molecules are freely diffusing equilibrium coils. Variations in α, U_0, $t_{\rm on}$ and $t_{\rm off}$ alter the dynamics of the molecules and can induce net transport [4].

3 Polymer Deformation

In this section we examine the effects of confining polymer chains within the asymmetric saw-tooth potential described in equation 3 and Figure 1. The application of this potential has a number of consequences, most notably the deformation of the polymer chain. The degree to which the chains are deformed (relative to free chains) is dictated by U_0 and α, larger U_0 yields larger deformation. In the limit of $U_0 \to \infty$ we obtain $2D$ *pancake* polymers in the y–z plane and the chains Flory exponent is $\nu_{\rm 2D} = 3/4$ [20, 21]. Conversely, in the absence of the potential (i.e., $U_0 = 0$) the Flory exponent is $\nu_{\rm 3D} = 3/5$ [20, 21]. Both $\nu_{\rm 3D}$ and $\nu_{\rm 2D}$ are strictly valid in the large chain limit (i.e., as $N_{\rm p} \to \infty$). In practice both the potential and resulting deformation are finite with $\nu \in [\nu_{\rm 2D}, \nu_{\rm 3D}]$. Larger U_0 also leads to sharper localization of the chains.

The asymmetry parameter of the potential, α, determines the position in the ratchet at which polymers localize. Defining $\rho_{\rm cm}(x)$ as the normalized probability distribution of the polymer center of mass the parameter α controls whether $\rho_{\rm cm}(x)$ is symmetric ($\alpha = 0.5$) or asymmetric ($0.5 < \alpha \leq 1$). The combined variation of α and U_0 modulate the position of the maximum in $\rho_{\rm cm}(x)$ and its sharpness and symmetry.

We use several metrics to gauge the effects α and U_0 on the polymer chains. The first is the averaged end-to-end distance:

$$\langle R_{\rm e} \rangle \equiv \langle |\mathbf{r}_1 - \mathbf{r}_{N_{\rm p}}| \rangle \tag{4}$$

where $|\mathbf{r}_1 - \mathbf{r}_{N_{\rm p}}|$ is the norm of the vector connecting the two terminal monomers of the chain and $\langle \ldots \rangle$ denotes a temporal average. For $U_0 = 0$ the end-to-end distance is predicted to scale like $R_{\rm e} \propto N_{\rm p}^{\nu_{\rm 3D}}$, for large $N_{\rm p}$ [20].

The other metrics of chain deformation are obtained from the gyration tensor given by

$$\mathsf{R}^2 = \begin{pmatrix} R_{11}^2 & R_{12}^2 & R_{13}^2 \\ R_{21}^2 & R_{22}^2 & R_{23}^2 \\ R_{31}^2 & R_{32}^2 & R_{33}^2 \end{pmatrix}. \tag{5}$$

The elements of this tensor are

$$R_{ij}^2 \equiv \frac{1}{N_{\rm p}} \sum_{k=1}^{N_{\rm p}} (x_{i,k} - x_{i,\rm cm})(x_{j,k} - x_{j,\rm cm}) \tag{6}$$

where $x_{i,k}$ and $x_{i,\rm cm}$ are the position of the $k^{\rm th}$ monomer and the center of mass respectively (direction $i = 1, 2, 3$ implies x, y, z). The trace of R^2 is the squared radius of gyration:

$$R_{\rm g}^2 \equiv \mathbf{Tr}\, \mathsf{R}^2 = R_{11}^2 + R_{22}^2 + R_{33}^2. \tag{7}$$

Equation 7 is equivalent to the standard expression for the radius of gyration

$$R_{\rm g}^2 \equiv \left\langle \frac{1}{N_{\rm p}} \sum_{i=1}^{N_{\rm p}} |\mathbf{r}_i - \mathbf{r}_{\rm cm}|^2 \right\rangle \tag{8}$$

where $\mathbf{r}_i - \mathbf{r}_{\rm cm}$ is the vector connecting the $i^{\rm th}$ monomer and the molecule's center of mass $\mathbf{r}_{\rm cm}$ which is defined by

$$\mathbf{r}_{\rm cm} = \frac{1}{N_{\rm p}} \sum_{i=1}^{N_{\rm p}} \mathbf{r}_i. \tag{9}$$

The radius of gyration, $R_{\rm g}$, is a common gauge of effective polymer size and unlike $R_{\rm e}$ it is useful for circular and branched polymers. For $U_0 = 0$, the radius of gyration behaves like $R_{\rm g} \propto N_{\rm p}^{\nu_{\rm 3D}}$ ($N_{\rm p} \gg 1$) [20].

Although $R_{\rm g}$ and $R_{\rm e}$ do give a measure of effective polymer size there is a caveat: neither $R_{\rm g}$ nor $R_{\rm e}$ yield information about the instantaneous conformational anisotropy (or shape) of the molecules at $U_0 = 0$. To characterize the relative anisotropy of the chains we calculate the principal radii of gyration of the molecules. They are the solutions of the characteristic equation $\det|\mathsf{R}^2 - \lambda \mathsf{I}| = 0$ for the eigenvalues $\lambda = R_{x'}^2, R_{y'}^2, R_{z'}^2$ (such that $R_{x'}^2 \leq R_{y'}^2 \leq R_{z'}^2$) [20]. The three principal radii of gyration are given by the average of these eigenvalues $R_{\rm g}^\beta = \langle R_\beta^2 \rangle^{1/2}$ ($\beta = x', y', z'$). They give us an indicator of the anisotropy (and deformation) of the molecules. In the $U_0 \to \infty$ limit, the minor axis is aligned in the x–direction and the two major axes are in the y–z plane.

We used these metrics to determine the size and anisotropy of molecules in our MD simulations resulting from the application of the ratchet potentials. The simulation cell used for these

calculations has dimensions $L_x \times L_y \times L_z$ ($L_\beta = 46.449\sigma$ or roughly 44 LJ beads wide). The width of the ratchet is $L_R = 11.612\sigma$, with four potentials per simulation cell. Systems are initially allowed to relax for a minimum of 100000 time steps. The potential is then turned on and the system is allowed to relax for an additional 100000 MD time steps followed by data collection for 2×10^7 MD time steps.

3.1 MD results for deformation

We begin the discussion by examining the chain metrics for $N_p \in [3, 41]$ and potentials with $U_0 = 0, 2, 4, 8$. For the $U_0 = 0$ case, we have a free chain (a self-avoiding random coil in the large N_p limit). Figure 2 shows a log-log plot of $R_g^{x'}$, $R_g^{y'}$ and $R_g^{z'}$ as a function of N_p. The inset of Figure 2 shows a semi-log plot of the ratio of $R_g^{z'}/R_g^{x'}$ and $R_g^{y'}/R_g^{x'}$ as a function of N_p and thus gives an effective measure of the molecular asymmetry. As expected in the $U_0 = 0$ case molecules appear anisotropic as measured in the principal axis system as evidenced in Figure 2. From Figure 2 it would appear that for

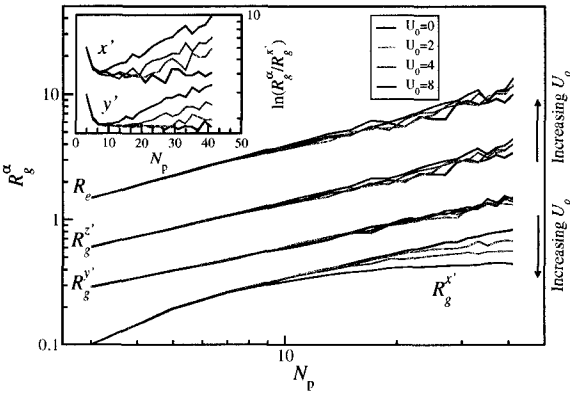

Fig. 2. *Log-log plot of the three principal radii of gyration $R_g^{x'}$, $R_g^{y'}$ and $R_g^{z'}$ and the end-to-end distance R_e as a function of N_p for well depths $U_0 \in [0, 8]$ (in units of k_BT) in increments of $U_0 = 2$. Inset figure is a semi-log plot of the ratio of $R_g^{y'}/R_g^{x'}$ and $R_g^{z'}/R_g^{x'}$ as a function of N_p, illustrating the effective asymmetry of the chains as measured in the principal axis system. The radius of gyration is not shown but is simply obtained from $R_g^2 = (R_g^{x'})^2 + (R_g^{y'})^2 + (R_g^{z'})^2$. As U_0 is increased the polymer is compressed by the asymmetric saw-tooth potential. For large N_p, $R_g^{x'}$ is a weakly decreasing function of U_0 while the other two principal radii are increasing functions of U_0.*

$U_0 > 0$ and $N_p \leq 10$ the chains are also essentially undeformed relative to the free chains. However, the molecules are anisotropic as the inset of Figure 2 clearly illustrates. For the short chains the degree of anisotropy is about the same as that for the free chains. However, for $N_p > 10$ the molecules have increased anisotropy as a result of a stronger competition between the ratchet potential and the chain entropy (both conformational and rotational). For large N_p, $R_g^{x'}$ begins to saturate with U_0 and the asymmetry of the chain is an increasing function of U_0. Larger U_0 would further constrain the polymers to the y–z plane. Clearly from Figure 2, $R_g^{x'}$ does not vary as a power law with N_p. As we increase U_0 the plateau value of $R_g^{x'}$ (for large N_p) decreases corresponding to the increasing confinement of the chain.

We have also calculated an effective Flory scaling ν as a function of U_0 (for R_g, R_e $R_g^{y'}$ and $R_g^{z'}$). The values of ν are extracted from a linear regression of the data in Figure 2. The calculated values of ν (for $N_p > 20$) are shown in Figure 3 as a function of U_0. Also shown are the asymptotic values for ν ($U_0 \to \infty$ ($\nu = \nu_{2D}$) and $U_0 \to 0$ ($\nu = \nu_{3D}$)) for ideal chains [20]. We see that for all measures of the chain size, ν plateaus with increasing U_0 as the chains are progressively more confined in the plane of the ratchet potential. For

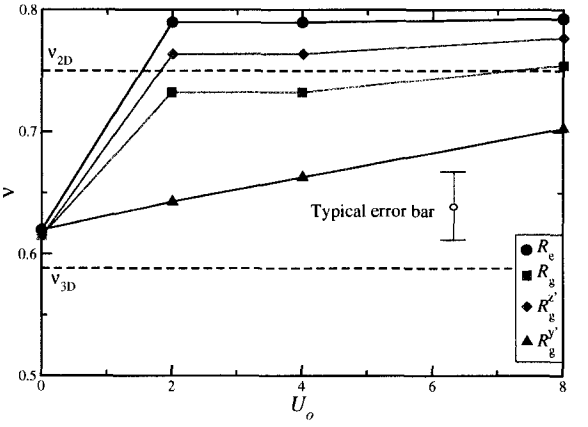

Fig. 3. *Flory exponent ν as a function of U_0, calculated for chains larger than $N_p > 20$ for the measures of chain size given by R_g, R_e $R_g^{y'}$ and $R_g^{z'}$. For $U_0 = 0$ the polymer are free chains, while as U_0 increases chains are squashed in the y-z plane. This illustrates the transition from three dimensional random coils to two dimensional pancaked chains. Also shown is a typical error bar for the values of ν.*

$U_0 = 0$ the calculated values of ν are slightly higher than ν_{3D}. Our relatively short chains appear somewhat stiff and skew ν towards a slightly higher value. Variations in U_0 also control the spatial localization of the polymers. It is usually assumed that (for large t_{on}) chains are fully localized to potential minima (i.e., $\rho_{cm}(x) = \delta(x - \alpha L_R)$, where $\rho_{cm}(x)$ is the probability distribution of the center of mass of the polymer) or that the width of the ratchet is much larger than the width of the $\rho_{cm}(x)$ [1, 4]. Of course as $U_0 \to \infty$ the distribution $\rho_{cm}(x) \to \delta(x - \alpha L_R)$. The assumption of complete localization greatly simplifies ratchet models; however, it is not necessarily realistic. Essentially one normally assumes that the polymer behaves as an equivalent point like particle, localized to the minimum in the potential.

3.2 Polymer localization

We examine the localization of the polymer chains by directly calculating $\rho_{\rm cm}(x)$ from our simulations. Figure 4 shows $\rho_{\rm cm}(x)$ for $N_{\rm p} = 5$ and $N_{\rm p} = 41$ as a function of the well depth U_0 and $\alpha = 0.90$. For $U_0 = 0$, $\rho_{\rm cm}(x)$ is a flat distribution with no spatial localization (not shown). For small U_0, the chains become localized to the minimum in the potential; however, $\rho_{\rm cm}(x)$ is still rather broad. The distribution $\rho_{\rm cm}(x)$ contains other information.

Treating the polymer as an equivalent point like particle, with a position corresponding to its center of mass, we can write $\rho_{\rm cm}(x)$ as

$$\rho_{\rm cm}(x) \propto \exp\left(-\frac{U_{\rm eff}(x)}{k_{\rm B}T}\right) \qquad (10)$$

where $U_{\rm eff}(x)$ is the effective potential felt by the polymer. For large U_0 the effective potential tends toward the ratchet potential (i.e., $U_{\rm eff}(x) \rightarrow U_{\rm R}(x)$) as ratchet potential greatly outweighs any contributions from the free energy of the chain. For intermediate U_0, $U_{\rm eff}(x)$ reflects contributions from both the ratchet potential and the chains free energy (internal entropy and excluded volume). The dominant contribution arises from the conformational entropy of the chain.

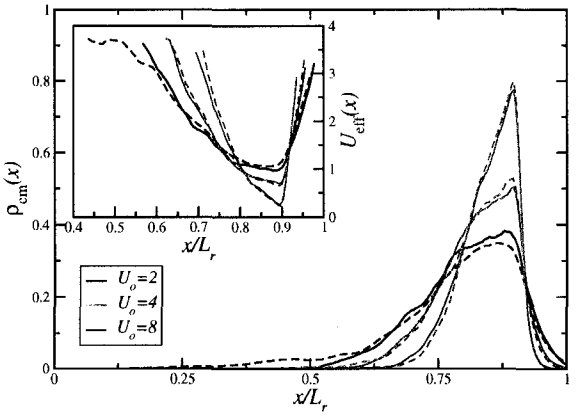

Fig. 4. *Probability distribution for the position of the polymer center of mass, $\rho_{\rm cm}(x)$, for $U_0 = 2, 4, 8$ (in units of $k_{\rm B}T$) for $N_{\rm p} = 5$ and $N_{\rm p} = 41$ (corresponding to dashed and solid lines, respectively). Inset figure shows semi-log plot of $U_{\rm eff} \equiv -\ln(\rho_{\rm cm}(x))$ as a function of x and thus the effective potential (in units of $k_{\rm B}T$) the polymer would feel if it were treated as a point like particle. As U_0 increases $U_{\rm eff}$ tends toward the actual shape of the ratchet potential, as expected.*

The parameter α controls the asymmetry of the ratchet potential. For $\alpha = 0.5$ the potential and the resulting center of mass distribution are symmetric. Symmetric flashing potentials are unable to induce net transport [4]. As $\alpha > 0.5$ the distribution $\rho_{\rm cm}(x)$ changes from being symmetric to asymmetric.

We examine the effect of the potential asymmetry by varying $\alpha \in [0.5, 1]$ ($\alpha = 1$ is ill-defined in our context). The range $\alpha \in [0, 0.5]$ simply reverses the direction of the ratchet if it were flashed off and on. Figure 5 shows $\rho_{\rm cm}(x)$ for a polymer with $N_{\rm p} = 41$ (both $U_0 = 2$ and $U_0 = 4$) as a function of α. For $\alpha = 0.5$ both the ratchet potential $U_{\rm R}(x)$ (defined in equation 3) and $\rho_{\rm cm}(x)$ are symmetric. As α is increased the peak in $\rho_{\rm cm}(x)$ shifts to the right following the shift in minimum in the potential.

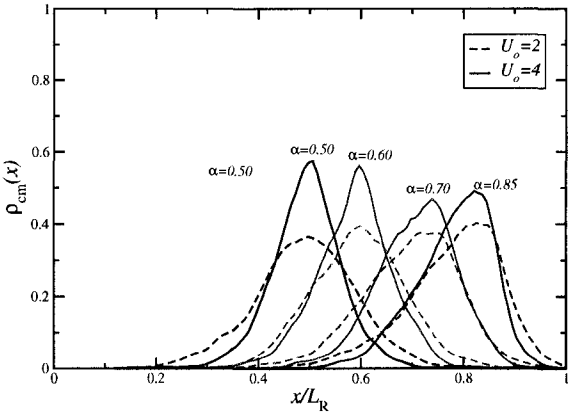

Fig. 5. *Probability distribution for the position of the polymer center of mass, $\rho_{\rm cm}(x)$ as a function of α for well depths of $U_0 = 2, 4$ (in units of $k_{\rm B}T$) and a chain length of $N_{\rm p} = 41$. For a purely symmetric potential $\alpha = 0.5$ the resulting $\rho_{\rm cm}(x)$ is also symmetric. As α is increased, $\rho_{\rm cm}(x)$ tends towards a skewed distribution, with a peak position corresponding closely to the minimum in the ratchet potential.*

To summarize, varying both the depth of the potential and the asymmetry parameter, U_0 and α, have a number of effects on a polymer in a ratchet potential. An increase in U_0 both increases the relative deformation of the molecules and leads to a sharper distribution $\rho_{\rm cm}(x)$, although the distribution always has a finite width. On the other hand α primarily controls the position of the peak in the $\rho_{\rm cm}(x)$ and the skewness of $\rho_{\rm cm}(x)$. It should be noted that this is an oversimplification and the variation of U_0 and α have coupled effects; however, the discussion above provides a good first order description of their effects.

4 Polymer Deformation and Diffusion

As illustrated in the previous section a polymer when treated as a point-like particle with position corresponding to its center of mass is not completely localized to a ratchet minimum. Nonetheless, this assumption is made in most ratchet models. In other words it is normally assumed that $\rho_{\rm cm}(x) \simeq \delta(x - x')$, where x' is the position of a ratchet minimum. While this is reasonable for ratchets which are wide compared to the width of the polymer center of mass distribution [1] it is not strictly valid for relatively narrow ratchets. However, it does greatly simplify analysis. In the calculations that follow we assume (for simplicity) that polymers are completely localized. The extension to finite width polymer distributions is relatively straight forward.

Working with the ansatz that $\rho_{\rm cm}(x) = \delta(x-x')$, the polymer center of mass distribution will evolve like

$$P(x,t) = \frac{1}{\sqrt{4\pi D t}} \exp\left[-\frac{(x-x')^2}{4Dt}\right], \qquad (11)$$

where D is the free diffusion coefficient of a polymer. At fixed $N_{\rm p}$, the diffusion coefficient D is normally treated as invariant to the application of the ratchet potential, i.e., the chains are assumed to be undeformed during the entire ratcheting sequence.

Even for moderate $U_0 \leq 10 k_{\rm B}T$ the diffusion coefficient undergoes a transition from $D = D_{\rm 3d}$ to the 2d (pancake) diffusion coefficient $D = D_{\rm 2d}$. It should be noted $D_{\rm 2d}$ refers to the diffusion coefficient of the polymer parallel to its minor axis and thus perpendicular to the plane of the ratchet potential. One could alternatively define two separate diffusion coefficients $D_{\rm 2d}^{||}$ and $D_{\rm 2d}^{\perp}$ to denote the diffusion coefficients that are parallel and perpendicular to the minor and major axes of the polymer, respectively. For simplicity of notation we use $D_{\rm 2d} = D_{\rm 2d}^{||}$ throughout. The transition from a 3d coil to a 2d pancake is evidenced by the change in the scaling of the polymer chain from ν_{3D} to ν_{2D} with increasing U_0 in section 3. Consequently, two deficits exist in most ratchet models: an assumption of complete localization and the lack of an accurate description of the polymer diffusion coefficients for moderate to large U_0. We will focus on the latter.

The diffusion coefficient, $D_{\rm 3d}$, of a freely diffusing (undeformed and hydrodynamically impermeable) polymer is

$$D_{\rm 3d} \sim \frac{k_{\rm B}T}{\eta R_{\rm H}} \propto N_{\rm p}^{-\frac{3}{5}} \qquad (12)$$

where $R_{\rm H} \simeq \frac{2}{3} R_{\rm g}^{\rm 3d}$ is the hydrodynamic radius of the polymer [21]. The diffusion coefficient of a pancaked (2d) polymer moving face-on to its minor axis is

$$D_{\rm 2d} \sim \frac{k_{\rm B}T}{\eta R_{\rm g}^{\rm 2d}} \propto N_{\rm p}^{-\frac{3}{4}} \qquad (13)$$

where $R_{\rm g}^{\rm 2d}$ is the in plane radius of gyration of the 2d disk-like polymer [22]. It is easily shown using a scaling argument that beyond a few monomers, $D_{\rm 2d} < D_{\rm 3d}$. As a result, polymer diffusion (during the off phase of the ratchet) is initially inhibited by the pancaking effect until the polymer has relaxed. In principle this idea should be valid for chains that are not random coils due to the inherent anisotropy of polymers. Similar calculations could be applied to stiff polymers as well.

As a result, a pancaked polymers diffusion coefficient will initially be $D_{\rm 2d}$ immediately after the potential is switched off. The polymer will then both diffuse and its diffusion coefficient will relax back to $D_{\rm 3d}$. This relaxation will occur in a similar way to that of the end-to-end vector [21] and we use a simple interpolation scheme to model the transition from $D_{\rm 2d}$ to $D_{\rm 3d}$ as

$$D(t) = D_{\rm 2d} e^{-\frac{t}{\tau}} + D_{\rm 3d}\left[1 - e^{-\frac{t}{\tau}}\right] \qquad (14)$$

where τ is a characteristic relaxation time scale for the polymer. A natural time scale over which is the polymer will relax is it's end-to-end vector relaxation time $\tau_{\rm R}$ and we assume that $\tau \simeq \tau_{\rm R}$. More robust methods exist for obtaining $D(t)$; however, equation 14 has both a simple functional form and allows an analytical result in the following discussion. The relaxation time [21] is given by the following scaling law

$$\tau_{\rm R} \simeq \frac{(R_{\rm g}^{\rm 3d})^2}{6 D_{\rm 3d}}. \qquad (15)$$

The polymer relaxes as it diffuses over a distance on the order its of own radius, $R_{\rm g}^{\rm 3d}$.

An inhibited diffusion coefficient has two consequences for operational modes of a ratchet. Firstly, polymer diffusion is slowed for off times $t_{\rm off} < \tau_{\rm R}$ and secondly, if the ratchet is subsequently switched on before the polymer has relaxed it will be deformed during the on phase of the ratchet.

The *classic* minimum operational ratchet off time for an undeformed polymer with diffusion coefficient $D_{\rm 3d}$ is

$$t_{\rm off}^{\rm opt} = \frac{r_{\rm eff}^2}{2 D_{\rm 3d}}. \qquad (16)$$

where $r_{\rm eff} = (1-\alpha) L_{\rm R}$ is the short side distance in the ratchet, i.e., the distance the polymer must diffuse to traverse to the next ratchet cell. Equation 16 thus assumes no polymer deformation. In the case of a pancaked polymer (i.e., a polymer with diffusion coefficient $D_{\rm 2d}$) equation 16 underestimates the actual minimum time required for the polymer to diffuse one well in the ratchet since $D_{\rm 2d} < D_{\rm 3d}$.

4.1 Modified Bader ratchet model

We now provide a derivation of a modified ratchet model discussed by Bader et al. [1] which includes the effects of polymer deformation and an associated time dependent diffusion coefficient. We solve the diffusion equation

$$\frac{\partial P(x,t)}{\partial t} = 2D(t) \frac{\partial^2 P(x,t)}{\partial x^2} \qquad (17)$$

for polymers which have time dependent diffusion coefficients given by $D(t)$. To solve for $P(x,t)$ we rewrite equation 17 as

$$\frac{\partial P(x,\sigma^2(t))}{\partial \sigma^2(t)} = \frac{\partial^2 P(x,\sigma^2(t))}{\partial x^2} \qquad (18)$$

where

$$\sigma^2(t) = 2\int_0^t D(t')dt'. \qquad (19)$$

Our expression for $D(t)$ (in equation 14) allows an analytical calculation of $\sigma^2(t)$ and is given by

$$\sigma^2(t) = 2D_{\rm 3d}t - 2\tau_{\rm R}\left(D_{\rm 3d} - D_{\rm 2d}\right)\left(1 - e^{-\frac{t}{\tau_{\rm R}}}\right). \qquad (20)$$

The probability distribution for the polymer is then

$$P(x,t) = \frac{1}{\sqrt{2\pi\sigma^2(t)}} \exp\left[-\frac{x^2}{2\sigma^2(t)}\right] \qquad (21)$$

with $\sigma^2(t)$ given by equation 20. In the case that $D_{\rm 3d} = D_{\rm 2d}$ we recover the standard result for the one dimensional diffusion equation with a non-time dependent diffusion coefficient,

i.e., $\sigma^2(t) = 2D_{3d}t$ [1]. Essentially $\sigma^2(t)$ represents a mean squared displacement of the polymer center of mass for polymers with time dependent diffusion coefficients.

An expression for δ the probability for a polymer to traverse (diffuse) forward in the ratchet can now be obtained. To jump forward the polymer must diffuse a distance, $r_{\rm eff}$, equal to the shortest dimension of the ratchet. The probability to do so is then obtained by integrating $P(x, t = t_{\rm off})$ from $x = r_{\rm off}$ to $x = \infty$,

$$\delta = \int_{r_{\rm off}}^{\infty} P(x, t_{\rm off})dx = \frac{1}{2}\mathrm{erfc}\left[\left(\frac{1}{2}\frac{r_{\rm eff}^2}{\sigma^2(t_{\rm off})}\right)^{\frac{1}{2}}\right], \quad (22)$$

where erfc[] is the complementary error function [23]. We can then rewrite the distance $r_{\rm eff}^2$ as $\sigma^2(t_r) = r_{\rm eff}^2$, which defines $t_{\rm r}$ as the time required to diffuse the distance $r_{\rm eff}^2$. The time $t_{\rm r}$ is obtained by inverting $\sigma^2(t_r) = r_{\rm eff}^2$ for $t_{\rm r}$ which gives

$$\frac{t_{\rm r}}{\tau_{\rm R}} = \mathrm{LambertW}\left[-\Delta_D e^{-(\Delta_t+\Delta_D)}\right] + \Delta_t + \Delta_D, \quad (23)$$

$$\Delta_D = \left(1 - \frac{D_{2d}}{D_{3d}}\right) \quad \text{and} \quad \Delta_t = \frac{t_{\rm off}^{\rm opt}}{\tau_R}$$

where $\mathrm{LambertW}(x)$ is the inverse function of $f(x) = xe^x$ [23]. To reiterate, $t_{\rm r}$ is simply the time a polymer takes to diffuse forward one well. When there is no deformation $D_{2d} = D_{3d}$ and this time is simply the conventional estimate $t_{\rm r} = t_{\rm off}^{\rm opt}$.

The resulting final probability δ is given by

$$\delta = \frac{1}{2}\mathrm{erfc}\left[\left(\frac{1}{2}\frac{\sigma^2(t_r)}{\sigma^2(t_{\rm off})}\right)^{\frac{1}{2}}\right] \quad (24)$$

$$= \frac{1}{2}\mathrm{erfc}\left[\left(\frac{1}{2}\frac{D_{3d}t_r - \tau_{\rm R}(D_{3d} - D_{2d})\left(1 - e^{-\frac{t_r}{\tau_{\rm R}}}\right)}{D_{3d}t_{\rm off} - \tau_{\rm R}(D_{3d} - D_{2d})\left(1 - e^{-\frac{t_{\rm off}}{\tau_{\rm R}}}\right)}\right)^{\frac{1}{2}}\right],$$

where t_r is given by equation 23. Equation 24 is simplified by dividing the numerator and denominator by $D_{3d}\tau_{\rm R}$. It is also useful to rewrite the time scales $t_{\rm off}$ and t_r in terms of the characteristic relaxation $\tau_{\rm R}$ as $t_{\rm off} = \beta_1\tau_{\rm R}$ and $t_r = \beta_0\tau_{\rm R}$. Doing this and simplifying the algebra we obtain

$$\delta = \frac{1}{2}\mathrm{erfc}\left[\left(\frac{1}{2}\frac{\beta_0 - \Delta_D\left(1 - e^{-\beta_0}\right)}{\beta_1 - \Delta_D\left(1 - e^{-\beta_1}\right)}\right)^{\frac{1}{2}}\right]. \quad (25)$$

Equation 25 is the probability for a deformed polymer with initial diffusion coefficient D_{2d} to diffuse one or more well(s) in the ratchet. Equation 25 has three parameters: β_0, β_1 and the ratio of the 2d to 3d diffusion coefficients (D_{2d}/D_{3d}). It should be noted β_0 is calculated from equation 23. In the case where $\Delta_D = 0$ the polymer is not deformed and we recover the original result of Bader et al., given by

$$\delta_{\rm Bader} = \frac{1}{2}\mathrm{erfc}\left[\left(\frac{1}{2}\frac{\beta_0}{\beta_1}\right)^{\frac{1}{2}}\right] = \frac{1}{2}\mathrm{erfc}\left[\left(\frac{1}{2}\frac{t_{\rm off}^{\rm opt}}{t_{\rm off}}\right)^{\frac{1}{2}}\right]. \quad (26)$$

the only difference being that the time scales are written in terms of $\tau_{\rm R}$.

Figure 6 shows a plot of the probability δ for a polymer to move forward, for three regimes. The solid black line is that corresponding to $D_{2d} = D_{3d}$, i.e., an undeformed polymer (corresponding to the original Bader expression). The other two curves on Figure 6 correspond to $D_{2d} < D_{3d}$ for a pancaked polymer and $D_{2d} > D_{3d}$ for the case where the pancaked diffusion coefficient is greater than the free diffusion coefficient. The later case is one in which deformation enhances diffusion in the pancaked state and is not of interest in our work. This Figure demonstrates several key features of our model.

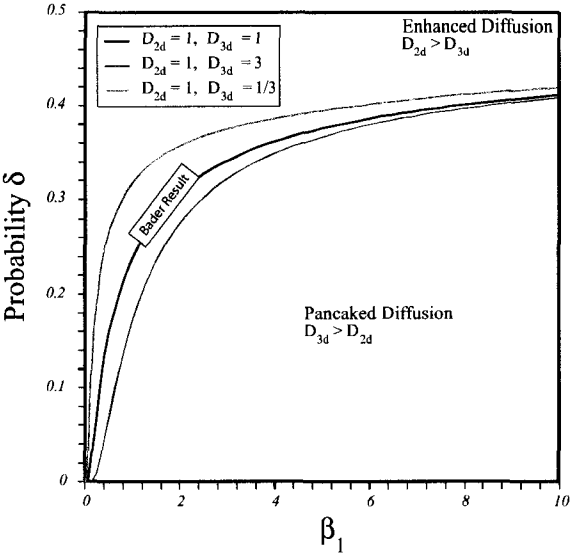

Fig. 6. *Probability, δ, for a polymer to diffuse forward in the ratchet as a function of the ratchet off time ($t_{\rm off} = \beta_1\tau_{\rm R}$). The solid black line corresponds to the Bader result for an undeformed polymer $D(t) = D_{3d}$. The region above the black line corresponds to $D_{2d} > D_{3d}$, while the region below the black line corresponds $D_{3d} > D_{2d}$ and is the pancaked diffusion domain. Polymers in the pancaked diffusion regime are slowed and the associated value of δ is decreased.*

Firstly, the transition probability, δ for a pancaked polymer ($D_{3d} > D_{2d}$) is decreased for short off times (i.e., small β_1). This suggests that deformation can be used to modulate the behaviour of polymers in ratchets and is one of he key result of our work. Moreover, since large chains relax more slowly than shorter chains this effect of deformation would enhance the separation capability of a ratchet by slowing the movement of larger polymers more than that of smaller polymers.

4.2 MD simulations and inhibited diffusion

We now turn to the results from our MD simulations. For illustrative purposes Figure 7 shows two typical trajectories of the polymer center of mass, for $N_{\rm p} = 13$ and $N_{\rm p} = 29$ from our MD simulations. This corresponds to a system with $L_{\rm R} =$

11.61σ. Figure 7 is for illustrative purposes and we do not present a systematic study of the ratchet velocity and its transport properties as a function of chain length N_p due to the time consuming nature of these calculations. We aim instead to verify the concept of inhibited diffusion in ratchets.

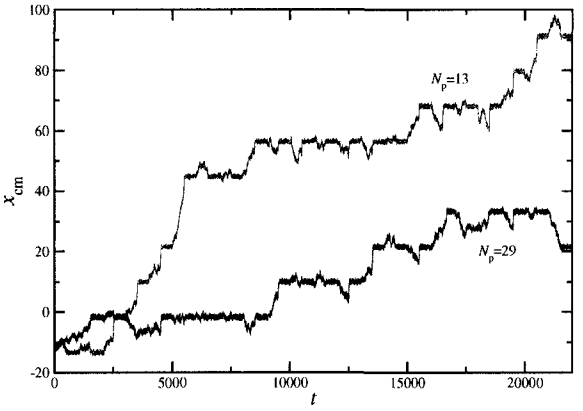

Fig. 7. *Typical trajectory of two different polymers with $N_p = 13$ and $N_p = 31$, for an off time of $t_{off} = t_{on} = 500$. The trajectories illustrate that the polymers are indeed undergoing a net motion which changes as a function of N_p. This is for illustrative purposes. For a ratchet with $U_0 = 4$ (in units of k_BT) and a width of $L_R = 11.61\sigma$*

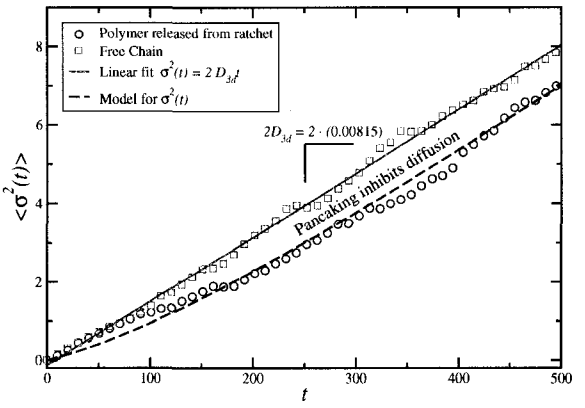

Fig. 8. *Averaged mean squared displacement $\langle\sigma^2(t)\rangle$ in x-direction as a function of time t for both a free polymer and a polymer released from a ratchet from the MD simulations. The free polymer (square symbols) undergoes normal diffusion (with a diffusion coefficient of $D_{3d} \simeq 0.00815$, obtained from a linear fit of the data). We can estimate the value of the relaxation time of the polymer from equation 15, with a calculated value of $R_g^{3d} \simeq 3.6$ from the simulations, this yields an approximate value of $\tau_R^{MD} \simeq 180$ calculated using equation 15. The polymer which is released from the ratchet is initially slowed and after a sufficient t returns to normal diffusive motion. This illustrates the effect of polymer pancaking on the reduction of the effective diffusion coefficient of a polymer released from a ratchet potential.*

To explore the functional form of equation 20 we have carried out a suite of MD simulations which examine a single polymer ($N_p = 31$) in the presence of a deep ratcheting potential with $U_0 = 10k_BT$, ensuring a high degree of deformation during the on phase of the ratchet. The on and off times of the ratchet are $t_{off} = 500$ and $t_{on} = 500$, given in MD time units. Evidently, t_{on} is much larger than the time scale required for the chain to be driven to the ratchet minima. From the MD simulations $R_g \simeq 3.6$ and the relaxation time calculated from equation 15 is $\tau_R \simeq 180$. The on and off times are then much larger than the relaxation time, τ_R. The value of t_{off} is also chosen so that the polymer will have relaxed during the off phase. By *flashing* the ratchet off and on many times we generate trajectories of the position of the polymer center of mass as a function of time after the ratchet has been switched off. We map all particle trajectories onto the unit cell and calculate $\langle\sigma^2(t)\rangle$ from the MD simulations for the polymer of center of mass as a function of time. Figure 8 shows the mean squared displacement for the polymer center of mass obtained from multiple cycles of the ratchet. The ratchet width is $L_R = 11.61\sigma \ll R_g \simeq 3.6$.

Figure 8 also shows (square symbols) the mean squared displacement of a single polymer ($N_p = 31$) which is freely diffusing, i.e., normal diffusion in the absence of a ratchet potential. The data labeled ratchet (with circles) is that for a polymer released from a ratchet, which was on for a sufficiently long time to localize the polymer to the ratchet. The data is averaged over many cycles of the ratchet.

By carrying out a linear regression (using $\sigma^2(t) = 2D_{3d}^{MD}t$) of the free chain data we obtained free diffusion coefficient of $D_{3d}^{MD} \simeq 0.00815$. In the case of the ratchet we fit the data with the expression $\sigma^2(t) = 2D_{3d}^{MD}t - \phi$ obtained from the large $t \gg \tau_R$ limit of equation 20. The constant $\phi = 2\tau_R(D_{3d}^{MD} - D_{2d}^{MD})$ and is simply the prefactor of the second term in equation 20. The calculated value is $\phi = 1.437$. Using the values of D_{3d}^{MD} and ϕ we fit the ratchet data over the entire range of t using $\sigma^2(t) = 2D_{3d}^{MD}t - \phi(1 - \exp(-t/\tau_R))$ (where τ_R was the only fitting parameter). The value of the relaxation time thus obtained is $\tau_R^{MD} = 140.94$. Using the values values of ϕ, τ_R and D_{3d}^{MD} we calculated a value of the pancaked diffusion coefficient of $D_{2d}^{MD} = 0.00305$. The calculated relaxation time from equation 15, $\tau_R \simeq 180$ agrees well $\tau_R^{MD} = 140.94$. The fitted line for the ratchet data is shown in figure 8 and describes well the data from the MD simulations over the whole range of t.

The MD simulation data illustrate and corroborate three important things. The first is that polymer diffusion is initially inhibited by the pancaking effect after release from the ratchet. The second is that after some time ($t_{off} \gg \tau_R$) the polymer resumes normal diffusion. As the polymer relaxes over several multiples of the relaxation its diffusion coefficient returns to the 3d free diffusion value. Finally, there is an inherent lag time for the pancaked polymers relative to free chains to diffuse the same mean squared distance $\sigma^2(t)$. For $t > \tau_R$, we can write $\sigma^2(t) \simeq 2D_{3d}t - 2\tau_R(D_{3d} - D_{2d})$ and thus the time taken to

diffuse $\sigma^2(t)$ is

$$t \simeq \frac{\sigma^2(t) + 2\tau_R(D_{3d} - D_{2d})}{2D_{3d}} \simeq \frac{\sigma^2(t)}{2D_{3d}} + 2\tau_R\Delta_D. \quad (27)$$

Equation 27 is then simply the time taken for a free chain to diffuse $\sigma^2(t)/2D_{3d}$ plus a finite correction term given by $2\tau_R\Delta_D$, with Δ_D given in equation 23. In other words by controlling Δ_D, i.e., the ratio of the pancaked state diffusion coefficient relative to the free diffusion coefficient it is possible to control this lag time and modulate the diffusion of polymers in a ratchet. The inhibited diffusion model and the diffusion occurring in the MD simulations agree well and the ratchet is slowed by the pancaking effec. This represents a novel operational technique and method to modulate polymer dynamics in a ratchet.

5 Conclusions

We have presented an examination of the effects of applied asymmetric saw-tooth potentials on the properties of polymer chains. We first illustrated that an applied ratchet potential both deforms the polymer chains and alters the Flory scaling of the polymers from free 3d polymers (ν_{3d}) to pancaked 2d polymers (ν_{2d}). This has the consequence of altering the polymers diffusion coefficient when compressed in the plane of the ratchet potential. The result is that polymer diffusion is inhibited after escape from a ratchet. We have also illustrated that the width of the distribution describing the position of center of mass of the polymer can be rather broad although we have not taken this in account in our theory.

We showed that a simple expression for the time dependent diffusion coefficient $D(t)$ written in terms of the 2d diffusion coefficient D_{2d}, the 3d diffusion coefficient D_{3d} and the relaxation time of the polymer τ_R can quantitatively account for the observed inhibited diffusion of polymers released from ratchets. Using this as our starting point we then derived a modified Bader ratchet model [1] which explicitly accounts for polymer deformation. We followed this by a derivation of an exact expression for the polymer transition probability, δ, with a simple functional form. This transition probability directly takes into account the effect of deformation induced by the ratchet and in the limit of $D_{3d} = D_{2d}$ collapses to the original Bader model.

Our modified Bader model yields a transition probability which for short times ($t_{off} < \tau_R$) is less than that predicted by the Bader model (for polymers starting from the pancaked state $D_{2d} < D_{3d}$). This is a direct result of the inhibited diffusion induced by the pancaking effect of the ratchet potential.

We demonstrated that using the MD simulations we can observed this slowing effect in a ratchet. We have showed that by directly examining the diffusion of a polymer immediately after it is released from a ratchet potential and comparing it to a freely diffusing polymer one can clearly see the effect of pancaking on diffusion. The result is that the pancaking effect slows the initial diffusion of the polymer chains and thus corroborates the proposed modified Bader ratchet model. The data from the MD simulations and the expression for $\sigma^2(t)$ have the same functional form and the diffusion of pancaked chains released from a ratchet are slowed initially. In limit of $t_{off} \gg \tau_R$ all particles will have the same probability to transit forward in the ratchet. However, our model predicts that operational times for ratchets which are less that a few relaxation times of the polymer can be used to modulate polymer migration in the ratchet. Moreover, a more natural time metric for the ratchets are defined in terms of the polymers relaxation time. The effect of pancaking can be used in an advantageous manner in experimental systems to control and optimize migration in ratchets. Since large chains will relax more slowly than smaller chains, this inhibited diffusion should enhance separation in ratchets.

6 Acknowledgements

The authors would like to acknowledge the support of the Natural Sciences and Engineering Research Council of Canada (NSERC) for financial support in the form a research grant to G. W. S. and a post-graduate scholarship to M. K. The authors would like to thank Owen Hickey for useful discussions. M. K. would also like to thank the Ontario Ministry of Training, Colleges and Universities for an Ontario Graduate Scholarship and the University of Ottawa for a National Excellence Scholarship. We also acknowledge the use of computational resources made available through both the High Performance Computing Virtual Laboratory (HPCVL) (**www.hpcvl.org**) and C3.ca (**www.c3.ca**).

References

1. J. S. Bader, R. W. Hammond, S. A. Henck, M. W. Deem, G. A. McDermott, J. M. Bustillo, J. W. Simpson, G. T. Mulhern, and J. M. Rothberg. DNA transport by a micromachined Brownian ratchet device. *PNAS*, 96(23):13165–13169, 1999.
2. M. Bier. Brownian ratchets in physics and biology. *Contemporary Physics*, 38(6):371–379, 1997.
3. L. P. Faucheux, L. S. Bourdieu, P. D. Kaplan, and A. J. Libchaber. Optical Thermal Ratchet. *Physical Review Letters*, 74(9):1504–1507, 1995.
4. P. Reimann. Brownian motors: noisy transport far from equilibrium. *Physics Reports*, 361:57–265, 2002.
5. M. T. Downton, M. J. Zuckermann, E. M. Craig, M. Plischke, and H. Linke. Single-polymer brownian motor: A simulation study. *Physical Review E*, 73(1):011909, January 2006.
6. E. M. Craig, M. J. Zuckermann, and H. Linke. Mechanical coupling in flashing ratchets. *Arxiv preprint cond-mat/0602097*, 2006.
7. J. C. T. Eijkel and A. Berg. Nanofluidics: what is it and what can we expect from it? *Microfluidics and Nanofluidics*, 1(3):249–267, 2005.
8. M. von Smoluchowski. *Physik Z.*, 13:1069, 1912.
9. R. P. Feynman, R. B. Leighton, and M. Sands. *The Feynman lectures on physics*. Addison-Wesley Redwood City, Calif, 1966.

10. M. O. Magnasco and G. Stolovitzky. Feynman's Ratchet and Pawl. *Journal of Statistical Physics*, 93(3):615–632, 1998.
11. R. D. Astumian and M. Bier. Fluctutation driven ratchets: Molecular Motors. *Physical Review Letters*, 72(11):1766–1769, March 1994.
12. M. Kenward and G. W. Slater. Molecular dynamics simulations with explicit hydrodynamics interactions i: On the friction coefficients of equilibrium and deformed polymers. *Euro. Phys. J. E*, 14(1):55–65, 2004.
13. M. Kenward and G. W. Slater. Molecular dynamics simulations with explicit hydrodynamics interactions ii: On the collision of polymers with molecular obstacles. *Euro. Phys. J. E*, 20(2):125 – 141, 2006.
14. K. Kremer, G. S. Grest, and I. Carmesian. Crossover from Rouse to reptation dynamics: A molecular dynamics simulation. *Phys. Rev. Letters*, 61(5):566–569, 1988.
15. K. Kremer. Computer simulation methods for polymer physics. In K. Binder and G. Ciccotti, editors, *Monte Carlo and Molecular Dynamics of Condensed Matter Systems*, pages 603–650. SIF, 1996.
16. K. Kremer and G. S. Grest. Dynamics of entangled linear polymer melts: A molecular dynamics simulation. *J. Chem. Phys*, 92(8):5057–5086, 1990.
17. M. P. Allen and D. J. Tildesley. *Computer Simulations of Liquids*. Oxford Science Publications, Oxford, 4^{th} edition, 1987.
18. G. Besold, I. Vattulainen, M. Karttunen, and J. M. Polson. Towards better integrators for dissipative particle dynamics simulations. *Physical Review E*, 62(6):7611–7614, 2000.
19. I. Vattulainen, M. Karttunen, G. Besold, and J. M. Polson. Integration Schemes for Dissipative Particle Dynamics Simulations: From Softly Interacting Systems Towards Hybrid Models. *Arxiv preprint cond-mat/0211332*, 2002.
20. I. Teraoka. *Polymer solutions*. Wiley New York, 2002.
21. M. Doi and S. F. Edwards. *The Theory of Polymer Dynamics*. Oxford University Press, 1986.
22. H.C. Berg. *Random Walks in Biology*. Princeton University Press, 1993.
23. G. B. Arfken, H. J. Weber, and L. Ruby. *Mathematical Methods for Physicists*, volume 64. AAPT, 1996.

5 Polymer Scission

Dans les champs de l'observation,
le hasard ne favorise que les esprits préparés.
—— **Louis Pasteur**
(1822–1895)

Flow–Induced Chain Scission as a Physical Route to Narrowly Distributed, High Molar Mass Polymers.
B. A. Buchholz, J. N. Zahn, M. Kenward, G. W. Slater, A. E. Barron.
Polymer, 45, (4), 1223–1234. 2004.

In this chapter we take a minor diversion from the preceding work in that the computational method used to study the system is not Molecular Dynamics. This chapter was a joint project with the Barron group at Northwestern University, Evanston Illinois. The experimental work was carried out by the Barron group while the numerical model and calculations were entirely my results [52]. This project was motivated by experimental work done in the Barron group on the scission of polymer chains being driven through narrow constrictions. Please note the added reference to Thorstenson et al. [53], this was inadvertantly missed as a reference in the followin article.

Available online at www.sciencedirect.com
SCIENCE DIRECT®
Polymer 45 (2004) 1223–1234
polymer
www.elsevier.com/locate/polymer

Flow-induced chain scission as a physical route to narrowly distributed, high molar mass polymers

Brett A. Buchholz[a], Jacob M. Zahn[a,1], Martin Kenward[b], Gary W. Slater[b], Annelise E. Barron[a,*]

[a]*Department of Chemical Engineering, Northwestern University, 2145 Sheridan Road, Room E136, Evanston, IL 60208, USA*
[b]*Department of Physics, University of Ottawa, 150 Louis-Pasteur, Ottawa, Ont., Canada K1N 6N5*

Received 18 August 2003; received in revised form 12 November 2003; accepted 17 November 2003

Abstract

We present data showing a substantial narrowing of the polydispersity index (PDI) of high polymers occurring as a consequence of random chain scission events in a transient elongational flow field. In our experiments, semi-dilute aqueous solutions of high-molar mass, polydisperse polymers (PDI > 1.4) were injected under pressure through an elongational flow field at the entrance of a capillary tube (i.d. 250 μm). Chain scission events occurring during multiple passes through the capillary entrance cause a marked decrease in PDI, to values as low as 1.12, along with the expected decrease of the average molar mass. The phenomenon appears to be entirely physical and independent of the chemical nature of the polymer, since similar results are obtained with polyacrylamide, polydimethylacrylamide, and poly(ethylene oxide). Statistical modeling of the evolution of the polymer molar mass distribution shows the results to be consistent with the random scission, near the mid-point, of those polymer chains that exceed a certain flow field-dependent critical chain length.

Keywords: Polymer degradation; Scission; Extensional flow

1. Introduction

Monodisperse high molar mass polymers are of interest for a number of industrial and research applications requiring stringent levels of material characterization and specific polymer phase behaviors [1–4]. A few chemical methods currently exist that allow the generation of low-polydispersity index (low-PDI) polymers with high molar mass. For example, in living polymerization, chain propagation proceeds, ideally, without termination or chain transfer [5]. If short chains are terminated early, they may be 'revived' in some approaches by the use of highly active metallic catalysts and carried out to a target molar mass, producing a relatively narrow molar mass distribution even for large polymers. However, because of side reactions that can occur in some cases, living polymerization gives access to low-PDI high polymers (i.e. polymers with PDI < 1.20 and M_w > 200,000 g/mol) of many, but not all chemical classes [5,6]. One important living polymerization method for the preparation of monodisperse polymers is ring-opening metathesis polymerization (ROMP), which involves the catalytic polymerization of strained cyclic olefins in a variant of the olefin metathesis reaction [3,5,7–9]. The high activity of catalysts used in ROMP can cause intermolecular reactions in some classes of monomers, which can broaden the final molar mass distribution [5]. Generally, living polymerization methods require carefully controlled reaction conditions and special metallic catalysts [10], and are most convenient to use for those polymeric species without reactive side-chains and subgroups, unless protecting groups are employed. In the following, we present an entirely different route to the generation of low-polydispersity polymeric materials of high molar mass, by a physical method that exploits an iterative process of controlled polymer degradation in a transient extensional flow field. Before describing the method and our results, we give background on prior, related observations.

It has long been known that high shear from mechanical action can cause chemical bonds in polymer chains to break [11]. Some of the earliest work in this area used statistical methods to treat a process of random chain scission

* Corresponding author. Tel.: +1-847-491-2778; fax: +1-847-491-3728.
E-mail address: a-barron@northwestern.edu (A.E. Barron).
[1] Present Address: Department of Chemical Engineering, Stanford University, Palo Alto, CA 94305, USA.

0032-3861/$ - see front matter © 2003 Elsevier Ltd. All rights reserved.
doi:10.1016/j.polymer.2003.11.051

[12–14]. Most of these early theoretical studies modeled initial polymer populations that were monodisperse (PDI = 1.0). Since then, the mechanical degradation of polymers in elongational flow fields, which leads to a reduction in average polymer molar mass, has been widely observed and studied. Passage through an elongational flow field exerts strong hydrodynamic forces upon a coiled polymer molecule in solution, causing it to stretch, orient and extend in the direction of flow. If elongational forces on the molecule are sufficiently strong, and the rate of chain stretching far exceeds the rate of chain relaxation, the polymer backbone can be severed. The precise mechanism of chain scission is not fully understood, and remains a matter of discussion in literature [15–20]. It was theorized in 1944 by Frenkel that as the molecule becomes elongated in the direction of flow, the forces acting upon the molecule are greatest at its center [15], which can lead in turn to chain scission near the middle of the chain.

Several different flow geometries can lead to the creation of an elongational flow field. Generally, sudden contractions in the direction of flow generate a transient elongational effect, as velocity streamlines converge, which is localized in the region of the contraction. Full elongation of polymer chains most likely only occurs along the centerline of the flow field, where the molecules should not experience any shearing deformations [21]. Merrill and Leopairat designed an apparatus with a contraction ratio of 37.5 and demonstrated that chain scission occurred near the center of the molecule. They also were able to show that with an increase in the number of passes through the orifice, the net number of molecules that had experienced scission increased [22]. Nguyen and Kausch have performed extensive studies of polymer degradation in convergent flow using contraction ratios similar to those of Merrill and Leopairat [19,23–26]. Along with the expected reduction in molar mass, these authors observed a slight narrowing of the PDI of a high molar mass polystyrene sample as the total number of midpoint scission events increased [23]. At an applied strain rate of 275,000 s^{-1}, a significant fraction of the polymers were found to undergo two degradation events during a single pass through the contraction [26]. In these transient elongational flow fields, polymer degradation was found to occur even when the residence time was insufficient to allow full elongation of the polymer molecules, and thus midpoint scission occurred in partially uncoiled polymer molecules. Other researchers have also studied the flow of polymer solutions through transient extensional flow fields created by an abrupt contraction, using contraction ratios on the order of 4:1 or 8:1 [27–30].

So-called constant or homogeneous elongational flow fields, which can also lead to flow-induced chain degradation, are more difficult to achieve physically. The use of a cross-slot device, which generates an opposing-jets geometry, can create an elongational effect in which a given fluid element or polymer molecule will have a residence time long enough to achieve a constant strain rate. The geometry generates a stagnation point (zero velocity point) in the center of the flow field, where the molecules can experience full elongation. Hence, in a cross-slot device, chain extension is limited to a small area of the flow field. These quasi-steady-state flow fields have been studied by Odell and Keller and colleagues [20,31–38]. Owing to the small number of molecules that pass close to the stagnation point and undergo elongation and chain scission, a large number of passes through the system, at least 250, typically are needed to observe central chain scission [35]. Birefringence measurements were used to determine the extent of chain elongation [35]. In both transient and constant elongational flow fields, the critical fracture strain rates for chain scission are observed to decrease with increasing molar mass, with the specific dependence on molar mass (M^{-1} or M^{-2}) differing as a function of the instrument and conditions used [24,37].

In at least two other degradation studies in addition to that of Nguyen and Kausch mentioned above [23], a decrease in the polydispersity of a polymer solution was observed under some conditions [39,40]. For example Ballauff and Wolf [39] examined the shearing of polystyrene in *trans*-decalin using a Couette device, while Tanigawa et al. [40] studied the degradation by ultrasonication of three nucleic acid polymers in water. For one of the DNA solutions, a reduction in PDI from 1.7 to 1.2 was reported (for DNA polymers with initial M_w of 3.1×10^5 g/mol and final M_w of 6.4×10^4 g/mol). However, such significant PDI reductions have not been shown for any other polymer classes, nor achieved by any other degradation method besides sonication.

In this work, we examine the evolution of the molecular mass distribution of three different, initially very polydisperse and high-M_w ($>2.5 \times 10^6$ g/mol) polymer solutions as they are forced through a sudden constriction (contraction ratio ~ 100:1) comprising a 250 μm-ID capillary. To our knowledge, this is the first polymer degradation study involving iterative capillary entrance flow; we have examined the effects of this treatment on three industrially important water-soluble polymers, including linear polyacrylamide (LPA), polydimethylacrylamide (pDMA), which should have backbone–backbone bonds of similar intrinsic strength, and poly(ethylene oxide) (PEO). Our experimental results show that with multiple passes through the constriction, the expected progressive reduction in weight-average molar mass (M_w) is accompanied by a remarkable drop of the PDI for all three polymer samples, to values in the range of 1.12–1.15.

In order to better characterize this process, we also developed and applied to the data a simple statistical model with three physically motivated free parameters. One goal of this modeling study was to show that, based on a few reasonable assumptions having a firm basis in the literature, we could explain the dramatic PDI reductions that we observe. Analysis of the experimental data with this model indicates that the evolution of the molar mass distribution

can be explained by a sequence of chain scission events, where the probability of breakage increases sharply beyond a flow field-dependent critical molecular size. We also conclude based on this analysis that scission occurs predominantly in the central ≅ 20% of the chain.

2. Experimental

High molar mass, polydisperse polymers ($M_w > 2.5 \times 10^6$ g/mol, PDI > 1.4) were injected in aqueous solution into fused-silica capillaries (Polymicro Technologies, Phoenix, AZ) by means of a custom-built pressure-loading device (Fig. 1). LPA (M_w 4.10×10^6 g/mol) and pDMA (M_w 4.30×10^6 g/mol) were prepared by free-radical polymerization. Acrylamide (Amresco, Solon, OH) and *N,N*-dimethylacrylamide (Monomer–Polymer and Dajac Labs, Inc., Feasterville, PA) were polymerized in an aqueous solution (7.0% (w/v) total monomer concentration, thermostated at 47 °C and degassed with nitrogen prior to initiation). Initiator V-50 (2,2′-azobis(2-amidinopropane) dihydrochloride, Wako Chemical USA, Inc., Richmond, VA) was dissolved in water and injected into the reaction flask. After the reaction was complete, the resulting solution was dialyzed for 10 days against distilled water and then lyophilized to recover the dry polymer. PEO (M_w 2.68×10^6 g/mol) was obtained from Aldrich Chemical Company (Milwaukee, WI).

The polymer samples were dissolved at low, dilute to semi-dilute concentrations (0.1% (w/v) and 0.3% (w/v)) in water. At such low concentrations, the viscosities of the solutions are not much higher than that of water

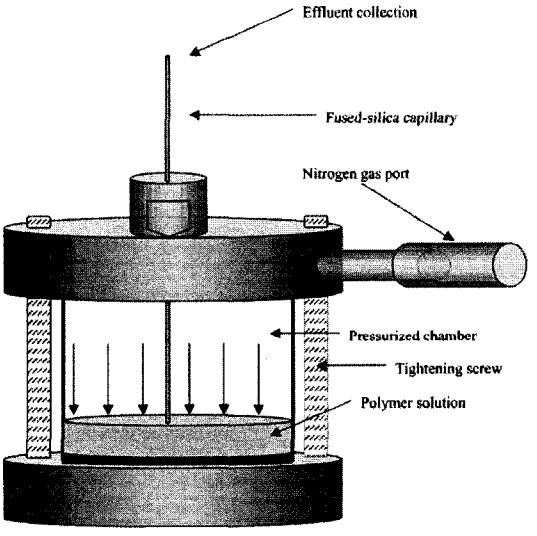

Fig. 1. A schematic illustration of the custom-built, aluminum pressure-loading device with a suspended capillary.

(<5 cP). At such low viscosities, the effects of shear thinning of the polymer solutions is expected to be minimal. The pressure-loading device (shown in Fig. 1) holds a charge of approximately 9 ml of polymer solution and was manufactured at Northwestern University. The top, bottom, and main body of the pressurized chamber are made out of aluminum. In addition to three screws that are used to tighten the device, O-rings on both the top and bottom of the pressurized chamber aid in sealing it. The capillary is extended into the polymer reservoir from the top of the device and sealed with a Swagelok™ valve. A side-mounted gas port allows the application of nitrogen gas in the pressurized chamber to propel the polymer solution from the reservoir through the capillary. In different experiments, the injection pressure was varied from 500 to 1000 psi (3.5–6.9 MPa); each run was performed at constant applied pressure. Capillaries used for different experiments had various inner diameters, ranging from 75 to 324 μm, and were cut to a length of 10–20 cm with a diamond capillary cutter to ensure a flat orifice, as confirmed after cutting by optical microscopy.

Injected polymer was collected in a reservoir and re-injected 4 additional times, for a total of 5 passes through the contraction defined by the capillary entrance. After each pass through the capillary entrance, a portion of the sample solution (~1 ml) was collected and lyophilized, and then analyzed by gel permeation chromatography (GPC) (Waters 2690 Alliance Separations Module, Milford, MA, with Shodex (New York, NY) OH-pak columns SB-806 HQ, SB-804 HQ, and SB-802.5 HQ connected in series) in tandem with a multi-angle laser light scattering system (MALLS) (DAWN DSP Laser Photometer and Optilab DSP Interferometric Refractometer connected in series (both from Wyatt Technology, Santa Barbara, CA)), in order to determine the molar mass distribution, the weight-average molar mass, and the PDI of the polymers [41]. The columns were kept at 25 °C and the aqueous mobile phase used contained 0.1 mNaCl, 50 mM NaH_2PO_4, and 200 ppm NaN_3 (pH 4.6). To ensure that there was always enough sample for analysis after the fifth pass through the capillary, in some cases we did not collect a polymer sample after the third pass. During polymer analysis, the flow rate through the GPC columns was kept extremely low (0.3 ml/min) in order to eliminate any possibility of additional degradation of the polymer molecules during passage through the columns. We confirmed that no polymer degradation occurred at this flow rate in a separate study (data not shown).

Capillary viscometry was performed to determine the characteristic relaxation time of the polyacrylamide sample used in one set of experiments. Solution concentrations of 0.20–1.99 mg/ml were analyzed using an Ubbelohde capillary viscometer. A plot of reduced viscosity vs. concentration was used to determine the intrinsic viscosity ($[\eta]_0$). The characteristic relaxation time τ_0 was estimated

with the equation [42]:

$$\tau_0 = \frac{[\eta]_0 M_w \eta_s}{N_A k_B T} \quad (1)$$

where η_s is the viscosity of the solvent, N_A is Avogadro's number, k_B is Boltzmann's constant, and T is temperature.

A schematic diagram of the converging streamlines in the elongational flow field created by the device, and their likely effect on polymer conformation for the majority of the experiments, is shown in Fig. 2. Individual polymer chains in a solution have a random coil conformation when unperturbed. As the polymer chains begin to enter the flow field they start to uncoil and stretch. Based on the observations of others [19,23–26], it is likely that some, but not all, chains become fully elongated as schematically shown in the diagram. Regardless of what fraction of chains are fully extended, it has been shown that chains only partially uncoiled can also break [26]. Given the simple design of the device and the goals of our experimental study, we did not attempt to determine to what extent polymers were stretched in the transient flow field we created. Instead, the experiments examined the effects of capillary entrance flow on the molar mass distributions of three distinct, high-M_w polymer samples in aqueous solution.

3. Results and discussion

3.1. Experimental results

Results of the experiments are shown in Fig. 3(a)–(c), in

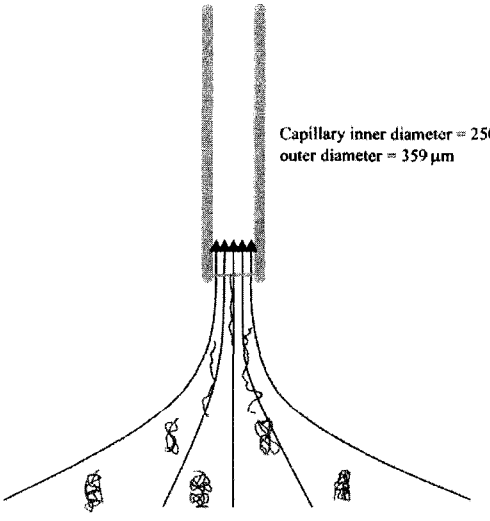

Fig. 2. Schematic illustration of the elongational flow field created by the pressure-loading device at the capillary entrance. Individual polymer chains in a dilute solution have a random coiled conformation when unperturbed. As the polymer chains begin to enter the flow field they start to uncoil and stretch, and in some cases can become fully elongated as schematically shown in the diagram.

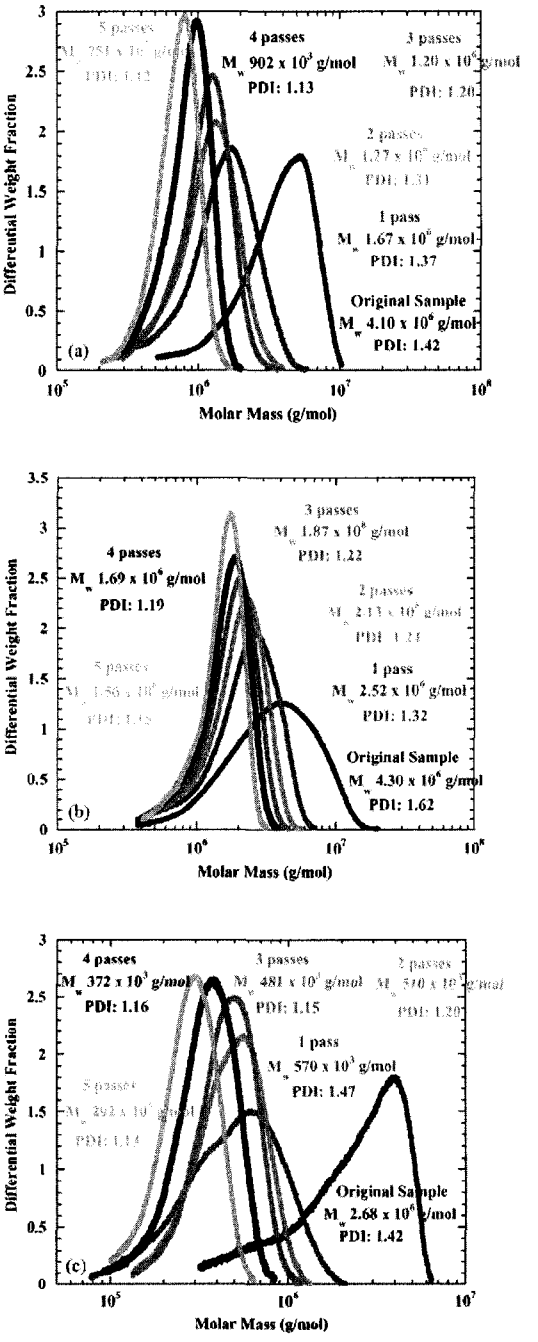

Fig. 3. Tandem GPC-MALLS characterization results obtained for (a) linear polyacrylamide, (b) polydimethylacrylamide, and (c) poly(ethylene oxide) in aqueous solution. The applied pressure was 1000 psi with a polymer solution concentration of $c = 0.1\%$ (w/v) in a 15 cm long capillary with an inner diameter of 250 μm.

plots of differential weight fraction vs. polymer molar mass. Each experiment for which results are shown in these figures was performed with a polymer solution concentration of $c = 0.1\%$ (w/v) using a 15 cm long capillary with an inner diameter of 250 μm, and an applied injection pressure of 1000 psi. In these figures, the integrated area under a given peak represents the normalized sum of the total polymer mass in the sample. As expected from previous work in the field, the average polymer molar mass decreases progressively after each pass through the capillary entrance (the peaks move to the left). However, of chief interest is the observation that the PDI of the degraded polymer samples also decreases sharply, even after only one injection through the capillary entrance. As can be seen in these plots, similar results were obtained for LPA (Fig. 3(a)), pDMA (Fig. 3(b)), and PEO (Fig. 3(c)), and the progressive effects of capillary entrance flow are particularly clear for the pDMA sample. With the decrease of the PDI, the molar mass distribution peaks increase in height after each subsequent pass, as expected.

Two aspects of the results shown in Fig. 3(a)–(c) should be stressed here. First, the molar mass distribution function changes most dramatically during the first pass. This seems to indicate, as would be expected, that it is easier to break longer molecules in a fixed elongational flow field. Second, the peaks apparently converge towards an asymptotic molar mass distribution for a large number of passes, a demonstration that, as expected from previously published studies, there is minimum (critical) molecular size below which the fixed flow field we generated is unlikely to lead to further chain scission events [43–46]. Both the average molar mass and the PDI continue to decrease after the first few passes, but at a much reduced pace. What is novel about these findings is our discovery that iterating the scission process quickly decreases not only the average molar mass but also the PDI, the latter to values of 1.15 or less in all three cases. To our knowledge, linear polyacrylamide, which has chemically labile side-chains, cannot be synthesized to such high molar mass ($M_w = 0.751 \times 10^6$ g/mol) with a PDI as low as this (1.12, the result obtained after five passes in Fig. 3(a)) by chemical methods, including living polymerization. We also note that to obtain a pDMA sample of such high average molar mass (1.56×10^6 g/mol) and low PDI (1.15), as shown in Fig. 3(b) (the fifth pass curve) would also most likely be difficult or impossible by chemical approaches.

Using the simple equation [47]

$$c^* = \frac{M_w}{\frac{4}{3}\pi N_A R_g^3} \tag{2}$$

where N_A is Avogadro's constant and R_g is the weight-average radius of gyration of the polymer obtained from the light scattering measurements, we estimated the entanglement threshold concentration, c^*, for each polymer sample studied. It has been shown that polymer coil overlap can be a factor in the degradation process and that entangled polymers experience greater tension near their midpoint than isolated polymer chains [44,46]. An increase in polymer concentration past the point of entanglement has also been determined to cause a corresponding increase in flow-induced chain scission [39]. We estimated using Eq. (2) that the initial (zero-pass) polymer solutions were slightly above their entanglement thresholds for LPA and pDMA ($c/c^* \sim 1.5–2.0$), and below c^* for consecutive passes. The PEO solution was near or above its entanglement threshold for all passes ($c/c^* \sim 1.5 - 3.0$). Hence there could be some effect of polymer–polymer entanglements on the chain scission process during capillary entrance flow, but the impact of this is most likely not dramatic since similar results were obtained in all cases.

In experiments such as these, determination of the amount of strain imparted on the viscoelastic fluid is important because, when coupled with information about the average polymer relaxation rate, one can predict the likely effect on polymer conformation. In dimensionless form, this is described by the Deborah number (De), which is the ratio of the characteristic relaxation time of the polymer solution to the characteristic flow time of the system [48]. If De is large, polymer molecules that become elongated in the flow field will not have time to relax their conformations during their residence in the elongational flow field. Capillary entrance flow is complex; fluid elements experience rapid elongation, but their elongation rate is inhomogeneous in both time and space. Using the method of Metzner and Metzner [21], we estimated the characteristic elongational strain rate under our experimental conditions to be about 45,000 s^{-1}. Viscometry data and Eq. (1) were used to determine the characteristic relaxation time for the zero-pass polyacrylamide solution to be approximately 2.6 ms. Correspondingly, the Deborah number was found to be on the order of 550. Due to the uncertainty in our estimate of the elongational strain rate, this De is only an approximation; however, clearly polymers are being stretched in the transient elongational flow field much more rapidly than they can relax.

Additional, exploratory experiments under a variety of conditions were performed using LPA solutions (data not shown), and these studies are still ongoing and will be discussed in detail in a future publication. In particular, we have investigated the impact of varying the initial polymer concentration, capillary inner diameter, and injection pressure over a limited range. We found that varying the applied pressure from 500 to 1000 psi (3.5–6.9 MPa) affected the final average molar mass, but did not significantly change the final PDI obtained. Specifically, at an injection pressure of 1000 psi, after five passes through the 250 μm capillary, a final M_w of 0.751×10^6 g/mol was obtained. Reducing the injection pressure to 750 and 500 psi led to successively higher final M_w values (1.2×10^6 g/mol and 1.4×10^6 g/mol, respectively). Hence, as would be expected, the polymer breakage process is significantly

affected by the applied strain rate: as the injection pressure is decreased, the strain rate is decreased. Therefore, the M_w after a fixed number of passes is larger for lower applied strain rates, as the size of the smallest molecules that undergo degradation is then also larger. Here a two-fold decrease of the pressure led to an approximately two-fold increase of the average molar mass, indicating that the critical molecular size is roughly inversely proportional to the strain rate. Interestingly, all three experiments produced virtually identical final PDI values, approximately 1.12, indicating that there was still a systematic reduction of the PDI with each pass and that the fundamental mechanistic process at the capillary entrance was not changed much by this two-fold reduction in applied pressure. The applied pressure thus appears to be a critical parameter for the control of the final average molar mass of the polymers, but has much less impact on PDI.

When we increased the LPA solution concentration from 0.1% (w/v) to 0.3% (w/v), we obtained results that were similar to those shown in Fig. 3(a), but which were less dramatic with respect to both the extent of chain breakage and the narrowing of PDI. Once again, the majority of breakage of LPA polymer chains occurred on the first pass through the system. After the fifth pass, the corresponding M_w was approximately 60% higher than the results obtained for 0.1% (w/v). This demonstrates that with even a slight increase of polymer concentration ($c/c^* \sim 6.0$ for the original 0.3% solution), the strain rate and elongational forces experienced by the polymers is affected. After five passes for this solution, c/c^* was reduced to about 1.2.

Although shear forces and turbulent extensional forces in tube flow are also known to have degradational effects on polymers [49], changing the length of the capillary tube from 15 to 10 or 20 cm resulted in no significant change in either final molar mass or final polydispersity. (Note that 10 cm was the shortest length that could be practically implemented with the flow device) That is, a shorter or longer exposure to the flow field in the capillary lumen did not affect the extent of chain scission that occurred. This is interesting because for all of the experiments for which results are shown in Fig. 3(a)–(c), we estimated that the Reynolds number of flow within the capillary tube exceeded the turbulent boundary (Re > 2200); a value of ~6600 was typical for experiments with the 250 μm-i.d. tube and 1000 psi applied pressure. In any case these results indicate that elongational deformations of polymer conformation at the capillary entrance are the dominant factor in polymer degradation. This has also been found in previous studies of contractile flows [50].

While results were on the whole very reproducible, our control over this chain scission process to produce polymers with a tailored, final average molar mass is relatively coarse with this apparatus. Further study, including the effect of temperature, will show whether this procedure can be tuned to generate monodisperse polymers of particular, designed molar mass.

3.2. Statistical model

In order to better understand our results and gain insight into the physical mechanisms that lead to this dramatic narrowing of PDI, we have developed a simple statistical model which captures the essential properties of the chain breakage process. We hoped to show that, using a model based on a few reasonable assumptions having a firm basis in the literature, we could explain the dramatic PDI reductions we observe. Our model is a variant of the form used by Ballauf and Wolf [16,39], Tanigawa et al. [40], Nguyen et al. [25], and Tayal and Khan [51]. We modeled the scission process with a set of 'master equations', or simple rate equations which, when rewritten in matrix form, transform the initial, experimentally obtained molar mass distribution data through a cascade of steps that mimic the multiple passes through the capillary system. With reasonable physical assumptions and a small number of physically motivated, adjustable parameters, this model is able to reproduce the successive molar mass distributions found experimentally, such as those shown in Fig. 3(a)–(c). Furthermore, the resultant model parameters yield fundamental, quantitative information about the scission process and why modifications to the experimental conditions (pressure, relative concentration (c/c^*), etc.) lead to different results.

The model relies on two basic assumptions. First, we assume that, consistent with prior experimental observations, stretched polymer chains tend to break predominantly around their mid-point, where the tension due to (transient) elongational forces reaches its maximum value [15]. Second, the model assumes that longer polymer chains have a higher probability of breaking in a given interval of time Δt, again consistent with previous observations by other groups [40]. Unlike previous models, however, we treat these two assumptions separately and adopt flexible fitting functions that allow for both assumptions to be violated. We make no other a priori assumptions about the breakage of the molecules and as we shall see, both the existence of a minimum molecular size for scission and the tendency for a chain to break near its middle point will emerge naturally from our modeling of the experimental data.

Let $n_i(t)$ be the number fraction of molecules of size i at time t, and $A_{i \leftarrow j} \equiv A_{ij}$ be the probability for a molecule of size j to be broken into pieces of size i and $j - i$ (with $j > i$, where i and j are integers such that $i, j \in [1 \ldots N_{max}]$) during a given interval of time Δt. We thus start by discretizing the initial experimental molar mass distribution $n_i(0)$ into $N_{max} = 200$ different molecular sizes. Note that the actual value of N_{max} does not affect the results of the calculations (all sufficiently large values of N_{max} lead to the same extent of agreement with experimental data); however, choosing a relatively small value of N_{max} greatly expedites the numerical calculations. One can then write a set of rate equations for the evolution of the populations $n_i(t)$ as a

function of time. A typical rate equation for a single molecular mass i simply reads

$$n_i(t+\Delta t) - n_i(t) = -n_i(t)\sum_{j=1}^{i-1} A_{ji} + \sum_{j=i+1}^{N_{max}} n_j(t)A_{ij} \quad (3)$$

The left-hand side of the equation gives the change in the population of molecules of size i during the period of time Δt. The first term on the right-hand side represents the scission of molecules of size i into two smaller molecules (of sizes j and $i-j$, with $j<i$), while the second term represents the formation of molecules of size i as the by-product of the scission of larger molecules (of size $j>i$). This set of linear equations can be written in matrix form as

$$n(t+\Delta t) - n(t) = An(t) \quad (4)$$

where $n(t) = \{n_1(t), n_2(t), \ldots n_{Nmax}(t)\}$ is the column vector that describes the number fraction molar mass distribution and $A = A(t, \Delta t)$ is a transition matrix that contains information about the most probable statistics of the chain breakage process during the period of time Δt at time t. Note that this equation can also be written as $n(t+\Delta t) = (A+I)n(t)$, where I is the $N_{max} \times N_{max}$ identity matrix; this form is often more practical from a computational point of view. The global matrix $A+I$ thus transforms the molecular size distribution $n(t)$ to $n(t+\Delta t)$.

In the $\Delta t \to 0$ limit, one can rewrite Eq. (3) as a set of differential equations, which is the standard way to deal with such problems when the shear is constant in time and uniform in space [40,51]. Indeed, if A is constant, one can in fact solve these equations exactly, as illustrated by Ballauff and Wolf [16,39]. However, we have a transient elongational flow in our case because the chain must go through the converging stream lines at the entrance of the narrow capillary [18]. Therefore, it is not possible to write a continuous time description of the process because it would require a precise knowledge of the time- and position-dependent matrix A. An alternative would be to carry out detailed computer simulations (e.g. using a molecular dynamics algorithm) of the dynamics of polymer chains in the converging flow [18]. Such simulations can provide useful information about the microscopic phenomena involved in the scission of individual chains, but cannot easily be used to analyze experimental data. Instead, we treat each pass as a sequence of $q \geq 1$ periods of time of duration Δt, and we use q as a fitting variable. We further assume that there exists an effective matrix A which reproduces the average effect of the shear during these periods of time Δt. In other words, we replace the (unknown) matrices $\{A(t=\Delta t), A(t=2\Delta t), \ldots, A(t=q\Delta t)\}$ that would be needed to properly calculate the scission statistics of the chains as they move through the high-shear region in a total period of time $q\Delta t$, by a single effective matrix A. Note that the actual matrix elements of A will be a function of q since in effect we are carrying out the following substitution:

$$\prod_{i=1}^{q}(A(i\Delta t)+I) \to (A+I)^q \quad (5)$$

As far as we can tell, this represents the first modeling of transient elongational flow degradation by effective kinetic equations and transformation matrices. This approach, together with the matrix elements described below, gives us full control over the parameters of the model and makes it easier to draw conclusions from their values, as we shall see. Note that these equations are conservative, in the sense that the total molar mass is a conserved quantity. It is also important to keep in mind that because the molar mass distribution and the viscosity of the solution change after each pass, the effective matrix A may in principle evolve from pass to pass.

An important part of our model is the choice of matrix elements A_{ij}. The latter are written as

$$A_{ij} = \begin{cases} 2S(i,j)P(j) & \text{for } i<j \\ -P(j) & \text{for } i=j \\ 0 & \text{for } i>j \end{cases} \quad (6)$$

where $P(j) = \sum_{i=1}^{j-1} A_{ij}$ denotes the total probability of breaking a molecule of length j during the period Δt, and $S(i \leftarrow j) \equiv S(i,j)$ is the probability that such an event generates molecules of size i and $j-i$. The factor of two arises from the fact that the function $S(i,j)$ is assumed to be symmetric about the center of the molecule ($j = i/2$) : the term $S(i,j)P(j) + S(i,i-j)P(j)$ then reduces to $2S(i,j)P(j)$. The terms $A_{ii} = -P(i)$ along the main diagonal give the total probability for a molecule of size j to be broken during that period of time, while the lower diagonal elements are null. These elements are null for the reason that we have not allowed, in this version of the model, chain recombination of fragments to form larger molecules. This choice of matrix elements explicitly decouples the probability of scission per unit time, $P(j)$, and the location of the scission along the chain $S(i,j)$.

The total probability of breakage $P(j)$ is a key parameter of all scission models. Instead of choosing an ad hoc function, which is generally the case with kinetic models, we propose the simple and very flexible step-like cutoff function

$$P(j) = \tanh\left[\left(\frac{j}{m_0}\right)^{\alpha}\right] \quad (7)$$

for the total probability of scission during the period of time Δt. Therefore, m_0 is roughly the molar mass cutoff for the scission while the exponent α is a measure of the effective sharpness of the cutoff. In fact, $P(j)$ becomes a sharp, step-like Heaviside function $H(m_0)$ when $\alpha \to \infty$ and a flat function, $P(j) = 1$, in the $\alpha \to 0$ limit. Moreover, the selected $P(j)$ function increases linearly with size j if $\alpha = 1$ and m_0 is larger than the largest molecular size (N_{max}) in

the system. This function can thus represent a wide range of behaviors, from sharp molecular thresholds for scission to size-independent scission probabilities. This approach is both more flexible and more general than previous ones in the literature [40]. In its current version, the model does not have an explicit probability for the molecules not to be affected by the elongational flow field during the period of time Δt; this is equivalent to assuming that all the molecules (on average) feel a similar effective elongational flow field at the entrance of the capillary. The strain rate distribution is difficult to project onto the model, given that the flow within the capillary tube exceeded the turbulent boundary, thereby rendering the flow unsteady. Although this is not an accurate description of the transient elongational flow present here, one should keep in mind that the matrix A represents an average description of the breaking process over a macroscopic time Δt here because we do not use a continuous time approach. In fact, we did study the problem with the function $P(j) = P_\infty tanh[(j/m_0)^\alpha]$, where the prefactor P_∞ was used to control the probability of not breaking during the given time period, but the results led to essentially the same quantitative agreement as those reported here (not shown). Therefore, this assumption ($P_\infty = 1$) does not appear to affect the ability of the model to describe the statistical properties of the polymer solutions after each pass.

We model the distribution $S(i,j)$ of breaks along the chain by a normalized truncated Gaussian distribution centered around the middle point of the chain (monomer $j/2$) and with a standard deviation σ:

$$S(i,j) = C^* \exp\left[-\frac{(i - j/2)^2}{2\sigma(j)^2} \right] \tag{8}$$

where C^* is a normalization constant defined by

$$\frac{1}{C^*} = \sum_{i=1}^{j-1} \exp\left[-\frac{(i - j/2)^2}{2\sigma(j)^2} \right] \tag{9}$$

We further use $\sigma = \sigma(j) = j \times \sigma_0$, i.e. the width of the distribution increases linearly with the molecular size j of the molecule that is being broken into two pieces. The parameter σ_0 can be thought of as a percentage of the total chain length that is susceptible to chain breakage. Hence, $\sigma_0 \to 0$ implies purely midpoint scission ($i = j/2$), while larger values of σ_0 create an increasingly random distribution of scission points along the chain (for instance, $j_0 \gg 1$ would correspond to a uniform probability of breaking the chain at any position). Again, our choice of modeling function allows essentially all possible types of behaviors to be recovered (for example random, central, or Gaussian scission). In this way, data analysis can give us fundamental information about the scission process with minimal ad hoc hypotheses.

The problem is thus reduced to finding the combination of parameters $\{\alpha, m_0, \sigma_0, q\}$ that reproduces the experimental observations. Note that because we decoupled the probability functions $P(j)$ and $S(i,j)$, and because of our specific choice of functions and free parameters, we do not need to choose a particular model for the scission, unlike some of the previous studies [16,51]. Instead, the values found for the fitting parameters will provide this information in a natural way, and the type of scission emerges naturally from the model.

In the unit system that we have defined, the residence time of the molecules in the high-strain region of the extensional flow field is $q\Delta t$. Since the total probability of breaking a molecule is $P(j)$ during each period of time Δt, Δt is directly related to the mean lifetime of an intact long molecule (for which $P(j) = 1$) in the high-strain region. As we will see, our analysis will find $q > 1$, which means that on average, each long molecule is involved in a cascade of $q > 1$ consecutive breaking processes during a given pass through the elongational flow field. In other words, according to this modeling of our experimental data, the mean residence time in the high-strain region is at least twice as large as the mean lifetime of the larger molecules in this strain field. Mathematically, this means that in order to reproduce the distribution function after each pass, we need to iterate the application of Eq. (4) to the molar mass data at least two times (in particular, it is impossible to explain the data after the first pass, even approximately, if we assume that $q = 1$). A complete study of the lifetimes and residence times will be presented elsewhere.

To be conservative we chose $q = 2$ and, in order to model the behavior of the differential weight fraction distributions, the three remaining parameters $\{\alpha, m_0, \sigma_0\}$ are those which minimize an error function which is based on the weighted differences between the calculated mean (or peak position), variance (or PDI), and skew (or peak asymmetry) of the model distribution and those values from the experimental data. The quality of the calculated distributions is gauged using the following function, which describes a relative error of the fit to the data in terms of the mean, μ, variance, σ, and skew γ. This function is the weighted sum of the relative errors in the properties of the calculated distributions relative to the experimental distributions, i.e.

$$f_{\text{error}} = A1\left(\left|\frac{\sigma_e - \sigma_c}{\sigma_e}\right|\right) + A2\left(\left|\frac{\mu_e - \mu_c}{\mu_e}\right|\right) + A3\left(\left|\frac{\gamma_e - \gamma_c}{\gamma_e}\right|\right) \tag{10}$$

the subscripts e and c refer to experimental and calculated values respectively. The parameters $A1$, $A2$ and $A3$ are constants which control the weight of each error on the fit. Values of $A1 = 2.5$, $A2 = 1$, and $A3 = 1$ were found to be optimal for reproducing the experimental data. Alternatively one can also use a least squares fit by comparing the calculated distributions and the experimental distributions at each step [16,39]. However, we decided that given the noise in the data, our approach is preferable because it

focuses on general trends in the distribution and not on the local details of the data.

In order to obtain the optimal values of these parameters we carried out a simple grid search of the $\{\alpha, m_0, \sigma_0\}$ parameter space to obtain the values that minimize this error function. Remarkably, we found that in almost all cases, $\sigma_0 \in [0.09, 1.15]$ was optimal for reproducing the experimental distributions. To further simplify, we thus fixed σ_0 with the average value for each data set and we minimized the fitness function for the other two parameters (these values are listed later). Note that previous modeling studies have often arbitrarily taken a value of $\sigma_0 = 0.2$ [40,51]. Yet our data analysis shows that in the transient extensional flow field we created, the distribution of chain breakage points is, in fact, more tightly centered around the middle of the chain. Moreover, the value of σ_0 emerges naturally from our minimization procedure.

To illustrate the agreement between the model and the experimental data, Fig. 4(a) shows a typical data set and our calculated distributions corresponding to data for an LPA experiment such as that shown in Fig. 3(a). The agreement is generally very good, though the calculated distributions sometimes slightly underestimate the peak height. A key point is that in order to achieve good quantitative agreement, we require at least $q = 2$. As mentioned above, this is especially the case when reproducing the first-pass distribution data, which makes sense since the initial distribution has a large number of very long chains. Fig. 4(b) and (c) shows the calculated and experimental distributions for the DMA and PEO samples, respectively.

In order to illustrate the behavior of the model parameters, Table 1 shows some typical results for $\{\alpha, m_0\}$, when σ_0 is chosen to be equal to 0.12. Interestingly, we see that the exponent α is a monotonically increasing function of the experimental pass number, which implies that $P(j)$ converges toward a step-like function. The initial α value of unity is fully consistent with previous assumptions of linear increases in $P(j)$ [40,51], but latter passes produce step-like functions that were not predicted by previous approaches. On the other hand, the critical size m_0 is a decreasing function of the number of passes (excluding the first pass). We are presently investigating the reasons for this pass-to-pass variation in m_0. It has been shown that a polymer solution (in a flow field) which is well below its entanglement threshold most likely will not be modified by the addition of polymer molecules [52]. Although it was determined for LPA that the 0.1% (w/v) (zero-pass) polymer solution was above the entanglement threshold c^*, in each subsequent pass the polymer solution was somewhat below c^*. Therefore, it is possible that the first-pass results are affected by interchain entanglements, as previously mentioned, and this could explain the smaller value of m_0 we found. The presence of entanglements might, for example, affect the critical molar mass value below which the molecules do not undergo scission [43–46]. One related, possible explanation of the later pass-to-pass reduction in m_0 is that, at constant pressure, a decrease in average molar mass leads to an increase of velocity and strain, hence a decrease of the minimum molecular size that can be broken in the device. In any case, these two trends (decrease of the critical molecular size m_0 and increase of the exponent α) indicate that the chain scission process at the capillary entrance naturally generates narrow molar mass distributions of 'small' polymers that cannot be broken any further in the given (fixed) strain (estimated for these experiments by the method of Metzner and Metzner to be about 45,000 s^{-1}) [21]. This is critical for the purpose of generating monodisperse polymer solutions.

Finally, we can predict how the molar mass distribution would evolve with further passes if we assume that the parameters $\{\alpha, m_0\}$ do not vary anymore after pass five. Fig. 4(a) also contains the extrapolated distribution for 50 passes under the assumption that the parameters $\{\alpha, m_0\}$ have already reached their asymptotic values, $\alpha = 10$ and $m_0 = 1200 \times 10^3$ g/mol. Here, we predict a $M_w = 546 \times 10^3$ g/mol and a PDI = 1.077.

Table 1
Table of calculated model parameters $\{\alpha, m_0\}$ for $\sigma_0 = 0.12$. These data correspond to the calculated distributions of LPA molar mass shown in Fig. 4(a)

Pass number	α	m_0 ($\times 10^{-3}$ g/mol)
1	1	2000
2	3	3100
3	6	1700
4	9	1600
5	10	1200

4. Conclusions

This study has demonstrated for the first time the potential of high-velocity capillary entrance flow to provide a general route to the creation of low-polydispersity high polymers, through a systematic reduction in PDI and M_w obtained by multiple passes through a well-defined contraction. It has never been shown before that such low PDI values (1.12–1.15) could be obtained via chain degradation, particularly for such high molar mass polymers (>200,000 g/mol). Experiments with the three different polymers yielded qualitatively similar molar mass distribution shifts and PDI decreases. While the finding is in this sense remarkable, an examination of the literature provides many clues which makes it surprising that this was not discovered long ago.

The method of elongational polymer degradation and polydispersity reduction that we describe here appears to be purely physical in nature. We have repeated these experiments many times and, in all cases, we noted the final PDI after five passes through the capillary to be in the range of 1.12–1.17 when capillaries with ID $\geq$ 150 μm

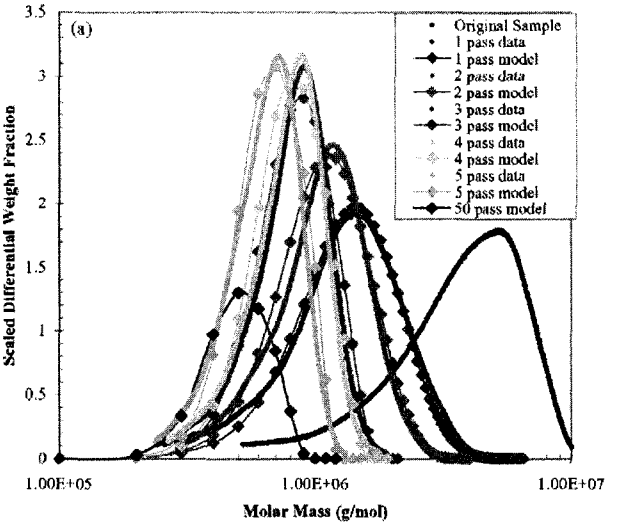

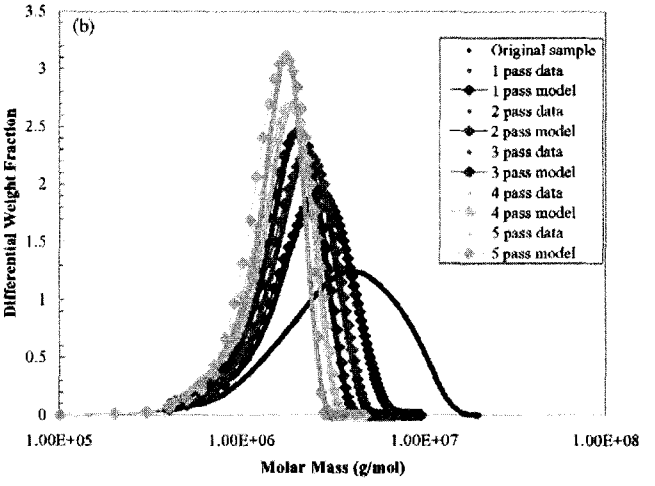

Fig. 4. Calculated and experimental molar mass distributions for (a) linear polyacrylamide, (b) polydimethylacrylamide, and (c) poly(ethylene oxide) solutions passed through the capillary entrances. Calculated distributions are shown with data points. The symbols correspond to the calculated distributions and the solid curves correspond to the experimental distributions. The distributions are generated from the normalized number fraction distributions; as a result their peak heights differ from the original molar mass distributions by a constant value. Experimental conditions are given in the Fig. 3 caption.

were used. We always observed most of the degradation to occur during the first pass, with the amount of degradation decreasing as the average molar mass shifted towards the critical molecular size m_0.

The results of our experiments in the application of a specific transient elongational flow field to high polymers suggest a novel method for the generation of diverse classes of monodisperse polymers of a relatively high molar mass. While so far we have only applied it to water-soluble polymers, the method appears to have good potential for broad applicability. The iterative nature of the method provides an additional degree of control over the final product. Elongational flow fields created by capillary contractions could be placed 'in parallel,' with polymer solutions automatically cycled through multiple passes under pressure to allow higher-throughput polymer processing, potentially producing monodisperse high polymers in quantities which are not feasible for production by any method save specialized chemical synthesis. (Note that in our experiments, the polymer mass flow rate through a

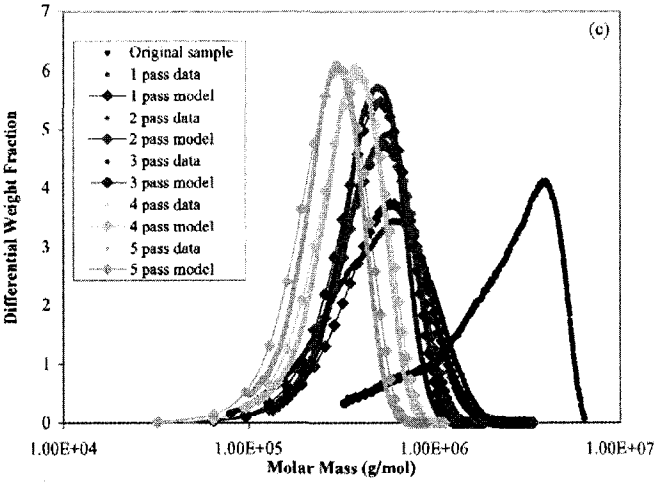

Fig. 4 (*continued*)

single capillary was 1 mg/s; hence with 1000 capillaries in parallel one could process 1 g/s). This method could provide a simple means to obtain monodisperse samples of some classes of polymers that are not conveniently synthesized by chemical methods, and hence are not easily accessed at high molar mass with low PDI, by any other means except preparative chromatography.

We developed a novel mathematical approach to model the experimental data, which explains the results and which has given us a better understanding of the characteristics of the chain scission process. The statistical model, which decouples the temporal (P) and spatial (S) probability functions and uses only three parameters to parameterize a wide range of possible functions, clearly indicates that as might be expected from previous work, the chains break multiple times at each pass ($q > 1$), and that the fixed strain rate cannot break molecules below a given molecular size ($\sim m_0$). Moreover, we find that the chains break over a much narrower region ($\sigma_0 = 0.12$) than previously assumed. It is these combined effects that allow us to generate increasingly monodisperse polymer solutions with only a few passes through the capillary entrance. A more detailed study of the relationship between the process parameters $\{\alpha, m_0, \sigma_0, q\}$ and the experimental conditions is currently in progress.

Acknowledgements

A.E.B. and B.A.B. acknowledge the Arnold and Mabel Beckman Foundation (Beckman Young Investigator Award) for support, and would like to thank Dr Wesley Burghardt and Victor Beck for helpful discussions on the subject and Donald H. Heckenberg for initial work on the project. G.W.S. and M.K. acknowledge a Research Grant and a Scholarship, respectively, from the Natural Sciences and Engineering Research Council of Canada (NSERC). M.K. would also like to thank the University of Ottawa for a National Excellence scholarship.

References

[1] Lee W, Lee H, Cha J, Chang T, Hanley KJ, Lodge TP. Macromolecules 2000;33:5111–5.
[2] Trzaska ST, Lee L-BW, Register RA. Macromolecules 2000;33:9215–21.
[3] Maughon BR, Morita T, Bielawski CW, Grubbs RH. Macromolecules 2000;33:1929–35.
[4] Hirao A, Nakahama S. Acta Polym 1998;49:133–44.
[5] Redakcji O, Qiu J, Charleux B, Matyjaszewski K. Polimery 2001;46:453–60.
[6] Matyjaszewski K. Macromol Symp 2001;174:51–67.
[7] Qiu J, Charleux B, Matyjaszewski K. Polimery 2001;46:663–72.
[8] Maynard HD, Okada SY, Grubbs RH. Macromolecules 2000;33:6239–48.
[9] Bielawski CW, Grubbs RH. Macromolecules 2001;34:8838–40.
[10] Kobayashi M, Okuyama S, Ishizone T, Nakahama S. Macromolecules 1999;32:6466–77.
[11] Staudinger H. Die Hochmolekularen Organischen Verbindugen. Berlin: Verlag Von Julius Springer; 1932.
[12] Kuhn W. Ber Chem Dtsch Ges 1930;63:1503–9.
[13] Kuhn WZ. Physik Chem (A) 1932;161:427–40.
[14] Montroll EW, Simha R. J Chem Phys 1940;8:721–7.
[15] Frenkel J. Acta Physicochim URSS 1944;19:51–76.
[16] Ballauff M, Wolf BA. Macromolecules 1981;14:654–8.
[17] Reese HR, Zimm BH. J Chem Phys 1990;92:2650–62.
[18] Knudsen KD, Cifre JGH, de la Torre JG. Macromolecules 1996;29:3603–10.
[19] Nguyen TQ, Kausch HH. Polymer 1992;33:2611–21.
[20] Odell JA, Keller A, Rabin Y. J Chem Phys 1988;88:4022–8.
[21] Metzner AB, Metzner AP. Rheol Acta 1970;9:174–81.
[22] Merrill EW, Leopairat P. Polym Engng Sci 1980;20:505–11.

[23] Nguyen TQ, Kausch HH. Chimia 1986;40:129–35.
[24] Nguyen TQ, Kausch HH. J Non-Newtonian Fluid Mech 1988;30: 125–40.
[25] Nguyen TQ, Liang QZ, Kausch HH. Polymer 1997;38:3783–93.
[26] Nguyen TQ. Chimia 2001;55:147–54.
[27] Quinzani LM, Armstrong RC, Brown RA. J Rheol 1995;39:1201–28.
[28] Quinzani LM, Armstrong RC, Brown RA. J Non-Newtonian Fluid Mech 1994;52:1–36.
[29] Boger DV, Crochet MJ, Keiller RA. J Non-Newtonian Fluid Mech 1992;44:267–79.
[30] Coates PJ, Armstrong RC, Brown RA. J Non-Newtonian Fluid Mech 1992;42:141–88.
[31] Odell JA, Keller A, Miles MJ. Polym Commun 1983;24:7–10.
[32] Keller A, Odell JA. Colloid Polym Sci 1985;263:181–201.
[33] Odell JA, Keller A. J Polym Sci: Part B: Polym Phys 1986;24: 1889–916.
[34] Muller AJ, Odell JA, Keller A. Polym Commun 1989;30:298–301.
[35] Narh KA, Odell JA, Muller AJ, Keller A. Polym Commun 1990;31: 2–6.
[36] Odell JA, Muller AJ, Narh KA, Keller A. Macromolecules 1990;23: 3092–103.
[37] Muller AJ, Odell JA, Carrington S. Polymer 1992;33:2598–604.
[38] Odell JA, Keller A, Muller AJ. Colloid Polym Sci 1992;270:307–24.
[39] Ballauff M, Wolf BA. Macromolecules 1984;17:209–16.
[40] Tanigawa M, Suzoto M, Fukudome K, Yamaoka K. Macromolecules 1996;29:7418–25.
[41] Buchholz BA. Electrophoresis 2001;22:4118–28.
[42] Larson RG. The Structure and Rheology of Complex Fluids. New York: Oxford University Press; 1999.
[43] Harrington RE, Zimm BH. J Phys Chem 1965;69:161–75.
[44] Bestul AB. J Chem Phys 1960;32:350–6.
[45] Glynn PAR, Van Der Hoff BME, Reilly PM. J Macromol Sci-Chem A6 1972;8:1653–64.
[46] Bueche F. J Appl Polym Sci 1960;4:101–6.
[47] Broseta D, Liebler L, Lapp A, Strazielle C. Europhys Lett 1986;2: 733–7.
[48] Bird RB, Armstrong RC, Hassager O. Dynamics of Polymeric Liquids. New York: Wiley; 1987.
[49] Horn AF, Merrill EW. Nature 1984;312:140–1.
[50] Jones DM, Walters K. Rheol Acta 1989;28:482–98.
[51] Tayal A, Khan SA. Macromolecules 2000;33:9488–93.
[52] Carrington SP, Tatham JP, Odell JA, Saez AE. Polymer 1997;38: 4151–64.

6 Concluding Remarks

I may not have gone where I intended to go,
but I think I have ended up where I intended to be.
—— **Douglas Adams**
(1952–2001)

In this thesis we have explored a number of different phenomena inspired in part by, or related to, microfluidics and or polymer separation (and DNA sequencing). It is worth bearing in mind that this conclusion is not meant to bring to finality those problems discussed in this thesis, since in fact, there are many avenues worthy of further exploration stemming directly from the topics discussed in the thesis. Instead, I aim to briefly summarize some key results and then suggest some further work which can be carried out.

6.1 Recap

Each of the preceding articles can be classified under the general rubric of methods and applications related to the manipulation of polymers and the theory and simulation of associated phenomena which occur as a result of this manipulation. In particular the work contained in Chapters 2, 3 and 4 are very closely tied to the topic of polymer transport with a leaning towards applications for separating polymers in microfluidic systems. Although Chapter 5 does not use the MD simulation method to explore the degradation of polymer chains in microfluidic systems, the topic itself is directly related to that of Chapter 3. In

fact, the effectively *monodisperse* polymer solutions created using the extensional flows would be an ideal media for testing the theory of single chain collisions.

In Chapter 2 we presented a systematic examination of the friction coefficients of solvent particles and polymers using MD. We first illustrated the ability (and utility) of MD simulations to explore the friction coefficients of random coil polymers, rigid rod polymers and hydrodynamically coupled polymers. We clearly demonstrated the effect of hydrodynamic coupling of rod-like polymers as a result of a weak dependence of a polymers friction coefficient on the ratio of its length to its diameter. We then explicitly explored the friction coefficients of rigid rods moving either parallel or perpendicular to applied fields. This was followed by a direct comparison of the MD results with the results from macroscopic hydrodynamics. We also discussed a crossover in which the friction coefficient of a coil is actually larger than that of a rigid rod moving perpendicular to an applied field. By examining the liquid in the interior of a polymer coil, we also showed that the concept of so called *hydrodynamic impermeability* of a polymer is in fact correct. Fluid trapped inside a polymer coil moves at or near the velocity of the polymer coil itself and can thus be treated as a solid ball with effective radius equal to the hydrodynamic radius of the polymer. The final key result was an examination of a polymer pulled by its middle monomer and the effect of the resulting deformation on its friction coefficient. In this instance we observed a novel transition in friction coefficient (for intermediate applied forces) in which the friction coefficient of the polymer initially increases then tends asymptotically to that of a hydrodynamically coupled rigid rod moving parallel to the applied field.

Once we had fully understood the fundamentals of the friction coefficients we brought to bear this knowledge in an examination of the collision of polymers with *obstacles*. These obstacles are either: fixed posts or other polymers. We explored three different scenarios: polymers (in the presence of an external force) colliding with fixed obstacles, polymers (in the presence of a fluid flow) colliding with fixed obstacles and polymers (in the presence of an external force) colliding with a free polymer. We presented a general (classical) model for the collisions which was shown to be applicable to all three collision regimes, in the first two cases simple exact solutions were obtainable, while in the case of the polymer-polymer collisions a series solution is presented, the first term of which provides a good estimate for the behaviour of the polymer-polymer collisions. In all three cases we carried out MD simulations to explore the collision dynamics. In the first two examples, (fixed

obstacle collisions) we clearly showed that the fluid flow and external force regimes lead to a universal behaviour and agreed well with the predictions from the collision model. The polymer-polymer collisions exhibit one unexpected complication, the appearance of an additional V-shaped conformation. This conformation corresponds to the case where the *arms* of the polymer effectively open for a V-shape and the arms of the molecule are not pointing in the direction of the applied field. This aspect complicated a direct comparison with the model calculations; therefore, we presented a separate numerical analysis of the predicted dynamics of the polymer-polymer collision system in the last section of the paper and thus gave a way of predicting overall trends in the collisions.

The article on ratchets and polymer deformation explored the effects of the application of an asymmetric saw tooth potential which was periodically switched off and on and is typically used to generate net migration of a polymer. In this article we presented a study of the deformation of the polymer chains induced by the application of the ratchet potential and illustrated that the polymers undergo a transition from 3d coils to 2d pancakes in the presence of moderate ratchet potentials with $U_0 \leq 10k_{\mathrm{B}}T$. This pancaking effect has been not be discussed previously in the literature in the context of ratchets.

We began with a simple theoretical expression to model the time dependence of a polymers diffusion coefficient, $D(t)$. We then derived a modified Bader ratchet model which explicitly takes into account polymer deformation and its effects on the probability of a particle to diffuse in a ratchet. This theory clearly indicates that polymer deformation slows a polymers diffusion (due to the pancaking effect). As a result it can be used to modulate the transport of a polymer in ratchet. We also presented results from our Molecular Dynamics model which explored this inhibited diffusion effect and compared the results directly with the modified Bader ratchet model.

In the final chapter we explored a more applied problem but still ultimately related to the general idea of polymer-polymer collisions in microfluidic devices. In collaboration with the Barron group at Northwestern University (Evanston, Illinois) we carried out a systematic examination of the degradation of polymer chains with extensional flow fields. The Barron group had carried out a thorough experimental investigation of the effects of periodically driving a dilute polymer solution through a narrow constriction using high pressure. At the entrance of this constriction there exists a narrowing of the flow field and thus an extensional flow, causing the breaking of polymer chains. The Barron group

showed that by sending a polydisperse polymer solution through such a device, you can systematically and predictably lower the polydispersity index (PDI) of a polymer solution. Using an empirical model, based on a master equation, we showed that one can recover the distributions of polymer degradation products, thus shedding light on the statistical nature of the polymer degradation process. One key element is that for the types of systems used in these experiments, polymers break a least twice during the initial pass through the apparatus. Although empirical, the model was able to predict the distribution of breaking along the polymer chain and allows us to predict distributions for higher numbers of pass through the experimental apparatus.

6.2 Looking forward

There are many possible extensions to the work discussed in this thesis either directly stemming from the articles which make up the thesis or related subjects. I will mention those which are of immediate interest to me and as such the choice of topics is highly biased.

A natural extension of the work on polymer friction coefficients is to examine more complex morphologies including: rings, knotted polymers and branched polymers (to mention a few). This would be a novel extension the calculations for the linear polymers which are discussed in Chapter 2. On this topic, it would be nice to examine equilibrium methods for examining polymer friction coefficients, by for example using Green-Kubo type methods to extract polymer friction coefficients as opposed to applying external forces to measure mean velocities and thus friction coefficients.

In particular, of those types of polymers mentioned in the previous paragraph, the friction coefficients of branched polymers are a very interesting avenue to explore. Branched polymers are used in a number of separation methods (most notably End Labeled Free Solution Electrophoresis (ELFSE)). In this method drag-tags (or molecular parachutes) are attached to charged polymers in order to induce molecular weight dependent mobility, in free solution, i.e., in the absence of a sieving media. Understanding the friction coefficients of the drag-tags (some of which are branched polymers) can be useful in determining the optimal geometry of the polymers which are used as effective molecular parachutes.

A glaringly obvious extension of this work is the inclusion of electrostatics. Biopolymers

are in general charged objects and electrostatic effects play a key role in polymer dynamics in solution. This is one aspect which we did not explore in this thesis. In fact, to model real microfluidic systems it is crucial to have electrostatic effects such as electroosmotic flow and polymer freedraining effects. The largest stumbling block to the inclusion of electrostatics is the (computationally) time consuming nature of these calculations. However, this being said as computational resources increase in both abundance and power (i.e., in terms of Floating point operation per second, FLOPS) electrostatic interactions become more tractable in reasonable time frames.

Although we have discussed a model for the single chain dynamics of polymer-obstacle collisions the natural next step for this work is to apply these calculations to examine the migration of polymers in real separation systems. As such it would be a logical next step to take these calculations and apply them to the statistics of polymer migrating in arrays of posts and/or dilute polymer solutions in order to calculate the efficiency of the arrays in sieving polymers, in the same vein as the recent work of Dorfman [60].

The polymer-polymer collision calculations can be easily extended to examine multi-polymer-polymer collisions such as those that occur in experimental systems. This can be used to model the migration of polymers in dilute polymer solutions. It is rather straightforward to add extra polymers to the general polymer-polymer collision model and include multi-polymer effects. This is something definitely worthy of further exploration.

Perhaps the most immediate and exciting extension of the work in thesis is a further study of polymer deformation in ratchets. Specifically it would be superb to examine this system experimentally and see if the theory accurately predicts the role of polymer deformation in the migration of polymers in ratchets. In light of this, it would be possible to construct ratchets that fully utilize the deformation effect and can in principle be used to optimize ratcheting mechanisms in experimental systems.

Bibliography

[1] P. Gravesen, J. Branebjerg, and O. S. Jensen. Microfluidics-a review. *J. Micromech. Microeng*, 3(4):168–82, 1993.

[2] D. J. Beebe, G. A. Mensing, and G. M. Walker. Physics and applications of microfluidics in biology. *Annual Review of Biomedical Engineering*, 4(1):261–286, 2002.

[3] D. A. Fitzgerald. Macro Opportunities in Microfluidics. *The Scientist*, 17:11–39, 2003.

[4] G. M. Whitesides and A. D. Stroock. Flexible methods for microfluidics. *Physics Today*, 54(6):42–48, 2001.

[5] A. Stone, H and S. Kim. Microfluidics: Basic issues, applications, and challenges. *AIChE Journal*, 47(6):1250–1254, 2001.

[6] http://gba.co.il/.

[7] http://www.ornl.gov/sci/techresources/human_genome/home.shtml.

[8] F. S. Collins, M. Morgan, and A. Patrinos. The Human Genome Project: Lessons from Large-Scale Biology. *Science*, 300(5617):286, 2003.

[9] M. J. Heller. DNA Microarray technology: Devices, Systems, and Applications. *Annual Review of Biomedical Engineering*, 4(1):129–153, 2002.

[10] R.C. Strohman. The coming Kuhnian revolution in biology. *Nature Biotechnology*, 15:194–200, 1997.

[11] E. S. Lander, L. M. Linton, B. Birren, C. Nusbaum, M. C. Zody, J. Baldwin, K. Devon, K. Dewar, M. Doyle, and W. et al FitzHugh. Initial sequencing and analysis of the human genome. *Nature*, 409(6822):860–921, 2001.

[12] F. J. Dyson. *The Sun, the Genome & the Internet: Tools of Scientific Revolutions*. Oxford

University Press, 1999.

[13] H. G. Elias. *An introduction to polymer science*. VCH Weinheim, 1997.

[14] A. Y. Grosberg, A. R. Khokhlov, and L. W. Jelinski. *Giant Molecules: Here, There, and Everywhere...*, volume 65. AAPT, 1997.

[15] Nobel Prize website. http://nobelprize.org/nobel_prizes/chemistry/laureates/1953.

[16] Wikipedia. http://en.wikipedia.org/wiki/rubber.

[17] F. Tessier. *Modelling of electrokinetic phenomena involving confined polymers: applications to DNA separation and electroosmotic flow control*. PhD thesis, University of Ottawa, 2005.

[18] Online bakelite museum, http://www.bakelitmuseum.de/. Web.

[19] http://en.wikipedia.org/wiki/main_page.

[20] http://www.ebay.ca.

[21] http://www.accessexcellence.org/rc/vl/gg/images/dna2.gif.

[22] http://www.ocean.udel.edu/deepsea/level-2/geology/vents.html.

[23] F. Pauli. Ask a geneticist – http://www.thetech.org/genetics/ask.php?id=69.

[24] R. Dawkins. *The Selfish Gene (New ed.)*. Oxford: Oxford University Press, 1989.

[25] http://www.accessexcellence.org/rc/vl/gg/images/structure.gif.

[26] J. D. Watson. *The Double Helix: A Personal Account of the Discovery of the Structure of DNA*. Penguin, 1970.

[27] http://homepage.smc.edu/hgp/
http://homepage.smc.edu/hgp/history.htm.

[28] N.C. Metropolis, J. Howlett, and G.C. Rota. *A History of Computing in the Twentieth Century: A Collection of Essays*. Academic Press, 1980.

[29] G. M. Whitesides. The origins and the future of microfluidics. *Nature*, 442(7101):368–73, 2006.

[30] J. Ouellette. A new wave of microfluidic devices. *Industrial Physicist*, 9(4):14–17, 2003.

[31] C. Williams. Ink–jet printers go beyond paper. *Physicsworld*, 19(1):24–28, January 2006.

[32] E. M. Purcell. Life at low Reynolds number. *Am. J. Phys*, 45(1):3–11, 1977.

[33] M. D. Haw. Colloidal suspensions, Brownian motion, molecular reality: a short history. *Journal of Physics: Condensed Matter*, 14(33):7769–7779, 2002.

[34] A. Einstein. On the motion of small particles suspended in liquids at rest required by the molecular-kinetic theory of heat. *Annalen der Physik*, 17:549–560, 1905.

[35] J. Crank. *Mathematics of Diffusion*. Oxford University Press, USA, 1980.

[36] G. Batchelor. *An Introduction to Fluid Dynamics*. Cambridge University Press, 1967.

[37] D.J. Tritton. Physical fluid dynamics, Clarendon, 1988.

[38] E. C. J. Oliver. Spinning and mixing: Two studies of microfluidic problems using molecular dynamics simulations. Master's thesis, University of Ottawa, 2006.

[39] M. Doi and S. F. Edwards. *The Theory of Polymer Dynamics*. Oxford University Press, 1986.

[40] H. Kleinert. *Path integrals in quantum mechanics, statistics, and polymer physics*. World Scientific Teaneck, NJ, 1995.

[41] D. C. Rapaport. *The Art of Molecular Dynamics Simulation*. Cambridge University Press, 1995.

[42] M. E. Tuckerman and G. J. Martyna. Understanding modern molecular dynamics: techniques and applications. *J. Phys. Chem. B*, 104(2):159–178, 2000.

[43] M. P. Allen and D. J. Tildesley. *Computer Simulations of Liquids*. Oxford Science Publications, Oxford, 4^{th} edition, 1987.

[44] K. Kremer, G. S. Grest, and I. Carmesian. Crossover from Rouse to reptation dynamics: A molecular dynamics simulation. *Phys. Rev. Letters*, 61(5):566–569, 1988.

[45] K. Kremer. Computer simulation methods for polymer physics. In K. Binder and G. Ciccotti, editors, *Monte Carlo and Molecular Dynamics of Condensed Matter Systems*, pages 603–650. SIF, 1996.

[46] A. Nakano, M. E. Bachlechner, R. K. Kalia, E. Lidorikis, P. Vashishta, G. Z. Voyiadjis,

T. J. Campbell, S. Ogata, and F. Shimojo. Multiscale simulation of nanosystems. *Computing in Science & Engineering [see also IEEE Computational Science and Engineering]*, 3(4):56–66, 2001.

[47] F. F. Abraham, N. Bernstein, J. Q. Broughton, and D. Hess. Dynamic Fractureof Silicon: Concurrent Simulation of Quantum Electrons, Classical Atoms. *MRS BULLETIN*, page 27, 2000.

[48] F. F. Abraham. Crack dynamics in brittle fracture: An atomistic study. *Nuclear Inst. and Methods in Physics Research, B*, 180(1-4):72–76, 2001.

[49] P. Reimann. Brownian motors: noisy transport far from equilibrium. *Physics Reports*, 361:57–265, 2002.

[50] R. P. Feynmann, R. B. Leighton, and M. Sands. The Feynmann Lectures on Physics. *Vol. III, (Addison Wesley, Reading)*, 1965.

[51] J. S. Bader, R. W. Hammond, S. A. Henck, M. W. Deem, G. A. McDermott, J. M. Bustillo, J. W. Simpson, G. T. Mulhern, and J. M. Rothberg. DNA transport by a micromachined Brownian ratchet device. *PNAS*, 96(23):13165–13169, 1999.

[52] B. A. Buchholz, J. M. Zahn, M. Kenward, G. W. Slater, and A. E. Barron. Flow-induced chain scission as a physical route to narrowly distributed, high molar mass polymers. *Polymer*, 45(4):1223–1234, February 2004.

[53] Y.R. Thorstenson, S.P. Hunicke-Smith, P.J. Oefner, and R.W. Davis. An Automated Hydrodynamic Process for Controlled, Unbiased DNA Shearing. *Genome Research*, 8(8), 1998.

[54] K. Freudenberg, W. Kuhn, and I. Bumann. Ber. deutsch. chem. *Ges*, 61:1735, 1928.

[55] W. Kuhn. Über die Kinetik des Abbaues hochmolekularer Ketten. *Chem. Ber*, 63:1503–1509, 1930.

[56] E. W. Montroll and R. Simha. Theory of Depolymerization of Long Chain Molecules. *Journal of Chemical Physics*, 8(9):721–726, 1940.

[57] J. Frenkel. Orientation and rupture of linear macromolecules in dilute solutions under the influence of viscous flow. *Acta Physicochim. URSS*, 19:51–76, 1944.

[58] M. Kenward and G. W. Slater. Molecular dynamics simulations with explicit hydro-

dynamics interactions i: On the friction coefficients of equilibrium and deformed polymers. *Euro. Phys. J. E*, 14(1):55–65, 2004.

[59] M. Kenward and G. W. Slater. Molecular dynamics simulations with explicit hydrodynamics interactions ii: On the collision of polymers with molecular obstacles. *Euro. Phys. J. E*, 20(2):125 – 141, 2006.

[60] K. D. Dorfman. DNA electrophoresis in microfluidic post arrays under moderate electric fields. *Physical review E*, 70, 2006.

[61] J. R. Dutcher, A. G. Marangoni, and D. Dutcher. *Soft Materials: Structure and Dynamics*. CRC Press, 2005.

Appendix A

The following appendix contains additional articles with which I have either participated in writing and/or carrying out research. They have not been included in the main body of the thesis to clearly delineate the distinction between my primarily independent research in the thesis and my collaborative role in the articles which follow. I have been fortunate to have participated to varying degrees in all of the following works and to clarify my contribution I discuss each article individually. Much of the work in the articles are directly related to the research contained in the main body of the thesis.

The first article: *Combinatorial design of passive drug delivery systems* is primarily the work of Sébastian Casault and will appear as a chapter entry in his Masters thesis. My contribution to this article was helping with various computational aspects of the article, including the early stages of developing the computer code for the exact enumeration method along with helping to analyze data and to derive and understand some of the results for the diffusion calculations in the article.

The second article – *Molecular Dynamics simulations of polymer in micro-environments* was published as conference proceedings at HCPS (High Performance Systems and Applications) 2003 and was a group effort. It was specifically written to highlight some of the exciting developments in the group as related to Molecular Dynamics simulations. The article provides a general overview of the application and utility of MD simulations in the modelling of polymers and fluids in micro-environments and several illustrative examples to show the scope of our work. I organized the writing of the article to clearly demonstrate the use of MD in the broader context of microfluidics and single polymer physics.

The third article was a joint effort which highlighted current trends in capillary electrophoresis entitled *The theory of DNA separation by capillary electrophoresis* published in Current Opinion in Biotechnology in 2003. My contribution was writing the section: *Dilute Solutions*, which provides a description of ultra-dilute polymer solutions used for separating DNA in capillaries. This was directly motivated by the work on polymer-polymer collisions discussed in Chapter 3. I also contributed to the editing and organization of the material in the article.

The fourth article – *Deformation, stretching and relaxation of single-polymer chains: Fundamentals and examples* published in Soft Materials in 2004 was an invited article which

also appeared in the book Soft Materials: Structure and Dynamics, Eds. Dutcher and Marangoni [61]. My contribution to this work was mainly the writing of the section entitled *Polymer Obstacle Collisions*, which was the precursor to the full theory of polymer-polymer collisions presented in Chapter 3. I also helped to write the introduction and organize the material in the article.

The fifth and final article entitled – *Theory of DNA electrophoresis 1999-2002*$\frac{1}{2}$ was a review article published in Electrophoresis. My contribution was the writing of the section on *Magnetic self-assembling sieves* which is one experimental system in which the polymer collision model discussed in Chapter 3 is observed. As an ancillary note, this article was one of the top cited articles in Electrophoresis in 2003.

Manuscript

Combinatorial design of passive drug delivery platforms

Sébastien Casault, Martin Kenward, and Gary W. Slater*
Department of Physics, University of Ottawa
150 Louis-Pasteur
Ottawa, Ontario K1N 6N5
Canada
(Dated: December 14, 2006)

We introduce a novel computational approach to designing passive drug delivery systems based on porous materials such as hydrogels. Our approach uses three tools: a method to establish the exact release pattern from all possible loading sites inside a given hydrogel; a method to generate a large number of hydrogel structures to be tested numerically, and finally an optimization algorithm which leads to the selection of optimal hydrogel structures. Using this approach, we show that controlled release curves can be obtained by using a genetic algorithm for the optimization step. Strategies to generalize this approach to other systems are also discussed.

PACS numbers: 66.10.Cb 82.56.Lz 87.15.Aa
Keywords: Drug Delivery; Controlled Release; Hydrogels; Optimization; Genetic Algorithm; Exact-enumeration

I. INTRODUCTION

Designing drug-delivery systems with a controlled rate of drug release is crucial for applications where dosage must remain in a prescribed therapeutic range over the entire term of treatment [1]. Currently, there exists active platforms relying on kinematic effects (*e.g.* swelling and dissolution) that feature controlled release characteristics [2, 3]. However, it proves much more challenging to achieve constant drug release from passive platforms, *i.e.*, those strictly relying on diffusion as a drug delivery mechanism, such as non-degradable hydrogels [4, 5]. Passive platforms would have the advantage of not heavily relying on environmental factors which can prove difficult to control. There is a definite need for a systematic approach which can quickly identify optimal design strategies for passive systems.

According to Cohen and Erneux [6], the most common drug delivery mechanism is diffusion from a polymeric system (such as a hydrogel). We will thus focus our study on hydrophilic drugs and the use of polymeric hydrogels. Several methods can be used to experimentally prepare hydrogels with specific internal structures (obstacle distributions). For example, Liang *et al.* [7] have shown that the density of a hydrogel can be controlled using a non-cytotoxic crosslinker.

We introduce the novel concept of combinatorial drug delivery platform design. We focus this proof of principle study on obtaining results which promote a constant drug release rate as a function of time although the technique can be used, in principle, to achieve virtually any desired release profile. The results presented in this paper are obtained using a lattice model of diffusion which is similar to that introduced originally by Majid *et al.* [8]. We neglect chemical details and adopt a coarse-grained view of the diffusion process. Studies which model polymers often rely on stochastic, Monte Carlo simulation methods where the diffusion of a drug molecule is represented by random, discrete jumps on a lattice occupied with obstacles. In contrast, our method has the advantage of producing numerically exact data by enumerating *all* possible walks on any given lattice matrix with obstacles (the latter represent the gel fibers present in a hydrogel matrix). We limit our work to diffusion in two-dimensions but the extension to 3D (or more!) poses no difficulty other than requiring more computational resources.

It is widely known that the internal structure of a hydrogel is important in modulating the release rate [9–13]. We show that by fine-tuning the structure of the hydrogel, one can effectively control the release rate of a given drug. Although the structure of the hydrogel is important, the initial loading of the drug itself inside the structure is equally critical. Accordingly, we will also use our optimization technique to investigate the placement of drug reservoirs inside the hydrogel.

It is also possible to obtain numerically exact values of the diffusion coefficient for practically any hydrogel structure [14–16]. However, the diffusion coefficient is not always the key factor in predicting the release characteristics of complex systems (*e.g.*, one must also consider the geometry and dimensionality of the hydrogel). For this reason, we use the exact enumeration model mentioned earlier. This numerically exact lattice calculation of the short-time diffusion dynamics of a particle is much quicker to perform than Monte Carlo simulations. This method essentially consists in finding the transfer matrix for any given obstacle configuration and their relative positions as a function of time. Thus, any minor change to either will equate to changing a single row in the transfer matrix and thus can be recomputed fairly easily. This allows one to very quickly perform changes in the initial conditions (e.g., modifying the obstacle pattern) and measure the resulting escape rates. Using a genetic al-

*Electronic address: gary.slater@uOttawa.ca

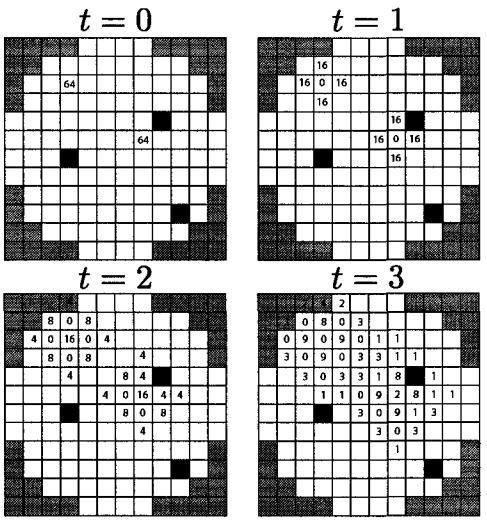

FIG. 1: Time evolution of a typical circular system with particles undergoing diffusion on a 2D square matrix with three obstacles (black). The absorbing boundary is shown in grey (the sides are also part of this boundary). The initial configuration is shown at $t = 0$ with the drug molecules completely localized on two sites.

gorithm as our optimization tool, it is then possible to study several thousand combinations of (evolving) hydrogel structures in order to rank them according to their usefulness in generating desired release rates.

This article is structured as follows: we begin by presenting the theory of the enumeration method followed by examples to test its validity. The optimization technique used throughout this paper is then presented in a systematic way. Finally, we present results obtained using our technique for drug delivery systems with different geometries.

II. ENUMERATION METHODOLOGY

A. Diffusion model

Enumeration methods allow one to obtain exact numerical results for problems related to diffusion, escape rates and transient effects [8]. To illustrate this, let us first examine diffusion on a simple 2D square lattice (figure 1). We compute all possible particle trajectories of a solute, based on its initial location and its probability to diffuse to any first nearest neighbour on the lattice. Figure 1 shows the evolution through 3 time steps of solute diffusion on a typical 2D square lattice with 3 obstacles.

The probability to diffuse in any given Cartesian direction is simply $p_{\pm x} = p_{\pm y} = 1/4$. In an isotropic system, a given solute particle has an equal probability to diffuse (or jump) to any four of the nearest neighbour sites. Time is discrete and all particles must attempt a jump at each time step. A move is simply rejected (*i.e.*, the particle is reflected) if the neighbouring site is occupied by an obstacle. Lattices with higher coordination numbers such as the hexagonal lattice were considered for this model; however they lead to prohibitively long computational times and marginal differences in release profiles.

A uniform probability of jumping is valid as long as there is no drug-hydrogel affinity, external field or other source of anisotropy. For example, in a real system the drug may exhibit affinity for the obstacles. This could be implemented by adding a probability p_o for the particle to stay on the same site when it is next to a "sticky" obstacle.

In the current study, obstacles are completely passive and do not respond to temperature variations or external effects (varying pH, electric fields, etc.). Also, the obstacle density is time-independent, *i.e.*, there are no degradation effects. Such active parameters would require major changes to the method introduced in this article since they generally involve a non-deterministic evolution of the hydrogel matrix.

The general two-dimensional master equation governing the probability of having a drug concentration $C_{x,y}(t)$ on a free site at (x, y) at time t is:

$$\begin{aligned} C_{x,y}(t+1) &= [C_{x-1,y}(t)(1-q_{x-1,y}) + C_{x,y}(t)q_{x+1,y}]\,p_{+x} \\ &+ [C_{x+1,y}(t)(1-q_{x+1,y}) + C_{x,y}(t)q_{x-1,y}]\,p_{-x} \\ &+ [C_{x,y-1}(t)(1-q_{x,y-1}) + C_{x,y}(t)q_{x,y+1}]\,p_{+y} \\ &+ [C_{x,y+1}(t)(1-q_{x,y+1}) + C_{x,y}(t)q_{x,y-1}]\,p_{-y}. \end{aligned} \tag{1}$$

In this equation, $q_{x,y}$ is the site occupation index; its value is 1 if the site at (x, y) is occupied by an obstacle and 0 if not. Note that for a given system, the value of $q_{x,y}$ is fixed for all lattice sites and is simply determined by the structure of the hydrogel. As schematically illustrated in figure 1, the calculation is done iteratively, from an initial drug concentration $C_{x,y}(0)$ for each site on the lattice. Solute particles do not interact with each other.

In order to model drug release from a finite-sized hydrogel system, one simply imposes absorbing boundary conditions $p_{\pm x} = p_{\pm y} = 0$ on the outer boundary of the hydrogel structure. The amount of drug crossing this boundary is the cumulative sum of all those probabilities which have crossed the boundary up to time t.

In this paper we restrict our work to examine simple cases which do not include surface kinetic effects. Nevertheless it is straightforward to tailor the surface properties of our simulated drug delivery system to reflect conditions which may arise from certain hydrogel/solute/environment configurations (e.g., resistance to escape at the boundary, pH or viscosity gradients at the surface of the hydrogel, etc).

If the various local concentrations $C_{x,y}(t)$ (including those in the absorbing layer) are grouped into a column

vector $|C(t)\rangle$ with s elements (one for each lattice site; note that we use Dirac's bra-ket notation), equation 1 can be rewritten as a matrix equation

$$|C(t+1)\rangle = \mathbf{T}|C(t)\rangle. \tag{2}$$

The $s \times s$ Markovian matrix $\mathbf{T}$ (which depends entirely on the positions of the obstacles) transforms the distribution at time t into the one at time $t+1$. This provides a simple computational method to carry out the iterations that are implicit in equation 1 starting from an initial drug load $|C(0)\rangle$. Mathematically, it is possible to use this equation backwards, *i.e.*, start with a given final release rate and calculate the corresponding initial configuration. This unfortunately yields unrealistic parameters (e.g. negative initial concentrations in certain regions) and is not useful in practice.

Using this exact enumeration method, we calculate the associated release rate curves. Our goal is to find an initial capsule configuration (which is defined by the obstacle locations $\mathbf{T}$ *and* drug loading $|C(0)\rangle$) which yields a desired release rate, e.g., a constant release rate for long time periods.

B. Notation

For the sake of clarity, we introduce the notation $\Gamma(t)$ to indicate the total drug released as a function of time:

$$\Gamma(t) = \Gamma_0 - \int_\Omega C(\vec{r}, t) d\Omega \tag{3}$$

where

$$\Gamma_0 = \int_\Omega C(\vec{r}, 0) d\Omega \tag{4}$$

represents the total initial amount of drugs present in a hydrogel. $C(\vec{r}, t)$ describes the drug concentration at position $\vec{r}$ at time t and Ω represents the area (or volume for three-dimensional simulations) of the hydrogel. We can write $\tilde{\Gamma}(t)$ as the normalized cumulative amount of drugs released at time t

$$\tilde{\Gamma}(t) = \frac{\Gamma(t)}{\Gamma_0}. \tag{5}$$

We can define an asymptotic release amount $\Gamma(\infty)$ (it is equal to the Γ_0 if no drug particle is trapped inside the hydrogel). Also, we introduce the parameter τ_ϕ which we define as the time at which a certain fraction, ϕ, of drugs has been released from the system

$$\phi = \frac{\Gamma(\tau_\phi)}{\Gamma_0}. \tag{6}$$

Finally, the rate of drug release is measured by the derivative

$$\dot{\Gamma} = \frac{\partial \Gamma}{\partial t}. \tag{7}$$

C. Fully-loaded gels: Empirical fits

A fully loaded gel is defined as having an equal concentration of solute on every non-obstacle site; drug is said to be *fully-loaded* in the hydrogel matrix. There is no lag time (*i.e.*, time lapse between the beginning of the enumeration and the arrival of the effective drug concentration *wavefront* at the boundary) in this scheme since there is a drug concentration near the boundary which escapes the hydrogel at $t = 1$. We later show that optimization of the hydrogel matrix can be related to this lag time and that schemes involving drug reservoirs that are non-adjacent to the boundary can be of crucial importance when searching for a constant rate of release.

We can simulate such a fully-loaded hydrogel and compare our numerical data with two widely-used empirical fits. According to Peppas [17], a simple power-law relationship can describe the time dependence of drug release until 60% of the initial load has been released:

$$\tilde{\Gamma}(t) = \left(\frac{t}{t_\alpha}\right)^\alpha \tag{8}$$

where α is the release exponent, and the resulting time scale t_α can then be compared to t_β for short times ($\tilde{\Gamma} \ll 1$). Since the Peppas equation is not bounded as $t \to \infty$ it cannot be used to model the escape at long times.

According to a more general statistical theory, the Weibull model predicts that the release rate behaves like a stretched exponential [18]:

$$\tilde{\Gamma}(t) = 1 - \exp\left[-\left(\frac{t}{t_\beta}\right)^\beta\right]. \tag{9}$$

The parameters are now the exponent, β and the time scale t_0. A series expansion of the Weibull function yields the Peppas law to first order and thus it is expected that $\beta \to \alpha$ as $t \to 0$. However, both these empirical fits suffer from an apparent lack of physical meaning associated with the free parameters.

D. Exact solution for a test system

It is possible to solve the 2D diffusion equation in polar coordinates for $C(r, t)$ to obtain a predicted release curve from a round hydrogel with radius r_0 [19] and uniform drug concentration. In this case, we simply replace the obstacles inside the capsule by an effective viscosity (or, more precisely, by an effective diffusion coefficient D^*) which models the retarded diffusive motion of the particles. Since the distribution of obstacles is assumed to be isotropic, D^* is simply a fitting parameter.

We study here a circular drug capsule with an isotropic obstacle distribution with a concentration well bellow the percolation threshold, C^*_{obst} ($C^*_{\text{obst}} \simeq 0.408$ for a 200×200 square lattice [20]). The capsule is said to be fully

TABLE I: The first four λ values and the corresponding $C_n(r_0)$ coefficients used in the diffusion equation with $r_0 = 1$.

n	λ_n	$C_n(r_0)$
1	2.4048	1.6020
2	5.5201	-1.0648
3	8.6537	0.8514
4	11.7915	-0.7296

loaded (*i.e.*, an equal drug concentration occupies every non-obstacle site. The $2D$ diffusion equation in polar coordinates can be written as

$$\frac{\partial C(r,t)}{\partial t} = D^* \left(\frac{\partial^2}{\partial r^2} + \frac{1}{r}\frac{\partial}{\partial r} \right) C(r,t) \qquad (10)$$

with boundary conditions

$$C(r,0) = \mathcal{H}(r - r_0)C_0 \qquad (11a)$$

$$C(r_0,t) = 0, \qquad (11b)$$

where $\mathcal{H}$ is the Heaviside function, and C_0 is the initial drug concentration of the free sites inside the capsule. Equation 11b accounts for the absorbing boundary. The solution to equation 10 is given by the following:

$$C(r',t) = \sum_{n=1}^{\infty} C_n(r_0) J_0(\lambda_n r') \exp\left[-D^* \left(\frac{\lambda_n}{r_0} \right)^2 t \right] \qquad (12)$$

where J_0 is the 0^{th} order Bessel function of the first kind, λ_n represents the n^{th} zero of $J_0(r)$, $r' = r/r_0$ is a scaled radial position, and the coefficients, $C_n(r_0)$, are given by:

$$C_n(r_0) = \frac{2C_0}{J_1^2(\lambda_n)} \int_0^1 \mathcal{H}(r - r_0) J_0(\lambda_n r') r' \, \mathrm{d}r'. \qquad (13)$$

Table I shows the first four $C_n(r_0)$ coefficients in the series solution to the diffusion equation. In the next two sections, we will compare our exact enumeration results to the Peppas and Weibull empirical fits as well as to this exact solution based on the existence of an effective diffusion coefficient D^* for the given system.

E. Round capsule with a periodic gel

We begin by constructing a simple periodic gel in order to compare our exact numerical results with empirical predictions and analytic results described in the previous section. We use a round 2D capsule constructed inside a 200×200 square lattice with a periodic obstacle distribution of concentration $\mathcal{C}_{\text{obst}} = 1/9$ (see figure 2). The drug was loaded uniformly inside the matrix (i.e., the initial drug concentration was normalized at $C_0 = \Gamma_0/s$ for all sites that are not occupied by an obstacle, where s is the number of such sites). We calculate the time evolution

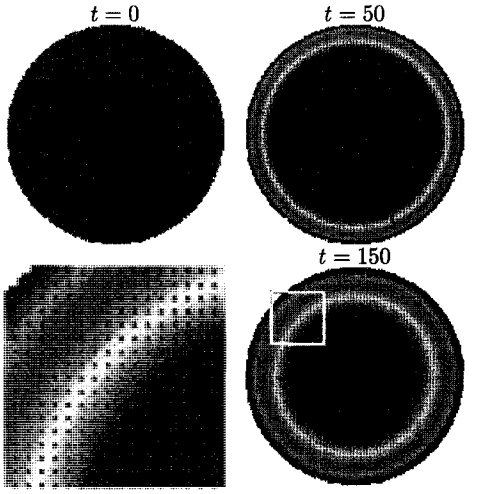

FIG. 2: Time evolution of the drug concentration inside a round drug capsule ($r_0 = 100$) with a periodic obstacle distribution ($\mathcal{C}_{\text{obst}} = 1/9$). Shown is the drug concentration from low to high concentrations (denoted by colours ranging from blue to red, respectively). The concentration of drug is uniform inside the capsule at $t = 0$. The bottom left figure is a blow up of the indicated section in the $t = 150$ figure.

of the population of non-interacting particles using equation 1 where t is given by the iteration step count, an integer.

We need to know the diffusion coefficient in order to compare our results to the analytical function. It is possible to fit the curve in order to extract the coefficient; however, there is a better way. The diffusion of a solute through an infinite lattice has been extensively studied by our group using another exact numerical approach [14–16]. Using that technique, the scaled diffusivity for a particle in a periodic 2D square lattice of concentration $\mathcal{C}_{\text{obst}}$ was found to be given by:

$$D^* \simeq \frac{1 - \pi\mathcal{C}_{\text{obst}} + \frac{\pi^2}{2}\mathcal{C}_{\text{obst}}^2 + \cdots}{1 - \mathcal{C}_{\text{obst}}}. \qquad (14)$$

This value for D^* is then used to calculate the release profile obtained by solving equation 10.

Figure 3 shows a plot of the release profile as a function of time as well as the three fits mentioned in the previous sections. The inset shows another view of the same data. The Weibull fit is in good agreement with our release profile up to $\tilde{\Gamma}(t) \simeq 0.9$ and the Peppas fit is valid up to $\tilde{\Gamma}(t) \simeq 0.65$. The values obtained for the fitting exponents α and β are consistent with findings made by Papadopoulou *et al.* [21] for Fickian diffusion. The value of $D^* = 0.8008$, as obtained from equation 14 for $\mathcal{C}_{\text{obst}} = 1/9$, is used to plot equation 12 in figure 3. The analytical solution is in remarkable agreement with

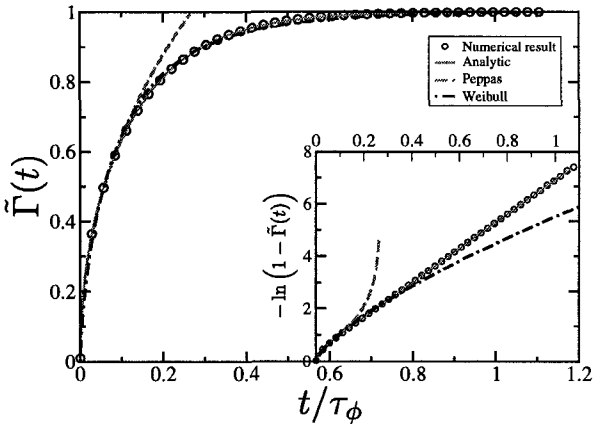

FIG. 3: Total drug release as a function of time for a round drug capsule of radius $r_0 = 100$ (see figure 2) with a periodic obstacle concentration $\mathcal{C}_{\text{obst}} = 1/9$. The parameters of the different fits are (see text for definitions): Peppas, $t_\alpha/\tau_\phi = 0.25$, $\alpha = 0.46$; Weibull, $t_\beta/\tau_\phi = 0.1$, $\beta = 0.72$, $\Gamma(\infty) = \Gamma_0$ here since there are no traps; analytic, $C_0 = 1.0$, $D^* = 0.8008$, 5 terms in the series. The value for τ_ϕ was computed using $\phi = 0.999$ and was used to transform the data from both the enumeration and the analytic solution. The curves were then fitted on this transformed graph. The inset shows very good agreement of our data with the analytical solution by using a $-\ln\left(1-\tilde{\Gamma}(t)\right)$ y-axis transformation.

our exact numerical results for the release rate. This indicates that periodic obstacles can indeed be replaced by a constant viscosity within the hydrogel.

This example is used as a benchmark to properly gauge the accuracy of our model. At first glance these empirical laws seem to limit our control of the release rate. However, it is important to keep in mind that they are based on idealized conditions (uniform distribution of drug and obstacles, etc.) and thus it is possible to change these characteristics and manipulate the diffusion process. In section III, we present a method for obtaining release profiles that are different from these *standard* release curves in order to systematically control the drug release.

F. Round capsule with a random gel

The characteristics of drug release are strongly influenced by the behaviour of drugs which linger inside the hydrogel (e.g., slowly decaying tail on the drug release curves for long times). This behaviour is affected by the obstacle configuration and density. We study the effects of altering the obstacle properties using a round capsule constructed inside a 200×200 square. The obstacles are now placed randomly inside the round matrix and the drug is distributed uniformly on the remaining empty sites. The release curves are shown in figure 4 for varying obstacle concentrations. The solid lines correspond to solutions of equation 10. Again, we can obtain the scaled diffusivity from Mercier *et al.* [14–16] for 2D square lattices with randomly placed obstacles with concentration below percolation:

$$D^* \simeq 1 - (\pi - 1)\,\mathcal{C}_{\text{obst}} - 0.8558\mathcal{C}_{\text{obst}}^2 + \ldots. \qquad (15)$$

The resulting curves are in remarkable agreement with our enumeration results in the limit of low obstacle concentrations, $\mathcal{C}_{\text{obst}} \lesssim 20\%$.

Due to the finite sizes of our hydrogels, the drug molecules will undergo anomalous diffusion for a certain portion of the release profile (except at $\mathcal{C}_{\text{obst}} = 0$) before making a transition to normal diffusion. This is a well documented phenomenon and corresponds to a transition from anomalous diffusion to normal (or Fickian) diffusion which occurs after the molecules have travelled a certain cross-over length (or time) [8, 17, 22–25]. This cross-over length becomes larger as $\mathcal{C}_{\text{obst}}$ is increased until it is on the order of the size of our system. At this point, anomalous diffusion is observed for all times in our enumerations. Drug escapes from connected and tortuous pathways with a large number of *dead ends* altering the shape of the release profile [26]. In the normal regime, diffusion is characterized by the random motion of particles in space. The total release profile is a sum of exponentials for the whole duration of the release profile (as seen in section II D and II E).

There is also an increasing percentage of drugs which remain trapped inside the hydrogel as the obstacle concentration is increased. This is seen on figure 4 for release curves from hydrogels of $\mathcal{C}_{\text{obst}} \geq \mathcal{C}^*_{\text{obst}}$. These profiles attain a plateau value which is not equal to unity. We have access to the exact number of trapped particles during an enumeration and we can set the value of Γ_0 to be $\Gamma(\infty)$ for use in the analytical fit. As seen, the analytical theory breaks down in the near percolation limit. It is also interesting to note that the drug release rate can also be higher than anticipated. This can be seen on the release profile associated with an obstacle concentration $\mathcal{C}_{\text{obst}} = 0.35$ where the initial release occurs at a faster rate than shown by its associated analytical fit. This is due to the creation of small drug "reservoirs" near the outer surface of the hydrogel which contributes an outward biasing effect.

This transition has direct implications in controlling the pharmacokinetic release profile. These results suggest that high obstacle concentrations may favour slow, more constant release rate and that linear release could occur in a specific case of a power law regime (*i.e.*, case II transport [27]) of anomalous diffusion. In search of such a constant drug release profile, we will study the effects of systematically varying obstacle concentations as a function of position. We will also compare drug release profiles from hydrogels with drug loaded uniformly versus hydrogels with discrete drug reservoirs. This will be

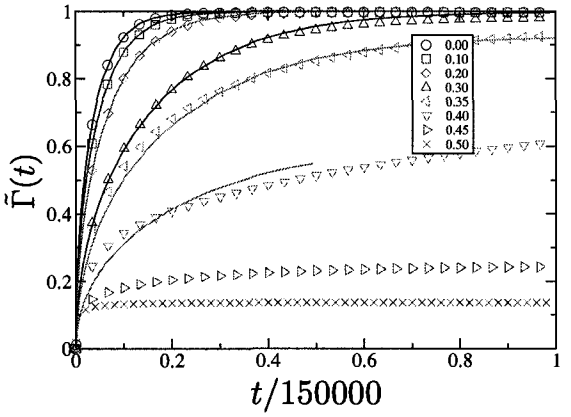

FIG. 4: Pharmacokinetic release profiles from circular random hydrogels with obstacle concentrations $\mathcal{C}_{\text{obst}}$ (shown in legend) with radius of $r_0 = 100$. There is a clear change in $\tilde{\Gamma}(t)$ as $\mathcal{C}_{\text{obst}}$ is increased. For the cases of $\mathcal{C}_{\text{obst}} = 0.35, 0.40$, $\Gamma(\infty)/\Gamma_0$ were estimated to be 0.927 and 0.612 respectively by calculating the average amount of trapped particles. The solid lines are solutions to equation 10 with values of D^* obtained from equation 15 for shown obstacle concentrations and using $\Gamma(\infty)$ as the value of the initial load.

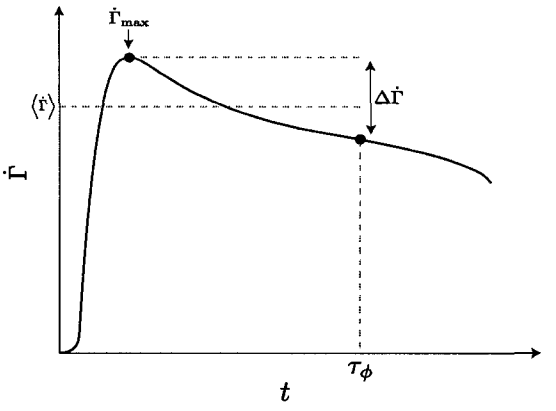

FIG. 5: Schematic illustration showing the parameters used to calculate the fitness parameter, $\mathcal{F}$, in equation 16. This is an idealized drug release rate profile as a function of time, $\dot{\Gamma}(t)$.

shown in section IV.

III. GENETIC OPTIMIZATION METHODOLOGY

A. Gel Structure

Determining optimal obstacle density and placement is a daunting task considering the large number of degrees of freedom, therefore we limit ourselves to the simplest experimental case and search for structures which may be tested in the laboratory. Should any symmetry or pattern be observed in the course of our optimization such as *onion* structures (*i.e.*, rings of varying obstacle densities), layers, or reservoirs we will use it to our advantage. Note that since we use a discretized version of the physical system and work on a 2D lattice, there is a finite number of spatial locations for the obstacles and solute particles. Finally, we restrict our examination to the low density drug limit where drug-drug interactions are negligible. In fact, there does not seem to be a significant change in the drug release profile from noninteracting particles compared to particles with hard-core excluded volume interactions [10].

B. Fitness parameter

Finding a *good* fitness parameter is a critical factor for any optimization process. Our algorithm needs to identify the hydrogel/drug configurations which produce a targeted release profile using a simple quantitative test. Since we are aiming to produce constant release rates (over specified time intervals) we compute the following fitness parameter (see figure 5 for schematic illustration),

$$\mathcal{F} = (1-\gamma)\Delta\dot{\Gamma} - \gamma\left\langle\dot{\Gamma}\right\rangle \ . \tag{16}$$

In this equation, $\Delta\dot{\Gamma} = \dot{\Gamma}_{\max} - \dot{\Gamma}(\tau_\phi)$ is the maximum value of the rate of drug release from our simulated hydrogel minus the value of the release rate at some upper time τ_ϕ (smaller values of $\Delta\dot{\Gamma}$ indicate a more constant rate of release over that period of time). $\left\langle\dot{\Gamma}\right\rangle$ is the average rate of release during this time interval. This fitness parameter thus measures the linearity of the drug release by minimizing the slope of the rate of release curve starting from its maximal peak value while increasing the average rate. The value γ is an adjustment parameter which favours either minimizing the slope or maximizing the mean release rate. Adjusting this rate permits the creation of interesting hydrogel structures which are not shown in this article (*i.e.*, γ is set to 0 except for section IV C where it is set to 0.9).

It is important to note that an inherent lag time often exists at the beginning of the release process which must be neglected in order to obtain our fit. This lag time is a transient effect due to the arrival of the effective drug *wave front* and it is related to the geometry of the system [28]. This explains why we strictly look at the

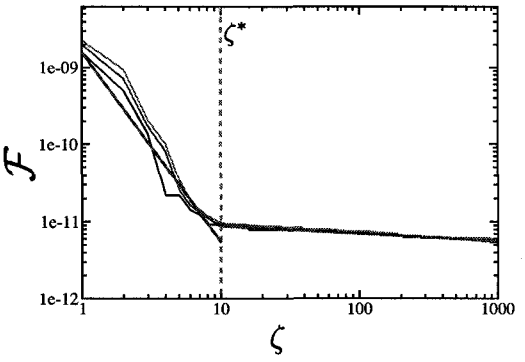

FIG. 6: Profiles of the fitness parameter, $\mathcal{F}$, as a function of generation number, ζ, for the three best candidates during a genetic algorithm optimization. We use the system discussed in section IV B for this demonstration although the general behaviour is similar for any system. The power law fits for the two regions are shown in grey and ζ^* in dashed grey. This type of data is a useful guide to gauge the required number of generations needed to attain sufficient convergence.

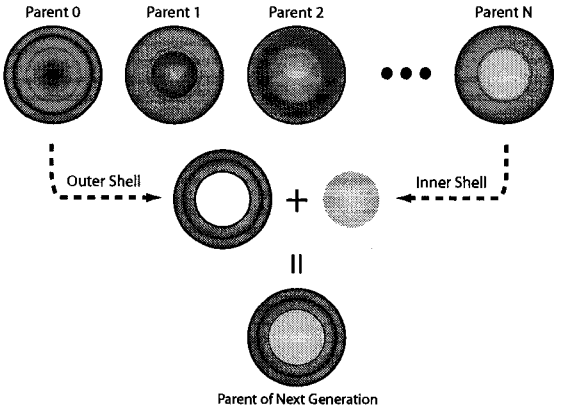

FIG. 7: Schematic illustration of a two ring cross-over from two randomly selected *good* parents to form an offspring in the next generation. The darker regions indicate higher concentrations of obstacles.

"post-peak" release process.

Our algorithm begins by initializing our first generation and calculating the fitness parameter, $\mathcal{F}$, for each individual. Each generation is built using genetic characteristics from the best parents of the previous generation following the rules of the algorithm outlined in section III C. In principle, it is possible to select an appropriate fitness parameter in order to achieve any desired functional form for the release profile, $\Gamma(t)$.

As an example consider a circular random hydrogel constructed inside a 100×100 square matrix. Fitness parameter data were obtained from the simulation perfomed in section IV B. Further details on the specifics used to implement the genetic algorithm are given therein. This system serves as our typical example here. Figure 6 shows that our fitness parameter converges with increasing numbers of generations. The fitness parameter, $\mathcal{F}$, is shown as a function of the generation number (ζ) for the three best candidates. In this example, the fitness parameter decreases sharply as a function of ζ until a cutoff generation $\zeta^* \simeq 10$. This has an important significance when determining the optimal number of generations needed to equilibrate each system. The fitness parameter decreases roughly as a power law for the region $\zeta < 10$ region: $\mathcal{F} \simeq 1.6 \times 10^{-9}\zeta^{-2.5}$. For $\zeta \geq 10$, the fitness parameter approximately behaves like: $\mathcal{F} \simeq 1.2 \times 10^{-11}\zeta^{-0.1}$ (shown in grey on the figure). This system has minimized the value of the fitness parameter very quickly at low values of ζ^*. Other systems usually follow a similar trend although they generally have higher values for ζ^*.

Figure 6 also illustrates the *learning* mechanism of the algorithm. It shows various instances where a candidate acquires a favourable trait (*i.e.*, sudden drop in effective fitness parameter) and passes those genetic characteristics to all others within a few generations.

C. Optimizing the initial obstacle distribution

We study the effects of "intelligently" placed obstacles and drug reservoirs using an extended Compact Genetic Algorithm (eCGA)[29]. Genetic algorithms are able to quickly scan a large portion of phase space (*i.e.*, the space of obstacle and drug placement locations) and thus efficiently find a minimum. They are a class of optimization algorithms which progress by acquiring successful traits from previous generations in order to quickly converge to a solution. In our case, an ensemble of drug capsules is first initialized based on a given basic design (e.g., an onion-like layering or chessboard pattern). Each drug capsule is then assigned a fitness parameter, $\mathcal{F}$ (see section III B for details). This parameter allows one to rank the capsules according to their ability to produce the desired output (e.g., a constant rate of escape). The entire ensemble (first generation) is then analyzed and ranked according to the fitness parameter. Once the best hydrogels are found, usually 10% are kept for the next generation (elitism) and a new generation of offspring is created using specific characteristics inherited from these "parents".

We use three genetic mechanisms to construct our subsequent generations (there are many more genetic mechanisms but these will suffice for our proof of principle study). First, using a *crossover* technique, we take the configuration of a predetermined section (e.g., ring-like structure) of a randomly selected parent and couple this

with various other (ring-like) sections from other randomly selected parents. We combine these traits to generate the next generation (figure 7 illustrates such a crossover for a circular drug capsule comprised of two rings). The second technique involves another type of crossover where a mother and a father each donate randomly selected parts of their configurations in a chessboard pattern to form unique offsprings. The former technique is useful for configurations that exhibit angular symmetry and the latter for those with Cartesian symmetry.

Thirdly, once a generation is formed, a certain percentage of mutations are introduced in these offsprings. There are three possible types of mutation. The algorithm randomly changes an obstacle for a void, it can create an obstacle from a void and it can also change the location of an obstacle (the relative probability for the mutation to be of one type is: 25%, 25%, and 50%, respectively). These mutations lead to a more thorough "scanning" of the phase-space by introducing configurations that may not be obtained through simple genetic recombinations.

The resulting offsprings are then ranked according to our fitness test and the entire process is repeated until a satisfactory candidate is found. As a caveat, note that although genetic algorithms are very efficient at locating local minima in phase space there is no way to tell if we have reached the global minimum. In our simulations, we try to minimize the chance of being trapped in a local minimum by using a large number of generations and a relatively large percentage of mutations ($\geqslant 2\%$ per generation).

D. Optimizing the initial drug reservoir position

The position and number of drug reservoir(s) may also need to be optimized in order to achieve our desired release rates. For example, in section IV C, the drug matrix is divided into a chessboard pattern, some sections of the capsule would then be given a probability of being a drug reservoir. The algorithm is free to optimally alter the number and placement of drug reservoirs within the matrix.

E. Computational details

Most of the computational work was performed on 15 dual-core UltraSPARC IV+ processors with 576GB of shared memory (`www.hpcvl.org`). Each simulation is executed over an average of 12 hours (depending on the size of the matrix, the total Monte Carlo *time* required to obtain sufficient drug release, and the number of generations). Individual analysis and smaller simulations not requiring combinatorial optimization is performed on a 3.2 GHz P4 processor with 2GB of memory.

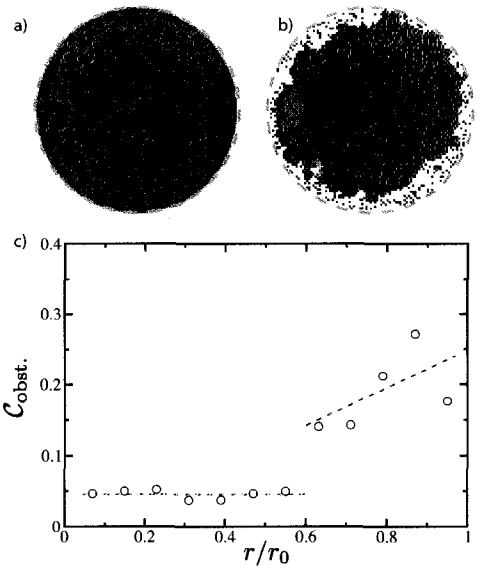

FIG. 8: a) Optimal initial ($t = 0$) hydrogel configuration of a $r_0 = 50$ capsule; obstacles are in black. The dashed grey line represents the outer boundary of the hydrogel. b) Retarding effect of the high obstacle concentration on the diffusion at $t = 1000$. There is also a very interesting visible feature – namely the formation of an obstacle barrier near the outer boundary of the hydrogel. The associated radial obstacle concentration profile is also shown in c). The hydrogel has been separated into two distinct regions. The first region $0 < r < 0.6r_0$ has a very low obstacle concentration of $\mathcal{C}_{\text{obst}} \simeq 0.05$ and the second region has an increasing obstacle concentration.

IV. RESULTS

A. Spherical geometry with continuous drug distribution

The genetic algorithm is initially applied to a fully loaded circular random hydrogel constructed inside a 100×100 square lattice with radius $r_0 = 50$. The optimization is performed on the release profile from the moment that $\Gamma(t)$ reaches its maximal value (this occurs at $t = 1$ since the hydrogel is fully loaded and there is no lag time in the drug release) until $\phi = 0.50$ and the adjustment parameter, γ, is set to 0. There are 1000 genetic generations and each generation is composed of 300 specimen.

Each hydrogel capsule is divided into 5 rings of equal thickness. The genetic algorithm creates new capsules using rings from 5 fit parents in the previous generation and randomly combines them as discussed earlier. Once a new hydrogel is created, mutations are introduced on 2% of the sites using the previously discussed mutation scheme.

The obstacle configuration of the optimized hydrogel can be seen on figure 8a. The associated obstacle concentration as a function of radial position, r, can be seen in 8c. By carefully observing figures 8a and 8b, one can notice the formation of a solid obstacle boundary at $r \simeq 45$ except for one small hole visible in the third quadrant of the circle. This boundary was created by the genetic algorithm in order to curtail the initial large release rate due to the bulk of the drugs' location near the surface of the hydrogel. The hydrogel has been divided into two sections with different obstacle concentrations: $\mathcal{C}_{\text{obst}} = 0.05$ in the first region while the second region has an increasing obstacle concentration. On average for the whole capsule, $\mathcal{C}_{\text{obst}} = 0.10$. Another feature of interest is that the centre of the hydrogel was chosen to contain very little obstacles (conversely, a large drug concentration). This would seem to minimize the overall impact of the initial release rate peak associated with the high drug concentration near the outer boundary of the hydrogel by locating the bulk of the drug in the centre. The ideal hydrogel seems to be one which tends to push the solid boundary of obstacles closer to the surface of the hydrogel. By systematically increasing the value of ζ (the number of generations), one can see that this solid boundary is pushed towards the outer boundary (not shown).

Figure 9 shows the cumulative release as a function of time for our optimized hydrogel (solid line) as well as a comparison with a hydrogel of uniform obstacle concentration $\mathcal{C}_{\text{obst}} = 0.10$ (dashed line). Since the hydrogel is initially fully loaded, drugs begin escaping the hydrogel as early as $t = 1$. This explains the steep initial slope observed for both hydrogels. However, once the drugs outside the bounded area observed in figure 8b have escaped, $\Gamma(t)$ in nearly lineary until $\phi \simeq 0.50$. The associated fitness parameters for the optimized hydrogel as well as for the hydrogel with uniform $\mathcal{C}_{\text{obst}}$ are $\mathcal{F} = -3.6 \times 10^{-7}$ and -6.8×10^{-7}, respectively.

The circular geometry discussed in this section is a good demonstration of the usefulness of our genetic algorithm in optimizing drug release profiles. The genetic algorithm is able to find an optimized structure which produces a remarkably constant rate of release. The genetic algorithm yields very interesting results. The creation of the obstacle barrier seems to be a key component in controlling the release profile. This single hole membrane model has been extensively used in the past to control drug delivery [30]. It is quite interesting to note that the genetic algorithm was able to form a similar structure with no prior assumptions. The optimization appears to eliminate drugs from the boundary at the same time as creating this barrier. It would be logical to further test these hypotheses.

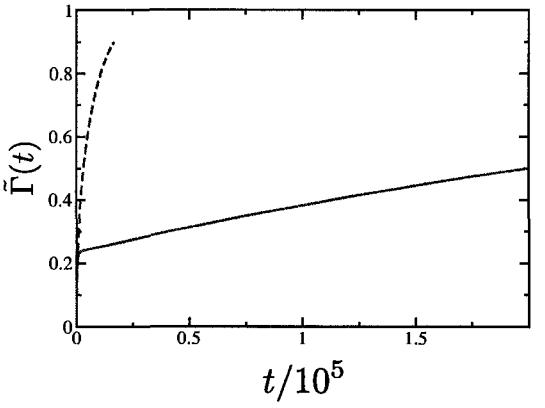

FIG. 9: Pharmacokinetic profiles of cumulative drug release as a function of time for the drug capsule shown in figure 8. This enumeration is performed until $\phi = 0.5$. There are 1000 genetic generations and each generation includes 300 specimen with a mutation percentage of 2%. The release is also compared to a control hydrogel with a uniform obstacle distribution equal to the average value of our optimized structure, $\mathcal{C}_{\text{obst}} = 0.10$ (dashed line). The optimized release profile has two distinct regions. A quick initial release of drugs near the outer boundary followed by a linear release of drugs enclosed within the created obstacle boundary (porous membrane).

B. Spherical geometry with central reservoir

We re-examine the drug capsule geometry used in the previous section. However, the drug will now be initialized in a single central reservoir of radius $r = 10$. The single reservoir will curtail the effects of the strong initial drug release rate observed previously. The round capsule is constructed inside a 100×100 square with drugs evenly distributed in the reservoir. For the first generation, we initialize the drug capsule with 5 rings. Each ring has a width of 10 matrix sites with randomly chosen obstacle concentrations $\mathcal{C}_{\text{obst}}$ (each below the 2D percolation threshold). Our genetic algorithm is then applied.

There are a total of 1000 generations each one of which is composed of 300 specimen. Each specimen is simulated for a maximum of 200000 time steps. Each generation is constructed using the first genetic technique discussed in section III C using a simple five ring swap (*i.e.*, five chromosomes involved in the genetic optimization step) between five parents. Mutations are introduced after the crossover at a rate of 2%.

The genetic algorithm is programmed to find the configuration of obstacles which would produce the most constant release rate in a specified range of drug release (from $\dot{\Gamma}_{\max}$ up to $\phi = 0.50$ and $\gamma = 0$ here as well). The upper bound, $\phi = 0.50$ was chosen to be sufficiently high to control the bulk of the release profile without worrying about the tailing effect.

The resulting optimal configuration is shown in figure 10a. Figure 10b shows the concentration of drugs in the hydrogel at $t = 5000$. The obstacle concentration profile has been divided into two sections (see figure 10c).

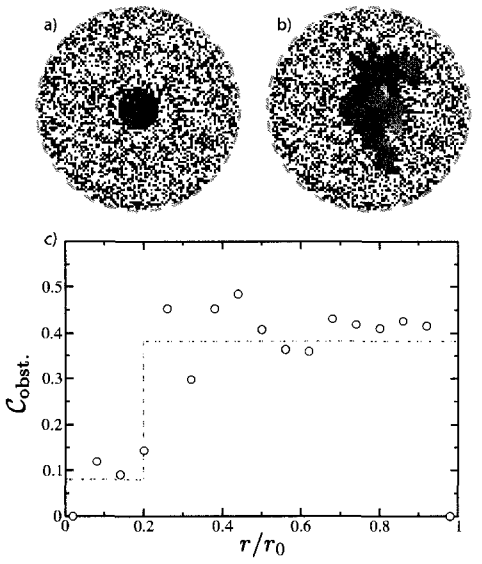

FIG. 10: a) Optimal hydrogel configuration of a $r_0 = 50$ capsule (drug reservoir in red), obstacles in black and free space in white. The dashed grey line represents the outer boundary of the hydrogel. b) Shows the retarding effect of the obstacles on the diffusion at $t = 5000$. The associated obstacle concentration profile is also shown in c). The average obstacle concentration is indicated for two regions of the hydrogel. The reservoir with a width of 10 matrix sites has $\mathcal{C}_{\text{obst}} = 0.08$ whereas the rest of the hydrogel is fairly uniform with $\mathcal{C}_{\text{obst}} = 0.38$. The overall obstacle concentration is $\mathcal{C}_{\text{obst}} = 0.32$.

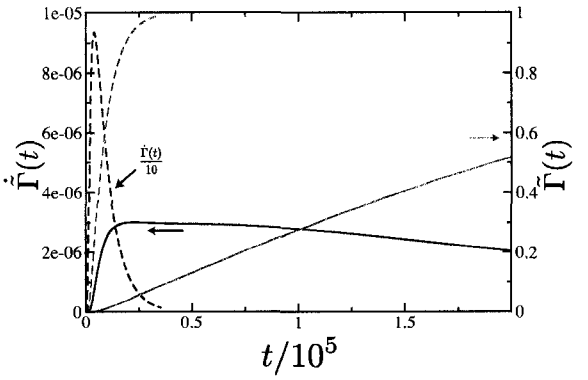

FIG. 11: Pharmacokinetic profiles of release rate, $\dot{\Gamma}(t)$, in red and total amount of released drugs as a function of time in black for the drug capsule shown in figure 10. This enumeration is performed until $\phi = 0.50$. There are 1000 genetic generations and each generation includes 300 specimens with a mutation percentage of 2%. The total release is also compared to a control hydrogel with isotropic obstacle distribution, $\mathcal{C}_{\text{obst}} = 0.32$ (dashed line). The curve obtained from the comparison hydrogel was divided by 10.

The first section has a very low obstacle concentration of $\mathcal{C}_{\text{obst}} = 0.08$ since it includes the drug reservoir (obstacles are allowed to enter the reservoir during genetic mutations). The second section has an average obstacle concentration of $\mathcal{C}_{\text{obst}} = 0.38$ nearly at the percolation threshold. This section is suspected to be mainly responsible for having altered the shape of our release curve through the creation of this slow leaking membrane, for example. The overall obstacle concentration is $\mathcal{C}_{\text{obst}} = 0.32$. At least one ring with very high obstacle density has been observed in all specimens with this geometry and would appear to be a necessity to achieve controlled release rates.

Figure 11 shows the escape rate and the cummulative amount of drug released as a function of time. The dashed line shows a comparison of our optimized results with a hydrogel of uniform obstacle concentration $\mathcal{C}_{\text{obst}} = 0.32$ equal to the average obstacle concentration of our optimal structure (the rate curve was divided by 10 in order to compare its shape). The comparison hydrogel also has a central drug resevoir of radius $r_0 = 10$.

The release profile has been improved in terms of linearity from the one observed in our standard (dashed line). It is possible to quantify this by looking at the fitness parameters. Our standard has a fitness parameter $\mathcal{F} = -2.9 \times 10^{-9}$. However, our optimal structure produces a much more constant release rate with $\mathcal{F} = -5.4 \times 10^{-12}$. This optimization can be seen on the release rate curves (black). The optimized hydrogel shows a more constant release rate since the initial peak is less pronounced and the decay is much slower than the release rate from the standard.

It is quite remarkable that we are able to significantly alter the pharmacokinetic release profile by simply reorganizing the obstacle distribution around a central drug reservoir. This could lead to the development of spherical hydrogel matrices which produce a controlled drug release rate.

C. Planar geometry with optimized reservoir distribution

We now examine a rectangular drug capsule which can be representative of a transdermal drug delivery system [31, 32]. The 2D system presented here can be seen as a cross-sectional slice of such a system. This transdermal-type hydrogel allows us to use periodic boundary conditions: where drug particles leaving the system to the right are re-introduced on the left and vice versa. The unit cell of our periodic matrix measures 100×100 lattice sites and is now divided into grids measuring 10×10 sites. Each grid is initially given an obstacle concentra-

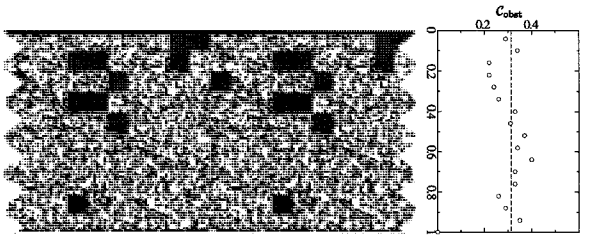

FIG. 12: Optimal drug delivery configuration of a 100×100 capsule with drug reservoirs in red, obstacles in black, and free space in white. Each drug reservoir is numbered and its contribution to the total release is shown on figure 13. There is a solid layer of obstacles on the top and bottom boundaries except for holes from which drugs can escape on the bottom. The obstacle concentration is shown to be quite constant inside the matrix ($C_{\text{obst}} \simeq 0.32$).

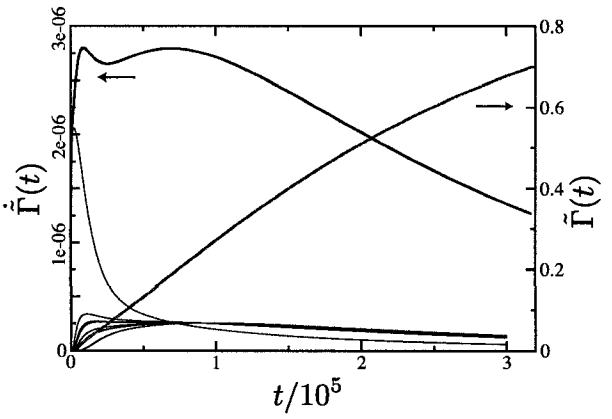

FIG. 13: Pharmacokinetic profiles of release rate (black) and total released drugs (solid red) as a function of time for the drug capsule shown in figure 12. This simulation ran for 3.3×10^5 time steps. There were 500 genetic generations and each generation comprised of 300 specimen. The genetic algorithm optimized the release profile up to $\phi = 0.5$. The contribution to the release rate by individual reservoirs is also shown in gray.

tion. We also allow the algorithm to choose the position and number of drug reservoir(s) in order to better control the drug release. The algorithm has a 20% chance of transforming a 10×10 obstacle grid into a drug reservoir during the initial creation of the hydrogel, $\zeta = 1$. These grids are now the chromosomes to be used by the eCGA.

We have incorporated the general trends observed in the previous sections directly into the initial conditions of our hydrogel in order to augment the efficiency of our optimization algorithm. In an attempt to reproduce the high obstacle concentration near the exit boundary, the lower boundary has been blocked with obstacles with the exception of 10 periodically-placed holes in the unit cell. Note that during genetic mutations, these holes are free to *move* or become blocked. The eCGA can now concentrate on finding optimal obstacle structures without having to invest reorganizing steps to form the previously observed high density layer of obstacles near the boundary.

This scheme allows for the optimization of both the obstacles and the placement of the drug reservoirs. The grid pattern allows for a greater number of chromosomes used in the optimization compared to the previous section. The eCGA also uses all three genetic recombination techniques discussed in section III C. Each capsule is allowed to diffuse for 2×10^5 time steps. There are 500 generations, each with 300 specimens and a mutation rate of 2%. The genetic algorithm optimizes the release profile up to $\phi = 0.5$ and here $\gamma = 0.9$.

The optimized hydrogel slice can be seen in figure 12. The unit cell is periodically repeated on both sides for illustrative purposes. It exhibits a number of interesting features. The obstacle concentration is fairly constant and near percolation throughout the drug matrix ($C_{\text{obst}} \simeq 0.32$). Remarkably, the eCGA has obstructed all of the holes on the boundary line (shown in green) except for two which were left open for drug release. Also, the density of drug reservoirs at each grid layer is increasing as the distance from the boundary increases.

Pharmacokinetic results obtained from this matrix are shown in figure 13. The drug release rate is rather linear for the range where 5% and 60% of the drug has escaped. Controlled release has therefore been obtained by adjusting the placement of obstacles and the initial position of drug.

Since our drug particles are non-interacting, we are able to perform the simulation one reservoir at a time. This allows us to investigate the contribution to the total release from each reservoir. Figure 13 shows the contribution of each reservoir to the total release curve (solid grey). The total release due to all the reservoirs is shown as the thick black curve. The total release rate from this matrix (solid red).

These results are quite remarkable and testify to the power of this combinatorial approach. It is clear that controlled release can be achieved using our method and that it is a matter of carefully organizing the drug matrix itself. The algorithm finds a simple structure which consists of a concentration of obstacles near percolation and a carefully placed drug pyramid-like drug placement which yields a constant release rate. A similar structure could be implemented experimentally (at least qualitatively) to serve as the basis for a constant release drug platform.

V. CONCLUSION

In this article we propose an exact enumeration model for drug diffusion which produces results that are in agreement with empirical fits and analytical data. Using this model, we can optimize the initial conditions of a given drug matrix in order to control the rate of drug release using a genetic algorithm. We use a linear regression fitting parameter in order to rank drug matrices according to their ability to produce our desired rate of release.

Each structure studied allowed us to gain valuable information pertaining to the pharmacokinetic behaviour of the release profile. We first showed that it is possible to favorably alter the release profile for the simple case of a round drug matrix with a central drug reservoir.

We can also control the release rate by using a rectangular transdermal-type drug matrix with horizontal periodic conditions. It is possible to control drug release by letting the eCGA optimize the location and number of drug reservoirs. The resulting matrix from this eCGA optimization was then used to show that it is possible to re-create a constant rate of drug release by removing degrees of freedom from the system (*i.e.*, the position and number of drug reservoirs). This allowed us to show the general characteristics drug matrices should have in order to produce a controlled rate of release.

To summarize we have demonstrated using a *proof of principle* study that we can systematically study the effects of drug matrix geometry on the behaviour of drug release. By beginning with a simple geometry with no immediately apparent structure and progressively removing degrees of freedom from the system we were able to control the rate of drug release from our capsules. In particular we have shown that we can obtain an increasingly linear release rate in a reproducible manner with particular geometries that can provide impetus for the design of future drug delivery systems. The new optimization method introduced in this article can in principle be used for a wide range of drug delivery challenges.

Acknowledgments

The authors would like to thank M. Bertrand, E. C. J Oliver, and F. Tessier for useful discussions. Computational analysis was supported by the High Performance Computing Virtual Laboratory (HPCVL). This work was financially supported by the Advanced Foods and Materials Network (AFMNet) and by the Natural Sciences and Engineering Research Council of Canada (NSERC) to GWS.

[1] N. A. Peppas and R. Langer, Science **263**, 1715 (1994).
[2] W. M. Saltzman and W. L. Olbricht, Nature Reviews **1**, 177 (2002).
[3] S. Mallapragada, P. Colombo, and N. Peppas, J. Biomed. Mater. Res. **36**, 125 (1997).
[4] O. M. Conaghey, J. Corish, and O. I. Corrigan, Int. J. Pharm. **170**, 215 (1998).
[5] X. Liu, K. Nakamura, and A. M. Lowman, Soft Materials **1**, 393 (2003).
[6] D. S. Cohen and T. Erneux, SIAM J. Appl. Math. **58**, 1193 (1998).
[7] H.-C. Liang, W.-H. Chang, H.-F. Liang, M.-H. Lee, and H.-W. Sung, J. Appl. Poly. Sci. **91**, 4017 (2003).
[8] I. Majid, D. Ben-Avraham, S. Havlin, and H. E. Stanley, Phys. Rev. B **30**, 1626 (1984).
[9] K. Kosmidis, P. Argyrakis, and P. Macheras, J. Chem. Phys. **119**, 6373 (2003).
[10] A. Bunde, S. Havlin, R. Nossal, H. Stanley, and G. Weiss, J. Chem. Phys. **83**, 5909 (1985).
[11] J. E. Hastedt and J. L. Wright, Pharm. Res. **7**, 893 (1990).
[12] B. Amsden, Macromolecules **31**, 8382 (1998).
[13] J. Siepmann and N. A. Peppas, Adv. Drug Del. Rev. **48**, 139 (2001).
[14] J.-F. Mercier and G. W. Slater, J. Chem. Phys. **110**, 6050 (1999).
[15] J.-F. Mercier and G. W. Slater, J. Chem. Phys. **110**, 6057 (1999).
[16] T. M. Nieuwenhuizen, P. F. J. van Velthoven, and M. H. Ernst, Phys. Rev. Lett. **57**, 2477 (1986).
[17] N. A. Peppas, Pharm. Acta Helv. **60**, 110 (1985).
[18] W. Weibull, J. Appl. Mech. **18**, 293 (1951).
[19] J. Crank, *The Mathematics of Diffusion, 2nd edition* (Oxford: Clarendon Press, 1975).
[20] P. J. Reynolds, H. E. Stanley, and W. Klein, Phys. Rev. B **21**, 1223 (1980).
[21] V. Papadopoulou, K. Kosmidis, M. Vlachou, and P. Macheras, Int. J. Pharm. **309**, 44 (2006).
[22] P. Chelminiak, R. E. Marsh, and J. A. Tuszuński, Phys. Rev. E **72**, 031903 (2005).
[23] J. Bonny and H. Leuenberger, Pharm. Acta Helv. **68**, 25 (1993).
[24] S. Havlin and D. Ben-Avraham, Adv. Phys. **51**, 187 (2002).
[25] M. J. Saxton, Biophys. J. **66**, 394 (1994).
[26] D. Stauffer and A. Aharony, *Introduction to Percolation Theory* (Taylor & Francis, 1992).
[27] D. J. Enscore, H. B. Hopfenberg, and V. T. Stannett, Polymer **18**, 793 (1977).
[28] R. M. Barrer, J. Phys. Chem. **57**, 35 (1953).
[29] K. Sastry and G. Xiao, IlliGAL Report **2001016**, 1 (2001).
[30] R. Langer, Nature **392**, 5 (1998).
[31] R. Langer, Adv. Drug Del. Rev. **56**, 557 (2004).
[32] B. J. Thomas and B. C. Finnin, Drug Discov. Today **9**, 697 (2004).

Molecular Dynamics Simulations of Polymers in Micro–environments

M. Kenward, F. Tessier, Y. Tatek, Y. Gratton, S. Guillouzic and G. W. Slater[a]

[a]Department of Physics, University of Ottawa, 150 Louis Pasteur, Ottawa, ON, K1N 6N5

We provide an overview of ongoing work using large scale Molecular Dynamics (MD) simulations to study systems comprising macromolecules and explicit fluid in various contexts relevant to emerging bioanalytical microdevices and single molecule manipulation techniques. In particular, we discuss the application of MD simulations to polymer translocation through a nanopore, electroosmotic flow control in small capillaries, polymer stretching, and polymer collisions with obstacles. We also present more fundamental applications of MD to the study of molecular-scale friction coefficients and planar perturbations in a fluid. The simultaneous increase in available computational resources and decrease in the relevant system dimensions offers unprecedented opportunities to perform realistic simulations to refine our knowledge of these issues and guide future technological developments in this field.

1 Introduction

With the development of micro- and even nanofluidic devices, more robust modeling is required in order to understand observed behaviour in these systems. Many of the physical mechanisms involved have no macroscopic analogue and are ill understood. For example, there is a major effort to design and utilize microelectromechanical systems (MEMS) in a variety of situations ranging from diagnostic tools to smart materials, and in order to effectively do so we need to understand the dynamics of the components which constitute these devices. Of particular interest to our group are systems which incorporate polymeric materials, at either the micro- or nanoscale. In this paper we combine computer simulations and theoretical methods to examine the behaviour of polymers and other macromolecules in a number of model systems.

Large scale computer simulations which aim to explore mesoscale systems (with upwards of millions of particles), have become an invaluable research tool. Simulation methodologies including Monte Carlo [1,2], continuum models such as Navier-Stokes [3], coarse grained and atomistic Molecular Dynamics [4,5] and Brownian Dynamics are the most prevalent form of simulation for these types of systems. The simulation method used depends on a balance between the:

1. Required level of detail (e.g., length scales).
2. Time scales associated with observed behaviour.
3. Available computational resources.
4. Effort required for a timely implementation.

Figure 1 illustrates the level of detail and computational time of each method. For the particular systems we are examining, coarse grained Molecular Dynamics provides the most useful length and time scales, along with the preservation of hydrodynamics and the molecular properties of the system.

1.1 Molecular Dynamics: A brief overview

Since the aim of this paper is to illustrate the application of MD simulations to a variety of systems and not to provide a detailed description of Molecular Dynamics, we only give a brief overview and list appropriate references for the interested reader. In short, from the perspective of a physicist, MD is the solution of the set of classical equations of motion for a fully interacting collection of objects (atoms for example) [6,5], i.e., the solution of the N-body equations of motion for a system.

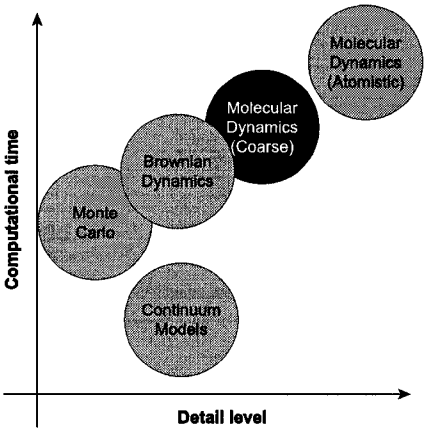

Figure 1. *Schematic illustration of several methods of simulation in terms of their relative computational time and level of detail.*

Since in general this solution cannot be obtained analytically, we must resort to numerical solutions. This amounts to discretizing the equations of motion using an appropriate finite difference scheme. In particular we utilize a second order method (in time), referred to as the Velocity Verlet algorithm [5]. This method is both relatively straightforward to implement and also allows relatively large time steps δt. Moreover the Velocity Verlet algorithm is amenable to parallelization [6].

The systems we examine contain one or several of the following components: polymers, solvent, walls, charged

species and external forces. One important addition to our simulations is the explicit inclusion of solvent and hence hydrodynamics. Although hydrodynamics is usually discussed in the guise of Navier-Stokes equations, its existence is really a molecular property of the system. Moreover it plays a crucial role in many phenomena at the microscopic and nanoscopic level, which may fall beyond the reach of a continuum description of fluid dynamics.

1.2 Model Fluid and Polymers

In this model we represent a single fluid particle as a soft sphere of radius $\sigma/2$ which interacts with other fluid particles via the Lennard-Jones potential given by

$$V_{\mathrm{LJ}}(r) = \begin{cases} 4\epsilon\left(\left(\frac{\sigma}{r}\right)^{12} - \left(\frac{\sigma}{r}\right)^{6}\right) + \epsilon, & r \leq r_{\mathrm{c}} \\ 0, & r \geq r_{\mathrm{c}} \end{cases}$$

We further simplify by choosing $r_{\mathrm{c}} = 2^{1/6}\sigma$ and we therefore have a fluid with purely repulsive interactions. All distances are expressed in terms of σ, masses in terms of m, times in terms of $\tau = \sqrt{m\sigma^2/\epsilon}$ and velocities in terms of $v = \sqrt{\epsilon/m}$. For all of the simulations presented here we work in the micro-canonical ensemble at fixed reduced temperature $T^* = 1$, reduced density $\rho^* = 0.85$ and a time step of $\delta t = 0.005\tau$ unless otherwise specified.

A schematic illustration of a Lennard-Jones fluid particle and the first layer of solvent around it is shown in Figure 2 b). To illustrate the fluid like structure, Figure 3 shows the radial distribution function of a pure Lennard-Jones fluid. This radial distribution function is characteristic of a fluid local packing with peaks at $r \approx \sigma,\ 2\sigma,\ 3\sigma \ldots$

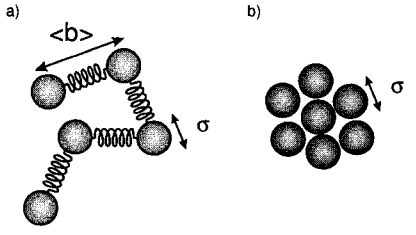

Figure 2. *Illustration of a) model polymers composed of Lennard Jones beads connected via FENE springs where $\langle b \rangle$ denotes the average bond length and σ the diameter of a bead b) model Lennard-Jones fluid particles with first layer of solvent.*

In order to model the polymers, we utilize a coarse grained approximation which replaces the real physical polymers with beads, representing one or many chemical units, and springs which represent the bonds between

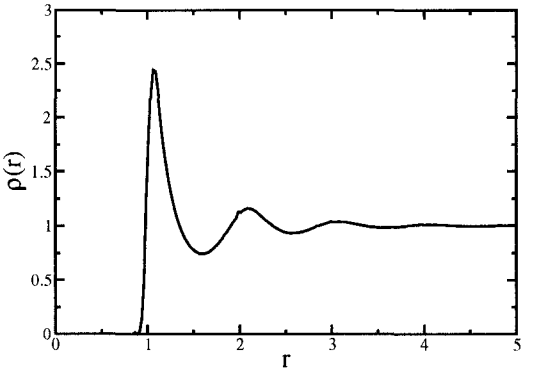

Figure 3. *Radial distribution function $\rho(r)$ for a pure Lennard-Jones fluid obtained from the MD simulations. Characteristic peaks are evident at $r \approx \sigma, 2\sigma, 3\sigma, \ldots$ corresponding to the first, second, third ... solvent layers.*

neighbouring units along a chain. The interactions between non-bonded beads along the chain are given by the Lennard-Jones potential whereas the bonded interactions are modeled via the Finitely Extensible Non-Linear Elastic (FENE) potential,

$$V_{\mathrm{FENE}}(r) = -\frac{k}{2}R_0^2 \ln\left(1 - \frac{r^2}{R_0^2}\right) \qquad (1)$$

where R_0 is an upper bound on the bond distance and k is essentially a "spring constant" [5]. For more detailed descriptions and implementation details, the reader can consult references [6,7,5,8,9].

Since our long term goal for these simulations is to examine mesoscopic and macroscopic systems with $> 10^6$ particles, we require the use of High Performance Computing resources such as those available via HPCVL (**www.hpcvl.org**). Parallelization of Molecular Dynamics simulations with short range interactions is typically done using either; so-called atom-, force-, and spatial-decomposition algorithms [10]. As such our next step will be the parallelization of the simulations using one of the above algorithms, in order to begin examining much larger systems.

1.3 Visualization Tools

Visualizing the results from a simulation provides not only an inherently useful debugging tool but also a physically intuitive way to examine a system and its properties. In this vein, we have developed some generic tools for the visualization of results from the Molecular Dynamics simulations. In particular we have written graphical interfaces, in **OpenGL**, which allow us to visualize our results in both real-time and post simulation modes. Snapshots from this Molecular Dynamics viewer are shown in Figure 4. Though there are similar tools

openly available, our viewer has the advantage of being tailored for our specific project. Furthermore we can easily add, modify, and adapt this viewer for a number of distinct projects in our group.

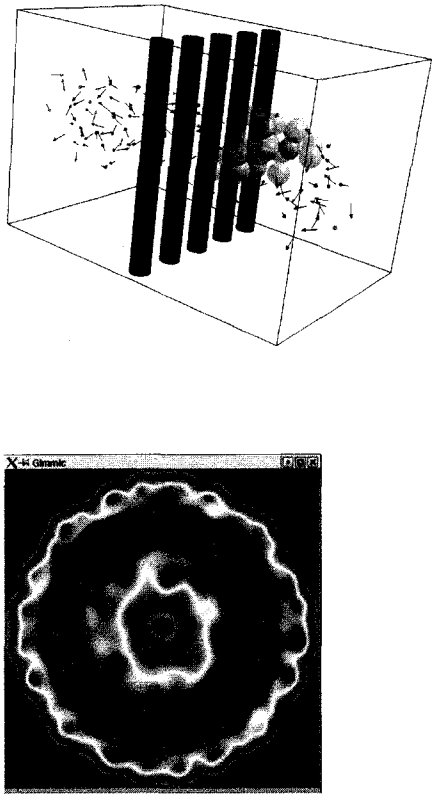

Figure 4. *Snapshots from our custom built Molecular Dynamics viewer, written in* **OpenGL**. *The top panel shows an image from a polymer–post collision simulation: the velocity field associated with a small volume of the fluid is illustrated by the small arrows. The bottom panel is a temperature plot of a cross–section of a capillary filled with a fluid.*

2 Molecular Dynamics: Applications and Examples

2.1 Polymer Translocation in Nanopores

The sequencing of the human genome has become one of the crowning achievements of human-kind. This information has the potential to lead to both better understanding and treatment of human diseases. Though the scientific community has managed to sequence a generic version of the genomic text, the ultimate goal is to sequence individual genomes in a short period of time (a few hours) which could allow for the diagnosis and prevention of diseases.

One promising sequencing method is the use of the translocation of single-stranded DNA molecules through a nanopore in a membrane or a solid surface [11–13]. As the polymer either diffuses or is pulled through the opening, the individual bases of the DNA strand can ideally be read, providing a tool for sequencing. This proposed method could potentially sequence the entire genome in minutes. In order to better understand the relevant physics, we have carried out MD simulations of polymer translocation. A schematic illustration of polymer diffusing through a nanopore is given in Figure 5.

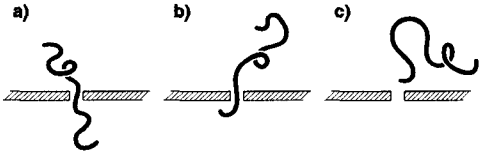

Figure 5. *Schematic illustration of a model polymer diffusing through a nanopore. a) The polymer is centered in the nanopore. b) The polymer begins to diffuse away from the pore. c) Eventually the polymer escapes.*

Our simulations consist of placing a polymer in a single void in a monolayer [111] face-centered cubic structure. We first let the polymer relax while fixing its center bead in the pore. After this relaxation period, we release the polymer and observe its behaviour, until it escapes.

A recent theory of Chuang *et. al.* [14] predicts the scaling behaviour of the mean end-to-end translocation time τ_{trans} of a polymer through a nanopore. In 3D, with no external force and no hydrodynamics, it scales as $\tau_{\text{trans}} \propto N^{2.2}$ while with hydrodynamics it scales as $\tau_{\text{trans}} \propto N^{1.8}$ (where N is the number of monomers in the chain). Chuang *et. al.* [14] also predict that the variance of the translocation coordinate s scales as $\langle \Delta s^2 \rangle \propto t^{1.12}$ when hydrodynamic interactions are present and $\langle \Delta s^2 \rangle \propto t^{0.92}$ when they are not (where the translocation coordinate is the length of the polymer on a given side of the pore).

From the MD simulations we obtain

$$\langle \Delta s^2 \rangle \propto t^{0.918 \pm 0.016} \tag{2}$$

and

$$\tau_{\text{trans}} \propto N^{\beta} \quad \text{with} \quad \beta \geq 2.27 \pm 0.04 \tag{3}$$

for the variance of the translocation coordinate and the mean escape times respectively. Although these results are preliminary, they agree nicely with the predictions of Chuang *et. al.* for translocation in the presence of excluded volume but with no hydrodynamic interactions. This seems to be reasonable since the presence of the wall is expected to screen hydrodynamic interactions to some extent [15].

2.2 Friction coefficients of Rigid Rods

A classic problem from fluid dynamics is determining the friction coefficient of an object. The so-called slender body theory of Batchelor [16] provides well known results for friction coefficients of arbitrarily shaped objects. These results are obtained from the solution of Navier-Stokes equations for low Reynolds number flow subject to appropriate boundary conditions and typically for macroscopic objects. Though these results are known to be accurate for macroscopic systems, when the objects under consideration are on the same scale as the fluid particles, these results do not necessarily remain valid.

We use MD simulations to explore fluid behaviour and microscopic fluid dynamics of objects on the same scale as the fluid. We have carried out simulations which directly determine the friction coefficient of rigid rods composed of spheres. Further to this we can illustrate as the size of the object is decreased to the scale of the fluid particles, the friction coefficient does indeed reduce to that of a single solvent particle. Here we present the case for all particle sizes from the fluid scale to an object composed of 60 fluid size particles. Similar work has been done experimentally for chains of spheres composed of magnetically induced linear chains of superparamagnetic particles, where the friction coefficient is measured during sedimentation [3,17], though the sphere size is much larger than the size of the fluid particles.

Slender body theory predicts friction coefficients ξ for rigid rods, moving either parallel $||$ or perpendicular $\perp$ to a field, of the form

$$\xi_{||}(L) = \frac{C\pi\eta L}{\ln(L/2b) + \gamma_{||}}, \quad \xi_{\perp}(L) = \frac{2C\pi\eta L}{\ln(L/2b) + \gamma_{\perp}} \quad (4)$$

where $C, \gamma_{\perp}$ and $\gamma_{||}$ are constants and η is the viscosity. The crucial thing to note is that this theory predicts the following relationship

$$\frac{\xi_{\perp}(L)}{\xi_{||}(L)} \approx 2 \quad (5)$$

Indeed, from the simulations we can recover this asymptotic behaviour and the crossover from microscopic to this large scale friction. Figure 6 illustrates the friction coefficients as a function of chain length and the ratio $\xi_{\perp}(L)/\xi_{||}(L)$. This illustrates that MD can be used to examine fluid dynamics starting from a non-continuum based description of the fluid. As we begin to examine larger systems, with on the order of millions of particles we can further examine the crossover from microscopic single particle fluid dynamics to mesoscopic and ideally macroscopic fluid behaviour.

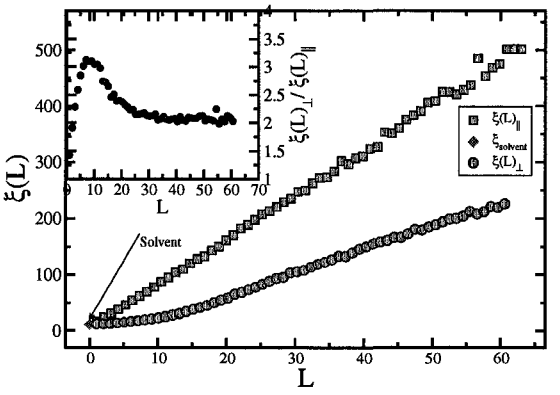

Figure 6. *Friction coefficients for a chain of spheres moving perpendicular $\xi_{\perp}(L)$ and parallel $\xi_{||}(L)$ to an applied field. Inset figure is the ratio of $\xi_{\perp}(L)$ to $\xi_{||}(L)$ as a function of L. Clearly the ratio tends asymptotically to a value of 2, as predicted by slender-body theory.*

2.3 Polymer–Obstacles Collisions

Another field where the use of computer simulations may reap many benefits is that of separation science, i.e., the separation of DNA, or other polymers by mass, charge or shape. Typically polydisperse solutions of polymers are separated using either gel or capillary electrophoresis [18–20]. A better understanding of the dynamics of polymers in microenvironments can lead to both optimized and novel methods of separating DNA. One such method is the use of self-assembled arrays of paramagnetic obstacles created by the application of a magnetic field to a suspension of super paramagnetic particles confined between layers of glass [21]. This results in the formation of small quasi-regular arrays of posts (or obstacles) which can serve as a sieve to separate polymer. Such as system has been designed, built and used effectively to separate double-stranded DNA by Doyle *et. al.* [21].

In such a system, the polymers migrate under the presence of an external electric field. They consequently collide with posts, are deformed and form pulley like structures. The release time of the polymer is dictated by its length and a competition between the opposing arms of the pulley like conformation which results. One of the long standing questions is to what degree does the presence of hydrodynamics dictate the release time of the polymer [22,23].

We have carried out extensive MD simulations which examine this process. Figure 7 shows a snapshot from

one of the simulations, illustrating a collision and release of a polymer. Using these simulations we can effectively carry out an autopsy of the collision dynamics of a single polymer chain with a post. Figure 8 shows the position of center of mass of a single polymer chain as it undergoes a collision with a post in the MD simulation. From this we can generate a good qualitative model of the behaviour of a polymer during collision. The polymer moves through the solvent with constant velocity v_0, until the center of mass is within about R_g of the post, it is then deformed by the presence of the post and later becomes trapped. There is a competition between the two arms of the resultant pulley like structure which forms, the longer arm winning. This results in the eventual release of the polymer. At this point, it accelerates and returns to a random walk conformation and eventually reaches constant velocity v_0 again.

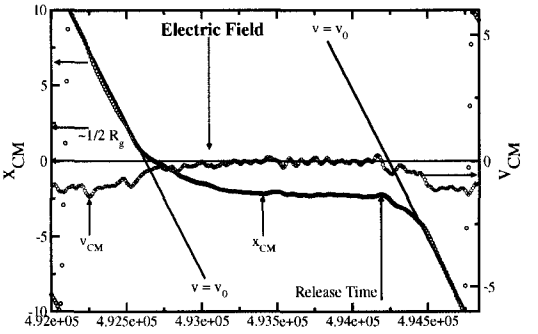

Figure 8. *Instantaneous position x_{CM} and velocity of the center of mass v_{CM} of a polymer before, during and after a collision with a post.*

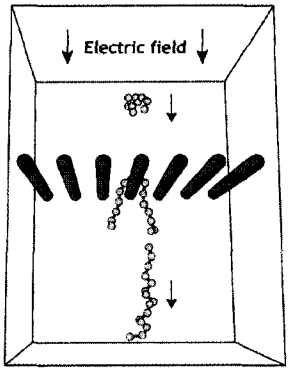

Figure 7. *Illustration of a polymer post collision sequence from the MD simulations.*

2.4 MD simulations of Electroosmotic Flow

Electroosmotic flow (EOF) refers to a fluid flow induced by an external electric field applied along a solid surface, and occurs when a space charge builds up in the fluid near the surface [24]. This interfacial charge may arise for different reasons, a common one being the dissociation of chemical groups from the solid and the ensuing accumulation of counterions or ions from the solution in an electrical double-layer (EDL) near the surface [25]. When an external electric field is applied parallel to the surface, this layer of mobile charges is set in motion and eventually drags the bulk of the fluid by viscosity into a flow with a flat profile (a so-called *plug flow*, see Figure 9). Hence EOF serves as a very efficient fluid transport mechanism in small capillaries [26]. Calculations based on mean-field arguments have been used time and again to characterize the EOF in various geometries, including channels with rectangular cross-section, cylindrical capillaries and narrow slits, in steady-state, transient, and oscillating regimes [27,28,26,29–31].

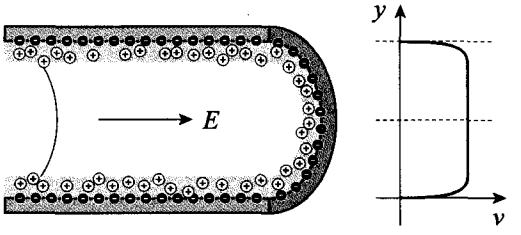

Figure 9. *Schematic representation of EOF generation inside a cylindrical capillary. Bound charges on the wall surface induce a net charge layer in the fluid. Upon the application of an external field, this mobile layer is set in motion, and eventually drags the whole fluid into a plug flow with a flat profile, depicted schematically on the right.*

The typical approach to treat this problem analytically or numerically is to consider on one hand the Poisson equation for the electrostatic potential $\phi(\mathbf{r})$ at position $\mathbf{r}$ in the system, and on the other hand the Boltzmann distribution for the density of mobile ions in the solution in terms of the valence z_k and the bulk concentration n_{ko} of each of the N ionic species [24]. These two expressions together yield the well-known Poisson-Boltzmann (PB) equation for $\phi(\mathbf{r})$ in a polyelectrolyte solution at thermal

equilibrium:

$$\nabla^2\phi(\mathbf{r}) = -\frac{e}{4\pi\varepsilon_o\varepsilon}\sum_{k=1}^{N} z_k n_{k0}\, e^{-ez_k\phi(\mathbf{r})/k_BT}, \qquad (6)$$

where ε_o and ε are the permittivity of the vacuum and the relative permittivity of the fluid, e is the elementary charge, and k_BT is a measure of the mean thermal energy. With appropriate boundary conditions, we can solve equation (6) numerically for any geometry, and by substituting the results in a finite difference Navier-Stokes equation solver we can obtain the flow field induced by the EOF, in both transient and steady-state regimes. Analytical work is also possible, albeit with a linearized version of equation (6) and for simple geometries only.

Despite all the knowledge gained in this way over the last thirty years, revisiting EOF with Molecular Dynamics simulations is interesting and important for two main reasons. First, as modern analytical chemistry devices shrink to the micrometer and even to the nanometer scale, the validity of the continuum picture of hydrodynamics itself becomes questionable. In particular, the correct representation of the velocity field near the fluid-solid interface (e.g. *slip* vs. *no-slip* boundary condition) becomes critical in devices so small that the *bulk* of the fluid lies, in fact, near a solid surface. Secondly, we want to study surface modification using polymer molecules grafted or adsorbed on the capillary wall. Such polymer coatings are of great industrial interest, especially for the control of EOF in bioanalytical microdevices [32]. However the complexity of the system is such that we cannot hope to describe it accurately within a model based on equation (6). Molecular Dynamics simulation, a firmly established and robust method to study fluids, electrolytes, macromolecules, etc., stands as a natural choice for a realistic investigation of EOF.

Studying EOF requires that we add charged species in our simulations. Long-range electrostatic forces generally pose problems because of interactions between ions in different periodic images, although robust schemes based on Ewald summations have been developed [33–35]. However, our narrow capillary here is essentially one-dimensional on large length scales and we can include electrostatics directly, provided that the periodic box is long enough. We moderate Joule heating inside the system by controlling the temperature of the wall. The first object of our investigation is the distribution of ions which we will compare with that predicted by equation (6), as we vary the capillary diameter and the ionic strength of the buffer solution. Further on, we will add an external electric field and study the transient and steady state EOF flows. Assuming we reproduce EOF correctly, we can then include grafted or adsorbed polymer chains on the wall to gain a sound understanding of their effect on EOF.

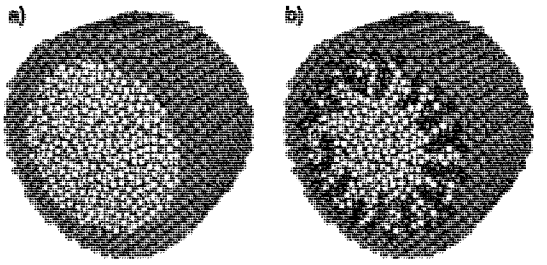

Figure 10. *a) A snapshot from an MD simulation of a short section of a capillary filled with fluid. b) A mock-up of the simulation of* EOF *control using polymer coatings we are setting out to perform, complete with polymer chains, ions on the capillary walls and counterions in solution.*

2.5 Stretching Single Polymers

Understanding the properties of single linear chains in good solvent is important to better describing single chains in microenvironments. With the development of techniques such as optical tweezers and single molecule fluorescence spectroscopy it is now possible to experimentally manipulate and observe single polymer chains. This technology enables us to stretch a DNA molecule and measure forces on the order of femtonewtons! One of the most useful analytical tools for examining polymers is the scaling theory developed by de Gennes [36]. In essence, this theory utilizes the fact that all properties in the system can be related to some universal scale (for example a length scale) such as the mean squared end-to-end distance $\langle h^2\rangle$.

This section presents a brief overview of two simple models: the Freely Jointed Chain (FJC) and the Rouse model applied to the stretching of a single polymer [36–38]. At first glance, a polymer looks like a random walk (RW) where every monomer is subjected to Brownian motion caused by the surrounding solvent. From this observation, a simplistic model can describe the polymer as a series of links of fixed length b (the Kuhn length) which allow all possible orientations. In RW theory, it is a well known fact that for a chain of N links, the mean squared end-to-end distance $\langle h^2\rangle$ is

$$\langle h^2\rangle = Nb^2 \qquad (7)$$

The Rouse model consists of a series of beads connected by springs [37]. Compared with the FJC model, the Rouse model re-groups $n < N$ links to form a spring. These Gaussian springs have an elastic constant of $K_n = 3k_BT/nb^2$ and a mean squared end-to-end distance $\langle b_n^2\rangle = nb^2$. The n links in a spring produce $M = N/n$ springs connecting $M+1$ beads. The Rouse chain conserves $\langle h^2\rangle$:

$$\langle h^2\rangle = M\langle b_n^2\rangle = Mnb^2 = Nb^2 \qquad (8)$$

One caveat in the Rouse model is the spring constant: it does not accurately model the finite extensibility of a real chain. A polymer will always have a maximum extension after which it will break. We need a more realistic spring constant which ensures finite extension of the chain while keeping the mean value fixed. One possibility is to use the Finitely-Extensible Nonlinear Elastic (FENE) model. It is important to note that these models do not take into account either the presence of a solvent (hydrodynamic effects) or excluded volume interactions.

There are two ways to describe polymer stretching: the stress and the strain ensemble. In the stress ensemble, an external force is applied to the ends of the chain. The strength of this force is fixed to $\pm f$ but the ends are able to move freely. One can then calculate the mean end-to-end distance $\langle h(F)\rangle$. It is given by [39]

$$\frac{\langle h(F)\rangle}{h_{\max}} \approx \coth(F) - \frac{1}{F} \tag{9}$$

For $F \gg 1$,

$$\frac{\langle h(F)\rangle}{h_{\max}} \simeq 1 - \frac{1}{F} \tag{10}$$

where $F = fb/k_BT$ is the scaled force. Note that for $F \gg 1$, $\langle h\rangle$ tends to $h_{\max} = Nb$. A polymer in the strain ensemble has it ends fixed in space and the force felt by the ends F(h) is measured. We do not discuss the strain ensemble here.

To understand the stretching of real chains, one must incorporate excluded volume interactions, i.e., those interactions which prohibit any two monomers from occupying the same volume of space. Excluded volume interactions tend to swell the polymer compared to the FJC model. Inclusion of excluded volume in theoretical calculations is highly non-trivial. The MD simulations implicitly include all of the aforementioned effects and allow us to analyze chain stretching with excluded volume and hydrodynamics.

The stretching of single polymer chains is classified by four distinct regimes. Figure 11 illustrates these four regimes along with the associated scaling relationships for the mean squared end-to-end distance. We have successfully used Molecular Dynamics simulations to investigate and recover known force extension relationships of single isolated polymers in the strong stretching regime of the stress ensemble, i.e., Figure 11 c). We have also determined the difference between the stress and strain ensembles along with examining the relaxation of a polymer following the removal of the forces $\pm F$. In the latter case, hydrodynamics leads to highly nontrivial effects.

2.6 Planar Perturbation in a Lennard-Jones Fluid

The present study is intended to examine a planar perturbation taking place in a Lennard-Jones fluid in terms of velocity, diffusion and absorption. There are several dissipation mechanisms like viscosity, heat conduction and relaxation taking place in a fluid. They are responsible for the amplitude reduction of sound waves. This phenomenon is different from the attenuation which takes place in a spherical wave field for example, which is a pure geometrical effect. As a result no energy is actually lost; instead it is spread over a larger area.

In our simulations a planar perturbation is propagated along the x-axis. Two different ways have been employed to simulate a planar perturbation. The first technique

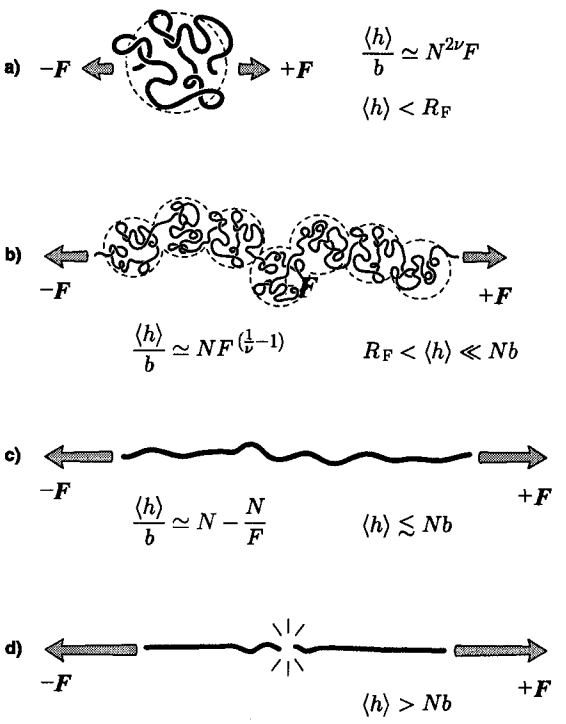

Figure 11. *Illustration of the four stretching regimes. a) The entropy of the polymer is able to keep both ends inside the Flory radius R_F. The forces applied to the polymer are too small to substantially deform it. This regime acts like an entropic spring and $\langle h^2\rangle/b$ scales as $N^{6/5}$ compared to N^1 for the FJC. b) The second regime is referred to as the Pincus regime. It corresponds to a stronger force which stretches the polymer beyond R_F. The polymer can then be treated as a series of "blobs"; the inside of the blobs is considered as a real chain while blobs are almost perfectly aligned. This regime predicts $\langle h\rangle \simeq F^{2/3}$ in 3 dimensions, but $\langle h\rangle \simeq N^1$ like the FJC model. c) In this regime the polymer is stretched to nearly full extension. We can treat it as an ideal chain since it is highly improbable that non-consecutive beads will interact with one another. d) The last regime occurs when one goes beyond an end-to-end distance of Nb. At this extension a polymer would be inclined to break into two subchains.*

consists in displacing a plane of particles perpendicular to the x-axis by 0.3σ. The thickness of the plane is also 0.3σ. The second way is by giving an impulse to particles belonging to a plane of the same width. The first technique leads to an increase of both the kinetic and potential energy whereas the second produces an increase only in the kinetic energy. In both cases there will be a slight increase in the temperature of the system.

We have calculated the displacement amplitudes of fluid particles at different distances in the x direction from the perturbation source. To do so we have averaged the displacement amplitudes over all the atoms in planes of width 0.3σ along the x direction. Figure 12 shows the displacement amplitude profiles for each plane. The curves present a quasi-symmetrical bell-shaped distribution with a decreasing maximum as x increases. The width of the distribution increases as the perturbation moves away from the source. This indicates that the perturbation diffuses along its trajectory. The diffusing tail becomes more and more pronounced when one is far from the source. As noted earlier, the diffusion is due to the dissipation taking place in the fluid. At a microscopic level the dissipation can be interpreted as a slow redistribution of the perturbation energy among all the particles.

Although the planes are equally spaced, the maxima in Figure 12 are not, leading to an apparent non-constant velocity of the perturbation. That is why we cannot compute the perturbation velocity by a simple peak to peak distance measurement. These distributions can be fitted with the well known Gaussian distribution

$$\langle \Delta x(D,x,v,t) \rangle \sim \frac{1}{\sqrt{Dt}} \exp\left(-\frac{(x-vt)^2}{4Dt}\right) \qquad (11)$$

where D is the diffusion coefficient of the plane and v its velocity. From Eqn. (11) we can derive the arrival time of the maximum amplitude

$$t_{\max}(x) = \frac{D}{2v^2}\left[2\sqrt{\frac{1}{4}+x^2\frac{v^2}{D^2}}-1\right] \qquad (12)$$

We can approximate relation (12) for two extreme values of x. When $x \gg D/2v$, $t_{max}(x)$ can be expressed by $t_{max} \sim x/v$, and the peak is moving with the same velocity as the perturbation. Near the source, i.e., at $x \simeq 0$, $t_{max} \sim x^2/2D$ and the peak movement is dominated by diffusion. We are currently looking at the measurement of fluid viscosity, the solvent diffusivity and the speed of sound using this novel approach. Our next step is to examine the effects of walls and polymers on this propagation phenomenon.

3 Conclusions and Remarks

With this survey of current projects, we have both illustrated the versatility of the Molecular Dynamics method to examine a wide variety of phenomena related to polymers in microenvironments and the scope of the research which our group is undertaking. We have hopefully illustrated the use of MD simulations in this regard.

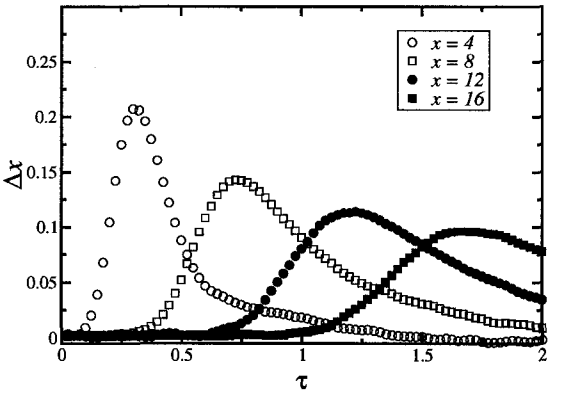

Figure 12. *Displacement amplitudes Δx of the perturbation at various positions from the source as a function of time τ. This simulations is carried out in a cube with $L = 41.8$ and reduced temperature $T^* = 1.1$.*

4 Acknowledgements

The authors would like to thank the Natural Sciences and Engineering Research Council of Canada (NSERC) for a Research Grant to GWS. MK and SG also thank NSERC for a postgraduate scholarship and a postdoctoral fellowship respectively. MK, YG and FT thank the University of Ottawa for scholarships. YT would like to thank Materials Manufacturing Ontario (MMO-EMK) for funding. We would also like to acknowledge computational resources provided by the High Performance Computing Virtual Laboratory (HPCVL) and C3.ca.

REFERENCES

1. R. G. Larson. Monte carlo simulation of amphiphilic systems in two and three dimensions. *J. Chem. Phys.*, 89(9):1642–1650, 1988.
2. R. G. Larson, L. Scriven, and H. T. Davis. Monte carlo simulation of model amphiphile–oil–water systems. *J. Chem. Phys.*, 83(5):2411–2420, 1985.
3. K. Zahn, R. Lenke, and G. Menke. Friction coefficient of rod-like chains of spheres at very low reynolds numbers. i. experiment. *J. Phys. II France*, 4:555–560, 1994.
4. K. Kremer and G. Grest. Molecular dynamics simulation for polymers in the presence of a heat bath. *Physical Review A*, 33(5):3628–3631, 1986.
5. K. Kremer, G. S. Grest, and I. Carmesan. Crossover from rouse to reptation dynamics: A molecular dynamics simulation. *Phys. Rev. Letters*, 61(5):566–569, 1988.

6. D. C. Rapaport. *The Art of Molecular Dynamics Simulation.* Cambridge University Press, 1995.
7. D. C. Rapaport. Molecular dynamics study of a polymer chain in solution. *J. Chem. Phys.*, 71(5):3299–3303, 1979.
8. K. Kremer and G. S. Grest. Dynamics of entagled linear polymer melts: A molecular dynamics simulation. *J. Chem. Phys*, 92(8):5057–5086, 1990.
9. M. P. Allen and D. J. Tildesley. *Computer Simulations of Liquids.* Oxford Science Publications, Oxford, 4^{th} edition, 1987.
10. S. J. Plimpton and B. A. Hendrickson. *Parallel Computing in Computational Chemistry*, chapter Parallel Molecular Dynamics Algorithms for Simulation of Molecular Systems, pages 114–132. American Chemical Society, Symposium Series 592, 1995.
11. M. Muthukumar. Translocation of a confined polymer through a hole. *Physical Review E*, 86(14):3188–3191, 2001.
12. M. Muthukumar. Polymer translocation through a hole. *Macromolecules*, 111(22):10371–10374, 1999.
13. J. K. Kasianowicz, E. Brandin, D. Branton, and D. W. Deamer. Characterization of individual polynucleotide molcules using a membrance channel. *Proc. Natl. Acad. Sci. USA*, 93:13770–13773, 1996.
14. Jeffrey Chuang, Yacov Kantor, and Mehran Kardar. Anomalous dynamics of translocation. *Physical Review E*, 65:011802, 2001.
15. O. B. Bakajin, T. A. J. Duke, C. F. Chou, S. S. Chan, R. H. Austin, and E. C. Cox. Electrohydrodynamic stretching of dna in confined environments. *Phys. Rev. Letters*, 80(12):2737–2740, 1998.
16. G. K. Batchelor. Slender-body theory for particles of abitrary cross section in stokes flow. *J. Fluid Mech.*, 44(3):307–312, 1970.
17. A. Meunier. Friction coefficient of rod-like chains of spheres at very low reynolds numbers. ii. numerical simulations. *J. Phys. II France*, 4:561–565, 1994.
18. A. E. Barron, H. W. Harvey, and D. S. Soane. A transient entanglement coupling mechanism for dna separation by capillary electrophoresis in ultradilute polymer solutions. *Electrophoresis*, 15:597–615, 1994.
19. B. Braun, H. W. Blanch, and J. M. Prausnitz. Capillary electrophoresis of dna restriction fragments: Effect of polymer properties. *Electrophoresis*, 18:1994–1997, 1997.
20. F. Han, B. H. Huynh, Y. Ma, and B. Lin. High–efficiency dna separation by capillary electrophoresis in a polymer solution with ultralow viscosity. *Anal. Chem*, 71(13):2385–2389, 1999.
21. P. S. Doyle, J. Bibette, A. Bancaud, and J. Viovy. Self–assembled magnetic matrices for dna separation chips. *Science*, 295(22):2828–2831, 2002.
22. P. André, D. Long, and A. Ajdari. Polyelectrolyte/post collisions during electrophoresis: Influence of hydrodynamics. *Eur. Phys. J. B*, 4(1):307–312, 1998.
23. E. M. Sevick and D. R. M. Williams. Long lived states in electrophoresis: Collision of a polymer chain with two or more obstacles. *Euro. Phys. Letters*, 56(4):529–535, 2001.
24. W. B. Russel, D. A. Saville, and W. R. Schowalter. *Colloidal Dispersions.* Cambridge University Press, 1989.
25. S. Griffin and R. E. Majors. Fused-silica capillary – the story behind the technology. *Lc Gc N. Am.*, 20:928–938, 2002.
26. J. P. Gleeson. Electroosmotic flows with random zeta potential. *J. Colloid Interface Sci.*, 249:217–226, 2002.
27. C. L. Rice and R. Whitehead. Elektrokinetic flow in a narrow capillary. *J. Chem. Phys.*, 69:4017–4024, 1965.
28. A. T. Conlisk, J. McFerran, Z. Zheng, and D. Hansford. Mass transfer and flow in electrically charged micro- and nanochannels. *Anal. Chem.*, 74:2139–2150, 2002.
29. P. Dutta and A. Beskok. Analytical solution of time periodic electroosmotic flows: Analogies to stokes' second problem. *Anal. Chem.*, 73:5097–5102, 2001.
30. P. Dutta and A. Beskok. Analytical solution of combined eloectoossmotic/pressure driven flows in two-dimensional straight channels: Finite debye layer effects. *Anal. Chem.*, 73:1979–1986, 2001.
31. S. Z. Qian and H. H. Bau. A chaotic electroosmotic stirrer. *Anal. Chem.*, 74:3616–3625, 2002.
32. E. A. S. Doherty, R. J. Meagher, M. N. Albarghouthi, and A. E. Barron. Microchannel wall coatings for protein separations by capillary and chip electrophoresis. *Electrophoresis*, 24:34–54, 2003.
33. M. Deserno and C. Holm. How to mesh up ewald sums. i. a theoretical and numerical comparison of various particle mesh routines. *J. Chem. Phys.*, 109:7678–7693, 1998.
34. M. Deserno and C. Holm. How to mesh up ewald sums. ii. an accurate error estimate for the particle-particle-particle-mesh algorithm. *J. Chem. Phys.*, 109:7694–7701, 1998.
35. C. Sagui and T. A. Darden. Molecular dynamics simulations of biomolecules: Long-range electrostatic effects. *Annu. Rev. Biophys. Biomolec. Struct.*, 28:155–179, 1999.
36. P.-G. de Gennes. *Scaling Concepts in Polymer Physics.* Cornel University Press, Ithaca, 1979.
37. M. Doi and S. F. Edwards. *The Theory of Polymer Dynamics.* Oxford Science Publications, New York, 1986.
38. I. Teraoka. *Polymer Solution: An Introduction to Physical Properties.* John Wiley & Sons, Inc., New York, 2002.
39. G. W. Slater, S. J. Hubert, and G. I. Nixon. Construction of approximate entropic forces for finitely extensible nonlinear elastic (fene) polymers. *Macromolecular Theory and Simulation*, 3:695–704, 1994.

58

CURRENT OPINION
www.current-opinion.com

The theory of DNA separation by capillary electrophoresis

Gary W Slater*†, Martin Kenward‡, Laurette C McCormick§ and Michel G Gauthier#

The Human Genome has been sequenced in large part owing to the invention of capillary electrophoresis. Although this technology has matured enough to allow such amazing achievements, the physical mechanisms at play during separation have yet to be completely understood and optimized. Recently, new separation regimes and new physical mechanisms have been investigated. The use of free-flow electrophoresis and new modes of pulsed-field electrophoresis have been suggested, while we have observed a shift towards single nucleotide polymorphism analysis and microchip technologies. A strong theoretical basis remains essential for the efficient development of new methods.

Addresses
*Department of Physics, University of Ottawa, 150 Louis-Pasteur, Ottawa, Ontario, Canada K1N 6N5
†Corresponding author: e-mail: gslater@science.uottawa.ca
‡e-mail: mkenward@science.uottawa.ca
§e-mail: lmccormi@science.uottawa.ca
#e-mail: mgauthie@science.uottawa.ca

Current Opinion in Biotechnology 2003, 14:58–64
This review comes from a themed issue on
Analytical biotechnology
Edited by Norm Dovichi and Dan Pappel
0958-1669/03/$ – see front matter
© 2003 Elsevier Science Ltd. All rights reserved.
DOI 10.1016/S0958-1669(02)00012-5

Abbreviations

BRF	biased reptation with fluctuations
BRM	biased reptation model
CE	capillary electrophoresis
dsDNA	double-stranded DNA
ELFSE	end-labeled free solution electrophoresis
ssDNA	single-stranded DNA

Introduction

Gel electrophoresis has been the workhorse of molecular biology for several decades. Traditionally, agarose gels are used to separate double-stranded DNA (dsDNA) fragments (e.g. for mapping), whereas polyacrylamide gels are used to separate single-stranded DNA (ssDNA). However, there are severe limitations; for example, one cannot generally separate fragments larger than ~40 kilo base-pairs (kbp) in agarose gels because they co-migrate at an amazingly high velocity [1••]. This limitation, which makes it difficult to manipulate chromosomal DNA, spurred current interest in the theory of gel electrophoresis. This led to the idea of biased reptation [1••], still the main concept for understanding DNA gel electrophoresis. Indeed, it was used extensively by the inventors of the pulsed-field methods [2].

After the 1980s, attention shifted to DNA sequencing, which rapidly moved towards a capillary format with entangled polymer solutions replacing gels [3]. The reptation models are still valid, but their predictions appear to be less reliable. This might be because the fields are very high and the matrix less stable. Because sequencing is actually limited by band broadening and not by band spacing, theoreticians had to model the diffusion processes during electrophoresis; unfortunately, the results of these investigations are not widely appreciated in the separation science community.

In this article, we review our current knowledge of the physical mechanisms involved in DNA separations and discuss what theory says about system optimization.

Free flow electrophoretic properties of DNA

Although DNA's free flow electrophoretic mobility (μ_0) is a function of several parameters (e.g. temperature T and buffer ionic strength I), it is regrettably independent of DNA size (M, in number of monomers) for most practical conditions. This is because the counter-ions effectively screen the long-range hydrodynamic interactions between the monomers. The monomers are then basically in free fall, and we say that the DNA is free-draining. As a consequence, both the force (F) and the friction (ξ) increase linearly with M, and their ratio $v = F/\xi$ (the velocity) is size-independent, hence the need for a sieving 'gel'. However, the mobility of very small DNA molecules increases slowly with M, up to ~200 bp or so [4,5]. In this limit, the contour and persistence lengths are comparable, and hence the transition may be linked to a rod-to-coil conformational change [4].

Recently, the free-flow DNA diffusion coefficient D_0 was found to be unaffected by the electric field (E) [6•]. Consequently, D_0, unlike μ_0, is purely mechanical in nature. The data also clearly indicated that $D_0 \sim 1/R_g$, where $R_g = R_g(M)$ is the radius of gyration of the DNA molecule. This means that the Nernst–Einstein equation,

$$\frac{D_0}{\mu_0} = \frac{k_B T}{Q} \qquad (1)$$

where $Q = Q(M)$ is the charge, is not valid for DNA free-flow electrophoresis. For instance, it was found that for ssDNA $\mu_0 \cong 1.83 \times 10^{-4}$ cm^2/Vs, while $D_0 \sim 1/M^{(0.68 \pm 0.03)}$ [6•]. Since $Q \sim M^1$, it is clear that Equation 1 cannot be

Figure 1

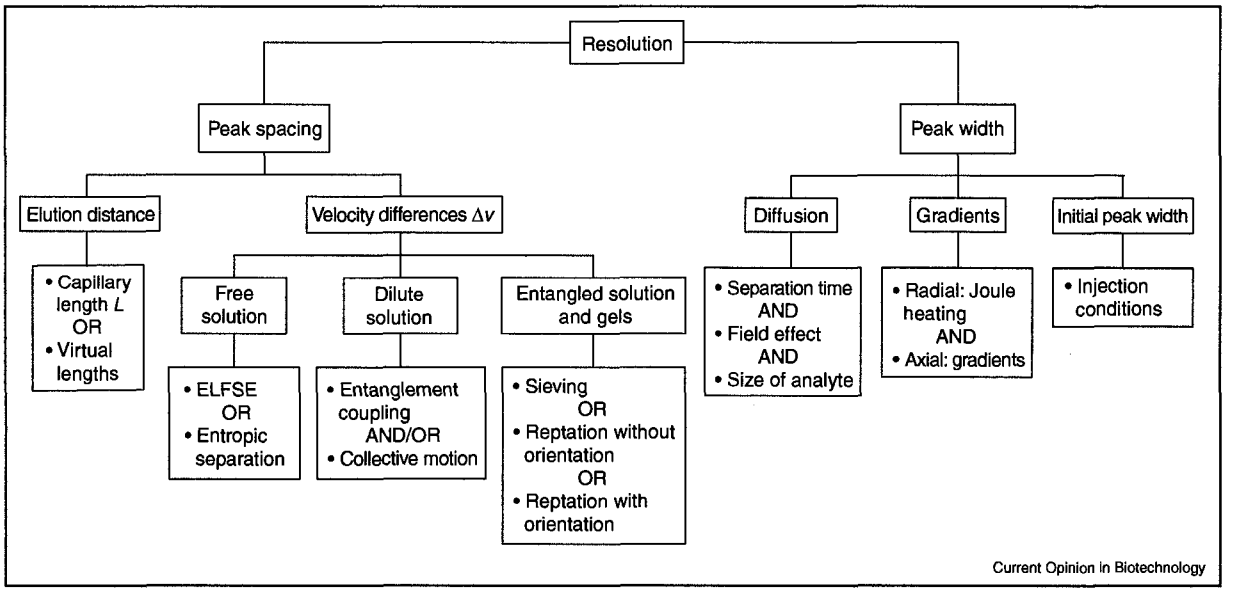

Flow chart of the main separation regimes and their properties. The resolution of a separation method depends on both the peak-to-peak spacing and the peak widths (the former must exceed the latter). Given a certain difference in velocity Δv between two analytes, the only way to increase peak spacing is to increase the duration of the separation (or, equivalently, the elution length). Velocity differences Δv are generated by the physical mechanism that retards molecular migration. Because DNA is free-draining, one must either label the DNA (ELFSE), exploit its internal entropy [54,55], or use dilute or concentrated solutions or gels to provide size-dependent retardation. Peak widths, besides their initial injection size, are due to analyte thermal diffusion, which increases with field intensity and elution time, and system gradients that affect the band shape and/or width. The relationship between the mobility and the diffusion coefficient of the DNA molecules is not fully understood for most separation mechanisms.

satisfied. This simple fact seems to have escaped everybody's attention for decades!

An illustrated overview

Apparently, a picture is worth a thousand words. If this is true, then Figures 1–3 provide us with several thousand words worth of information. The captions and the next sections give a complete description of these three basic diagrams. Figure 1 is a modified version of the flow chart originally proposed by Heller [7••–10••]. It provides a clear picture of the different physical effects that control capillary electrophoresis (CE) resolution. In Figure 2, we present a schematic mobility-size ($\mu - M$) diagram that shows the key separation regimes for DNA CE. Regimes II and III correspond, respectively, to the Ogston and reptation regimes (see below). Finally, Figure 3 presents a schematic field-size ($E - M$) phase diagram showing the different regimes. We added three critical lines (A–C) that highlight some of the less understood factors that seem to affect DNA sequencing.

The Ogston regime

The low-field electrophoresis of small analytes in a gel of concentration C (Figure 2, regime II) is often interpreted using the Ogston model [11–13], which assumes that the ratio $\mu(C)/\mu(C=0)$ is equal to the fractional gel volume $\phi(C)$ the analyte can visit during migration. Geometric models relating ϕ, C, the particle radius R and the mean pore size $a(C)$ then complete the model. For example, Ogston's calculation for random gels predicts that (for $R < a$) [11,13]

$$\frac{\mu(C)}{\mu_0} = \phi(C) = \mathrm{e}^{-KC} = \mathrm{e}^{-\frac{\pi}{4}\left(\frac{R}{a}\right)^2} \qquad (2)$$

where $K \sim R^2$ is the retardation factor and $a \sim C^{-1/2}$. Equation 2 readily suggests to plot $\ln(\mu)$ versus C (the Ferguson plot) and to infer the mean pore size a from the size R of the particle for which $\mu/\mu_0 \cong 1/\mathrm{e}$. But, it is hard to test this assumption since ϕ cannot easily be measured. Instead, our group used a lattice model of gel electrophoresis [14–18,19•] to demonstrate that the mobility should in fact be written as a polynomial function in $1 - \phi$ of which the coefficients depend on the gel structure. Using various theoretical methods, other authors have also concluded that $\phi(C)$ is not sufficient to describe sieving in tortuous media [20–24]. For random gels, we suggested the alternative relation [19•]

$$\frac{\mu(C)}{\mu_0} \cong \frac{1}{1+\frac{2}{3}(1-\phi)} = \frac{1}{1+KC} \qquad (3)$$

Figure 2

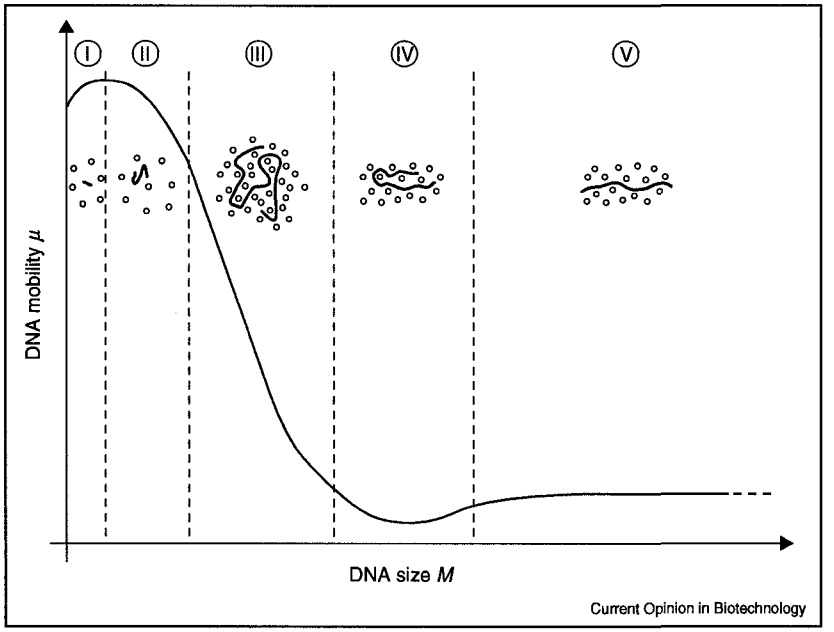

DNA separation in a sieving matrix: a schematic diagram showing a generic mobility (μ) versus size (M) relationship. Five different regimes are shown (with cartoon pictures of the mechanisms at play for each; note that the circles represent the polymer/gel fibres whereas the strands are DNA fragments). I, Short, rod-like DNA molecules migrate essentially as if in free-flow, and the mobility sometimes increases slightly with DNA size [4]. II, The Ogston regime. Short random-coil fragments are well-sieved by the porous matrix. III, Large DNA molecules must reptate head first through the maze. If they do not deform/orient, the mobility is a strong function of the DNA size and separation is possible. IV, In the intermediate size regime, DNA molecules may get trapped in U-shaped conformations. If this happens, a shallow minimum appears and the mobility ceases to be a monotonic function of the DNA size [1••]. V, Large DNA molecules orient in the field direction and no separation is possible.

Unlike Equation 2, this relation predicts concave Ferguson plots, which is a common situation. Nevertheless, Ferguson plots remain useful in practice. It is not clear whether such models, which assume rigid spherical analytes, apply to the separation of small semi-flexible DNA molecules. Moreover, these are low-field models. High fields might lead to new physics, such as DNA deformation around obstacles and pulley effects [25,26].

DNA reptation in gels

The migration of longer DNA fragments in gels is best described by the biased reptation model with fluctuations (BRF) of Viovy and colleagues [27], a generalization of the earlier biased reptation model [28,29]. Applicable when the DNA molecule is too large to fit inside a single pore and is forced to deform and migrate head-first through the gel, the BRF utilizes the concept of a tube within which the DNA migrates. As the chain migrates through the gel, it creates (chooses) new tube sections of length a, the mean gel pore size. The electric forces orient these chain sections to minimize their potential energy. The BRF also allows for reptation tube length fluctuations during the migration. In the BRF, the DNA size is measured in terms of the number N of pores occupied by the DNA 'snake' (of course, $N \sim M$), while the scaled field intensity is defined as in [1••]

$$\varepsilon = \frac{\eta a^2 \mu_0 E}{k_B T} \tag{4}$$

where η is the solvent's viscosity. The reptation model predicts three different regimes (Figure 2): in regime III, small DNA molecules retain a random-coil conformation during migration, leading to a $\mu \sim \varepsilon^0/N^1$ behaviour and excellent separation; V, is a plateau regime where long molecules orient and migrate at a common velocity ($\mu \sim \varepsilon^1 N^0$); and IV represents an intermediate regime (around $N\varepsilon \cong 1$), where the mobility is minimum and molecules assume U-shaped conformations (this is usually of negligible importance). Viovy [1••] proposed the following useful interpolation formula based on the predictions of the BRF

$$\frac{\mu}{\mu_0} \approx \left[\left(\frac{1}{3N}\right)^2 + \left(\frac{2\varepsilon}{5+2\beta\varepsilon}\right)^2\right]^{1/2} \tag{5}$$

where $1/\beta$ gives the ratio μ/μ_0 for very strong fields. The predictions of the BRF have been confirmed experimentally by many authors [1••,7••–10••,30]. Equation 5 is

Figure 3

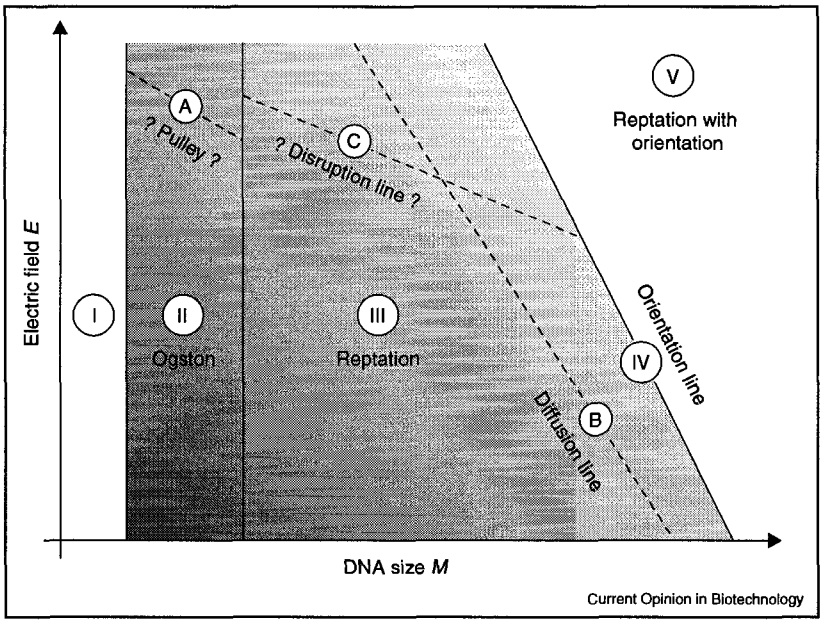

Schematic phase diagram for the separation of DNA molecules in gels or polymer solutions. The roman numerals correspond to the regimes shown in Figure 2. Regime IV is shown as a line as it is the place where molecular orientation starts and resolution disappears. Three lines were added: A, B and C. A, It is quite possible that small but flexible DNA molecules undergo a coil-to-pulley transition at high fields wherein the electric forces lead to chain deformation upon collision with the matrix fibres. Such an effect has not been studied, but may very well become important when using extremely high fields for single nucleotide polymorphism (SNP) analysis. B, The diffusion line. The diffusion coefficient (hence, the peak widths) increases rapidly beyond a certain line, and this happens before the DNA molecules orient in the field direction (line IV). This is the main limiting factor for DNA sequencing and it is due to the fact that the field actually accelerates the diffusion processes. C, The disruption line. Long DNA molecules can probably disrupt the polymer entanglements of the matrix (this cannot happen in a gel). The location of this line is not known, but this process is believed to also limit sequencing of DNA by CE. DNA sequencing normally takes place in the shaded areas, and better results are obtained in the darker areas, near the bottom left corner.

valid for the usual experimental situation wherein the pore size is greater than the Kuhn length of the DNA (when the opposite is true, the BRF predicts many new mobility regimes [1••,3,27]).

Vital to an accurate analysis of the sources of band broadening and to system optimization, are the three diffusion regimes predicted by the BRF

$$D \sim \frac{1}{N^2} \quad N < \varepsilon^{-2/3} \tag{6a}$$

$$D \sim \frac{\varepsilon}{N^{\frac{1}{2}}} \quad \varepsilon^{-1} > N > \varepsilon^{-2/3} \tag{6b}$$

$$D \sim \varepsilon^{\frac{3}{2}} \quad N > \varepsilon^{-1} \tag{6c}$$

Often unappreciated is the fact that in the second regime (6b), which comes into play before the mobility becomes size-independent, D increases with field and decreases rather slowly with DNA size. These predictions were nicely confirmed by Tinland and colleagues [31,32]. Therefore, Figure 3 shows that sequencing starts failing close to the diffusion line (B) (see Equation 6b), and not close to the orientation line (IV), as is usually assumed.

Equations 5 and 6 provide a complete analysis of gel electrophoresis of large DNA. The BRF (correctly) predicts that high fields orient DNA molecules, reduce peak spacing and increase diffusional band broadening. One must therefore choose the proper combination of pore size, elution length and field intensity to achieve a given separation in a minimal amount of time. However, these equations also indicate that diffusion imposes a strict limit on the number of bases one can sequence. With typical experimental numbers, this limit is found to be in the 1000–1500 base pair range, in agreement with current data.

Reptation and entangled polymer solutions

Polymer solutions have replaced gels because the latter cannot easily be used in capillaries. As the polymer entanglements have finite lifetimes, we cannot assume that such solutions behave like cross-linked gels for DNA separation/sieving. Indeed, the polymer molecules also

reptate, and this tends to 'release' the matrix 'constraints' that force DNA molecules to reptate. In essence, the 'gel' slowly moves away from the path taken by a DNA fragment. Viovy and Duke [33] examined this issue and concluded that the DNA's total mobility μ_{tot} is given by

$$\mu_{tot} = \mu_{rep} + \mu_{CR} \quad (7)$$

where μ_{rep} is due to DNA reptation (adequately described by the theory of DNA reptation in gels), and μ_{CR} is due to constraint release. Unfortunately, theory predicts that the additive term μ_{CR} is the same for all DNA molecules. Therefore, one cannot separate DNA molecules if $\mu_{CR} \gg \mu_{rep}$. The only way to ensure that constraint release remains negligible is to use a strongly entangled polymer solution. This is the case if its concentration C greatly exceeds the concentration C^* at which entanglements start to form. For a polymer with a radius of gyration R_g, C^* simply corresponds to one polymer molecule in a volume $\sim R_g^3$.

How should we define a 'reptation mean pore size' here? While one can easily define a pore size in a cross-linked gel, it is not so easy in a polymer solution where the entanglements form, move and disappear. Polymer physicists have invented the concept of polymer 'blobs' to describe the mean spacing between entanglements in polymer solutions [34]. According to Grossman and Soane [35], it is the blob size that matters when DNA reptation takes place in entangled polymer solutions. The blob size is given by

$$a = 2.86 R_g \left(\frac{C}{C^*}\right)^{-3/4} \quad (8)$$

Note that we have $\alpha \sim C^{-3/4}$ here, while Ogston's calculation for a gel predicts $\alpha \sim C^{-1/2}$.

On the one hand, we want $C \gg C^*$ to limit constraint release, but on the other hand, $C \gg C^*$ may mean extremely small pore sizes, a situation which does not allow very large DNA fragments to be resolved (small DNA molecules, however, are better resolved at high concentrations [7••–10••]). This is why very high molecular weights (and low polydispersity) are preferred: one can then get the best of both worlds and benefit from large pore sizes and long-lived entanglements. Indeed, the longest read lengths ever achieved made use of extremely large molecular weight linear polyacrylamide solutions with low polydispersity and relatively low concentrations [36].

To evaluate different polymers, one must use equal blob sizes. Any other test (e.g. at fixed concentration) would be equivalent to comparing apples and oranges. This is why it is rather difficult to determine which polymers possess the best performance by looking at the published results. We strongly recommend the experimental approach proposed by Cottet, Gareil and Viovy [37] to understand polymer solutions.

Finally, it should be mentioned that the theory leading to Equation 7 assumes that reptation and constraint release are two independent mechanisms. In fact, it is widely believed that long DNA molecules can actually deform the polymer matrix during their migration, which would accelerate constraint release, decrease peak spacing and probably increase peak widths (see line C in Figure 3). This point has yet to be studied carefully.

Dilute solutions

Barron *et al.* [38] first illustrated the unexpected separation of dsDNA using dilute ($C < C^*$) solutions of neutral polymers along with a qualitative explanation of the relevant mechanism, the 'transient entanglement mechanism' wherein the DNA undergoes repeated collisions with the free polymers. The balance between the rates of collision and disentanglement results in a size-dependent mobility $\mu(M)$ and hence separation is possible. The theory of Hubert *et al.* [39] later verified that such a mechanism can account for the DNA size-dependence of $\mu(M)$. Recent results by Ekani Nkodo and Tinland [40,41] suggest an additional effect, the collective dynamics of the polymer solution in the immediate vicinity of the DNA molecules.

Computational studies by Starkweather and coworkers [42,43••,44] and by Noguchi and Takasu [45–47] have explored this novel regime. Indeed, a transient entanglement mechanism is observed: the DNA undergoes collisions with the free neutral polymers subsequently forming U- or J-shaped conformations in the field direction, followed by release of the DNA downfield. These observations coincide with direct experimental observations of DNA collisions using fluoresence microscopy [48].

Although the use of dilute solutions to separate DNA affords many advantages (e.g. ease of integration in automated systems, lesser degradation of capillaries and possible shorter separation times), the details of efficient separation in dilute solutions remain elusive. In particular, band broadening and diffusion have been largely ignored.

Separating DNA without a sieving matrix

End-labeled free solution electrophoresis (ELFSE) is a separation process wherein the complications of a sieving matrix are eliminated [49,50]. Separations of streptavidin end-labeled ssDNA (S-DNA) by free solution CE have been achieved [50], made possible by the charge-to-friction ratio imbalance created by the streptavidin. Our theory [49] follows that of Long and coworkers [51] for the electrophoresis of polyampholytes. The

overall mobility for a DNA strand of M bases is found to be

$$\mu(M) = \frac{\mu_0}{1 + \frac{\alpha}{M}} \quad (9)$$

where α is the size (in bases) of a DNA section that would have the same friction coefficient as the streptavidin. Interestingly, as α depends on DNA stiffness, the measured mobility yields the DNA persistence length. Theory also predicts that the S-DNA molecule remains a random-coil up to fields ~10 kV/cm. Therefore, the diffusion coefficient is expected to still scale like $D \sim 1/R_g$ (yet to be confirmed). Based on these elements, we predicted that an ELFSE label about 10 times larger than streptavidin could allow sequencing of 500–1000 bases in less than an hour. Finding this label has been the stumbling block of ELFSE, and available data only show sequencing of ~100 bases in ~10 min.

Conclusions

DNA sequencing is one of the most important applications of CE. The current technology has allowed us to sequence the human genome and the genomes of several other organisms; however, we certainly cannot claim to have a complete understanding of the processes. For example, the separation of small fragments, typical of single nucleotide polymorphism (SNP) analysis, falls under the ill-understood Ogston regime. Also, diffusional band broadening and matrix deformation/rupture in polymer solutions have not been investigated. Clearly, there is much room for improvement in the case of this mature technology, especially as microfluidic formats (and extremely high electric fields) are likely to replace capillaries in the next few years.

Among the developments to watch out for in the next few years are the use of polymer concentration gradients [52], a new pulsed-field ratcheting scheme [53], the use of entropy as a means to separate polymers in channels [54,55], the use of empirical mobility functions which describe all separation regimes at once [56], and the separation of DNA molecules in dilute polymer solutions [38,43••] or by ELFSE [50]. Theory, computer simulations and systematic experimental investigations will remain necessary for sustained progress in the CE analysis of DNA molecules.

Acknowledgements

This work was supported by a Discovery Grant from the Natural Sciences and Engineering Research Council (NSERC) of Canada to GWS, and by scholarships from NSERC and the University of Ottawa to LCM, MK and MGG.

References and recommended reading

Papers of particular interest, published within the annual period of review, have been highlighted as:

- • of special interest
- •• of outstanding interest

1. Viovy JL: **Electrophoresis of DNA and other polyelectrolytes: physical mechanisms.** *Rev Mod Physics* 2000, **72**:813-872.
•• This is the most comprehensive and in-depth review of the theory of DNA electrophoresis. Viovy has contributed enormously to the field, and this review covers most of the important subtopics that are relevant here. An extensive list of references is provided. Although already two years old, this is still the recommended starting point for someone who wants to attain an understanding of the theoretical concepts of DNA separations by electrophoresis.

2. Pulsed-field gel electrophoresis. *Methods in Molecular Biology*, vol 12. Edited by Burmeister M, Ulanovsky L. Totowa: Humana Press; 1992.

3. **Analysis of nucleic acids by capillary electrophoresis.** Edited by Heller C. Germany: Vieweg & Sohn Verlagsgesesellschaft mbH; 1997.

4. Mohanty U, Stellwagen NC: **Free solution mobility of oligomeric DNA.** *Biopolymers* 2002, **49**:209-214.

5. Hoagland DA, Arvanitidou E, Welch C: **Capillary electrophoresis measurements of the free solution mobility for several model polyelectrolyte systems.** *Macromolecules* 1999, **32**:6180-6190.

6. • Ekani Nkodo A, Garnier JM, Tinland B, Ren H, Desruisseaux C, McCormick LC, Drouin G, Slater GW: **Diffusion coefficient of DNA molecules during free solution electrophoresis.** *Electrophoresis* 2001, **22**:2424-2432.
An experimental investigation of the diffusion coefficient D of ssDNA and dsDNA fragments during free-flow CE. The results clearly demonstrate that diffusion is not affected by the field (one could say that the DNA molecules are not free-draining for diffusion), and that the diffusion coefficient is inversely proportional to the radius of gyration $R_g(M)$ of the fragment. These are fundamental results for CE.

7. •• Heller C: **Principles of DNA separation with capillary electrophoresis.** *Electrophoresis* 2001, **22**:629-643.
Together with [8••–10••], this forms a remarkable series of four single-authored papers that examine the separation of DNA fragments by CE. Heller uses his knowledge of the theoretical principles to extract as much information as possible from the experimental data. The importance of peak width and peak spacing are well described, and the concept of blobs and entanglements are introduced. This series provides a guide for experimentalists who want to fully characterize a DNA separation system based on entangled polymer solutions and CE.

8. •• Heller C: **Influence of electric field strength and capillary dimensions on the separation of DNA.** *Electrophoresis* 2000, **21**:593-602.
See annotation for [7••].

9. •• Heller C: **Separation of double-stranded and single-stranded DNA in polymer solutions: II. Separation, peak width and resolution.** *Electrophoresis* 1999, **20**:1978-1986.
See annotation for [7••].

10. •• Heller C: **Separation of double-stranded and single-stranded DNA in polymer solutions: I. Mobility and separation mechanism.** *Electrophoresis* 1999, **20**:1962-1976.
See annotation for [7••].

11. Ogston AG: **The spaces in a uniform random suspension of fibres.** *Trans Faraday Soc* 1958, **54**:1754-1757.

12. Morris CJOR: **Gel filtration and gel electrophoresis.** *Protides of the biological Fluids, 14th Colloquium.* Edited by Peeters H. Elsevier, New York, 1967, pp 543-551.

13. Rodbard D, Chrambach A: **Unified theory of gel electrophoresis and gel filtration.** *Proc Natl Acad Sci USA* 1970, **65**:970-977.

14. Slater GW, Guo HL: **An exactly solvable Ogston model of gel electrophoresis: I. The role of the symmetry and randomness of the gel structure.** *Electrophoresis* 1996, **17**:977-988.

15. Slater GW, Guo HL: **An exactly solvable Ogston model of gel electrophoresis II. Sieving through periodic gels.** *Electrophoresis* 1996, **17**:1407-1415.

16. Slater GW, Treurniet JR: **An exactly solvable Ogston model of gel electrophoresis III. Percolation and sieving through two-dimensional gels.** *J Chromatogr A* 1997, **772**:39-48.

17. Mercier J-F, Slater GW: **An exactly solvable Ogston model of gel electrophoresis: IV. Sieving through periodic three-dimensional gels.** *Electrophoresis* 1998, **19**:1560-1565.

SOFT MATERIALS
Vol. 2, Nos. 2&3, pp. 155–182, 2004

Deformation, Stretching, and Relaxation of Single-Polymer Chains: Fundamentals and Examples[#]

Gary W. Slater,* Yannick Gratton, Martin Kenward, Laurette McCormick, and Frédéric Tessier

Department of Physics, University of Ottawa, Ottawa, Ontario, Canada

ABSTRACT

We review the basic theory for the static and dynamic properties of ideal and real chains. We describe the stretching of single ideal chains in both the strain and the stress ensembles, give scaling arguments for the deformation of real chains, and also consider the impact of chain rigidity by discussing the stretching of worm-like chains. We complement this theoretical outlook with specific examples that highlight the relevance of the single-molecule deformation in a practical perspective: the translocation of a macromolecule over a potential barrier, the collision of a single chain with fixed obstacles or other chains, the dynamics of a thethered chain in a strong shear flow, and some remarkable predictions concerning the deformation of composite chain molecules during free-solution electrophoresis.

Key Words: Polymer dynamics; Polymer stretching; Separation science; Microfluidics.

[#]This article is a corrected version of a paper which has already appeared in *Soft Materials* [G. W. Slater, Y. Gratton, M. Kenward, L. McCormick, F. Tessier, *Soft Materials* 1, 365 (2003)]. Due to problems in the publishing process at the time, the original publication contained an excess of errors. This was not the fault of the authors. The editors wish to apologise to authors and readers. Florian Müller-Plathe, Editor-in-Chief.

*Correspondence: Gary W. Slater, Department of Physics, University of Ottawa, 150 Louis-Pasteur, Ottawa, Ontario, Canada, K1N 6N5. E-mail: gslater@science.uottawa.ca.

DOI: 10.1081/SMTS-200056264 1539-445X (Print); 1539-4468 (Online)

INTRODUCTION

Numerous practical problems involve the deformation (and the subsequent relaxation) of single polymer chains by external factors (forces, fields, confinement, etc.).[1] Although this fully justifies why scientists study the statistical properties of single-polymer chains under various constraints, such investigations are also important for fundamental reasons. First, single-molecule studies represent a strong test of our understanding of basic physics; for instance, we can access microscopic information such as molecular conformations and trajectories, not only ensemble averaged values. Second, the simplicity of such problems suggests that it should be possible to develop models with fewer approximations, thus leading to exact solutions. Third, current computing power makes it possible to simulate many single-molecule problems with atomistic or united-atom molecular dynamics algorithms.[2–5] Finally, current experimental techniques such as single-molecule fluorescence microscopy allow us to visualize single-polymer molecules for long periods of time, thus allowing us to test our models and simulations in great detail.[6] It should also be mentioned that our understanding of many-chain problems implicitly relies on our knowledge of the behavior of single-polymer chains in various environments.[7–10]

In this review article, we present some basic theoretical ideas as well as several problems related to deformed polymers in good solvents. The selection of topics is obviously based on the personal interests of the authors. We begin with a short summary of the equilibrium properties of single polymers. The second section describes the physics of polymer chains stretched by external forces. In the third and fourth sections, we look at the role of polymer deformation on the sieving properties of new microfluidic devices. A related problem, that of tethered polymer chains stretched by strong flows, is examined in the fifth section. In some cases, free polyelectrolytes may stretch during electrophoresis because of subtle electromechanical effects; we present such an example in the last section.

An isolated polymer placed in a good solvent, subjected to Brownian motion induced by the surrounding fluid, behaves like a three-dimensional random-walk (RW) with nodes that move randomly while keeping the connectivity of the chain. In reality, however, backbone rigidity (BR), as well as excluded volume (EVI) and hydrodynamic (HI) interactions, often modify this simplistic picture in nontrivial ways. Nevertheless, because RW models can be solved exactly, they still play a major role in polymer science. Our approach in this Introduction will thus be to introduce RW concepts first, and then to discuss the impact of nonideal factors such as BR, EVI, and HI.

Static Properties of Polymer Chains

The freely jointed chain (FJC), the simplest possible model of a polymer (Fig. 1a), is a series of N links of fixed length b connected by perfect joints.[9] The mean square end-to-end distance $\langle h^2 \rangle$ of a RW is given by the exact result

$$\langle h^2 \rangle = Nb^2. \tag{1}$$

For long chains, the probability distribution function $p(h)$ becomes Gaussian:

$$p(h) \sim \exp\left(-\frac{3h^2}{2\langle h^2 \rangle}\right) = \exp\left(-\frac{3h^2}{2Nb^2}\right) \quad N \gg 1; \quad h \ll Nb. \tag{2}$$

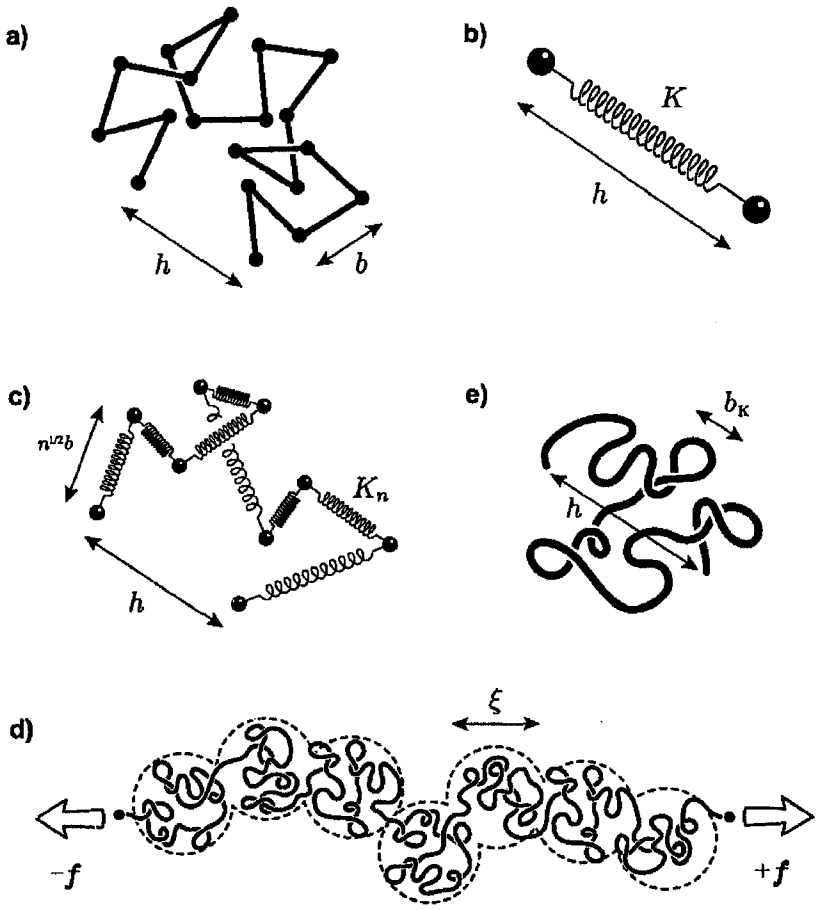

Figure 1. a) The freely-jointed chain (FJC) is made of N links of fixed length b. Since there is no constraint on the angle between two consecutive links, we have $\langle h^2 \rangle = Nb^2$. b) The dumbbell: two beads are connected by an entropic spring with a spring constant $K = 3k_BT/Nb^2$, giving it a mean thermodynamic extension $\langle h^2 \rangle = Nb^2$. The spring replaces the N links of the FJC. c) The Rouse chain: groups of n links are replaced by a spring (K_n) and a bead. The bead-spring chain is made of M springs and $M+1$ beads, and we still have $\langle h^2 \rangle = Nb^2$. d) The Pincus blobs for a stretched chain. e) A worm-like chain (WLC) is characterized by the Kuhn length b_K that plays the role of the segment size b in the FJC.

The statistical properties of the end-to-end vector $\boldsymbol{h}$ are thus identical to those of a "dumbbell" consisting of two beads connected by a harmonic spring of strength:

$$K = \frac{3k_BT}{Nb^2} = \frac{3k_BT}{\langle h^2 \rangle}. \tag{3}$$

Indeed, the spring potential energy $U = 1/2Kh^2$ then leads to a Boltzmann distribution given precisely by Eq. (2). This is called an "entropic spring" because $\ln(p(h)) \propto K$ is related to the entropy of polymer conformations with an end-to-end distance h. For a

given value of h, the entropic force keeping the chain ends together is thus given by

$$f(h) = \frac{\partial(1/2\ Kh^2)}{\partial h} = \frac{3k_BT}{Nb^2}h. \tag{4}$$

This indicates that the equilibrium length of the spring is zero.

Although long RW chains can be replaced by two beads and an entropic spring (Fig. 1b), such a dumbbell model cannot describe short length scales. Because RWs are additive, however, we can use $M>1$ springs and $M+1$ beads instead of a dumbbell (Fig. 1c). We thus replace $n < N$ consecutive links of length b by an entropic spring (of mean length $n^{1/2}b$) with an elastic constant $K_n = 3k_BT/nb^2$. The end-to-end distance of the resulting chain of $M+1$ "beads" and $M = N/n$ springs is conserved: $\langle h^2\rangle = M \times (nb^2) = Nb^2$. This bead-spring (or "Rouse") chain has the same statistical properties as the FJC. However, the Rouse chain also allows one to calculate dynamical properties.

Dynamics of Polymer Chains

A polymer chain in a good solvent continuously changes conformation in response to random Brownian forces. The equilibrium dynamics of a Rouse chain (Fig. 1c) can be analyzed in terms of relaxation (normal) modes. With harmonic springs, we can actually decouple these modes. If $R \equiv \{R_1, \ldots, R_N\}$ are the positions of the N Rouse beads, the Langevin equation of motion can be written as (in matrix form):

$$\zeta\frac{\partial R(t)}{\partial t} = -KAR + \Phi(t). \tag{5}$$

The forces acting on the beads are: the friction with the solvent (ζ is the bead's friction coefficient), the forces due to the entropic springs connecting the beads ($-KAR$), and finally the stochastic forces $\Phi(t)$ due to the collisions with the solvent molecules (these forces have a zero-mean Gaussian distribution). Inertia is neglected because we are in a viscous fluid. This system of coupled harmonic oscillators is fully defined by the $N \times N$ force matrix A. For a linear chain, we can diagonalize the tri-diagonal matrix A to obtain the frequencies and amplitudes of the modes. The eigenvalues of A are given by

$$\lambda_i = 4\sin^2\left(\frac{i\pi}{2N}\right) \cong \left(\frac{i\pi}{N}\right)^2 \qquad i = 0, 1, 2, \ldots, N-1, \tag{6}$$

where the last result applies when $i \ll N$. Eigenmode i ($i \geq 1$) describes chain relaxation on an intermediate length scale that corresponds to the relative motion of chain "blobs" containing N/i Rouse elements. The translation of the center of mass (the 0-th mode) predicts that the diffusion coefficient should scale like $D \sim 1/N$. Note that this result can also be derived from the Central Limit Theorem, because the beads of the Rouse chain are hydrodynamically independent, such a chain is called a free-draining chain.

Of particular interest is the relaxation of the chain as described by the decay of the autocorrelation function for the end-to-end vector $\boldsymbol{h}(t)$:

$$C(t) \equiv \frac{\langle \boldsymbol{h}(t)\cdot\boldsymbol{h}(0)\rangle}{\langle h^2\rangle} = \frac{8}{\pi^2}\sum_{i:odd}\frac{1}{i^2}\exp\left(-\frac{t}{\tau_i}\right). \tag{7}$$

The global equilibrium conformation of a Rouse chain thus relaxes (i.e., loses memory of its initial state) following a sum of exponentials with characteristic times:

$$\tau_i = \frac{\zeta}{\lambda_i K} \cong \frac{1}{i^2} \times \frac{\zeta N^2 b^2}{3\pi^2 k_B T} \equiv \frac{1}{i^2} \times \tau_1, \tag{8}$$

The long-time ($t > \tau_3 = \tau_1/9$) decay is described by the *terminal* relaxation time $\tau_1 \sim N^2$.

We recently examined the relaxation of Rouse chains with random spring constants.[11] Although such disorder can lead to broad distributions of relaxation times, the relaxation spectrum retains well-separated modes. Therefore, random chains still decay according to a single exponential at long times. However, the long-time relaxation of ensembles of random chains is better described by a stretched exponential:

$$C(t) = \exp\left(-\left[\frac{t}{\tau}\right]^{\beta}\right), \tag{9}$$

where the stretched exponent $0 < \beta \leq 1$ decreases with increasing disorder. Such behavior has been reported for complex disordered systems, including randomly branched polymers.[12]

Real Chains and Real Solvents

Adding HI and EVI to the Rouse model is more realistic, but it leads to models that cannot be solved exactly. One must then rely on scaling arguments.[7] The inclusion of EVI leads to chain swelling, and Eq. (1) then becomes

$$\langle h^2 \rangle \cong N^{2\nu} b^2. \tag{10}$$

Here, Flory's exponent $\nu \cong 3/5$ replaces the RW value $\nu = 1/2$, and b is an effective segment size. The swelling driven by EVI is more important for longer polymer chains. A direct impact of this swelling is the reduction of the entropic spring constant now given by

$$K \cong \frac{3k_B T}{\langle h^2 \rangle} \sim \frac{1}{N^{2\nu}} \sim \frac{1}{N^{6/5}}. \tag{11}$$

EVI reduce the entropy of swollen chains, thus softening the entropic springs.

HI affect only the dynamics of a chain. Zimm showed that HI transform the free-draining chain into a hydrodynamically impermeable coil with a friction coefficient given by[8]

$$\zeta_H = 6\pi\eta R_H, \tag{12}$$

where η is the solvent's viscosity, and $R_H \sim \langle h^2 \rangle^{1/2} \sim N^{\nu}$ is the chain's hydrodynamic radius. Furthermore, the diffusion coefficient now scales like $D = k_B T/\zeta_H \sim N^{-\nu}$. The scaling relation $D_\tau \sim R_H^2$ then leads to the scaling of the chain terminal relaxation time:

$$\tau_1 \sim \frac{R_H^2}{D} \sim R_H^2 \sim \langle h^2 \rangle^{3/2} \sim N^{3\nu}. \tag{13}$$

These changes to the various laws actually introduce qualitatively different physical effects in many situations of practical interest.[7]

PULLING THE ENDS: THE FINITE EXTENSIBILITY OF POLYMER CHAINS

Although a FJC cannot be stretched beyond its maximum extension $h_{max} = Nb$, harmonic springs do not have such a limitation. Therefore, the spring-bead models described in the previous sections cannot be used to study the effect of extensional forces on FJCs (unless we remain in the $h \ll h_{max}$ range). For a more realistic physical picture, a nonharmonic spring with finite extensibility is required, i.e., we need an entropic spring potential that diverges when $h = h_{max}$. Such springs are called finitely extensible nonlinear elastic (FENE). Unfortunately, most FENE potentials actually change the exact mean value $\langle h^2 \rangle = Nb^2$. In this section, we derive FJC FENE potentials in the stress and strain ensembles. We also examine the stretching of real chains by external forces.

Stretching an Ideal FJC: the Stress Ensemble

Here, fixed forces f are applied to the chain ends, and the end-to-end distance h fluctuates (h and f are conjugate thermodynamic variables, much like P and V, or H and M). We thus want to compute the mean value $\langle h(f) \rangle$. Each FJC segment is like a dipole forced to orient in the direction of an external field. The exact solution to this problem is well-known:[13]

$$\frac{\langle h(F) \rangle}{h_{max}} = L(F) \equiv \coth(F) - \frac{1}{F} \cong \begin{cases} \frac{1}{3}F - \frac{1}{45}F^3 + \frac{2}{945}F^5 - O(F^7) & F \ll 1 \\ 1 - \frac{1}{F} & F \gg 1, \end{cases} \tag{14}$$

where $F = fb/k_BT$ is the scaled force and $L(F)$ the Langevin function. As expected, the harmonic result 4 is the first term $F/3$ of the $F \ll 1$ expansion, while $\langle h \rangle \to h_{max}$ when $F \to \infty$. Because the Langevin function cannot be inverted analytically, we must invert the series expansions to obtain a replacement for Eq. (4):

$$F(H) = L^{-1}(H) \cong \begin{cases} 3H + \frac{9}{5}H^3 + \frac{297}{175}H^5 + O(H^7) & H \ll 1 \\ \frac{1}{1-H} & 1 - H \ll 1, \end{cases} \tag{15}$$

where $H = \langle h \rangle / h_{max}$ tis the scaled chain extension. Simple interpolation formulas based on Eq. (15) can be constructed using the ratio of two polynomials; the simplest one is:[14]

$$F(H) \cong \frac{3H - H^3}{1 - H^2}. \tag{16}$$

Strangely, however, the Warner approximation[14] $F(H) = 3H/(1 - H^2)$, is more widely used, even though it overestimates the force by 50% close to full extension.

The stiffer FENE potential correctly limits the maximum spring extension to $h_{max} = Nb$, but it also reduces the spring equilibrium extension by a factor $\cong N/(N+1)$. Therefore, replacing a FJC by a Rouse chain that uses the FENE force defined by Eq. (14) does not conserve the size $\langle h^2 \rangle$ of the original molecule. This is because the stress ensemble actually describes the mean chain extension $\langle h(f) \rangle$ for a fixed external force f. In the Rouse model of polymer dynamics, on the other hand, we need to know the mean force $\langle f(h) \rangle$ pulling together the ends of an entropic spring with instantaneous end-to-end distance h. This problem is, in fact, related to the strain ensemble.

Stretching an Ideal FJC: The Strain Ensemble

Calculating the mean force $\langle f(h) \rangle$ given a fixed end-to-end distance h is quite a complicated problem. Although Treloar did derive an exact solution,[13] the latter is not analytic and cannot easily be used. More recently, Glatting et al.[15] developed an alternative (and analytic) approximate expression with the following limits:

$$F(H) \cong \begin{cases} \left(-\frac{3}{N}+3\right)H + \left(-\frac{99}{25N}+\frac{9}{5}\right)H^3 \\ \quad +\left(\frac{297}{175}-\frac{837}{175N}\right)H^5 + O(H^7) & H \ll 1 \\ \frac{1}{NH}+\frac{N-2}{N(1-H)} & 1-H \ll 1. \end{cases} \tag{17}$$

Thus, the two ensembles simply differ by factors of order $1/N$ [compare Eqs. (15) and (17)] and thus become identical in the thermodynamic limit $N \gg 1$, as expected. The simplest interpolation formula is now:

$$F(H) \cong \frac{3(1-(1/N))H - (1+(1/N))H^3}{1-H^2} \tag{18}$$

This expression, which gives the leading terms of Eq. (17) in both limits, is quite good for the whole range of extensions $H \in [0,1]$, even for very small values of N. It is important to realize that the properties of the entropic springs now depend on N, the number of polymer segments they replace in the construction of a Rouse chain. With strain-ensemble FENE potentials, the exact relation $\langle h^2 \rangle = Nb^2$ is now satisfied to a very high degree of accuracy (the error is of order $1/N^2$). In conclusion, in order to replace a given FJC by a series of beads and springs that has the proper maximum extension *and* mean square end-to-end distance, we need a strain-ensemble FENE potential.

Stretching a Real Chain: Scaling Arguments

In the absence of exact solutions for EVI chains, we will rely on scaling arguments to study a real chain being stretched by constant forces $\pm f$ applied at both ends—the stress ensemble. We can actually predict the existence of four different regimes

here. In the low-force limit, the spring constant of Eq. (11) gives the linear regime (using $f \sim Kh$):

$$\text{I: } \frac{\langle h \rangle}{b} = \frac{1}{b} \times \frac{f}{K} \cong \frac{N^{2\nu} b}{k_B T} f \cong N^{2\nu} F \sim N^{6/5} f^1, \qquad F < N^{-\nu}. \tag{19}$$

The linear regime applies only to small deformations $\langle h \rangle < N^{\nu} b$. For a given scaled force F, Eq. (19) is thus limited to chains with $N < g \cong F^{-1/\nu}$ segments; the corresponding critical coil size is $\xi = \langle h(g) \rangle = g^{\nu} b \cong b/F$. The so-called Pincus regime[16] occurs when $\xi < \langle h \rangle \ll Nb$. The polymer conformation is then an ideal chain of N/g aligned "Pincus blobs" of size ξ (Fig. 1d), and the chain conformation inside each blob is essentially unperturbed by the external force. The extension is given by

$$\text{II: } \frac{\langle h \rangle}{b} \cong \frac{N}{g} \times \frac{\xi}{b} \cong N \times N^{1/\nu - 1} \sim N^1 f^{2/3}, \qquad N^{-\nu} < F < 1. \tag{20}$$

The change from $\langle h \rangle \sim f^1$ to $\langle h \rangle \sim f^{2/3}$ is quite radical.

EVI can be neglected when the chain is highly stretched. This occurs roughly when $F \cong 1$. In this regime, one is back to a FJC, and we should recover Eq. (14):

$$\text{III: } \frac{\langle h \rangle}{b} \cong N \times \left(\coth(F) - \frac{1}{F} \right) \cong N^1 \times \left(1 - \frac{1}{F} \right), \qquad F > 1. \tag{21}$$

Finally, the last regime (IV) is found when the force is large enough to disturb the chemical bonds, such that we may get $h > Nb$. The behavior of the chain is then nonuniversal, i.e., it is related to its chemical structure. Beyond a certain critical force, one may even observe chain scission. These effects are beyond the scope of this article.

Worm-Like Chains

In this section, we neglect EVI and instead explore the effects of finite rigidity. Indeed, real polymers possess nonzero bending rigidity (BR), which is usually described in terms of a Kuhn length b_K.[9] If L_c is the contour length of such a semiflexible polymer chain (Fig. 1e), Eq. (1) can be rewritten as $\langle h^2 \rangle = bL_c$, with $L_c = Nb$. With BR, the polymer swells, and this relation is no longer valid. The Kuhn length of a polymer with BR is defined as the length which allows us to replace Eq. (1) by

$$\langle h^2 \rangle = b_K L_c \tag{22}$$

for very long polymer chains ($L_c \gg b_K$). If we further define $N_K \equiv L_c/b_K$ as the size of the polymer in terms of Kuhn lengths, we recover the equivalent of Eq. (1): $\langle h^2 \rangle = N_K b_K^2$. In other words, a long semiflexible chain behaves like a normal FJC chain if we replace the real segment (or monomer) size b by the Kuhn length b_K.

For shorter chains, however, Eq. (22) is inadequate. A detailed calculation, based on the theory of worm-like chains (WLC) actually gives the following expression:[9]

$$\langle h^2 \rangle = b_K \times \left[L_c + \frac{b_K}{2} (e^{-2L_c/b_K} - 1) \right] \cong \begin{cases} L_c^2 & L_c \ll b_K \\ b_K L_c & L_c \gg b_K \end{cases}. \tag{23}$$

The properties of semiflexible chains are still poorly understood. Because DNA is very rigid ($b_K = 100$ nm) and has been extensively studied using, e.g., optical tweezers and AFMs, there has been a growing interest in the theory of WLCs over the last decade. Of central interest is the force-extension relation for semiflexible chains in the stress ensemble. The presence of a bending potential changes the physics in a fundamental way, and Eq. (15) is no longer applicable. The most used WLC force-extension law is the interpolation formula derived by Marko and Siggia:[17]

$$F_K(H) = 2H = \frac{1}{2} + \frac{1}{2(1-H)^2} \cong \begin{cases} 3H + O(H^2) & H \ll 1 \\ \dfrac{1}{2(1-H)^2} & 1 - H \ll 1, \end{cases} \tag{24}$$

where the scaled force is now given by $F_K = fb_K/k_BT$, because b_K is the relevant segment length for a semiflexible chain. We note that to first order, the weak force result $F_K \cong 3H$ is identical to the one found for the FJC [see Eq. (15)]. The stretching process actually follows two steps. First, the effective segments orient along the direction dictated by the external force, and the semiflexible nature of the chain plays no direct role (besides a trivial redefinition of the segment length b_K). However, when $F_K > 1$, the force is large enough to affect the molecular conformation on scales smaller than the segment size b_K. In this second stage, the force begins to stretch the semiflexible effective segments. For instance, we note that Eq. (23) predicts that at equilibrium, the effective segments, which have a contour length b_K, possess a root mean square end-to-end distance of only $\cong (3/4)b_K$. This second stage thus requires additional energy. A useful way to compare these results is to look at the asymptotic behavior:

$$1 - H \sim \begin{cases} \dfrac{1}{F} & \text{FJC} \\ \dfrac{1}{\sqrt{F_K}} & \text{WLC.} \end{cases} \tag{25}$$

Close to full extension $H = 1$, the two models thus predict different power laws. For a given value of H, the force required to stretch a WLC is larger than that required to stretch a FJC. Experimental data for DNA[1] clearly indicates that the FJC formula (15) underestimates the force, and that the WLC law $(1 - H) \sim 1/\sqrt{F_K}$ applies.

More recently, Winkler[18] proposed a theory for semiflexible chains of Gaussian segments. For long chains ($L_c \gg b_K$), his work suggests the alternative force-extension law:

$$F_K(H) = \frac{3H}{(1-H^2)^2} \cong \begin{cases} 3H + 6H^3 + O(H^5) & H \ll 1 \\ \dfrac{3}{4(1-H)^2} & 1 - H \ll 1. \end{cases} \tag{26}$$

This result is slightly different from the Marko and Siggia formula, but it does agree with it in the two asymptotic limits. In particular, the $(1 - H) \sim 1/\sqrt{F_K}$ law still applies. In the short-chain limit ($L_c \ll b_K$), on the other hand, Winkler predicts

$$F_K(H) = \frac{3H \times (1 + (1/N_K))}{(1 - H^2)}. \tag{27}$$

Interestingly, this is essentially Eq. (16). We note that stretching the Kuhn segments to full extension also requires a force that scales like $F_K \sim 1/(1 - H)$.

POLYMER STRETCHING OVER POTENTIAL BARRIERS

The theoretical concepts introduced above have significant practical applications. Indeed, the deformation of single macromolecules can often improve—or in some cases lie at the very heart of—the operation of analytical devices. In particular, recent leaps in the designability of fluidic systems at the microscopic or even nanoscopic level offer unprecedented opportunities to modulate the conformation of individual macromolecules by means of molecular-scale obstacles and confinement. The induced conformational changes give rise to significant "entropic forces" that can be brought to serve a useful purpose, for example, sorting biopolymers according to size or topology (linear chain, ring, knot, etc.). The perspective adopted here is slightly different compared to the previous section, in that we are not actively deforming the polymer by pulling on its ends. Rather, we consider how a polymer deforms when it encounters a potential barrier, and how this deformation, in turn, affects how the polymer may escape from the potential well.

A striking example of the relevance of conformational entropy for the design of analytical tools is the entropic trap array built by the Craighead group.[19–23] Schematically represented in Fig. 2a, it consists of a microfluidic channel with alternating deep wells, where the polymer molecule sits comfortably, and shallow constrictions, which the molecule can only cross by adopting an elongated shape. Elongation incurs a large entropy cost, thus at equilibrium, the molecule is, in fact, confined to a given well (hence the name *entropic trap*). With an external force oriented along the channel direction, however, the molecule is encouraged to travel from one trap to the next by slithering across the constriction. The rate at which this *translocation* process occurs is determined by the balance between the external and the entropic forces.

The prevailing model for this system simply considers scaling relations for the change in free energy ΔF when a coil section of length x—a hernia—stretches out inside the constriction. For the case at hand, an electric field of strength E is pulling on a DNA

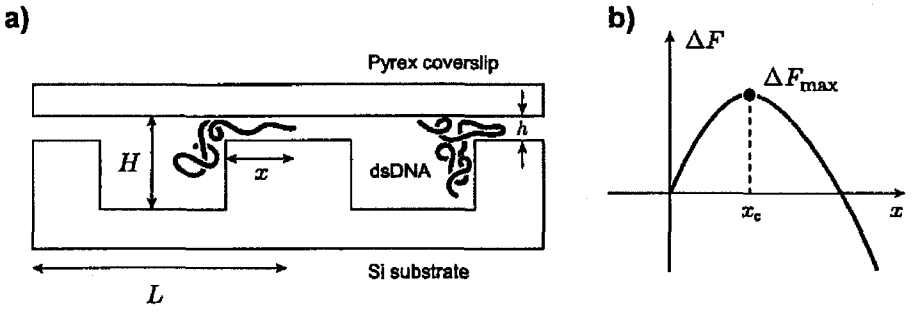

Figure 2. a) The microfluidic channel built by the Craighead research group to separate double-stranded DNA (dsDNA) according to size. In the actual devices, $H \approx 1$ μm, $h \approx 0.1$ μm, and the period L can range from a few microns to a few tens of microns. The molecules are pulled towards the right by an external electric field, but their migration is hindered by the shallow constrictions. b) A sketch of the change in the free energy ΔF of the molecules as a function of the hernia length x. The effective activation energy corresponds to the maximum of ΔF, which occurs at a critical hernia length x_c.

strand (a polyelectrolyte) inside the channel, so we have $\Delta F_{\text{entropic}} \sim x$ (because conformational entropy is an extensive molecular variable) and $\Delta F_{\text{electric}} \sim -x^2 E$ (because both the charge and the span of the hernia are proportional to x). Hence the total change in the free energy of the polymer as a function of hernia size follows

$$\Delta F \sim (x - x^2 E). \tag{28}$$

Eq. (28) reveals the presence of a potential barrier (see Fig. 2b), and differentiation predicts that both the critical hernia length x_c and the corresponding barrier height $\Delta F_{\max}$ scale like $1/E$. The net rate of crossing, κ, thus takes the Arrhenius form:

$$\kappa = \kappa_0 e^{-\Delta F_{\max}/k_B T} = \kappa_0 e^{-E_0/E}, \tag{29}$$

where κ_0 and $E_0 \sim 1/k_B T$ are independent of the field intensity E. In Eq. (29), there is no explicit dependence of the rate κ on the total number of monomers N, because we have overlooked the three-dimensional aspect of the system (going *into* the page in Fig. 2a). In reality, larger coils expose more monomers to the constriction than smaller ones, thus generate more herniae per unit time, and therefore increase their chances of escaping from the well. This contribution turns up as an N-dependence of the pre-factor κ_0, making size separation possible. Furthermore, the field E pushes the coil against the constriction, which enhances this effect. Note that although they lose more entropy in the narrow channel, longer molecules move faster here!

The system discussed above is, of course, but one example of a microdevice intended to manipulate and analyze macromolecules, and recent literature abounds in clever designs that exploit conformational behavior (stretching and relaxation) of single molecules. The kind of model presented above is generic and thus generally helpful to describe the operation of devices that rely on similar principles. However, it is possible to further refine our understanding by considering not only the dynamics of the polymer chain as a whole, but of each of its segments explicitly. The fundamental question here is: *How does a polymer chain cross a potential barrier?* This is a generalization of the well-known Kramers problem for Brownian particles to the case of string-like objects, and Sebastian and Paul have published instructive accounts of the solution for the case of long chains, i.e., chains with a contour length much larger than the barrier width.[24–28] The mathematical derivation of the translocation rates and the total crossing time are rather involved, extending beyond the scope of this short account, so we only review here the simple calculation of the activation energy.

The approach is based on the Rouse model,[8] introduced in the first section I, considered here in the continuum limit (i.e., we treat the bead index n as a continuous variable ranging from 0 to N), a reasonable approximation for long chains. The polymer is placed in a potential double-well, such as the one shown in Fig. 3, and we investigate how it may overcome the potential barrier. Taking $\boldsymbol{R}(n, t)$ as the position of bead n at time t, and $V(\boldsymbol{R}(n, t))$ as its potential energy, we can write Newton's equation of motion for the (massless) beads:

$$\zeta \frac{\partial \boldsymbol{R}(n, t)}{\partial t} = K \frac{\partial^2 \boldsymbol{R}(n, t)}{\partial n^2} - \nabla V(\boldsymbol{R}(n, t)) + \boldsymbol{\Phi}(n, t), \tag{30}$$

where ζ is the friction coefficient of a bead, and $\boldsymbol{\Phi}(n, t)$ is a random force. The spring constant K accounts for entropic effects; as before, $K = 3k_B T/\langle h^2 \rangle$, with $\langle h^2 \rangle$ the mean

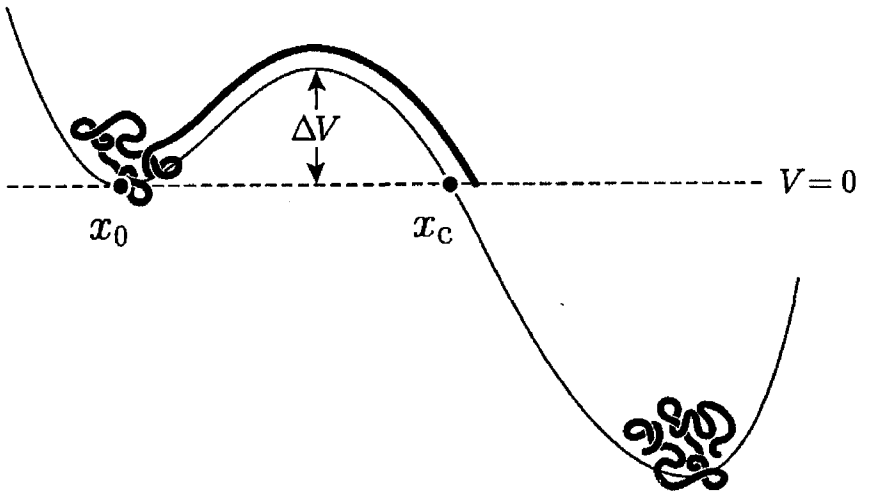

Figure 3. Schematic representation of a polymer coil crossing a potential barrier. The coil is initially localized around the potential minimum at x_0, and initiates translocation by stretching over the potential barrier ΔV up to a point x_c where $V(x_c) = V(x_0)$.

square length of the springs. In addition, we impose the boundary conditions $(\partial \boldsymbol{R}/\partial n)|_{n=0} = (\partial \boldsymbol{R}/\partial n)|_{n=N=0}$ to reflect the fact that the two ends of the chain are free.[8]

For our purpose, it suffices to restrict the analysis to a one-dimensional case and to the deterministic part of Eq. (30) (i.e., $\boldsymbol{R} = x$ and $\Phi = 0$). We are primarily interested in the situations of static equilibrium, where the positions of the beads are independent of time. In this case, the equation of motion reduces to

$$K\frac{d^2x(n)}{dn^2} = \frac{dV(x(n))}{dx} \tag{31}$$

An obvious solution of this equation is when the beads are localized in one potential well, for then both sides of Eq. (31) vanish. But there is another solution where a portion of the chain just straddles the potential barrier, as depicted in Fig. 3. The total free energy of the chain is then most interesting, as it gives the activation energy for the onset of translocation, i.e., the effective barrier height seen by the polymer. Indeed, following,[24] we notice that Eq. (31) is, in fact, Newton's equation of motion for a particle of mass k moving in a potential $-V$, where n plays the role of time. By analogy with conservation of energy, we at once have that the quantity

$$U = \frac{k}{2}\left(\frac{dx}{dn}\right)^2 - V(x) \tag{32}$$

is conserved as one moves along the chain contour, from $n = 0$ to $n = N$. Recalling that $(dx/dn) = 0$ at either end of the chain, we have $U = 0$, because the tail of the chain lies at a point where we chose $V = 0$, hence, the equality

$$\frac{k}{2}\left(\frac{dx}{dn}\right)^2 = V(x) \tag{33}$$

holds everywhere along the chain. In particular, the head of the straddling portion of the chain must also lie at the point (denoted x_c in Fig. 3 where $V=0$ on the other side of the barrier. This state of unstable equilibrium is intuitively correct when one thinks, for example, of a frictionless rope resting over a bump. To calculate the activation energy for translocation, we introduce the free energy density along the chain contour, i.e.,

$$\mathcal{F}(n) = \frac{k}{2}\left(\frac{dx}{dn}\right)^2 + V, \tag{34}$$

where the first term on the right is the contribution from the local stretching around bead n, while the second term is simply the potential energy of bead n. The total free energy of the chain may then be expressed as

$$F = \int_0^N \mathcal{F}(n)\, dn. \tag{35}$$

Combining Eqs. (33) to (35) and assuming that $x(n)$ is an increasing function of n, we find the activation free-energy for the crossing process to be

$$\Delta F_a = \int_0^N 2V\, dn = \int_{x(0)}^{x(N)} 2V\left(\frac{dn}{dx}\right)dx = \int_{x_0}^{x_c} \sqrt{2kV}\, dx. \tag{36}$$

This result is independent of the total length of the polymer: *the extension of the head of the chain across the barrier is sufficient to initiate translocation.* When compared with the energy $N\Delta V$ that would be required to move the N beads across the barrier *all at once*, it becomes clear that the effective height of the barrier is greatly reduced by stretching for long chains. There is yet a third solution of Eq. (31) corresponding to a chain hairpin, instead of a chain end, resting atop the potential barrier. This translocation mechanism is increasingly probable as N grows, and its activation energy is easily seen to be twice that of the end-activated crossing. Such results can be applied to situations of practical interest and, in the case of the Craighead device discussed above, they agree in character with Eq. (29) and with experimental data.

Park, Lee and Sung have also published a thorough analysis of the Kramers problem for a Rouse chain, for polymer contour lengths that are not necessarily large compared to the barrier width.[29–31] They showed that the stretching induced by a convex barrier *always* reduces the activation energy for chain translocation. Therefore, the rate of crossing is always larger than in the globular limit where N beads rigidly cross the barrier simultaneously. This conformational effect is stronger for longer chains, while it becomes insignificant for small polymers crossing wide barriers. Most interesting, there is a maximum in the effective barrier height at intermediate values of N, i.e., there is a critical chain length at which the crossing rate is minimized, because of the competition between surmounting the barrier and stretching at the barrier top.

From this short overview, we gather that molecular deformations play a determining role in the escape dynamics of polymer chains from potential wells, including those arising for entropic reasons. Qualitatively, the key point to bear in mind regarding this kind of process is that only a fraction of a long flexible macromolecule needs to overcome the potential barrier in order to initiate the directed translocation of the whole chain. The analogy with a siphon, wherein a relatively small amount of energy is required to

trigger fluid to flow naturally over a gravitational potential barrier, provides a helpful picture to remember this aspect of the polymer translocation process.

POLYMER–OBSTACLE COLLISIONS

As mentioned in the previous section, polymer deformation, stretching, and relaxation play a crucial role in the separation of biological macromolecules. Many separation microdevices, such as those utilized to analyze biological macromolecules (including DNA), often exploit molecular collisions between a moving analyte and various obstacles. These collisions, and the molecular deformation they generate, slow the analyte in such a way that useful separation can be achieved. The importance of these devices in the biosciences (e.g., it is the invention of powerful DNA separation methods that allowed the human genome to be mapped and sequenced years ahead of schedule) has spurred a renewed interest in the dynamical behavior of single isolated polymers.[32–36] Two excellent model systems for examining single-chain dynamics and the effects of hydrodynamics are either microscopic obstacles (or arrays of obstacles) fabricated using microlithography[32] or magnetically self-assembled super paramagnetic ferro-fluid particles[33,37] that can form quasi–regular arrays of posts.

Electrophoresis uses an electric field to move charged analytes through a sieving system. When a DNA molecule collides with an obstacle, it generally deforms and slides around it in order to continue its migration. During the collision, the presence of both electric and mechanical forces may lead to subtle effects that will be briefly discussed in the next section. Here, we will neglect these combined effects and examine polymer–obstacle collisions from a purely mechanical point of view. Several authors have looked at different aspects of this problem, because these single-polymer systems represent, in some sense, the fundamental unit of separation in such devices.[32,34,36]

We can, in fact, think of two, apparently analogous, methods of moving a polymer through a microfluidic device. One can either apply a uniform mechanical force directly on each monomer (e.g., a sedimentation force), or alternatively, one can use a low Reynold's number fluid flow with velocity v_s to force the molecule through the device. Although these approaches lead to nearly identical molecular behavior, there is a subtle difference related to the hydrodynamic properties of deformed polymer chains. It is on this interesting difference that we will focus our attention.

Mechanical Forces

First consider a quiescent isotropic viscous fluid in which a polymer is moving under the influence of a uniform external field (this correponds to Fig. 4a). Thus, each of the N monomers experiences an identical external force f_0 regardless of the chain conformation. The simplest such example is a rope moving in a gravitational potential. In the case of a polymer moving in a viscous liquid, this uniform external force alone is unable to deform the polymer. Without obstacles, the motion of the chain is dictated by the retarding effect of the friction between the polymer and the solvent.

The chain friction can be described by two different models, the local hydrodynamically permeable (Rouse) and nonlocal hydrodynamically impermeable (Zimm)

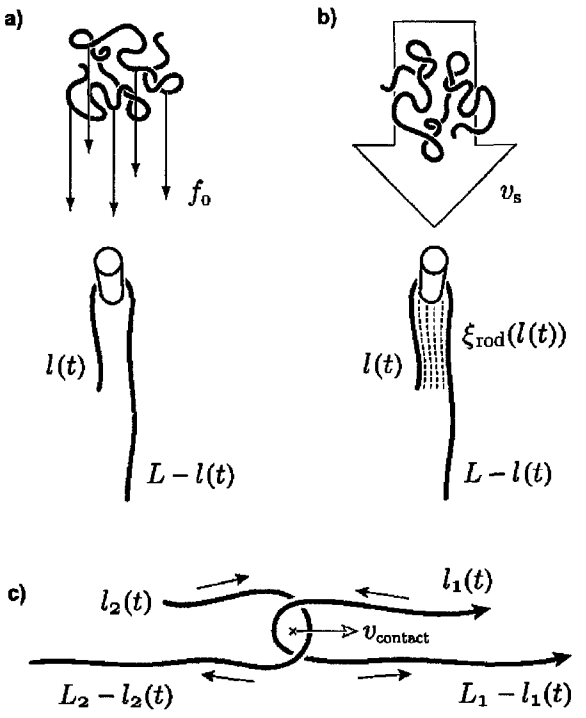

Figure 4. Schematic illustration of polymer-obstacle collisions in the external force and fluid flow regimes. a) Polymer in the presence of an external force per monomer f_0 colliding with a fixed obstacle. b) Polymer in the presence of a fluid flow with velocity v_s colliding with a fixed obstacle (the hatch marks are intended to illustrate the effective hydrodynamic coupling of the chain in the fluid flow). c) Polymer in the presence of an external force per monomer f_0 colliding with a free polymer. All three scenarios result in the formation of pulley like conformations.

friction models. The friction coefficient in the Rouse regime (subscript R) is given by $\xi_R = N\xi_1$, where $\xi_1 \cong 6\pi\eta b$ is the Stokes friction coefficient of a monomer of size b. Note that ξ_R is the same for all molecular conformations. However, when we include (nonlocal) hydrodynamic interactions (subscript HI), the instantaneous friction coefficient is conformationally dependent and is given by $\xi_{HI} = 6\pi\eta R_H$, where R_H is the instantaneous hydrodynamic radius of the polymer. In equilibrium, Eq. (10) applies, and we have $R_H \sim N^{\nu}$.

Because the friction coefficient changes with the molecular conformation in the nonlocal model, it is clear that the two models will predict different collision dynamics. The question then is: How does the presence of nonlocal hydrodynamic interactions modify the retarding effect of the polymer–obstacle collisions in a sieving system?

A complete collision process comprises a series of four consecutive steps: free-flow migration, deformation, trapping-release, and relaxation. First, the polymer migrates through the solvent under the influence of the applied field, with constant velocity $v_0 = N f_0/\xi$, where ξ is the friction coefficient in either the local ($\xi = \xi_R$) or nonlocal

($\xi = \xi_{HI}$) friction model. In free-flow electrophoresis, the local model applies, because the charged chain is free-draining;[38] in this case, $v_0 = N f_0/\xi = f_0/\xi_1$ is independent of the polymer size N, hence, the need for sieving media. A useful collision (at time $t = 0$) will then deform the polymer, and the latter will take a pulley-like conformation (Fig. 4a), with stretched arms of length $L - l(0)$ and $l(0) \leq L/2$. The limiting case is that of central trapping, where $l(0) = L/2$. A simple approximation to the pulley formation time is to assume that the ends of the polymer travel at velocity v_0 until the pulley is fully formed. To first order, the pulley formation time is thus $\tau_p \approx (L - l\ (0))/v_0$. The third stage of this process (rate-determining step), the competition between the two downfield arms, then begins. This competition dictates the release time of the polymer, which we denote by τ_{esc} [see Eq. (40)]. When the polymer is released from the obstacle, it is in a highly extended state. In the fourth and final stage, it relaxes to its equilibrium random coil conformation while drifting away from the obstacle, and it subsequently returns to velocity v_0. The relaxation of a chain after collision is also still not well understood.[37] If the device has periodic sets of obstacles, the polymers will undergo consecutive collisions, and the mean trapping time and probability of collision will likely depend on N, the degree of polymerization. In essence, this is a simple concept for the separation of flexible biopolymers via sieving.

In the pulley-like conformation, the polymer is no longer a random coil and is highly elongated in the field direction. For simplicity, we assume that the polymer is fully extended, and that $L = L_c = Nb$ (the contour length of the polymer). This is the high field regime, frequently used in sieving devices. More precisely, this means that the field dominates Brownian motion;[36] this occurs when $F = Nf_0 \gg k_B T/b$.[36]

In order to study the escape from the pulley-like conformation, we need to estimate the chain's friction coefficient in this state. In the Rouse picture, the friction coefficient does not change, as it is independent of conformation and is given by $\xi_R^{\cap} = N\xi_1$, where the superscript $\cap$ is meant to denote the friction coefficient in the pulley (or $\cap$-shaped) conformation, though it is equal to ξ^R here. In the nonlocal case with HI, we can treat the polymer as cylinder of length $L \sim Nb$, which moves along the contour of the chain. We thus ignore the bending, the friction due to the polymer–obstacle contact, and the possible hydrodynamic coupling due to the shear-like opposing motion of the two arms. The friction coefficient of such a cylinder (from the slender body theory of macroscopic hydrodynamics[39]) is given by

$$\xi_{HI}^{\cap} = \frac{2\pi\eta L}{\ln(L/b) + \gamma^{\parallel}} \cong \frac{1}{3\ln(N)} \times \xi_R^{\cap} \tag{37}$$

where $\gamma^{\parallel} \cong 1/2$ is simply a numerical constant. We note that $\xi_R^{\cap} \sim \xi_{HI}^{\cap} \sim N$ to leading order. Therefore, we expect rather similar escape times.

We now analyze the equation of motion of a chain in a pulley state with an initial parameter $l(t = 0) \equiv l(0)$. At time $t \geq 0$, the driving force for the escape of the polymer is the unbalanced length $L - 2l(t)$. The equation of motion is thus

$$\frac{dl(t)}{dt} = -\frac{f_0}{\xi^{\cap}} \times \frac{L - 2l(t)}{b}. \tag{38}$$

and its solution is

$$l(t) = \frac{L}{2} - \left(\frac{L}{2} - l(0)\right) \exp\left(\frac{2f_0 t}{\xi^{\cap} b}\right) \tag{39}$$

where we obtain the results for the local and nonlocal models by substituting the appropriate value of the friction coefficient $\xi^{\cap}$. The escape time of the polymer can be simply obtained by solving for $t = \tau_{esc}$, at which $l\ (\tau_{esc}) = 0$. Subject to this constraint, we can invert Eq. (39) and solve explicitly for the escape time of the polymer:

$$\tau_{esc}(l(0)) = \ln\left(\frac{L}{L - 2l(0)}\right) \frac{\xi^{\cap} b}{f_0} \tag{40}$$

We note that this time diverges when $l(0) = L/2$. In this case, the two arms of the pulley are of equal length, and the net force is zero though the net force on the obstacle is maximum. The escape time, however, is not infinite in this situation, because Brownian motion quickly allows the system to get out of this unstable equilibrium state; as soon as $l(t)$ becomes non-negligible, the deterministic escape process described above starts. Finally, we must average the previous result over all possible values of $l(0)$ between 0 and L/2. For a uniform distribution of initial conditions, this average gives the remarkably simple result

$$\langle \tau_{esc} \rangle = \frac{\xi^{\cap} b}{2f_0} = \frac{L}{2}\left(N \frac{f_0}{\xi^{\cap}}\right)^{-1} \tag{41}$$

We note that the escape time is that required to move over a distance L/2 given the effective velocity $v_0^{\cap} = N\, f_0/\xi^{\cap}$, which is essentially independent of the molecular size N. We thus see that the escape time increases proportional to L in both models, but that its magnitude is smaller in the model with HI [see Eq. (37)]. However, this similarity is hiding a key difference. Indeed, while $v_0^{\cap} = v_0 \sim N^0$ in the Rouse model, $v_0 \sim N^{1-\nu}$ in the model with HI. Therefore, the collisions affect the mean velocity of the molecules through the sieving device in very different ways according to these two models.

The situation with electrophoretic forces is even more complicated than this, but it has yet to be studied in detail. In short, while the polymer chain behaves like a Rouse chain between collisions, it actually behaves like a chain deformed by a strong counterflow during the collision; this type of collision is discussed next.

Fluid Induced Polymer Motion

In this section, we consider a polymer in a solvent flowing at velocity $v_s = v_0$, see Fig. 4b. We outline how the presence of a solvent flow modifies the escape dynamics of a polymer from an obstacle. We begin by examining a centrally trapped position where $l(0) = L/2$. The force on the polymer due to the obstacle is the same as the frictional force of the two arms of the pulley imparted by the flowing solvent. The crucial qualitative difference in this example is that because the interarm distance d is much smaller than the length of the chain, we can consider the pulley to be a hydrodynamically coupled object. The entire chain can be treated as a composite object of length $L/2$ and

effective diameter $d \cong b$.[36,39] The frictional coefficient of the chain is that of a rod of length $L/2$, i.e., $\xi_{HI}^{rod}(L/2)$ (in the centrally trapped position). The associated frictional force F_s on the chain due to the solvent flow is

$$F_s = v_s \xi_{HI}^{rod}(L/2) \tag{42}$$

This is a rather subtle point, and if, for example, the interarm spacing of the pulley was much larger (e.g., $d > L/2$), this hydrodynamic coupling would be negligible.

We now consider the general case $l(0) < L/2$. The equation of motion is a balance between the sliding motion of the chain (around the post) at speed $v_c = -dl(t)/dt$ (with a frictional resistance proportional to the total contour length L) and the driving force due to solvent flow (at velocity v_s) acting on the unbalanced length $L - 2l(t)$:

$$\xi(L) \times \frac{dl(t)}{dt} = -v_s \times \xi(L - 2l(t)) \tag{43}$$

In the limit where the polymer strands are fully stretched, the friction coefficients all scale like $\xi(x) \sim x$, and we immediately recognize that this is the same equation of motion as that which we obtained for the case of a mechanical force. Therefore, although the total force is reduced by the hydrodynamic coupling, the sliding motion is unaffected. Using Eq. (37) for $\xi^{HI}(x)$, the mean escape time is found to be given by

$$\langle \tau_{esc} \rangle = \frac{L}{2v_s} \times \frac{2\ln(L/b) - 1}{2\ln(L/b) + 1} \tag{44}$$

Although the effective hydrodynamic coupling affects the nature of the forces, the polymer escape time is virtually the same as that given by Eq. (41).

As pointed out by Andre et al.,[36] the effects of hydrodynamic coupling would be most prominent in the case of a chain hooking on the obstacle with multiple loops: the frictional force would be reduced significantly due to the weak dependence of the friction coefficient on the diameter of the chain,[36] and the competition between several unbalanced loops would lead to different results. This will not be treated here.

Though these simple approaches to treating the escape time of a polymer provide useful results, more detailed modelling is required in order to determine effects due to interarm interactions, shear coupling due to the relative motion of the arms of the pulley, and effects of the size of the obstacle on the escape time. Moreover, at lower field intensities, the forces are not large enough to fully stretch the two arms of the pulley, and the friction coefficients must be modified accordingly. From a practical point of view, understanding how these variables affect polymer dynamics can lead to ways of optimizing separation systems. In the next section, we study a variant of the polymer–obstacle collision, the polymer–polymer collision.

Polymer–Polymer Collisions

An interesting combination of the previous two examples occurs when an external force is applied to a polymer (the polymer labeled 1 in Fig. 4c) which then collides with a free polymer (labeled 2). This collision typically results in the formation of a

double-pulley-like conformation as depicted in Fig. 4c. This effectively combines the two effects of a fluid flow (the relative motion of the contact point, at velocity $v_{contact}$, is in fact analogous to a fluid flow) and an external force on the polymer. These collisions play a crucial role in the size separation of polymers in dilute solution capillary electrophoresis.[40,41] In this sieving regime, a dilute neutral solution of polymers is used as a "mobile" sieving matrix to separate charged biomolecules such as DNA. The exact mechanism responsible for this separation is not well understood. There are currently two suspected causes for this separation. The first, proposed by Barron et al.,[40,41] is that of a so-called transient entanglement mechanism, wherein the charged species collides with one or many neutral polymers, dragging them through the solvent. In turn, this slows the motion of the chains. The other mechanism recently proposed by Ekani-Nkodo et al.,[42] is that the dilute matrix affects the hydrodynamic flow field of the polymer, in effect increasing its hydrodynamic radius. Much work is still required in order to better understand separation in this system. In particular, it is important to understand the effects of hydrodynamics on the motion of both colliding chains.

One can immediately see that the case of a fixed post is a subset of the more general situation (above), though the calculation of the escape of a polymer from a polymer–polymer collision is somewhat more involved than the previous two examples. Here we outline the methodology of the calculations. Figure 4c is a schematic illustration of a polymer–polymer collision. The key phenomenological difference between this example and the previous two is that here we have a nonzero contact point velocity $v_{contact}$ of the two-molecule system. This has the added consequence of inducing a further frictional term due to the relative motion of the whole system with respect to the stationary surrounding fluid. Moreover, compared to the case of a fixed post, the applied force is now performing two functions. First, it serves to unhook the molecule from the free polymer (if the free polymer is much larger than the molecule to which the force is applied, then we effectively recover the case of a polymer–post collision). However, in this scenario, we do not have a fixed contact point, a fraction of the total force $F_{contact}$ is used to generate the center of mass motion. We can write the expression for the contact point velocity as (similar to the previous two sections)

$$v_{contact} = \frac{F_{contact}}{\xi_f + \xi_a} \tag{45}$$

where ξ_f and ξ_a are the total friction coefficients of the free polymer and the polymer to which the force is applied (at any given time). This contact point velocity is defined self-consistently through the solution of the equations of motion for the escape of the two polymers, because it depends on the instantaneous lengths of short legs of the molecules, $l_2(t)$ and $l_1(t)$. The force that drives the escape of the chain is due only to the unbalanced length: $f_0 \times (L_1 - l_1(t))/a$. So, for example, in a symmetric hairpin conformation, all of the applied force is contributing to the contact point velocity. Alternatively, as $l_1(t)$ tends to zero, all of the applied forces tend to contribute to the chain unhooking.

We are currently examining all three systems using molecular dynamics simulations with explicit solvent particles in order to test the predictions from the calculations outlined in this section. This work can greatly enhance our fundamental knowledge of the dynamical behavior of polymers in a variety of microenvironments.

TETHERED POLYMER CHAINS AND STRONG SHEAR FLOWS

The ideal case of a free, tethered polymer deforming in a strong flow has been studied by Brochard-Wyart.[43,44] Although this situation is experimentally relevant (a unique example will be briefly described in the next section), a more common situation is that of a polymer attached to a wall and subject to a shear flow. Although these two problems appear to be somewhat similar, the dynamics of the polymer attached to the wall is not trivial, largely due to the nature of the flow. In this section, we will examine this latter case, which is of particular interest for colloidal stabilization, biological systems,[45] and lubrication.[46] We will assume that the wall does not absorb the polymer, and that we have a good solvent.

We will thus study the case of a polymer attached to a wall and deformed in a shear flow of the type $v_x(y) = \dot{\gamma}y$, where $v_x(y)$ is the flow velocity, $\dot{\gamma}$ is the shear rate, and y is the distance perpendicular to a wall (see Fig. 5). One can generate such a flow by moving one wall at constant speed while keeping the opposite one fixed: the appropriate velocity gradient would then be obtained due to friction between the solvent particles in contact with the plates. A simpler method is to use a pump to create a Poiseuille flow profile inside a tube: if the diameter of the tube is large enough compared to the size of the chain, the velocity gradient near the walls would be essentially linear. The shear flow is characterize by the Weissenberg number $\mathrm{Wi} = \tau\dot{\gamma}$, which is simply the longest relaxation time of the polymer in equilibrium τ times the shear rate $\dot{\gamma}$.

Buguin and Brochard-Wyart[44,47] have studied the extension of the chain near a wall and found that it strongly depends on the value of Wi. These authors described four regimes, shown schematically in Fig. 6(b–e). Similar regimes were also predicted for a free polymer in a uniform flow.[44] In the present case, however, the polymer is maintained in an asymmetric conformation due to the presence of the wall, and the nature of the flow will lead to subtle fluctuation effects, as we now describe.

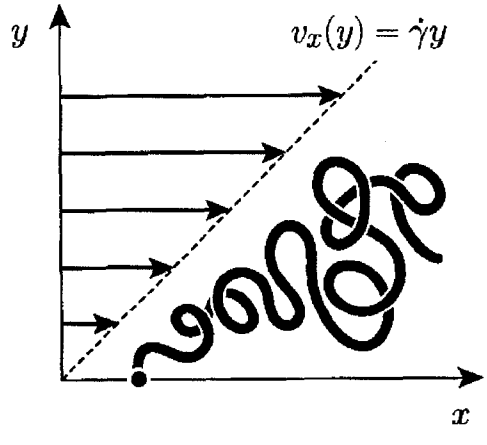

Figure 5. Illustration of a tethered chain in shear flow of type $v_x(y) = \dot{\gamma}y$.

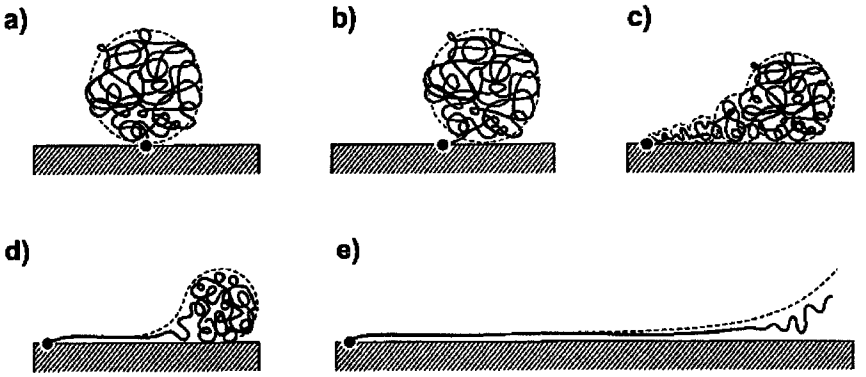

Figure 6. Schematic representation of a polymer chain in the five deformation regimes: (a) when Wi is small, the chain is left unperturbed; (b) at slightly higher velocities, the coil is displaced but not deformed; (c) when Wi increases, the chain first deforms in a series of blobs of increasing size because the tension decreases away from the fixed point: this is called the trumpet conformation; (d) for even larger values of Wi, the tension near the fixed point becomes large enough to fully stretch a part of the chain and we have the so-called stem-and-flower conformation; (e) finally, large enough shear rates can fully extend the chain and we obtain a rod conformation. (Inspired From Buguin and Brochard-Wyart.[44]

Fluctuations of a Tethered Polymer in Shear Flow

Doyle, Ladoux and Viovy[48] (DLV) have reported multiple "fluctuation regimes" for a polymer in the situation shown in Fig. 7. For $Wi < 1$, the polymer is slightly stretched and undergoes small fluctuations. The second shear flow regime ($Wi \cong 1-20$) is characterized by an increase in both the mean chain extension and fluctuations about the mean. When $Wi > 20$, the polymer extends slowly to its maximum extension, while

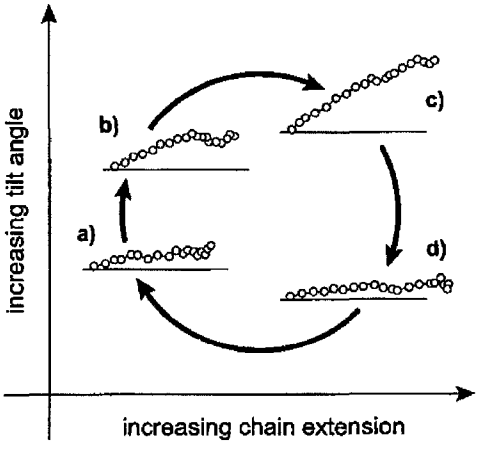

Figure 7. Schematic description of the cyclic chain dynamics found by Doyle et al.,[48] as discussed in the text.

fluctuations are reduced compared to the second regime. The interesting fluctuation regime is thus the intermediate one.

DLV actually found that in the second regime, the fluctuations in the extension of the chain were more than double what is normally observed in equilibrium or in the high-flow regime, a result that was reproduced by simulations.[48] In fact, it was found that the chain was displaying a continuous recirculating motion or a type of cyclic dynamics. As an example, we will take a chain partially elongated near the surface (Fig. 7a). Eventually, it will encounter a particularly strong fluctuation that will bring it away from the wall and into a stronger flow (Fig. 7b). The stronger flow will then lead to an additional extension (Fig. 7c) while the chain is slowly pushed toward the wall by the resulting torque. This rotating motion will take it back into the slower flows found near the wall, and the chain will quickly shrink back to a less extended state (Fig. 7d) until another strong enough fluctuation restarts the cycle. No specific cycling time has been determined from simulation or experiment. In other words, the cycling time depends entirely on random fluid and polymer fluctuations. This is a remarkably simple and elegant system with nontrivial dynamics.

Extensions of a Tethered Polymer in Shear Flow

Ladoux and Doyle[49] have designed models for the FJC and the WLC. In both cases, it is assumed that HI are negligible (which is not unreasonable, because stretched polymers tend to be free-draining; furthermore, the presence of the wall partly screens HI). As a consequence, the friction coefficient of the chain is again assumed to be given by the expression $\xi_R \simeq N\xi_1$, where $\xi_1 \simeq \eta b$ is the friction coefficient of a monomer of size b.

For the FJC model, these authors used the harmonic approximation[50] to relate the force f and the chain extension h:

$$f = k_{\parallel} h, \tag{46}$$

where $k_{\parallel}$ is the longitudinal (entropic) spring constant. Note that we have $k_{\perp} = k_{\parallel}$ in the linear regime. In the transverse direction (y), the thermal motion follows the equipartition law:

$$\frac{1}{2} k_{\perp} \delta y^2 = k_B T, \tag{47}$$

where δy^2 is the variance of the chain's transverse fluctuations. From Eqs. (46) and (47), we can obtain the coupling between transverse fluctuations and the restoring force:

$$\delta y = \left(\frac{2k_B T h}{f}\right)^{1/2} \sim f^{-1/2}. \tag{48}$$

Using Eq. (25), we define the fraction of the total contour length yet to be stretched as

$$\varepsilon \equiv 1 - \frac{h}{h_{max}} \cong \frac{1}{f}, \tag{49}$$

or $f = \varepsilon^{-1}$. In the absence of HI, the equality between the friction and spring forces gives

$$f \cong \xi_R \dot{\gamma} \delta y. \tag{50}$$

From Eqs. (48), (49), and (50), we find the scaling relation between the unstretched polymer fraction ε and the shear rate $\dot{\gamma}$ for a FJC:

$$\varepsilon \sim \dot{\gamma}^{-2/3}. \tag{51}$$

For the WLC, Eq. (25) leads to the scaling law $f \sim \varepsilon^{-2}$, which leads to

$$\delta y \sim \varepsilon \tag{52}$$

when used with Eq. (48). The WLC scaling law relating ε and $\dot{\gamma}$ is then, from Eqs. (48), (50), and (52),

$$\varepsilon \sim \dot{\gamma}^{-1/3}. \tag{53}$$

In contrast, Buguin and Brochard-Wyart's result[47] for the stem-and-flower regime predicts

$$\varepsilon \sim \dot{\gamma}^{-1}. \tag{54}$$

(Ladoux and Doyle[49] have compared their models with Brownian simulations and with experiments using λ-phage DNA molecules. The simulations agree with the predicted scaling laws in both cases (FJC and WLC). Experimental data also agree with the $\varepsilon \sim \dot{\gamma}^{-1/3}$ scaling law, thus indicating that λ-phage DNA is indeed a WLC. The success of their approach appears to support their assumption that HI are not important in the high-extension limit. Nevertheless, it is somewhat surprising that taking into account the effect of the flow on the polymer while neglecting the effects of the polymer on the flow (i.e., the model is not self-consistent) provides such a successful model.

POLYMER STRETCHING DURING ELECTROPHORESIS

An interesting example of polymer stretching that has been predicted but is yet to be observed is presented in Fig. 8(a,c,e). Here, a charged molecule (e.g., a short DNA fragment) is attached to a long uncharged polymer. If an electric field is applied, the composite molecule will drift under the action of the electrostatic forces pulling the charged component through the liquid. The neutral polymer simply acts like a "molecular parachute" that slows the natural electrophoretic drift of the charged molecule. This novel electrophoretic technique, called free-solution conjugate electrophoresis (FSCE), has been successfully used to fractionate unstretched neutral polymers [namely, polyethylene glycol (PEG)] of varying sizes using small uniform pieces of single-stranded DNA (typically 10–30 monomers in length) as the charged "engines".[51,52] The separation of the various PEG sizes is due to their varying coefficients of friction that resulted in different net electrophoretic velocities.

Because the frictional force generated by the neutral polymer is a function of its conformation, it is important to understand the effect of the electrophoretic motion on the neutral parachute of the composite molecule. As we saw previously, stretched

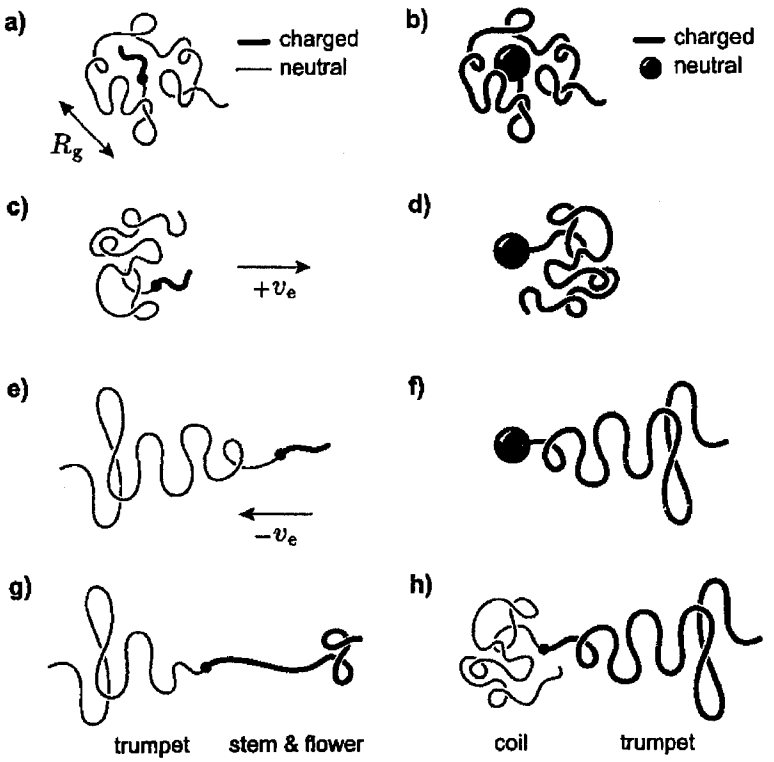

Figure 8. Schematic of free solution electrophoresis of composite molecules. The hydrodynamic friction forces can deform flexible polymers during the electrophoresis, as discussed in the text.

polymers have larger friction coefficients than coiled ones. This is an interesting problem, as the neutral polymer stretches in response to the drift (at velocity $+v_e$) in the immobile fluid: it is as if the fluid is moving at a velocity $-v_e$, while the polymer is held fixed at its end (see Fig. 8e). On the other hand, the drift velocity would be reduced if the polymer was to stretch. We thus have a self-consistent problem with a negative feedback loop. The only known experimental results were consistent with a model[53,54] where the polymer retained a coil conformation (in other words, the velocity was too low to stretch the "parachute," see Fig. 8a).

However, as discussed in Desruisseaux et al.,[55] one can, in principle, expect a series of conformational deformations similar to the ones predicted by Brochard-Wyart[44] and shown in Fig. 6. The first stage would be the *hydrodynamic segregation* of the charged and uncharged molecules (see Fig. 8c). The critical velocity v_e^* required to achieve this minimal amount of deformation can be estimated using a simple argument. If the charged DNA segment is small compared to the coil of size R_g, segregation is expected to happen when the drag force exceeds the entropic force, keeping the composite molecule as a single object (i.e., in a random coil conformation):

$$\xi v_e > \frac{k_B T}{R_g}, \tag{55}$$

where, for an impermeable coil, $\xi \cong 6\pi\eta R_g$. We thus get $v_e^* \cong k_B T/6\pi\eta R_g^2$. Using typical room-temperature values, we find that this is equivalent to $v_e^* \cong (2R_g)^{-2}$ m/sec, where R_g is in nm. We thus need fairly large molecules to have reasonable critical velocities (electrophoretic velocities are generally of the order 0.001–0.1 cm/s). In the stages beyond segregation (i.e., for even higher velocities, see Fig. 8e), the trumpet, stem-and-flower, and rod conformations can also appear. As far as we know, this has yet to be observed.

The reverse process consists in attaching uniform uncharged parachutes to a family of charged polyelectrolytes. In this case, electrophoresis is used to fractionate the polyelectrolytes: this method is called end-labeled free-solution electrophoresis, or ELFSE.[56] The relevant theory[54] says that the retardation due to the uncharged molecule is actually like a fluid counterflow. If this is the case, one also expects molecular deformation (this time of the leading polyelectrolyte engine), as described schematically in Fig. 8(b,d,f). Again, this rather counterintuitive deformation (against the direction of net motion!) has yet to be observed.

Finally, one may even consider the case of two long polymers attached together, one charged and the other not. We expect a global coiled conformation at low velocity. But, as the electric field is increased, we first expect the segregation of the two subcoils. As the field is further increased, we would expect each polymer to go through a series of stretched conformations; this may start occurring for one chain before the other, depending on their properties, such as their contour and persistence lengths. Overall, one can imagine no less than 16 different cases, two of which are shown in Fig. 8(g,h). Again, this situation has yet to be investigated, despite its potentially rich phase diagram.

CONCLUSION

In this review article, we have provided an introduction to the topic of polymer stretching and relaxation in good solvents. This is currently a very active area of investigation, both experimentally and theoretically, and hundreds of articles are published every year that treat at least one aspect of this problem. Although our review was certainly not exhaustive (it could not realistically be), it described the main elements typically used to understand the physics of polymer problems when molecular deformations are involved. We also presented four different systems that have attracted much attention over the last several years. These examples are related to the fields of microfluidics and separation science, where polymer entropy, deformation, and relaxation play a central role. In fact, in most of these cases, it is the understanding of these fundamental molecular phenomena that has led to the design of new devices with improved performances. With the advent of nanofluidics, more work will be needed to understand polymer behavior in the limit where surface interactions dominate and the concept of a "bulk fluid" ceases to make sense.

Some issues remain ill understood at this point in time. We would like to conclude by discussing two of them. First, current models are usually not self-consistent. For instance, let us take the general problem of a tethered polymer deforming in a given flow (see the previous two sections). This is a classical problem with dozens of variations and applications. In essentially all cases, past theoretical work was aimed at predicting the deformation of the polymer under the specified fluid flow. However, the polymer must

disturb the flow pattern in its vicinity. Therefore, one should in principle, treat this aspect of the problem in a *self-consistent* manner. In spite of this possible deficiency, current models appear to reproduce experimental data rather well, which is perhaps a little surprising. This deserves further investigation. Second, current models (except for molecular dynamics simulations with explicit solvent) generally assume some kind of effective and instantaneous hydrodynamic interaction between the monomers (and possibly the walls of the device)—for instance, they often use the Oseen tensor to calculate the local effect of HI.[8] However, HI cannot propagate at infinite speed. Although it is not clear whether the instantaneous HI approximation can lead to errors for slow processes, one would expect this kind of approach to fail when the phenomenon under study involves short transient effects (e.g., the early stages of polymer stretching that follow the sudden application of a shear flow) or high-frequency periodic perturbations (e.g., a high-frequency oscillatory flow). This is a rather unexplored territory.

ACKNOWLEDGMENTS

We acknowledge the support of the Natural Science and Engineering Research Council of Canada for a Discovery Grant to GWS and scholarships to MK and LM, the Fonds Nature et Technologies of the Province of Qubec for a scholarship to YG, the Government of Ontario for an OGS scholarship to FT, and the University of Ottawa for scholarships to YG, MK, LM, and FT.

REFERENCES

1. Larson, R.G. *The Structure and Rheology of Complex Fluids*; Oxford University Press: New York, 1999.
2. Allen, M.P.; Tildesley, D.J. *Computer Simulation of Liquids*; Oxford Science Publications: New York, 1987.
3. Grest, G.S.; Kremer, K. Phys. Rev. A **1986**, *33*, 3628–3631.
4. Rapaport, D.C. *The Art of Molecular Dynamics Simulation*; Cambridge University Press: New York, 1995.
5. Rapaport, D.C. J. Chem. Phys. **1979**, *71* (5), 3299–3303.
6. Chu, S. Philos. Trans. R Soc. Lond. Ser. A—Math Phys. Eng. Sci. **2003**, *361*, 689–698.
7. de Gennes, P.G. *Scaling Concepts in Polymer Physics*; Cornell University Press: Ithaca, 1979.
8. Doi, M.; Edwards, S.F. *The Theory of Polymer Dynamics*; Oxford Science Publications: New York, 1986.
9. Teraoka, I. *Polymer Solution: An Introduction to Physical Properties*; John Wiley & Sons: New York, 2002.
10. des Cloizeaux, J.; Jannink, G. *Les Polyméres en Solution: leur Modélisation et leur Structure*; Les Éditions de physique: Les Ulis, 1987.
11. Slater, G.W.; Crisan, S.; Pépin, M.; Gratton, Y. Physics in Canada **2003**, *59*, 57–66.
12. Kemp, J.; Chen, Z.Y. Phys. Rev. E **1997**, *56*, 7017–7022.

13. Volkenstein, M.V. *Configurational Statistics of Polymeric Chains*; Interscience: New York, 1963.
14. Slater, G.W.; Hubert, S.J.; Nixon, G.I. Macromol. Theory Simul. **1994**, *3*, 695–704.
15. Glatting, G.; Winkler, R.G.; Reineker, P. Macromolecules **1993**, *26*, 6085–6091.
16. Pincus, P. Macromolecules **1976**, *9*, 386–388.
17. Marko, J.F.; Siggia, E.D. Macromolecules **1995**, *28* (26), 8759–8770.
18. Winkler, R.G. J. Chem. Phys. **2003**, *118*, 2919–2928.
19. Han, J.; Turner, S.W.; Craighead, H.G. Phys. Rev. Lett. **1999**, *83*, 1688–1691.
20. Han, J.; Craighead, H.G. Science **2000**, *288*, 1026–1029.
21. Han, J.; Craighead, H.G. Anal. Chem. **2002**, *74*, 394–401.
22. Tessier, F.; Labrie, J.; Slater, G.W. Macromolecules **2002**, *35*, 4791–4800.
23. Tessier, F.; Slater, G.W. Appl. Phys. A **2002**, *75*, 285–291.
24. Sebastian, K.L.; Paul, A.K.R. Phys. Rev. E **2000**, *62*, 927–939.
25. Sebastian, K.L. Phys. Rev. E **2000a**, *61*, 3245–3248.
26. Sebastian, K.L. J. Am. Chem. Soc. **2000b**, *122*, 2972–2973.
27. Sebastian, K.L. Phys. Rev. E **2000c**, *62*, 1128–1132.
28. Kumar, K.; Sebastian, K.L. Chem. Phys. Lett. **2002**, *359*, 101–108.
29. Park, P.J.; Sung, W. J. Chem. Phys. **1999**, *111*, 5259–5266.
30. Lee, K.; Sung, W. Phys. Rev. E **2001a**, *64*, 041801.
31. Lee, K.; Sung, W. Phys. Rev. E **2001b**, *63*, 021115.
32. Bakajin, O.B.; Duke, T.A.J.; Chou, C.F.; Chan, S.S.; Austin, R.H.; Cox, E.C. Phys. Rev. Lett. **1998**, *80* (12), 2737–2740.
33. Doyle, P.S.; Bibette, J.; Bancaud, A.; Viovy, J. Science **2002**, *295* (22), 2828–2831.
34. Sevick, E.M.; Williams, D.R.M. Europhys. Lett. **2001**, *56* (4), 529–535.
35. Starkweather, M.E.; Muthukumar, M.; Hoagland, D.A. Macromolecules **1998**, *31* (16), 5295–5501.
36. Andre, P.; Long, D.; Ajdari, A. Eur. Phys. J. B **1998**, *4* (1), 307–312.
37. Mayer, P.; Bibette, J.; Viovy, J.L. Mat. Res. Soc. Symp. Proc. **1997**, *463*, 529–535.
38. Viovy, J.L. Rev. Mod. Phys. **2000**, *72*, 813–872.
39. Batchelor, G.K. J. Fluid. Mech. **1970**, *44* (3), 410–440.
40. Barron, A.E.; Harvey, H.W.; Soane, D.S. Electrophoresis **1994**, *15*, 597–615.
41. Barron, A.E.; Sonada, W.M.; Blanch, H.W. Electrophoresis **1996**, *17*, 744–757.
42. Ekani-Nkodo, A.; Tinland, B. Electrophoresis **2002**, *23* (16), 2755–2765.
43. Brochard, F.; Buguin, A. Comptes Rendus Acad. Sci. Ser. II-B **1995**, *321*, 463–466.
44. Brochard-Wyart, F.; Buguin, A. *Flexible Polymer Chains in Elongational Flow*; Nguyen, T.Q., Kausch, H.H., Eds.; Springer: New York, 1999; 41–66.
45. Lipowski, R. Coll. Surf. A **1997**, *128*, 255–264.
46. Klein, J.; Kamiyama, Y.; Yoshizawa, H.; Israelachvili, J.N.; Fredrickson, G.H.; Pincus, P.; Fetters, L.J. Macromolecules **1993**, *26*, 5552–5560.
47. Buguin, A.; Brochard-Wyart, F. Macromolecules **1996**, *29*, 4937–4943.
48. Doyle, P.S.; Ladoux, B.; Viovy, J.L. Phys. Rev. Lett. **2000**, *84*, 4769–4772.
49. Ladoux, B.; Doyle, P.S. Europhys. Lett. **2000**, *52*, 511–517.
50. Hatfield, J.W.; Quake, S.R. Phys. Rev. Lett. **1999**, *82*, 3548–3551.
51. Vreeland, W.N.; Desruisseaux, C.; Karger, A.E.; Drouin, G.; Slater, G.W.; Barron, A.E. Anal. Chem. **2001**, *73*, 1795–1803.
52. Vreeland, W.N.; Slater, G.W.; Barron, A.E. Bioconjugate Chem. **2002**, *13*, 663–670.

53. McCormick, L.C.; Slater, G.W.; Karger, A.E.; Vreeland, W.N.; Barron, A.E.; Desruisseaux, C.; Drouin, G. J. Chromatogr. A **2001**, *924*, 43–52.
54. Long, D.; Dobrynin, A.V.; Rubinstein, M.; Ajdari, A. J. Chem. Phys. **1998**, *108*, 1234–1244.
55. Desruisseaux, C.; Drouin, G.; Slater, G.W. Macromolecules **2001**, *34*, 5280–5286.
56. Ren, H.; Karger, A.E.; Oaks, F.; Menchen, S.; Slater, G.W.; Drouin, G. Electrophoresis **1999**, *20*, 2501–2509.

Electrophoresis 2002, *23*, 3791–3816 3791

Review

Gary W. Slater
Steve Guillouzic
Michel G. Gauthier
Jean-François Mercier
Martin Kenward
Laurette C. McCormick
Frédéric Tessier

University of Ottawa,
Ottawa, Canada

Theory of DNA electrophoresis (~1999–2002½)

Over the last two decades, the introduction of new methods such as pulsed-field gel electrophoresis and capillary array electrophoresis has made it possible to map and sequence entire genomes, including our own. The development of these experimental methods has been helped by the progress of theoretical and computational sciences, and the interactions between these three *modi operandi* of modern science are still pushing the limits of our technologies. We now see a clear trend towards proteomics and microfluidic (even nanofluidic!) devices. In this review, we take a look at the progress of the field over the last 3 years using the glasses of the theoretical scientist and focusing mostly on new ideas and concepts. About a dozen different subfields are discussed and reviewed. We conclude by giving a commented list of some of the best review articles published over the last 2–3 years.

Keywords: Capillary electrophoresis / Computer simulations / Entropic trapping / Microfluidics / Review / Theory of electrophoresis EL 5176

Nucleic acids

Contents

Correspondence: Professor Gary W. Slater, Département de Physique, Université d'Ottawa, 150 Louis-Pasteur, Ottawa, Ontario K1N 6N5, Canada
E-mail: gslater@science.uottawa.ca
Fax: +613-562-5190

Abbreviations: BD, Brownian dynamics; **FENE**, finitely extensible nonlinear elastic; **SNP**, single-nucleotide polymorphism

1 Introduction

Clearly, microfluidic devices are on the verge of creating a whole new family of technologies and industries (indeed, it is already happening). Although the main interest in these systems is due to the fact that we can make macroscopic systems more efficient (and more robust) by reducing their scale, we should not forget that microfluidic systems also allow us to use new separation and physicochemical processes unknown on a macroscopic scale. An example is that of entropy-based separation systems where one of the dimensions of a channel is smaller than the normal geometric size (*e.g.*, the radius of gyration) of a polymeric analyte [1, 2]. Understandably, the theoretical work has been somewhat biased towards the micro- and even nanofluidic world over the last 5 years or so. Although this review will not focus entirely on the theoretical issues surrounding this new technological paradigm, it will itself suffer from this bias.

Of course, we had to make a selection of topics. This selection is certainly driven to some extent by what the authors find stimulating and promising these days. Two of the exciting topics that we nevertheless chose to ignore are the problems related to sample injection in microfluidic devices and the phenomenon of dielectrophoresis. Injection is an extremely important issue for the optimization of separation devices and even represents one of the most remarkable difference between CE and microfluidic systems; however, injection is not a separation process as such and is thus slightly beyond the scope of the present review. Dielectrophoresis, on the

 0173-0835/02/22-2312–3791 $17.50+.50/0

other hand, can be used as a separation tool, even for DNA, but it does not rely on the same transport properties that make electrophoretic separations possible; therefore, we decided to avoid this topic for the present review.

We also decided not to include a specific section about the development of new separation matrices for DNA separations. Although the development of new polymeric sieving matrices remains an active field, the benefits appear to have become largely technical (lower viscosities for easier injection, *etc.*). Indeed, no major improvements in either sequencing readlength or elution times have been reported that can be directly related to a revolution in sieving matrices. We must add, however, that in some cases, the separation process is probably novel and remains to be investigated [3, 4].

We do not cover the fields of electroosmotic flow (EOF) and capillary coatings. This is truly a remarkably dynamic field of investigation, both theoretically and experimentally. Although the fundamentals of EOF are well-understood, we still have no clear understanding of the effects of dynamic polymer coating agents (*e.g.*, polydimethylacrylamide) on the EOF. Would it be better to use branched or monodisperse polymers? Can we coat the capillary walls to avoid analyte-wall interactions while retaining a uniform and strong EOF for fluid pumping purposes? What kind of covalent polymer brushes would better control the EOF? Beside these standard CE issues, others are more directly related to microfluidics: *e.g.*, can we use inhomogeneous EOF flows to mix liquids in μm-size devices? These are immensely interesting topics, but we had to make a selection of topics for this review.

On a similar note, we do not review the recent progress in our understanding of the effect of curves in microfluidic devices. Modeling has led to an excellent understanding of the race-track effects inherent to such devices, and several clever new designs have been suggested. However, the subject matter is yet to be fully understood. Indeed, essentially all current models apply to free-flow electrophoresis where both the mobility (μ) and the diffusion coefficient (D) of the analyte are independent of the local field intensity (E). This is clearly not the case for DNA separation in sieving polymer matrices. Strangely, the impact of these nonlinear field effects has never been studied in this context.

The next fourteen sections present different topics related to the separation of DNA molecules. In each case, we discuss some of the main outstanding issues and the progress made over the last 2–3 years. The last section concludes with a commented list of some of the best relevant reviews published over that period of time.

2 Nanopore technologies

While microfluidics is still in its infancy, recent developments suggest that it may be rendered obsolete by nanofluidics before it even had a chance to become a success story! Indeed, as noted in our previous review [5], *in vitro* polymer translocation through nanopores has emerged as a promising technique for DNA analysis and sequencing. Experimental articles published since that review have furthered our knowledge about this process. For instance, Kasianowicz' group [6] has determined that the rate of entry of ssDNA into an α-hemolysin channel increases linearly with DNA concentration and exponentially with the voltage difference applied along the channel. They also found that the rate of entry is higher when the DNA enters the channel through the protein's larger vestibule rather than through the other end. Meller and co-workers [7] also studied this particular system in the presence of a voltage difference along the channel. They found that the translocation speed of long ssDNA strands, *i.e.*, longer than the channel, is independent of the polymer length. However, for polymers shorter than the channel, the translocation speed increases as the polymer length decreases. They also found that the translocation speed depends nonlinearly on the driving voltage. It thus appears that the confined geometry within the pore plays a nontrivial role in the translocation dynamics.

It is believed that a single nanopore could eventually allow a ssDNA strand to be read at a rate of several thousand bases per second [8]. Two key requirements for this to become reality are: (i) A reproducible and heavy-duty nanopore. In this respect, recent work on ion-sculpting promises to yield solid-state pores that could replace the currently used α-hemolysin channel [9]. (ii) A process to sequentially read the individual bases as the polymer threads through the pore, which may require the ssDNA strand to be threaded relatively slowly and the stochastic movement due to thermal motion to be minimized. This has yet to be accomplished.

Although DNA cannot yet be sequentially read using translocation, alternate ways of analysing DNA with the help of nanopores and ionic currents have recently been designed. In one case, Howorka and co-workers [10, 11] have shown that a given sequence of ssDNA can be detected using an α-hemolysin channel in which the complementary DNA sequence has been attached. Indeed, the target DNA binds to its complementary sequence and takes longer to translocate than the other chains. Another analysis method has been implemented by Kasianowicz' group [12]. In this case, DNA sequences are first designed to bind with a given analyte and are then allowed to translocate. In the absence of the analyte,

Electrophoresis 2002, *23*, 3791–3816

the DNA strands translocate normally across the nanopore. However, when the analyte of interest is present and binds to the DNA, two phenomena occur: (i) the rate of DNA entry into the pore decreases and (ii) once the DNA has entered the pore, the analyte prevents the DNA strand from getting through. Designing different signatures for different analytes could allow the simultaneous detection of various types of analytes using a single nanopore. Finally, Vercoutere and co-workers [13] have succeeded in distinguishing among various hairpins in ssDNA, down to a single-nucleotide resolution. Indeed, the hairpin must unfold during the translocation in order for the DNA strand to cross the channel, and the different sequences yield different signatures of ionic current.

Over the years, several theoretical papers have attempted to capture the dynamics of polymer translocation [14–27]. In almost all cases, however, the dynamics is being projected onto a quantity known as the translocation coordinate and defined as the length (or the fractional length) of the polymer on one side of the pore. In order for this approximation to be valid, the polymer on each side of the membrane is implicitly assumed to relax on a time scale much smaller than the one on which the translocation process is taking place. Even if experimental results do support some of the conclusions arising from current models, the separation of time scales assumption is probably not valid in the general case [28]. To our knowledge, [19] is the only theoretical paper to forgo this assumption. In addition, all current models neglect the effect of hydrodynamic interactions. The contribution of these interactions is likely to be nontrivial because of the presence of an obstruction, namely the membrane across which the translocation is taking place, and the nonequilibrium nature of the process. Consequently, although the basics of polymer translocation are now well understood, a lot of work remains to be done at the theoretical level before the intricacies of this process have been fully explored. In this context, we are currently studying this phenomenon using Molecular Dynamics simulations with explicit solvent, in which the excluded volume and the hydrodynamic interactions are explicitly taken into account (see Fig. 1). This approach should allow us to determine under what experimental conditions, if any, the separation of time scales assumption is valid.

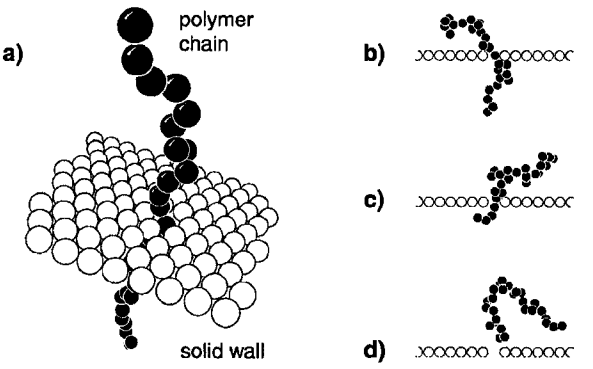

Figure 1. (a) In our current Molecular Dynamics simulations of polymer translocation, we study the unbiased translocation of a polymer chain through a pore in a thin membrane. The polymer (black beads), the membrane (white beads) and the solvent (not shown) are represented by identical point-like particles interacting through a purely repulsive Lennard-Jones interaction. In addition, the monomers of the polymer chain are held together by a FENE interaction and the membrane particles are simply kept immobile. The explicit inclusion of the solvent particles allows the hydrodynamic interactions to be taken into account. A schematic representation of actual simulation data is shown in (b)–(d): (b) the polymer is initially placed midway through the pore and the mid-monomer is held in place for a given relaxation period; (c) the mid-monomer is then released and the polymer is allowed to move back and forth freely through the pore; (d) the polymer eventually exits on either side of the membrane.

3 Surface electrophoresis

Pernodet and co-workers [29] recently proposed and tested a novel method for the separation of DNA fragments based on the strikingly simple process of inducing electrophoretic migration near a smooth surface. Using this approach, DNA strands migrate across a planar substrate, and the interactions between the DNA molecule and the substrate apparently act as a source of friction. In their proposed picture of the process, this friction is more significant for longer fragments than for shorter ones, hence the mobility becomes length dependent and separation is achieved. In some sense, this new idea lies somewhere between conventional electrophoresis and chromatography: an electric field drives molecules across the device, but the length dependence of the mobility arises due to surface interactions, rather than topological constraints. This research group has studied surface electrophoresis experimentally as well as with computer simulations, and they have updated their findings in two articles published this year [30, 31].

The experimental procedure is as follows. First, a SiOH-rich oxide layer about 2 nm thick is grown on a rectangular, flat and clean silicon substrate. A droplet containing a solution of fluorescently dyed dsDNA is then deposited at one end of the substrate and allowed to air-dry. Differential evaporation within the droplet focuses DNA fragments into a very thin band on the rim of the droplet, and these fragments bind (electrostatically) with the surface. The

substrate is then placed in a buffer-filled electrophoresis cell and an electric field is applied parallel to the surface. Finally, the fluorescence of the migrating molecules is detected as a function of time at a fixed distance from the injection point. Results indicate that the mobility (μ) scales with molecular size (M) as

$$\mu \sim 1/M^{0.25} \quad (1)$$

over an impressive range of molecular sizes spanning 3 orders of magnitude [30], from 125 bp to (at least) 164 kbp. The resolution (R) follows the predicted scaling law $R \sim M^{0.75}$, and appears to be mainly limited by the initial loading width, thus indicating that thermal diffusion is of a lesser importance under these conditions [30]. This new separation method offers three clear advantages: (i) the device fabrication and the mode of operation are very simple; (ii) there are no topological constraints, hence very long fragments can be separated (in fact, it is still not known if there is a maximum molecular size which can be separated); (iii) it can be readily integrated into emerging silicon-based microfluidic systems.

In order to better understand the separation mechanisms at work in surface electrophoresis, Luo and Gersappe [29, 31] performed Brownian Dynamics simulations of adsorbed chains subjected to a low intensity electric field. They used a standard coarse-grained approach in which all monomers interact *via* a Lennard-Jones (LJ) potential while adjacent ones interact *via* a finitely-extensible nonlinear elastic (FENE) potential [32]. The chain monomers and the surface atoms interact *via* an LJ potential with a tunable interaction strength, to mimic the surface interactions in the experiments. The simulation results confirm that the weakly and the strongly adsorbed cases correspond, respectively, to a 3-D and a 2-D free-draining regime, and that consequently no separation is possible in either of these limits. For intermediate interaction strengths, however, separation is observed and is attributed to the length-dependent chain conformations and to the formation of "trains" of adsorbed monomers and unbound loops extending in solution (see Fig. 2).

As with any new separation method, surface electrophoresis raises its share of new questions. However, owing to the simplicity of the design, it is reasonable to hope that these will be addressed and answered over the next few years. In particular, understanding the precise nature of DNA-surface interactions and finding ways to control them are issues calling for immediate attention. Some polymer coatings have already been studied [30], and current work focuses on the possibility of using surface nano-patterns to amplify and optimize the separation [31]. Roughening of the surface with a deposited film of microscopic beads has also been cleverly used to

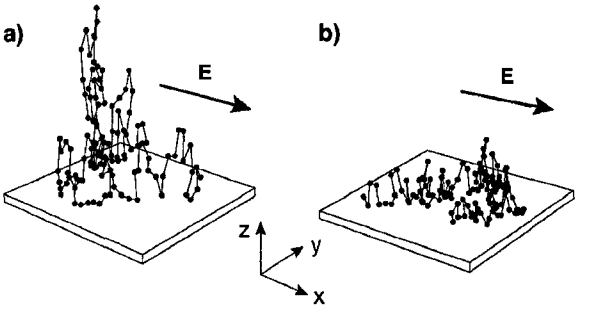

Figure 2. Snapshot of a polymer chain during computer simulations of surface electrophoresis performed by Luo and Gersappe. The chain is attracted to a planar substrate and is driven parallel to the surface by the electric field E. In (a) the surface interaction is weak and the chain behaves as a free-draining coil. In (b), the surface interaction is strong, hence the chain is tighly bound to the surface and apparently behaves as a 2-D free-draining coil. Separation according to molecular size is obtained for an intermediate attraction strength between these two limits. Reprinted from [31], with permission.

show that separation is indeed due to surface friction rather than topological constraints [30]. The design of a new loading mechanism amenable to integration on-chip is also needed for this method to find applications in microscopic analytic devices. Finally, as the exact nature of the separation mechanism remains elusive at this point, there is a pressing need for a more elaborate theory that includes electrostatic and hydrodynamic effects, both of which play a major role when DNA approaches a solid-liquid interface. Similarly, the computational model could be extended to explicitly include solvent molecules, electrostatic interactions and counter-ions (and the Debye layer near the surface) so as to continue to steer research on this topic towards a more realistic model.

To summarize, it appears worthwhile to follow developments in surface electrophoresis. Not only can it potentially serve as a simple and more efficient separation mechanism, but a better understanding of polymer-surface interactions has direct applications in microfluidic devices where polymers travel in highly confined environments.

4 Ratchets

A ratchet is a device that can induce directional motion of particles or molecules without a net external force or gradient. The operating principle of ratchets relies on the rectification of the effects of either thermal motion or a zero-average external field [33, 34]. This fascinating concept continues to permeate many fields, from quantum

Electrophoresis 2002, *23*, 3791–3816

mechanics to biophysics, and perhaps the current level of enthusiasm for ratchets is best illustrated by the special issue on the subject published recently in *Applied Physics A* [35]. From our standpoint, ratchets are interesting for three main reasons: (i) they can operate as novel separation systems, or enhance the performance of existing ones; (ii) they can serve as a transport mechanism for particles or molecules on the microscopic scale, a task pertinent to the integration of electrophoresis technologies on chip; (iii) because of the first two points, they may be used as complementary and orthogonal techniques for the separation of complex mixtures of analytes.

The development of theoretical and computational models of ratchet systems flourishes [35–44] and is essential for the design of new separation methods and the interpretation of experimental observations. One of the challenges encountered in describing the operation of real electrophoresis-based ratchets is the faithful representation of the field lines in microfabricated electrophoretic devices. A vivid example of this difficulty is given in a recent article by Austin *et al.* [45] where they consider the curved field lines present in an asymmetric array of insulating deflectors; Austin's group [46] has successfully used this type of array to separate DNA molecules in a continuous mode. They show that if the obstacles are perfect insulators and if the particle density is symmetric, then there can be no deflection of particles on average, so no separation should be observed. The fact that separation does occur experimentally can be attributed to various factors (such as partly conducting obstacles or the deformation of the macromolecules), but this example illustrates that a realistic representation of the field lines can become crucial in the interpretation of experimental results. On the other hand, the curvature of the field lines around obstacles does not always affect the dynamics; indeed, our group has shown that in general, in the zero-field limit, the electrophoretic mobility and the diffusion coefficient of a point-particle is independent of both the field lines curvature and the obstacle shape [47].

Computer simulations of ratchet systems are useful for the optimization of separation techniques. Since the quality of separation is mostly affected by diffusion, it is important that new models of ratchets take into account the dispersion of particles in addition to their average dynamical properties. This question is addressed by Keller *et al.* [36] in a paper where they calculate not only the macroscopic drift velocity, but also the diffusion tensor of particles in a 2-D geometric ratchet, *via* a lattice Monte Carlo simulation. This allows them to evaluate the quality of the angular separation Q of two different kinds of particles using both their average position $\langle x \rangle$ and their dispersion σ:

$$Q = \frac{|\langle x_1 \rangle - \langle x_2 \rangle|}{\max(\sigma_1, \sigma_2)} \quad (2)$$

Their calculation reveals that the quality of a separation does not rely solely on the magnitude of the ratchet effect (which is often considered a measure of the quality of ratchets). The diffusion process resulting from the ratcheting effect obviously plays a major role in determining the value of Q and should not be overlooked in future models.

Current models of ratchets often impose other restrictions that should be overcome in the forthcoming years. One example is the adiabatic approximation in which the frequency (ω) of the applied force is supposed small compared to the relaxation time of the analyte. In 2002, Fistul [37] calculated the motion of an overdamped Brownian particle in a ratchet beyond this approximation. His derivation offers an explanation for the sign reversal of the velocity function $v(\omega)$ with increasing ω, previously found in numerical studies. This illustrates the fact that unexpected and useful dynamical properties of ratchets can be uncovered if we extend current models to higher frequency regimes. Finally, we want to point out that most of the theoretical studies still deal with point-like particles. However, one of the most interesting applications in separation technologies – the sorting of DNA or polymers – involves macromolecules, which possess a large conformational entropy that can be used as a separation parameter. An example of a ratchet exploiting molecular entropy was first described by Slater *et al.* [2] and we think that efforts should continue in this direction, both theoretically and experimentally.

It is by now well established that ratchet devices work in practice, and ongoing work focuses on exploiting them for separation purposes. Marquet and co-workers [48] designed a promising ratchet system which exploits both dielectrophoresis and electrophoresis effects. Their system induces directed motion of latex beads (1–6 μm in diameter) using an oscillating electric field (of zero mean value) in a microfabricated channel with an asymmetrically modulated diameter. Another prime example of a successful Brownian rectifier is the one built by Bader and co-workers [49–51] for DNA oligomer separation in free solution. Their device consists of interdigitated electrodes which produce a simple asymmetric sawtooth potential (see Fig. 3). During the field-on periods, DNA molecules drift to the bottom of the potential wells, while during field-off periods, they undergo free diffusion. Owing to the asymmetry of the potential profile, the molecules tend, on average, to drift in a given direction. In a recent report, the application of this device to fast genotyping of single-nucleotide polymorphisms (SNPs) is discussed [49]. Another type of functional ratchet is the field-rectifying device conceived by Griess and Serwer [34, 52,

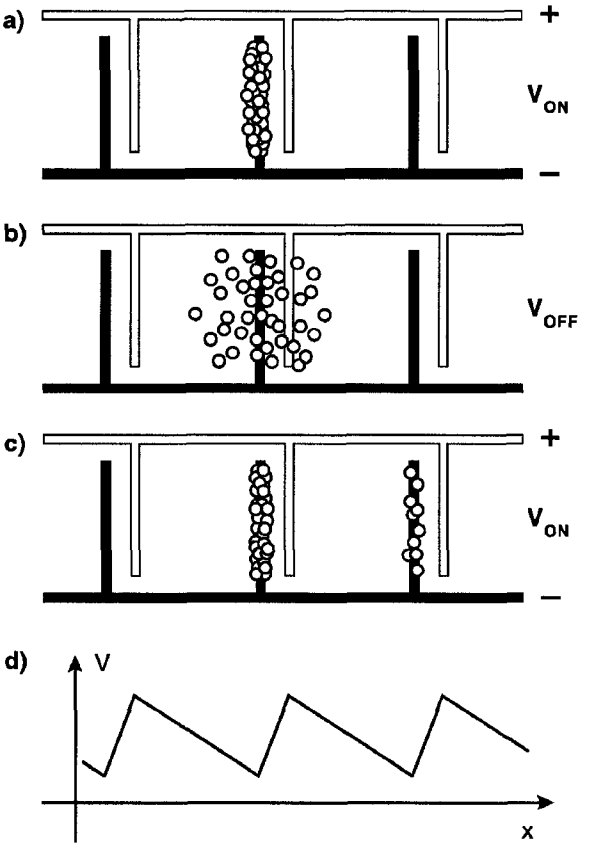

Figure 3. A simple Brownian ratchet device. An asymmetric saw-tooth potential $V(x)$ is created using interdigitated electrodes (d). When the field is on, the positively charged particles are trapped near the negative electrode (a). When the field is turned off, the particles (with a diffusion coefficient D) diffuse symmetrically around this electrode (b). When the field is turned back on again, the particles that have diffused beyond the neighboring positive electrodes are trapped by the next negative electrodes (c). Since these electrodes are asymmetrically distributed in the space, it results a net motion of the particles with a velocity directly related to D (inspired by Fig. 1 of [51]).

53] for the separation of DNA. They use a standard gel matrix as the separation media, but drive the molecules with an electric field E that slowly alternates between long low-intensity strides in the forward direction, and short high-intensity steps in the reverse direction (with an average force over time of zero). Since the mobility of DNA in the gel is both E-dependent and size-dependent, net motion is induced and interesting migration regimes arise. Most notably, by alternating between a ratchet mode and a continuous mode, the resolution can be increased to a limit set only (at least in principle) by the detection sensitivity [53]. Griess and Serwer [34] also describe a circular preparative electrophoretic cell in which strands of different lengths could migrate at different angles. Other applied work includes a computer simulation of an existing microfluidic separation system by our group. We modeled the microfluidic device fabricated by the Craighead group [1, 54] and found that, in the ratchet regime, the drift of the macromolecules is rectified, and that strands of different lengths can be forced to migrate in opposite directions when a small field bias is applied [55]. Moreover, we studied an asymmetric version of the Craighead channel and showed that it can rectify the motion of molecules subjected to an unbiased square-pulse driving field; this is an example of the entropic ratchet concept introduced by Slater *et al.* [2] a few years ago.

As bioanalytical tools are integrated on-chip, transport of fluids in μm-size channels becomes a challenge. Ajdari [56, 57] has proposed a clever way to combine electroosmotic and ratchet effects to build a pump that relies exclusively on small local oscillations of the electric field. The idea is to create small electroosmotic vortices with electrodes on the channel walls. When the electrodes are placed in some asymmetric fashion, the vortices themselves become asymmetric and net momentum is transferred to the bulk fluid. Interestingly, this method allows for the transport of small droplets since everything occurs locally. A prototype of such a pump has been built [58] and appears to operate as predicted. Another experiment exploiting a ratchet effect to control microdrops is based on a channel whose diameter is modulated with an asymmetric saw-tooth shape [59]. Applying an oscillating electric field or even a mechanical vibration disrupts the contact lines between the fluid and the walls, and the asymmetry of the structured surface rectifies the motion of the drop. Along similar lines, functional drift ratchets in which the fluid in pumped back and forth in asymmetric pores in order to separate suspended particles have been built [60].

Overall, the fundamental questions about ratchets we asked in our previous review continue to hold [5]. Band broadening remains an issue for Brownian ratchets, which are based on diffusion and are thus inherently stochastic. Perhaps resorting instead to strategies without a diffusive step proper, as in shifted ratchets [61] or field-rectifying ratchets [62] can help to address this problem. Ratchets are also still limited in the molecular size range they can handle, because of the physical size of their features. However, field-rectifying ratchets offer the possibility to work with traditional media, amenable to a broad size range, or perhaps with surface electrophoresis where there are simply no obstacles and therefore no preferred length scale (see Section 3 herein). Finally, no

Electrophoresis 2002, *23*, 3791–3816

ratchet separation scheme based on substantially new molecular properties has been proposed. On the other hand, potent new ratchet mechanisms, involving EOF and surface tension effects, have been devised for the control and transport of fluids in microscopic channels.

5 Entropy-based separation systems

Internal conformational entropy is certainly one of the dominant properties of flexible macromolecules such as DNA. Moreover, internal entropy is directly proportional to the molecular contour length (*i.e.*, it is an extensive property), so it only seems natural to devise schemes that utilize entropic effects to achieve size-separation of macromolecular objects, such as DNA fragments. Such schemes are typically rooted in the process of entropic trapping (ET), which consists in trapping molecules in regions where their conformational entropy is maximized (*e.g.*, voids inside a cross-linked gel). ET was first introduced as a generic concept over a decade ago by Baumgärtner and Muthukumar [63–65], and has since been the object of numerous experimental and computational studies [66–72]. In one recent article, Liu, Li and Asher [73] report on a novel way to construct sieving gels comprising a periodic array of voids by selective etching out of self-assembled silica beads (~100 nm in diameter) included during gelation. The regularity of the void spacing has made the direct experimental verification of ET possible *via* diffraction measurements. At a recent American Physical Society meeting, Hoagland [74] reported using a somewhat similar approach to template a 2-D gel with close-packed spherical beads, and observing the discrete "hopping" of DNA molecules between traps directly *via* fluorescence microscopy. It will be most interesting to see the properties of these gels when used as sieving media for electrophoresis.

At the risk of giving the reader more reasons to believe that we suffer from the bias acknowledged in the introduction of this article, we think that the most striking demonstrations of entropic effects lie in recent experiments performed in microfluidic channels. Members of the Craighead research group from Cornell have built and tested microfabricated devices for the separation of DNA which exploit entropic effects. This group's most recent experimental system consists in a quasi-2-D channel in which some regions are populated with a dense array of nanopillars (35 nm diameter) [75]. Long DNA molecules can be driven trough the pillared region with an electric field, but since the pillars are closely spaced (160 nm apart), the DNA must elongate in order to migrate downfield, at a great cost in conformational entropy (see Fig. 4). When the field is turned off, molecules that have only partially entered this region quickly recoil in the pillar-free region in order to maximize their conformational entropy. Not only can this device be developed into a functional separation tool (for instance, because longer DNA molecules take more time to enter the pillared region), but it also allows first-hand observation, *via* fluorescence microscopy, of the recoiling DNA molecules. This can certainly improve our understanding of the dynamics induced by entropic effects.

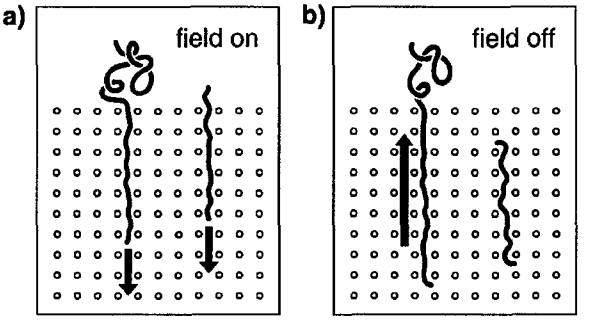

Figure 4. A schematic top view of the recent microfluidic separation device built on chip by the Craighead research group. The pillars, shown as small circles, are approximately 35 nm in diameter and 160 nm apart. In (a), the electric field pulls DNA fragments in the low-entropy pillared region. In (b), the field is turned off, and molecules that straddle the interface rapidly recoil to return in the open region. Molecules that have completely entered the pillared region, however, have no impetus to recoil and simply relax locally (inspired by [75]).

Earlier, the same group built another separation device that also relies on entropic effects. It consists of a periodic array of alternating deep and shallow regions [1, 54]. DNA in the 10–100 kbp range is electrophoresed through the structure and becomes trapped at the entrance of the shallow constrictions, before it manages to escape in a slithering motion. The typical trapping time of the molecules is length-dependent and, surprisingly, long molecules migrate faster than shorter ones (it turns out that this a geometric effect: bigger coils expose more monomers to the shallow region entrance and thus increase their chances of escape per unit time). In a recent paper, Han and Craighead [76] further developed a theoretical model of this device, identified the optimal conditions for enhancing resolution, and discussed ways to scale the method to smaller fragments or even megabase strands. Monte Carlo simulations of this device by our group [77] largely support the proposed scaling relationship for the mean trapping time τ in the low field regime,

$$\tau \sim \frac{1}{\sqrt{M}} \exp\left(\frac{\alpha}{E_S k_B T}\right) \tag{3}$$

where M is the number of monomers in the chain, E_s is the field strength in the constriction, T is the absolute temperature and α is a constant. The simulations also highlight some finer aspects of the geometric and relaxation effects and also suggest the possibility of resolving topological objects such as rings and knots. When extended to the case of alternating driving fields [55], our simulations indicate that the system could operate in various low-frequency ratchet regimes, and reveal an interesting resonance effect occurring when the frequency of the driving pulse is commensurate with the mean trapping time of the molecules.

We should also mention that microfabricated separation systems typically demand fairly long channels, so having them curve back and forth on the chip surface is sometimes required for proper packaging. Incidently, this curvature itself gives rise to subtle entropic effects, because there is more volume per arc length (hence more entropy) along a curved channel section. This phenomenon has been addressed analytically before [78], and is currently under experimental investigation by Ueda and co-workers [79], along with interesting and potentially useful electric field gradients and polymer stretching effects in curved geometries.

While it is true that there has been significant progress on the experimental aspects of ET brought about by microfluidic technologies, strides have also been taken on the theoretical front. The reason behind the vigorous development of theory in this area is that ET is ultimately related to the problem of barrier crossing for macromolecules. In order to understand ET, one must also understand how flexible objects escape from potential wells. This fundamental problem is very generic (equivalent to the Kramers problem for Brownian particles [80]) and fosters a unified perspective on the behavior of macromolecules in constrained environments. Current models mainly attempt to describe how flexible chains stretch to reduce the effective height of potential barriers. Following the work of Park and Sung [81], Sebastian and Paul [61, 62] studied the Kramers problem for macromolecules using a Rouse model, in the case where the barrier width is smaller than the polymer contour length. They identified two escape mechanisms, namely end-crossing and hairpin formation, and derived expressions for the activation energy, the crossing time and the net crossing rate. Lee and Sung [82, 83] studied the same problem from the point of view of a coil-stretch transition of polymer chains and rings, and explained how conformational fluctuations also participate in lowering the barrier. Muthukumar [22] developed the theory for the translocation of a confined polymer through a small pore, by analogy with a nucleation and growth process. Of note, his Brownian Dynamics simulations uphold his prediction that the mean escape time τ scales as

$$\tau \sim M(M/\rho)^{1/3\upsilon} \quad (4)$$

where M represents the number of monomers, ρ is the initial density in the vesicle and $v = 3/5$ is the Flory exponent in 3-D. Finally, Reguera and Rubí [84] have developed a kinetic model for the diffusion of particles in the presence of entropic barriers based on a Ficks-Jacob equation. If their formalism can be extended to deformable objects and to cases where trapping occurs (non-ergodicity), it could provide a very general framework to analyze the dynamics of macromolecules in the presence of entropic barriers.

6 Magnetic self-assembling sieves

Microlithographically fabricated devices such as quasi-periodic arrays of fixed obstacles etched on a silicon surface have been employed as a separation medium for DNA [85]. The production of these devices is a sophisticated and costly procedure with little tunability after construction. A promising new alternative [86, 87] is the use of quasi-regular arrays of columns, formed by the application of a homogeneous magnetic field (> 10 mT) to a suspension of superparamagnetic particles (with a diameter on the order of a few micrometers) confined between two parallel flat plates. Doyle *et al.* [86] have employed such a medium composed of self-assembled posts of a Fe_2O_3 ferrofluid with inter-post spacing of 5 μm to effectively separate 48.5 kbp λ-DNA and associated fragments of 15 and 33.5 kbp in 10–15 min, see Fig. 5. The λ-DNA electropherograms were reproducible within approximately 6% with each subsequent replacement of the sieving medium. The resolution ranged from 5.5 kbp for the 15–33.5 kbp samples to 11.6 kbp for the 33.5–48.5 kbp samples. Size separation in these systems is achieved due to polymer post entrapment [88]. The polymer forms a pulley like structure, where the two downfield arms of the polymer compete to release the molecule. The time it takes to disentangle from the post is a function of the molecular contour length and hence separation is possible [87–90]. This is unlike gel electrophoresis where a long DNA molecule is actually colliding with many gel fibers simultaneously.

Earlier work by Liu *et al.* [91] provided the initial impetus for the possible application of self-assembled ferrofluids as separation media. By comparing experiments and results from a mean field model, they indicated that the average post separation, d^*, can be controlled by varying the height of the microchannel, L, and the ferrofluid volume fraction, and that in particular, post spacing is related to channel height *via* a power law of the form

$$d \propto L^{0.37} \quad (5)$$

Electrophoresis 2002, 23, 3791–3816

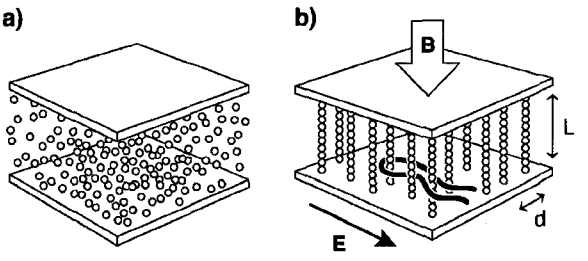

Figure 5. (a) A schematic representation of a microchannel of height L which contains a suspension of superparamagnetic particles (~ few μm in diameter), before application of external magnetic field. (b) With the application of an external magnetic field B (~mT range) these particles self-assemble into a quasi-regular array of posts, of height L and average inter-post spacing d. When DNA is placed in this array and an electric field is applied the polymer chain becomes hooked around a post in a pulley-like conformation, the escape time is dependent on the molecular weight of the DNA and separation is possible (inspired by [86]).

at fixed magnetic field strength and ferrofluid volume fraction. This clearly indicates the tunability of post spacing. More work is required in order to understand the effects of the magnetic field strength, the volume fraction and the channel width on post spacing, en route to building arrays specifically suited to particular separation tasks.

Several models for the entrapment of polymers by isolated fixed immovable obstacles currently exist, notably those developed by Nixon *et al.* [89], Sevick *et al.* [90] and André *et al.* [88]. Nixon *et al.* [89] were the first to carry out simulations of polymers colliding with fixed immovable objects using 2-D Brownian dynamics; these simulations confirmed that the DNA becomes trapped in a pulley-like configuration. One key aspect missing in most simulations is the inclusion of the effects of hydrodynamics, which can play a crucial role in the dynamics of DNA post collisions and the subsequent escape mechanism as illustrated in the theory of André *et al.* [88]. Our group is currently carrying out molecular dynamics simulations, which examine the effects of hydrodynamics (*via* the explicit inclusion of solvent) on the escape times of DNA colliding with such obstacles.

The use of self-assembled arrays of posts as a separation medium has several key advantages over existing microlithographic etched arrays: (i) the post separation, or effective pore size is tunable and reproducible to within about 5% [86] by modifying the strength of the applied magnetic field and/or the concentration of ferrofluid (typical post separations range from 1 to 100 μm); (ii) self-assembled arrays do not require costly and sophisticated techniques (such as lithography) in their construction, making this method feasible for many more researchers; (iii) suspensions of ferrofluids have low viscosity in the absence of a magnetic field and are well suited for injection into narrow channels; (iv) self-assembled arrays can be altered on the fly (*e.g.*, by changing the magnetic field intensity, even during separation) for specific applications. This last point is unique to this system. Thus, as a separation medium, self-assembled arrays hold a great deal of promise, and ultimately can find a number of applications in separation science and lab-on-a-chip technologies.

7 Electrophoresis of composite molecules

Molecules composed of sections differing in character, such as in stiffness or charge density, can exhibit interesting electrophoretic behaviour. Due to their inhomogeneity, they can exhibit a size and/or charge-distribution dependent mobility even in free solution, a very promising conceptual breakthrough which, in the case where it is applied to DNA separations, may be exploited to overcome the need for filling the capillary with a sieving matrix. This is in contrast with uniformly charged polyelectrolytes such as DNA, which comigrate regardless of length (this is the famous free-draining property of DNA that is so annoying). This behavior is due to the presence of counter-ions around the charged DNA. Were they not there, a buildup of hydrodynamic interactions between the monomers would occur, and the fluid within the DNA coil would be moved along with the electrophoretic motion of the chain. This would result in a hydrodynamic friction coefficient ξ proportional to the 3-D size of the chain ($\xi \sim R_G \sim M^{1/2}$, where R_G is the radius of gyration of a molecule of M monomers), such that the electric force each monomer experiences would not be balanced locally by the hydrodynamic force [92]. In such a hypothetical case, the electrophoretic velocity would be given by $v = QE/\xi \sim M^{1/2}$, where Q, the charge of the molecule, scales as M and separation would be achieved. This line of thinking, unfortunately, applies only to mechanical forces and does not normally apply to electrophoresis (the only exception would be a case where the Debye length exceeds R_G, an impractical limit). With counter-ions present around the chain, a force equal to the one pulling the DNA in one direction, pulls the counter-ions in the other direction. This effectively cancels the long-range hydrodynamic interactions between the monomers, resulting in a local balancing between the friction and the electric force, rendering the mobility size-independent ($\mu \sim Q/\xi$, where both Q and ξ scale as M), see Fig. 6a. In effect, the chain is in free-fall in the solution. This free-draining property of DNA has been well established

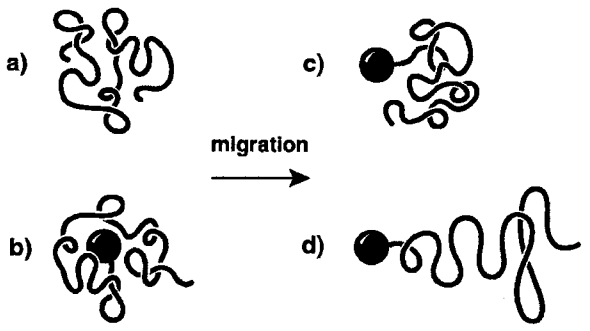

Figure 6. Schematic of free-solution electrophoresis of (a) naked DNA; streptavidin end-labeled DNA in (b) a random coil conformation, (c) a segregated conformation, and (d) a stretched conformation.

experimentally [93]. However, it is with nonuniform molecules that this local charge balance can be broken, and that separation can be, and has been achieved.

The electrophoresis of polyampholytes (molecules containing both positive and negative charges) has been examined theoretically by Long *et al.* [92]; they took into account hydrodynamic interactions, and have assumed a Gaussian chain comprising monomers of identical hydrodynamic radii. They showed that hydrodynamic interactions are indeed sometimes very important in the electrophoresis of nonuniformly charged chains, for the usual condition of high salt concentration. Since the counterions are not evenly distributed along the length of the chain, but rather vary with each monomer's charge, the hydrodynamic effects are no longer such that the friction coefficient scales identically to the net or total charge of the molecule. This exciting result indicates that the mobility can become size-dependent and hence separation is (perhaps) achievable. For circular chains, they found that the mobility is simply the uniformly weighted average of the individual monomer mobilities, while for linear chains the details of the charge distribution play a role. This is due to "end-effects" wherein monomers located, on average, in the outer regions of the coil, such as the monomers at the ends of the chain, are subject to higher overall hydrodynamic friction than those located inside the coil. Hence for linear chains, the end monomers have a higher weighting in the average yielding the total mobility, while the inner monomers (approximately 90% of the chain) have about equal weighting.

The theoretical approach presented by Long *et al.* [92] for the electrophoresis of composite molecules has been recently extended to end-labeled free solution electrophoresis (ELFSE), so as to better understand and utilize the experimental results [94, 95]. These authors analyzed the successful separation of streptavidin end-labeled ssDNA (S-DNA) by free solution CE. Modifications to the pre-existing theory involved accounting for the different hydrodynamic sizes (and therein friction coefficients) of the DNA and the streptavidin through a regrouping of the composite molecule into units of equal hydrodynamic size. The overall mobility was found to be:

$$\mu \sim \mu_0/(1 + \alpha/M) \quad (6)$$

where μ_0 is the electrophoretic mobility of DNA in free solution, and α is the molecular size (*i.e.*, number of bases) of a random coil DNA section that would have the same friction coefficient as the streptavidin. Since the latter depends on the stiffness of the coil, the measured mobility yielded the DNA persistence length as a function of ionic strength. In fact, this measured dependence of α on the ionic strength invalidates the simple picture wherein the mobility is the ratio between the effective charge Q, proportional to the contour length, and an electrophoretic friction coefficient also proportional to the contour length, as would be the case were the two units segregated (Fig. 6c). They showed that for the DNA to be segregated from the streptavidin, unrealistically high electric fields would be necessary. For their experimental conditions, they estimated the limiting electric field for which the composite molecules start to lose their random coil conformation (Fig. 6b) to be approximately 10 kV/cm, which is much higher than that commonly used in electrophoresis. Beyond this segregation regime, at even higher fields (or for much larger uncharged molecules than streptavidin), the DNA would begin to stretch (Fig. 6d), as discussed in [94]. It is interesting to note however that the diffusion coefficient in the random coil regime is expected to scale as $M^{-1/2}$, whereas in the stretched conformation regime the expected scaling would be M^{-1}, and hence sharper bands would be anticipated were very high fields to be used.

As a means of better understanding the electrophoretic behaviour of composite molecules, Slater and co-workers [95] also examined the migration of these molecules in semidilute (entangled) and dilute solutions of non-cross-linked polymers, wherein additional factors may come into play, including collisions with the neutral polymers and steric trapping. In free solution and dilute polymer solutions the separation of S-DNA molecules is due to the extra hydrodynamic friction provided by the streptavidin, hence larger (more charged) molecules move faster. In contrast, for S-DNA migrating in a sufficiently concentrated polymer solution, the larger molecules are subject to more collisions, and can also become sterically trapped more so than smaller molecules, and hence move more slowly. Therefore, in the regime intermediate to free solution and semidilute polymer solutions, non-monotonic mobility-size relationships are observed. Their

results even suggest a universal relationship between the mobility of S-DNA and naked DNA, applicable in free solution, polymer solutions and gels:

$$\mu_{S-DNA}(M) \approx \mu_{DNA}(M+\alpha)\frac{M}{M+\alpha} \quad (7)$$

This work additionally confirmed the random-coil conformation of the S-DNA composite, as opposed to the segregated conformation (see Fig. 6). Their experimental results indicate that collisions with the polymers in solution had the same effect on the mobility of both DNA and S-DNA of the same effective molecular size; hence, both are in a random coil conformation. The good agreement they found between their theoretical predictions and experimental data further supports the proposed hydrodynamic coupling between the streptavidin and DNA.

Successful separations of uncharged polymers, based on the same concept, have been achieved, where the DNA was utilized as a uniform, charged "engine" to characterize polydisperse samples of synthetic uncharged polymers [96, 97]. Their composite molecules, for example, ssDNA-poly(ethylene glycol) (DNA-PEG) yielded single monomer resolution in free solution CE. Similar to ELFSE, separation with free solution conjugate electrophoresis (FSCE) is made possible by the extra hydrodynamic drag of the neutral PEG polymer. While the electromotive force is the same for all molecules (as each has an identical DNA section), the different lengths of the neutral PEG components give them different mobilities. FSCE compares quite well with matrix assisted laser desorption ionization-time of flight (MALDI-TOF) [96] and reversed-phase high performance liquid chromatography (RP-HPLC) [97]; in fact, FSCE was shown to produce separation resolutions approximately five times higher than with the more traditional RP-HPCL, and increase separation efficiencies by 150%. In addition, this method of molar mass profiling has the advantage of not requiring internal standards or calibration, and is amenable to chip-based electrophoretic systems.

A theoretical model, similar to the one for ELFSE, was developed for FSCE [98], wherein for the most favourable, diffusion-limited electrophoresis conditions, an optimal DNA size for separation of the neutral polymer was predicted. The theory, being in good agreement with the available preliminary experimental results, also offers a means of estimating the persistence length of the uncharged polymer through mobility measurements.

It is also important to note that with both the ELFSE and FSCE theories, the end-effects predicted by Long *et al.* [92], which are purported to increase the weighting of the terminal monomers, (significantly for the last approximately 5% of each end), have been neglected. While the predictions still fit the experimental data nicely, there is some indication that end-effects could become relevant under certain conditions. In FSCE, for example, neglecting the end-effects yields similar (and sufficiently accurate) values for the PEG persistence length when the PEG is 3.4 or 5.0 kDa; however, this approximation leads to a slightly different value for a much larger drag molecule of 20 kDa, where the composite molecules are larger and the charged monomers constitute a smaller relative percentage. Such high-precision experiments could lead to the first experimental confirmation of the purported end-effects.

The work being done on the electrophoresis of composite molecules is also relevant to otherwise inhomogeneous molecules, such as those with varying sulfonation rates, *i.e.*, where not all monomers have the same effective charge. Similar to ELFSE and FSCE, these chains will have different local friction coefficients for charged and uncharged monomers, and the force and friction need not locally balance such that separation can be achieved based on the degree of sulfonation and even on the distribution of charges at a fixed degree of sulfonation. For examples of electrophoretic separations based on such heterogeneities, see Zhang *et al.* [99], or Cottet *et al.* [100], who have studied of the mobility of polystyrenesulfonates of varying sulfonation rates.

Composite and otherwise inhomogeneous molecules present an exciting means of pushing the useful limits of electrophoretic systems, and furthering our theoretical understanding of the fundamentals underlying electrophoresis. Their study also illustrates the necessity, in general, of taking into account hydrodynamic interactions, and charge and size inhomogeneities within chains. They open up the possibility of separation without the need of sieving matrices, not only for charged species, but also for uncharged entities that can be specifically attached to a suitable charged "engine". We should keep in mind that proteins are indeed inhomogeneously charged polymer chains (with the added twist, however, that they are often folded).

8 Small DNA molecules

Between any two individuals, only slight differences in the sequence of DNA exist; however, they are responsible for one's genetic predisposition to disease. These differences, being indeed small at around one part-per-thousand, also form the basis of forensic identification and paternity determination [101]. In order to analyze these tiny differences, including mutations and SNPs, extremely sensitive separation techniques are often necessary. In particular, it is with small fragments of DNA that adequate

sensitivity can be attained. Hence, in order to improve the capabilities and accuracies of such analyses, a deeper understanding of the electrophoretic behaviour of small DNAs is invaluable. Such an understanding is also of fundamental importance in theoretical physics since it should in principle be possible to make quantitative predictions about small molecules with few internal degrees of freedom. This section presents recent advances in this regard.

Stellwagen and co-workers have made significant contributions to our knowledge of the free solution mobility of small DNA molecules. In 1997 they confirmed that while the free solution mobility of DNA was independent of molecular mass from around 400 bp through to 48.5 kbp, for shorter fragments it decreased monotonically [102]. Recently, however, this group [103] performed capillary zone electrophoresis measurements of mobility wherein mobility markers were utilized to account for small EOF differences from run to run and thereby uncover very small variations in the mobility of various analytes. For example, to compare the mobilities of small DNAs, a 403 bp DNA was used as a marker, its mobility averaged over the entire course of experiments ($<\mu_{marker}>$) and then added to the difference ($\Delta\mu$) between the two mobilities (marker and analyte) in a given run in order to yield the EOF-corrected mobility of the analyte:

$$\mu_{corr} = <\mu_{marker}> \pm \Delta\mu \quad (8)$$

By this method (and by studying a greater number of fragment lengths in the critical range) they elucidated more precisely the molecular mass at which DNA mobility becomes size-independent; rather than 400 bp, they found the value to be approximately 170 bp in 40 mM Tris-acetate-EDTA. They point out that this limiting length for the leveling off of the mobility *versus* molecular weight may be related to a transition from rod-like to coil-like conformation to a coil. Through use of mobility markers they were also able to observe very small mobility differences between oligomers of the same size. On analyzing 20 bp dsDNA of different sequences, those containing three or more adjacent adenine residues (A-tracts) were found to migrate more slowly than those void of A-tracts. A-tract DNAs have been linked to a bent conformation [104]; Stellwagen and co-workers also caution that different buffers may have different effects on the sequence dependency of DNA bending. For single stranded oligomers, they suggest that composition may affect mobility more so than the actual sequence. In their review article, Righetti *et al.* [105] discuss the effect of the ionic strength of the solution on mobility, indicating that it is also important to properly take into account such effects when comparing the mobilities obtained from different experimental conditions. Due to the lack of theory predicting their results on the sequence dependent nature of the free solution electrophoretic mobility of DNA, Stellwagen and co-workers point out that further study is indubitably needed.

The mobility of short DNA fragments migrating within a gel is governed by different underlying physical mechanisms than that of free solution electrophoresis, and this difference presents another interesting area of research. The known increase in free solution mobility of DNA with molecular size, up to about a couple hundred base pairs, was utilized by Mohanty and McLaughlin [106] to develop a model of polyacrylamide gel retardation data for oligomeric DNA. The model seems to predict the experimentally observed behaviour of mobility increasing with increasing size, reaching a maximum (the location of which depends on the mean pore size of the gel), followed by a decrease. Brownian dynamics (BD) was recently used by Allison *et al.* [107] to model the gel electrophoretic mobility of short rod-like dsDNA fragments, 10–50 bp in length; their results suggest an interaction between the DNA and the gel (the gel was modeled by a 3-D cubic lattice). Taking into account excluded volume interactions, they validated the BD methodology by successfully reproducing independent mobility values for spherical particles. In applying this method to short DNA fragments, however, they found that it was necessary to include strong attractive interactions between the DNA and the gel in order to obtain good agreement with experiment, namely to obtain the same mobility dependence on gel concentration as observed experimentally in Tris-acetate buffer and polyacrylamide gels. They suggest that the anomalous migration of "bent" DNAs found experimentally [108] may be due to the formation of an unusually stable complex between the bent DNA and the polyacrylamide gel fibre. This group plans to expand their model to investigate bent DNA and the anomalous mobility associated with certain sequences of DNA fragments.

It was recently shown that the Nernst-Einstein equation, despite its common usage, is not valid for free-flow electrophoresis of DNA molecules [109]; analysis of the diffusion coefficient of various DNA lengths revealed that, unlike mobility, diffusion is not modified by the free-draining nature of the DNA during electrophoresis. This is because mobility depends on the net flow of solvent around and through the DNA coil (see Section 7), while diffusion is related to fluctuations in the flow of solvent. The former are affected by the electric field (the electric forces make the DNA coil permeable to the counter-ions and the solvent) while the latter are not. Hence the mobility, μ, is related to electrostatic factors, while the diffusion coefficient, D, is purely mechanical, and the Nernst-Einstein equation,

$$\frac{D}{\mu} = \frac{k_B T}{Q} \tag{9}$$

where Q is the charge, cannot be valid. The paper points out that the diffusion properties of small ssDNA are, however, well explained by the Zimm equation,

$$D(M) = \frac{k_B T}{6\pi\eta R_H(M)} \tag{10}$$

where η is the buffer viscosity, M is the number of DNA monomers and R_H is the hydrodynamic radius of the DNA molecule. However, the situation of gel electrophoresis is different: gel fibres screen the hydrodynamic interactions over distances larger than the pore size, such that the Nernst-Einstein equation is valid in the limit of low field intensities. The scaling of the ssDNA free-solution diffusion coefficient with the number of monomers was found to be approximately $D \sim M^{-0.86}$, the same as reported by Stellwagen *et al.* [110] for short dsDNA fragments.

Recently, the diffusion coefficient of very small DNA fragments was investigated by Stellwagen and Stellwagen [103]. They found that, in contrast to their mobility, the diffusion of dsDNA oligomers was sequence-independent. This result was accompanied by a comparison between single- and double-stranded DNAs of the same length; the diffusion of the dsDNA was shown to be approximately half that of the ssDNA (for 20 nucleotides), in keeping with the much larger persistence length of dsDNA (about 50 nm *vs.* 3 nm). In this paper, they also express concern over the validity of the Nernst-Einstein equation for very small rod-like DNA in free solution, indicating a desire for an extension of the Ekani Nkodo *et al.* [109] results into the regime of rod-like DNA to ensure that the behaviour holds. Theory actually suggests that the Nernst-Einstein relation should be valid in the limit where the size of the molecule is smaller than the Debye length of the ionic solvent solution.

Indeed, there is need for further investigation into the fundamental basis of the electrophoresis of small DNA molecules. In order to move beyond sequencing, and improve the reliability and ease of identifying minute differences in the genetic code, a more complete analysis and theoretical understanding of this regime of electrophoresis, both in gel (does the Ogston model apply to small DNA molecules being separated by capillary gel electrophoresis?) and free solution, is required.

9 Dilute solutions of sieving polymers

Nearly a decade has elapsed since Barron *et al.* [111] first demonstrated that, remarkably, dsDNA is separable in dilute ($c < c^*$) and ultradilute ($c \ll c^*$) solutions of neutral polymers (where c is the concentration and c^* denotes the entanglement concentration). Many subsequent studies have aptly illustrated the wide applicability of this technique for separating double-stranded (dsDNA), single-stranded DNA (ssDNA) and supercoiled DNA (scDNA) under a variety of experimental conditions [112–117]. Still pending, however, is a complete understanding of the optimal conditions under which to carry out dilute and ultradilute CE and the mechanisms responsible for separation.

Barron *et al.* [111] also proposed the first qualitative explanation of the mechanism involved in ultradilute CE, the so-called transient entanglement mechanism. In this picture the DNA undergoes collisions with the neutral polymers; the average number of polymers that the DNA is dragging along at any given time is dependent on the molecular weight of the DNA and hence separation is achievable. The theory of Hubert *et al.* [118] indicated that this mechanism can quantitatively account for the observed electrophoretic motion, although their model was limited to dilute solutions of small polymers. Recent experimental results from Ekani Nkodo *et al.* [116, 117] on the electrophoresis of λ-DNA in dilute solutions of dextran call into question this general "collision" mechanism for the dilute regime. It appears that the separation mechanism may be related to the collective dynamics of the neutral polymer solution in the immediate vicinity of the randomly coiled DNA. The DNA is perturbed from its free draining behaviour due to the dextran molecules it is dragging along; hence, the DNA interacts hydrodynamically with surrounding dextran, causing a collective motion of many additional dextran molecules in its vicinity. This perhaps suggests a new separation mechanism in the dilute solution regime. Ekani Nkodo *et al.* [116] present an elegant study of the induced mobility of the polymer solution. It remains to be seen whether there is an inherent difference in the essential separation mechanism in dilute and ultradilute solutions.

With the increase in popularity and the development of new technologies, video microscopy is being used to visualize the dynamics of individual DNA under a variety of conditions. Todorov *et al.* [112] recently developed a technique to visualize, in 3-D, the migration of fluorescently stained dsDNA in a semidilute solution of hydroxyethylcellulose (HEC). This has greatly improved the experimental knowledge of the conformational dynamics of DNA, and such techniques should ultimately help in gaining a better understanding of dilute solution CE especially in terms of the mechanism responsible for separation.

Several computational [119–123] and theoretical [118, 124] investigations are also beginning to shed some light on the mechanisms involved in electrophoretic separa-

tions in dilute polymer solutions. Noguchi *et al.* [122] have carried out BD simulations of a polyelectrolyte chain in the presence of an external field. An anisotropic friction tensor is used to model the effects of the gel or dilute solution of polymers (this a novel idea that actually allows the study of electrophoresis in gels as well as in dilute polymer solutions), although no explicit hydrodynamics are included. These simulations appear to reproduce (at least at the qualitative level) the behaviour seen experimentally using video microscopy in terms of the repeated cycles of entanglement and escape of polymers. These cycles consist of the DNA forming either U-shaped or J-shaped conformations in the field direction. The subsequent release of the DNA results in its contraction to a random coil conformation [122]. Noguchi *et al.* also model the antiresonance behaviour of DNA seen in pulsed-field gel electrophoresis. Other groups have also carried computer simulations which examine the dynamics of colliding chains, most notably Starkweather *et al.* [115, 119, 120] have used extensive Monte Carlo simulations of the collision of charged polymers with both fixed and flexible polymer chains. André *et al.* [88] have very succinctly illustrated the importance of including hydrodynamics when examining the entanglement dynamics of polymers, a crucial element which most current computer simulations are lacking.

With the culmination of experimental, theoretical and computational studies of dilute and ultradilute CE of DNA, a better understanding along with predictive capabilities for optimal separation conditions, will be obtained. Dilute solution CE has several potential benefits including a low viscosity sieving medium with possible integration in automated systems and microfluidic devices, more reusability of capillaries and higher reproducibility (since less capillary degradation occurs compared with gel CE) and potentially much shorter separation times. As with most new and emerging separation methods, much work is required before an accurate and complete model for dilute CE is obtained; however, current progress is indicative that this technique will indeed become a useful experimental separation technique.

10 A universal mobility relation for gel electrophoresis?

Sieving is still the main mechanism used to separate large DNA molecules. This requires the use of a dense matrix, generally an entangled polymer solution or a cross-linked gel, although artificial arrays of posts can also be used. The different modes of electromigration of DNA molecules in such sieving media have been studied extensively over the last two decades, and we have now achieved a rather good understanding [125].

It is generally accepted that there are three main regimes of migration for a DNA molecule in a gel: (i) the Ogston limit for analytes whose physical size (*e.g.*, radius of gyration R_g) is smaller than the mean pore size of the "gel", see Section 14; (ii) the biased reptation regime, for molecules of intermediate size that occupy many pores but remain small enough for their conformation to retain an isotropic random-walk shape during their migration; and finally (iii) the regime of biased reptation with molecular orientation for the longest (comigrating) molecules. Let us digress to discuss the naming of the last two regimes. It is unfortunate that many authors still refer to (ii) as the reptation regime and to (iii) as the biased reptation regime. Indeed, this is certainly inaccurate since unbiased reptation, like what we observed in a polymer melt [126], cannot lead to any net velocity. Reptation must be biased to observe an electrophoretic velocity. Even a very weak electric field biases the reptative motion of the chains. For high fields and large DNA molecules, it is the conformation that becomes biased (or, more precisely, oriented) in the field direction, not the reptation. Therefore, we strongly recommend the nomenclature that we suggested above (or something equivalent).

It is now well understood that the diffusion coefficient D of reptating DNA molecules also increases with the field intensity E during gel electrophoresis [125, 127]. This theoretical prediction has been elegantly verified by Tinland *et al.* [128]. This is in fact one of the main factors limiting the read length of DNA sequencing apparatuses.

Unfortunately, our understanding of mobility and diffusion is through a series of so-called power-laws. For example, the reptation theory predicts the following:

$$\mu(M) \sim +\frac{1}{M} + \alpha E \qquad M < M^* = \frac{1}{\alpha E}$$
$$\mu(M) \sim -\frac{1}{2M} + \beta E \qquad M > M^* = \frac{1}{\alpha E} \tag{11}$$

where E is the field intensity, M is the molecular size (*e.g.*, in bases), and the parameters α and β are functions of the gel concentration C. These two limiting cases have been clearly observed both in agarose and polyacrylamide gels, and Rousseau *et al.* [129] reported that $\beta = 2\,\alpha$. Similar relations exist for the diffusion coefficient D [125–126].

The theoretical predictions are not as useful as one might think, however, because they essentially offer piecewise advice to the experimentalist. Each regime is rather narrow, and the transition between them is not really part of the models. Ideally, one would like to have a single function that would describe the mobility across all regimes, *i.e.*, for all molecular sizes from a few bases to very large

Electrophoresis 2002, *23*, 3791–3816

sizes. Theoreticians are not likely to come up with such a function simply because the usefulness of a model is always limited by its assumptions.

In fact, such a function was recently suggested by a group of experimentalists [130, 131].

$$\mu(M) = \frac{\mu_s}{1 + a(1 - e^{-M/m})} \quad (12)$$

Here, it is clear that μ_s is the $\mu \to 0$ limit of the mobility (the subscript *s* thus stands for "small") and *a* is a fitting parameter. The critical size *m* plays the role of the transition size $M^* = 1/\alpha E$ in the previous equation. Figure 7 shows an example taken from [131]. Clearly, this function can fit their own agarose gel electrophoresis data from about 200 bp to at least 10 kbp, a remarkable achievement given that this range of molecular sizes spans all three regimes mentioned above. In a more recent paper, the authors extended their experimental test of the fitting function and showed that in some extreme cases, especially when entropic effects [71] become important, the fitting is not as good [131]. But these effects, as well as band inversion, are quite unusual and practical separation conditions do not normally lead to such anomalous effects. Therefore, in practice, this is a superb equation to use.

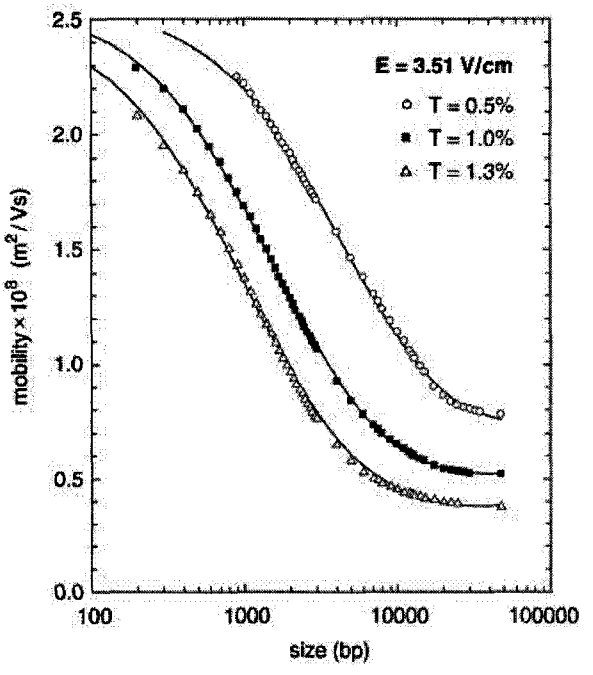

Figure 7. An example of mobility-size data fitting using the new mobility relation (12). Double-stranded DNA fragments in the 200 bp to 48 kbp range were used. Here, *T* is the agarose gel concentration, *E* is the electric field intensity. Reprinted from [131], with permission.

Of course, it is an empirical function, not based on any new theory. Nevertheless, Slater [132] recently showed that this function is related to the equations predicted by theory for the three regimes mentioned above. Amazingly, Eq. (12) does reduce to the theoretical predictions in the three relevant limits (small, intermediate and large molecular sizes). This, of course, explains to some extent why the function is so good at fitting data over a wide range of sizes.

This function should definitely be tested with polyacrylamide gels and with entangled polymer solutions. Perhaps slight modifications will be needed in that latter case since some new physics, probably related to the dynamics of the sieving matrix itself, then enter into the problem [125].

More importantly, however, what is now needed by experimentalists is the equivalent empirical function for the diffusion coefficient $D(M)$. With such a tool, one could actually fully describe a separation system and, from a good data set and Eq. (12), optimize it. All that one then needs is the dependence of the fitting parameters upon the experimental conditions, especially the gel concentration *C* and the field intensity *E*. At this time, the experimentalist is forced to study each regime separately, and to use local fits to understand the separation process in a selected size range. Although equations like the one suggested by van Winkle *et al.* do not provide fundamental information about the mechanisms involved in the separation, they would be invaluable for the optimization of practical devices. Therefore, there is still room for empirical progress in the mature field of gel electrophoresis after all: [130] and [131] provide a new, fresh approach to characterizing and optimizing all gel electrophoresis systems, including those based on capillaries and microchannels.

11 Nonlinear focusing of DNA

DNA migration in gels is an inherently nonlinear process. For instance, the mobility μ is a function of the electric field intensity *E*, as in Eq. (11), which means that the velocity $v = \mu E$ is not increasing linearly with *E*. Nonlinear dynamics can lead to a number on interesting effects that have no equivalent in the "boring" world of linear phenomena. For instance, we discussed the ratchet effects in Section 4.

In 1997, our group suggested a totally different concept based entirely on this gel electrophoresis nonlinearity [133]. It is important to note that if we can write the velocity of a DNA molecule in a gel as $v = \mu(E)E$, where $\mu(E)$ is an monotonically increasing function of *E*, then the mean

velocity of the molecule in an oscillating field may be opposite to the direction of the mean field intensity (in fact, the velocity can be nonzero even if the mean field is zero). Let us take, for example, the case of biased reptation as described by the velocity relation:

$$v = \mu_0 E\left(\frac{M_a}{M} + \frac{|E|}{E_0}\right) \tag{13}$$

where μ_0 is the mobility of DNA in free solution, M is the molecular size the DNA (in bp), E is the field intensity, and M_a and E_0 are constants that depend solely on the gel concentration. Furthermore, we consider a time-varying field like the one shown in Fig. 8a: the field alternates between a low intensity E_L for a long period of time T_L and a high intensity $-E_H$ (reverse direction) for a short period of time T_H such that $E_H T_H < E_L T_L$ (we have a small positive bias). Note that other choices are also possible. The net (or mean) velocity of the DNA molecule in the gel is then given by:

$$\langle v\rangle = \mu_0 \frac{M_a}{M}\langle E\rangle + \mu_0 \frac{1}{E_0}\langle E|E|\rangle \tag{14}$$

We now have the interesting situation that the net velocity is positive if both fields E_L and E_H are low (because the $\langle E\rangle$ term then dominates) while the net velocity is negative at high fields (the $\langle E|E|\rangle$ nonlinear term then dominates). Clearly, the net velocity is zero for a molecule of critical size:

$$M^* = -M_a \frac{E_0\langle E\rangle}{\langle E|E|\rangle} \tag{15}$$

For a given field condition, molecules of size $M < M^*$ would have a positive velocity, molecules of size $M > M^*$ would have a negative velocity, while $M = M^*$ molecules would not move (see Fig. 8b).

Our suggestion was actually to run this nonlinear system in the presence of an electric field that varies in space. Each DNA molecule of size M would then move towards the position x on the gel where the local field intensity is such that the local critical size $M^*(x) = M$. This position would thus be a stable attracting point for this molecule, a trap. This is effectively the equivalent of an isoelectric focusing system for DNA, except that subtle nonlinear mobility effects are replacing the pH effects exploited in the standard isoelectric focusing systems used for proteins. Of course, with a field gradient, each molecular size of the sample would move towards different zero-velocity critical points in the gel, and separation could be achieved. Similar results could in principle be obtained with gel concentration gradients.

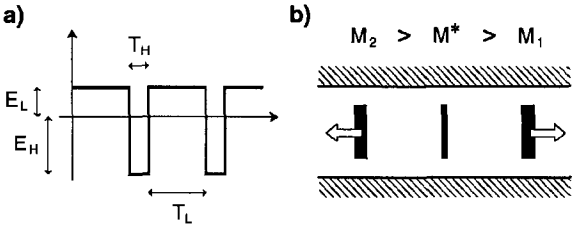

Figure 8. (a) The time variations of the applied electric field; (b) the result of this special kind of nonlinear dynamics: small molecules have a net positive velocity (towards the right) while large molecules move in the opposite direction. A critical molecular size M^* exists that has no net velocity. Furthermore, the band formed by the $M = M^*$ molecule is self-focusing.

This proposal stayed untested for several years, until the group of Frumin *et al.* [134] published experimental results in 2001. As predicted, the DNA molecules (in the 10–30 kbp range) migrated towards their zero-velocity points in their agarose gels, after which the bands simply kept sharpening. The final position of the bands were indeed molecular size dependent and did not depend on the loading position of the molecules in the gel. The gels had a wedge shape so that a strong field gradient was present. This is a superb example of nonlinear physics in action.

The idea of using nonlinear physics to build self-focusing separation systems is very attractive indeed. However, it does require a nonlinear system, and not all separation system are nonlinear. For example, free flow electrophoresis is typically perfectly linear (*i.e.*, the velocity increases linearly with field intensity). The next section presents a brand new idea that could be used to circumvent this problem in free-flow microfluidic systems. Otherwise, one must rely on nonlinear effects provided by sieving media.

12 Nonlinear dynamics for point-like objects

The question to be examined here can be summarized very simply using the title of a recent article by Baskin and Zilberstein: "*Nonlinear electrophoresis of point-like particles: Is it possible?*" [135]. As we mentioned in the previous section, gel electrophoresis of long (reptating) DNA molecules is a very nonlinear process. This can be exploited in order to build various new systems such as ratchets or self-focusing systems. However, the electrophoresis of point-like particles (which could be small analytes, but also DNA molecules in the context of free-solution electrophoresis) is normally a linear process. This raises a very important question: will it ever be possible to build new devices based on nonlinear dynamics for these particles? This is more than a theoretical issue.

Indeed, it would be a lot easier if we could build efficient separation systems that do not need viscous gels, especially in the world of microfluidics.

Baskin and Zilberstein examine a completely new idea. These authors propose that a linear system with traps that can capture some of the particles from the original sample may do the trick. The mean velocity of the whole population of particles is always increasing linearly with the field intensity, but because of the traps, this mean velocity is useless. Experimentally, it is not the mean velocity that counts but the velocity of the maximum of the "packet" (their nomenclature) formed by the molecules, *i.e.*, the maximum density of the "electrophoretic band" (a more common notation). As the band moves through the system, under the influence of the electric field, it continuously looses molecules to the traps. This is the price to pay to get the reward: under certain conditions, the velocity of the band is a nonlinear function of the field intensity! For a comb-like microfluidic structure (where the side channels act as traps for the particles moving along the backbone of the structure), for example, they show that the velocity of the packet may increase as the square of the electric field [135]. In principle, this finding applies to free-flow electrophoresis of any type of charged particle as long as their molecular size is smaller than the features of the microfluidic channels. [135] actually shows the first experimental evidence that this very subtle nonlinearity can indeed be exploited to separate molecules which cannot normally be separated by free-flow electrophoresis. This is perhaps one of the most innovative ideas of the last few years. Time will tell whether this new idea, inspired by deep theoretical concepts, can actually be used to build a practical and competitive device. This would be particularly useful in the field of proteomics where sieving mechanisms are often rather limited.

13 Improving CE resolution with gradients

In this section, we discuss recent efforts to improve resolution in electrophoretic systems through the use of spatial gradients in the separating medium. As the field of electrophoresis becomes more and more advanced, most contributions to band broadening, beyond the inexorable thermal diffusion, have been eliminated. Hence, possible means of combating diffusion are of paramount importance. This research has been approached both theoretically and experimentally. In the former case, various viscosity/velocity gradients have been utilized as a simple means of investigating the effect on resolution [136], while in the latter case, gradients of polymer concentration were created in capillaries (or gel slabs) and the resulting separations analyzed [137]. The idea behind this area of investigation is that a spatial gradient, wherein the velocity of a migrating molecule is reduced along the gradient such that the advancing edge of the band is slowed relative to the trailing edge, will produce a band sharpening effect. Although it may seem straightforward that a decrease in band width would improve resolution, the sharpening is due to a decrease in velocity. This decrease is necessarily accompanied by a longer separation time, which in turn allows for more diffusion. Furthermore, the same reduced velocity decreases peak spacing. The net result of such gradients is thus nontrivial and actually depends on the method of measurement as well. For instance, gradients are obviously useful in a snapshot mode where the total duration of the separation is fixed (e.g., in a slab gel format) because molecules of different sizes visit different parts of the gel [136, 138, 139]. Indeed, various gradients such as pH, in the case of isoelectric focusing of proteins, have been shown to improve the resolution obtained with snapshot systems. However, the situation is not as simple with finishline systems since all the molecules then migrate over the same elution length and hence migrate through the very same gradient (see Fig. 9).

A theoretical study of electrophoresis in the presence of viscosity gradients [136] recently examined the performance of systems comprising both step-like and continuous variations in viscosity. These calculations were based on the linearity of the relationships between the separating medium viscosity (η) and the analyte velocity (v), as well as between the viscosity and the diffusion coefficient (D). The system studied was free-flow CE with finishline detection. A step gradient, despite the positive effect on band width due to the above mentioned difference in velocity between leading and trailing edges, was shown to decrease the resolution of the system. The only exception is for the experimentally poor condition wherein the injection width contributes in a major way to the final peak width, as opposed to the ideal situation wherein the leading contributor is diffusion. However, even in this exception, a maximal improvement to the resolution of the system is obtained for a viscosity "step" located at the start of the separation length; hence, this is the commonly exploited phenomenon of injection stacking wherein the analyte is introduced in such a way as to increase its concentration during the injection process. These calculations also revealed another important result: even when the initial loading is poor, placing the step too close to the detector will actually reduce the resolution despite the additional stacking it will induce!

The result that step-like viscosity jumps do not improve resolution unless there is poor initial loading was supported by more thorough calculations based on a micro-

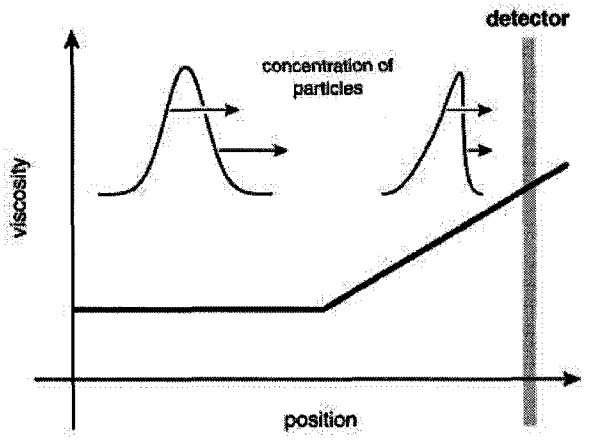

Figure 9. The speed at which DNA molecules drift and diffuse during electrophoresis decreases as the viscosity of the medium increases. Because of this, a symmetrical electrophoretic band that enters a region of monotonically increasing viscosity tends to become narrower and skewed in such a way that the longer tail of the concentration profile points toward lower viscosities, as shown in the figure. In snapshot mode, a viscosity gradient can thus significantly skew electrophoresis bands. Things are, however, somewhat different in finishline mode. Indeed, as DNA molecules drift toward the detector, those that are farther away from it are in a lower viscosity region than those closer to it and therefore move faster. This tends to reduce the skewness of the passage times in front of the detector. In the end, the skewness introduced by a viscosity gradient is thus much smaller in finishline mode than in snapshot mode. This is a simple but quite illustrative example of the fundamental differences between these two modes of electrophoresis.

scopic approach using analytical tools developed in the field of stochastic processes [136]. In this approach the position of each molecule is first modeled as a diffusion process, and the moments of first passage time in front of the finishline detector are then calculated, yielding the resolution, again for a capillary electrophoretic system. This approach allowed for the calculation of the resolution power for systems with either a step gradient or an exponential increase in viscosity. The former supported the macroscopically based calculations, while the latter again showed that the resolution can only be improved by a viscosity gradient (in this case, exponential) when the injection width is nonnegligible, otherwise a uniform viscosity is preferable. Numerical comparisons between step and exponential gradients showed that the "step" gradient located at the beginning of the tube gives the highest resolution. These results demonstrate that for a capillary electrophoretic system with finishline detection, a viscosity gradient is not useful to increase the resolution unless there is poor initial loading, and in this case it is best to have a uniformly higher viscosity so as to increase the injection stacking, *i.e.*, a "step" gradient located at the beginning of the capillary.

With the above theoretical investigation, the situation taken was one governed by equilibrium thermodynamics. In this case, a static gradient is not expected to overcome the fundamental limitations of the system because without adding energy to the system, diffusion cannot be overcome (an interesting example of a nonequilibrium system with energy pumping is given in [140]). However, this may not be the case for nonequilibrium systems. If a molecule's conformational degrees of freedom were able to absorb energy through interacting with a particular spatial gradient, then it may indeed be possible to increase the resolution. A temporal gradient analogue to this would be pulsed-field electrophoresis, which has been proven to be useful in increasing resolution [5, 125, 141]. If a gradient were possible on the length-scale of the molecule (this would require a microlithographic system with molecular-sized features) then again remarkable separations may be possible due to the changes of the experimental parameters being in resonance with some natural time/length scale of the separation. Another possible successful use of spatial gradients could be in nonlinear systems where the diffusion coefficient and velocity are nonlinear functions of the local conditions; as far as we know, there is no theoretical study of such cases.

Another group [142] has approached calculations of the effect of gradients by different means. They applied the propagator (retarded Green function) formalism to velocity gradients along capillaries to obtain the time evolution of bands as they enter regions where they migrate with different velocities. They have shown that diffusion plays a small but nonnegligible role in the concentration profile of band compressions. Their method may also lend itself to calculations of the time evolution of bands that collide with obstacles such as large counter-propagating charged particles.

Experimentalists have recently designed a pump method that produces stable and reproducible polymer concentration gradients in capillaries. In a recent article, Liang *et al.* [137] investigated the effect of step concentration gradients of polyacrylamide-*co*-poly(*N*-dimethylacrylamide) (PAM-*co*-PDMA) on the separation of DNA varying from about 100 bases to over 1000 bases. They compared the performance of three capillaries, one with a uniform concentration of 2% w/v PAM-*co*-PDMA, one having a step from 2% to 4%, and one with a uniform concentration of 4%. As expected, the concentration gradient reduced peak broadening. They report that the larger the DNA, the larger the sharpening effect. Their results showed that the number of steps in the gradient

Electrophoresis 2002, *23*, 3791–3816

was not important, however, the average concentration, and/or location of the step were. They made note of the fact that while higher polymer concentrations give higher resolutions in general, lower concentrations are necessary for good resolution of longer DNA. Hence, as expected, the 4% single concentration column gave the best resolution, followed by the intermediate of 2–4% step, and the 2% gave the poorest resolution, with the only exception being for the DNA larger than 380 bases for which the intermediate exhibited better resolution (see Fig. 10). Unfortunately, only 2% and 4% single concentration capillaries were compared to the 2–4% step capillary. It could be useful to repeat this experiment with uniform concentrations between 2% and 4% in order to determine if the increase in resolution observed for large DNA strands in the presence of the gradient step is due to the optimum concentration for this length range being closest to the average of the 2% to 4% step, rather than being due to the presence of the step itself.

Additionally, their experimental study took a look at the effect of the location of the step. These results are in line with the results of our theoretical investigation, namely that the location of the step is important, with the optimum position (for poor loading conditions) being near the start of the capillary, and a decrease in resolution is possible when the step is too close to the end of the capillary. For three columns, each with a step from 2% to 4%, the capillary having the step closest to the end showed the lowest resolution, the one with the step at the midpoint showed intermediate resolution, while the third, having a step closer to the beginning of the capillary, exhibited the best resolution. However, for larger DNA (greater than 700 bases), the capillary with the step in the middle exhibited better resolution. This could be expected from the aforementioned superiority of lower concentrations for resolution of larger DNA; the step closer to the middle rather than the end is accompanied by a higher overall concentration.

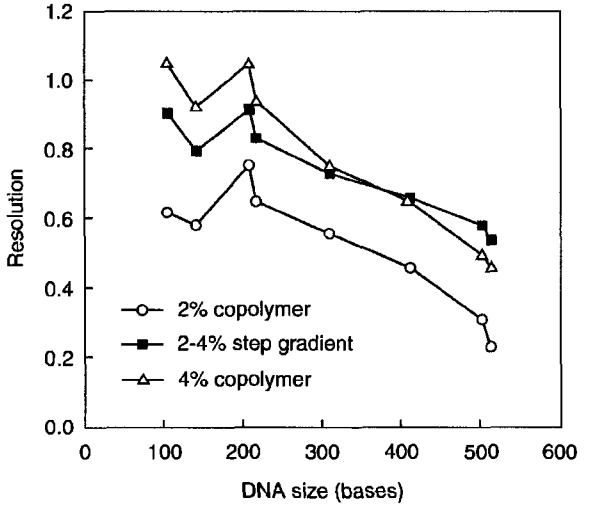

Figure 10. Resolution of DNA separations resulting from a copolymer concentration gradient, and single concentrations, as a function of DNA size. Electrophoresis conditions: 1 × TT + 5 M urea running buffer; 40 cm effective capillary length, 100 μm ID; running electric field strength, 150 V/cm; electrokinetic injection at 300 V/cm for 10 s. Reprinted from [137]).

A possible use of concentration gradients may be in accommodating two (or more) different optimal concentrations for different regimes (governed by the size of the analyte), for very polydisperse samples. However, it is not clear whether there exists an intermediate single concentration that would provide the best overall results, avoiding the possible decrease in resolution caused by a step in a diffusion-controlled system. This new field of investigation is thus open to further fundamental theoretical and experimental investigations.

14 Ogston sieving

This section deals with possibly the simplest electrophoresis problem possible: the electrophoretic migration of a small (hard) analyte in a porous media. Surprisingly enough, this very basic problem still draws some intense discussions in the electrophoresis community [143, 144]. Traditionally the Ogston-Morris-Rodbard-Chrambach (OMRC) [145–147] model of gel electrophoresis is the central paradigm in this regime. The basic assumption of this model is that the scaled mobility μ^*, *i.e.*, the ratio between the mobility μ in the separation media and the free-solution mobility μ_0, is equal to the fraction f of the volume available to the particle (without violating the condition of volume exclusion with the media):

$$\mu^* = \frac{\mu}{\mu_0} = f(C,M) \tag{16}$$

where C is the gel concentration and M is the molecular size of the particle. To estimate the available volume, it is common to use an early result of Ogston [145], sometimes with correction terms. Using geometrical and statistical arguments, Ogston showed that the fractional volume available to a spherical particle in a random array of infinitely long (but not cross-linked) fibers is given by

$$f(C,M) = \exp(-KC) \tag{17}$$

where $K = K(M)$ is the retardation factor of the analyte of size M. Even though Eq. (16) has never been properly tested experimentally, in large part because μ and f cannot be measured independently for a given system, it is

widely used and leads (combining Eqs. 16 and 17) directly to the Ferguson plot ($\ln(\mu)$ *vs.* C) as the standard data analysis method in gel electrophoresis of small analytes (including small DNA molecules).

Another motivation for developing an expression or a calculation technique for the scaled mobility μ^* is the fact that, in the limit where the external field goes to zero, it is directly related to the scaled diffusion coefficient D^* using the modified Nernst-Einstein relation [148]:

$$\frac{D}{D_0} = \lim_{E \to 0} \frac{\mu(E)}{\mu_0} \tag{18}$$

This means that all the results obtained for thermal diffusion in the zero field limit can be reinterpreted as low mobility data and *vice versa*. Of course, models of diffusion in gels and porous systems have extremely important applications beyond the realm of electrophoresis.

It is in a large part to test the validity of Eq. (16) that our group has, over the last several years, developed a new lattice model of gel electrophoresis [47, 72, 149–154]. Although very simple, the model has the advantage that both the scaled mobility μ^* and the available volume f can be calculated exactly and independently; therefore, it provides a straightforward way to test Eq. (16) for a large variety of sieving systems. For each case we investigated, we described our mobility results in term of a polynomial expression:

$$\frac{\mu}{\mu_0} = 1 + a_1\phi + a_2\phi^2 + a_3\phi^3 + \ldots \qquad (\phi = 1 - f) \tag{19}$$

where ϕ is the obstructed volume due to the gel itself. Therefore, if the OMRC hypothesis, *i.e.* Eq. (16), is correct, the coefficient a_1 should be unity and all $a_{i>1}$ should be zero for all gel structures. The model was used to study the mobility of small analytes in a large variety of gel structures varying from simple periodic 2-D obstacles to realistic 3-D gels [148, 154–156]. Our results indicate that $a_1 \neq 1$ and $a_{i>1} \neq 0$, in contradiction with the fundamental OMRC hypothesis. For example, Mercier and Slater [154] showed that the first coefficient (a_1) is affected by the shape of the obstacles but is independent of their spatial distribution. However, the other coefficients were found to be functions of the geometry of the gel; for example, the sign of a_2 was related to the degree of disorder in the gel structure ($a_2 > 0$ for periodic gels while $a_2 < 0$ for random ones). Furthermore, the results were in very good agreement with other independent studies [157–160].

For example, Trinh, Arce and Locke [157] have recently used Monte Carlo simulations to investigate the effect of the physical properties of the gel itself on the effective diffusivities of point-like particles, which is related to the mobility by Eq. (18). More precisely, they focused on geometrical structural parameters like the porosity, the percolation threshold and the dimensionality of the systems studied. They compared the diffusivities calculated for different obstacle shapes (spherical or cubic) in several configurations (body centered, face centered, *etc.*) to determine if the porosity is sufficient to correctly predict the effective diffusion coefficient of an analyte in a given medium. Their results showed that the effective diffusivity of two isotropic gels with the same porosity but different percolation thresholds can be significantly different and that the magnitude of this gap increases as the percolation threshold is approached. Finally, they also demonstrated that the dimensionality (2-D or 3-D) of the media studied has a clear effect on the diffusion coefficient, but this last parameter has less influence than the percolation threshold.

Recently, Amsden [161–163] derived an obstruction-scaling model for diffusion in homogeneous hydrogels composed of flexible polymers. This model is restricted to low polymer volume fractions and situations where the interactions between the polymer and the analyte can be neglected. It is based on the premise that the physical obstruction of polymer chains is the major factor affecting the analyte diffusion. Instead of looking at the fractional volume of the gel available, he proposes to study the distribution of the openings between the polymer chains that are larger than the hydrodynamic radius of the analyte. This distribution is described by the expression derived by Ogston [145] for the distribution of spherical spaces in a random distribution of straight fibers. The results obtained with this model, which is based on a more complex dependency of $D(f)$ than the OMRC hypothesis, seem to be in good agreement with experimental data. It thus confirms the fact that the free volume fraction (f) of a gel is not sufficient to determine the diffusion of an analyte in this gel. It is important to emphasize that these findings (*i.e.*, the fact that the geometric parameter $f(C)$ is not sufficient to describe the precise sieving properties of a gel, even for low gel concentrations) are actually very positive since they suggest that it is indeed possible to design gels with specific sieving characteristics.

The calculation technique that Slater *et al.* used to reject the OMRC hypothesis (and most of the models used to study low field mobility) was developed for uniform and 1-D field lines (even in the presence of non-conducting gel fibers) and is restricted to low field intensities. It was suggested by Locke and Trinh [143] that this assumption of uniform field lines, even near the fibers, is the reason why our results disagree with the Ogston hypothesis. This suggestion was tested by Slater *et al.* in a recent paper [47] in which they extended their model to take into account the curvature of the field lines around non-conducting gel fibers. Their results showed that the

Electrophoresis 2002, *23*, 3791–3816

dependence of the mobility of a point-like particle upon the concentration of the gel is not affected by the field line distortions in the low field intensity limit. Therefore, Locke and Trinh's claim was incorrect and the OMRC hypothesis is invalid for both straight and curved field lines. These authors' predictions were based on numerical results obtained using a volume averaging approach for nonconducting obstacles. However, in a recent paper [164], Locke extended the results of his formal theory and arrived at a similar conclusion than Slater about the OMRC hypothesis. In fact, the similarity between the results obtained with these two different methods suggests that these approaches are probably related in some fundamental way. Brenner and Edward [165–168] also have a macrotransport theory that should be included in a comparison with the two previously mentioned approaches. Future work should be done to extract the fundamental concepts shared by these three theoretical approaches.

During the past year, our group has also extended this calculation technique to finite (*i.e.*, non-negligible) values of the external electric field. Such a generalized model can be used to study how the relation between the mobility and the gel concentration, given by Eq. (19), is modified when the field intensity is increased. Preliminary results obtained for 2-D periodic and random distributions of obstacles showed that the nature of the series in Eq. (19) changes with the electric field and that this transformation depends on the geometry of the gel. For example, in random gels, the obstacles can form dead-end regions where the particles can be trapped due to the directional electric forces. These traps induce an exponential decay of the mobility with field intensity that cannot be correctly expressed by Eq. (19) only.

It is clear that the generation of better and less restrictive models for the Ogston sieving regime could be of great interest to study the mobility and the diffusion of macromolecules. For example, hydrodynamic interactions between the solvent and the surrounding particles or obstacles should be added to existing models. These theoretical tools could be useful for the development of new technologies in many fields, like electrophoretic separation. This is particularly true for the separation of proteins and small DNA fragments typical of SNP analysis.

15 Modeling gel electrophoresis with reptons

Past history has clearly demonstrated that theoretical models for the dynamics of macromolecules can be quite useful to optimize gel electrophoresis systems and even propose new separation concepts [125]. The current theories for the gel electrophoresis of long DNA molecules come from the basic concept of polymer reptation proposed by de Gennes in 1971 [169]: in the presence of a dense gel, free polymers can only move like snakes due to the fact that lateral displacements are restricted by the gel itself. Of course, in the case of gel electrophoresis, this reptation motion is biased by the external electric field. An excellent and detailed review of the biased reptation theories of gel electrophoresis has been written by Viovy [125]. These theories generally treat the DNA molecule as an entity and make simplifying assumptions regarding the details of the internal motion of the DNA in the gel.

The three most commonly used microscopic computational representations of reptation have been the bond fluctuation model [170], the cage model [171] and the repton model [172]. These theoretical tools are all based on squared lattice representations of the polymer motion. Heukelum and Barkema [173] recently presented a brief overview of these models in which they compared the different characteristics of these approaches. In this section, we will focus on recent developments and polemics that have emerged during recent years.

One of the most studied properties of polymers in a gel is the diffusion coefficient as a function of the polymer length $D(L)$. A scaling relation was derived by Doi [174]:

$$D(L) = \frac{A}{L^2}\left(1 + \frac{B}{L^\gamma}\right) \tag{20}$$

where A and B are system-dependent constants. The leading term in $1/L^2$ has been verified experimentally by numerous groups [175–178]. The exponent γ of the asymptotically negligible correction term was predicted to be 1/2 in a study relating the diffusion coefficient to the tube renewal time [179]. However, two Monte Carlo simulation studies 1-D reptation motion in a 3-D space [180, 181] using different models of polymer reptation suggested an exponent $\gamma = 2/3$ when fitting the data for the correction term. Therefore, until a recent paper of Carlon, Drzewinski and van Leeuwen [182], the question of the value of the exponent γ was still unresolved. Carlon *et al.* performed accurate calculations using the repton model and density matrix renormalization group (DMRG) techniques in 1-D, 2-D and 3-D. Their numerically exact results showed unequivocally that the exponent $\gamma = 1/2$ for all dimensions and that the erroneous prediction of 2/3 was due to the facts that these studies were constrained to 1-D systems and too small a range of values for the polymer size L.

Recent fundamental developments in reptation theories are also confronted to the challenge of the integration of an external field for the study of gel electrophoresis. The majority of the models for polymer electrophoresis are

restricted to vanishing values of the external field. However, when we try to extend these models to higher fields, new phenomena have to be considered. For example, Heukelum and Beljaars [183] used an extension of the cage model to study high field mobility of polymers in a gel as a function of the polymer length L. They observe three regime of the electric field: the linear regime where $\mu \propto E/L$, the quadratic regime where $\mu \propto E|E|$ and a new regime for stronger fields where the mobility decreases exponentially with E. The two first regimes are well-known experimentally and are indeed predicted by the biased reptation model with fluctuations [125], but the third one was not reported and it is probably an artifact of this model [173]. Critics of this results argued that, at relatively high field, the polymer chain hooked around a post is fully extended, which make the tensile forces dominate the dynamics (see Fig. 11). Unfortunately, Monte Carlo methods do not normally include such forces; in fact, chain pinning is then a direct result of the algorithm and has nothing to do with the real physics of the process. Azuma and Takayama [184] developed a new bond fluctuation model (BFM) in which they incorporated a sliding motion of the polymers hooked around the gel fibers. Without this modification, the simulations performed using the traditional BFM show an anomalous trapping of the polymers at high fields. With the modification, their results do not show a third regime, a clear indication that it is tricky (but may be not impossible) to model highly biased motion on lattices using Monte Carlo methods.

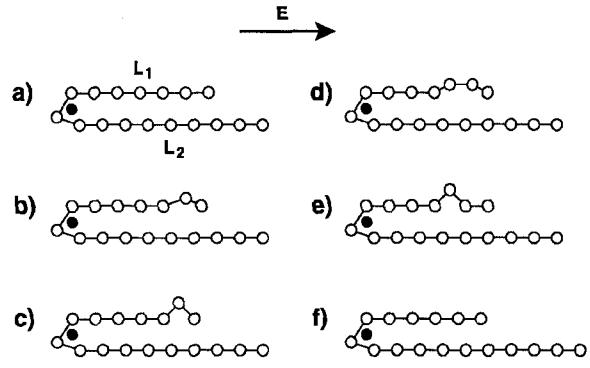

Figure 11. In the presence of high electric field E, the polymer chain hooked around a post is fully extended (a) and only the first and last monomers can move. In local-move algorithms, there is no sliding motion and the only way for the chain to go around the obstacle is to form a bulge (b, c) that moves against the field (d, e) to finally obtain a situation were one monomer has moved from the smaller arm of length L_1 to the longer arm of length L_2 (f). The probability of such a transition is proportional to $\exp(-QL_1E/k_BT)$, where Q is the charge of one monomer, k_B is the Boltzmann's constant and T is the temperature. The sliding produced by such algorithm is thus very slow, but this is purely an artifact of the algorithm.

Another controversial point in reptation theories for polymer electrophoresis is the range of values (E) of the external field for which the models may actually apply. The problem is that most of the models use a time scale similar to one used in the repton model, which is proportional to $\cosh^{-1}(E)$ [185]. Although this choice does recover the decrease of the jumping time brought about by the electric forces, it not clear that it is the correct choice. Slater *et al.* [186] showed that this time scale should be proportional to $\tanh(E)/E$ instead. Since these two expressions differ to order $O(E^2)$, high field repton models should probably be considered valid to $O(E)$ only.

Over the last decade, our group [47, 72, 149–154] has developed a numerically exact calculation technique for the mobility μ and the diffusion coefficient D (which are essentially the same in the zero field limit, see Section 14) of small analytes evolving on a lattice in the presence of immobile obstacles. In a recent paper [72], we presented an extension of our model that used the BFM to treat the case of macromolecules. This allowed us to study the mobility (or diffusion coefficient) of short polymers in periodic patterns of obstacles. We observed various effects such as the transition from Ogston sieving to reptation when the concentration of obstacles increased, the effect of entropic trapping and the relation between anisotropic gels and polymers molecular orientation. More importantly, our results showed, by comparing retardation factors, that flexible linear polymers cannot be treated as effective spherical objects when we study their sieving. This preliminary result is of some concern since the Ogston model is still widely used to analyze DNA gel electrophoresis data in the limit where the molecules are too small to reptate. Clearly, there is a lot of room for further theoretical (and experimental) studies here. A reliable high-field model of DNA gel electrophoresis is missing.

In summary, simulation theories of polyelectrolytes for gel electrophoresis are reliable for vanishing external fields but their extensions to stronger fields are still in development. As we increase the field strength or the length of the polymer chain, new physical properties have to be integrated in the models. Some of these, like the sliding motion of the polymers when the chains are stretched by the field, seem to have been successfully added to the simulations [184], but more work has to be done to compare such models to experimental data. In many cases, we still cannot study the very large chain sizes that would allow a useful comparison to data.

16 Discussion: an annotated list of useful articles

We finish this long, and yet incomplete review of the recent work on the theory of DNA electrophoresis by a short list (in no particular order) of relevant articles that we highly recommend.

1) *Electrophoresis of DNA and other polyelectrolytes: physical mechanisms* [125]. Jean Louis Viovy is the author of the best review article on the theory of DNA electrophoresis to date. A must read that nobody can afford to miss.

2) *Capillary electrophoresis for the analysis of biopolymers* [101]. This article, by Hu and Dovichi, is part of the regular review articles published by *Analytical Chemistry*. It is an excellent and very complete overview of the recent progress in the field, mostly from experimentalists' perspective.

3) *Structure and mechanics of single biomolecules: experiment and simulation* [187]. Although this is not really a reference about electrophoresis, it presents an in-depth study of the mechanical properties of DNA. Such properties are of importance for many separation systems, in gels and microfluidic systems.

4) *Functional materials for microscale genomic and proteomics analyses* [188]. Vreeland and Barron present a good review of the polymers used as sieving matrices and coating agents for DNA separations in capillaries and microchannels.

5) *Micro Total Analysis Systems. 1. Introduction, theory and technology and Micro Total Analysis Systems. 2. Analytical Standard Operations and Applications* [189, 190]. A pair of extensive review articles by Manz, Auroux, Iossifidis and Reyes. More than 700 references! Cannot be missed for those interested in μTAS.

6) *The evolution of capillary electrophoresis: Past, present and future* [191]. Robert Weinberger is the author of this short and unpretentious historical overview of the development of this technology.

7) *Recent progress in DNA analysis by capillary electrophoresis* [105]. A well-balanced review by Righetti, Gelfi and D'Acunto. Covers experimental, technical and fundamental issues.

8) *Replaceable polymers for DNA sequencing by capillary electrophoresis* [192]. An excellent review of this crucial field by Quesda and Menchen. Includes lots of data about polymers and useful theoretical concepts.

9) *Physics and applications of microfluidics in biology* [193]. Beebe, Mensing and Walker present an interesting and accessible review of the main concepts. Includes a useful section on theory.

10) *Mobility, diffusion and dispersion of single-stranded DNA in sequencing gels* [194]. Mark Burns and co-workers present an excellent study of the physical mechanisms at play during sequencing in gels. Provides a good guide for data analysis.

11) *Principles of DNA separation with capillary electrophoresis* [195]. Heller has published several seminal papers in this field. This recent review presents an excellent overview of his work. Figure 1 is highly recommended.

12) *New DNA sequencing methods* [196]. Marziali and Akeson present an accessible review of the new methods being currently developed for DNA sequencing.

13) *Recent advances in DNA sequencing by capillary and microdevice electrophoresis* [197]. The review of Mitnik *et al.* covers instruments, mechanisms, results and theory. A good starting point.

14) *Sorting biomolecules with microdevices* [198]. Chou *et al.* give a great overview of the new devices being designed by these authors. Important reading for those who are interested in the new ideas that can be tested using microdevices.

15) *Microchannel DNA sequencing matrices with switchable viscosities* [199]. An excellent review of the various types of novel polymers being developed to carry out DNA sequencing in microchannel systems. The emphasis is on polymers that can take very low viscosities under certain conditions, so as to allow easy loading in the channel.

16) *Lab-on-a-chip: a revolution in biological and medical sciences* [200]. This is a short and accessible review on some of the challenges and promises of these new technologies.

17) *Ratchets and Brownian motors: Basics, experiments and applications* [35] in *Applied Physics A*. This special issue offers a comprehensive collection of articles, including a clear introduction to the physics of Brownian motors by Reimann and Hänggi [33], and several articles which discuss the use of ratchets for practical applications in separation science.

18) *Brownian motors: noisy transport far from equilibrium* [201]. A huge review by Reimann focusing on directed motion in thermal ratchet systems. Key theoretical aspects, such as symmetry conditions and current reversals, as well as practical experimental realizations and biological applications, are discussed.

19) *Single-molecule studies of DNA mechanics* [202]. Bustamante *et al.* present an overview of recent progress in single-molecule manipulation techniques which enable the analysis of biological processes such as DNA replication.

The authors would like to thank the Natural Sciences and Engineering Research Council of Canada (NSERC) for a Research Grant to GWS and a postdoctoral scholarship to SG. Also, LM, MG, FT, JFM and MK would like to thank NSERC and the University of Ottawa for Post-Graduate Scholarships.

Received July 23, 2002

17 References

[1] Han, J., Craighead, H. G., *Science* 2000, *288*, 1026–1029.

[2] Slater, G. W., Guo, H. L., Nixon, G. I., *Phys. Rev. Lett.* 1997, *78*, 1170–1173.

[3] Rill, R. L., Locke, B. R., Liu, Y., van Winkle, D. H., *Proc. Natl. Acad. Sci. USA* 1998, *95*, 1534–1539.

[4] Song, L., Fang, D., Kobos, R. K., Pace, S. J., Chu, B., *Electrophoresis* 1999, *20*, 2847–2855.

[5] Slater, G. W., Desruisseaux, C., Hubert, S. J., Mercier, J.-F., Labrie, J., Boileau, J., Tessier, F., Pépin, M. P., *Electrophoresis* 2000, *21*, 3873–3887.

[6] Henrickson, S. E., Misakian, M., Robertson, B. Kasianowicz, J. J., *Phys. Rev. Lett.* 2000, *85*, 3057–3060.

[7] Meller, A., Nivon, L., Branton, D., *Phys. Rev. Lett.* 2001, *86*, 3435–3438.

[8] Deamer, D. W., Akeson, M., *Trends Biotechnol.* 2000, *18*, 147–151.

[9] Li, J., Stein, D., McMullan, C., Branton, D., Aziz, M. J., Golovchenko, J. A., *Nature* 2001, *412*, 166–169.

[10] Howorka, S., Cheley, S., Bayley, H., *Nat. Biotechnol.* 2001, *19*, 636–639.

[11] Howorka, S., Movileanu, L., Braha, O., Bayley, H., *PNAS* 2001, *98*, 12996–13001.

[12] Kasianowicz, J. J., Henrickson, S. E., Weetall, H. H., Robertson, B., *Anal. Chem.* 2001, *73*, 2268–2272.

[13] Vercoutere, W., Winters-Hill, S., Olsen, H., Deamer, D., Haussler, D., Akeson, M., *Nat. Biotechnol.* 2001, *19*, 248–252.

[14] Sung, W., Park, P. J., *Phys. Rev. Lett.* 1996, *77*, 783–786.

[15] Park, P. J., Sung, W., *Phys. Rev. E* 1998, *57*, 730–734.

[16] Park, P. J., Sung, W., *J. Chem. Phys.* 1998, *108*, 3013–3018.

[17] Park, P. J., Sung, W., *Int. J. Bifurcation Chaos Appl. Sci. Eng.* 1998, *8*, 927–931.

[18] Di Marzio, E. A., Mandell, A. J., *J. Chem. Phys.* 1997, *107*, 5510–5514.

[19] Boehm, R. E., *Macromolecules* 1999, *32*, 7645–7654.

[20] Lubensky, D. K., Nelson, D. R., *Biophys. J.* 1999, *77*, 1824–1838.

[21] Muthukumar, M., *J. Chem. Phys.* 1999, *111*, 10371–10374.

[22] Muthukumar, M., *Phys. Rev. Lett.* 2001, *86*, 3188–3191.

[23] Muthukumar, M., *Electrophoresis* 2002, *23*, 1417–1420.

[24] de Gennes, P.-G., *Physica A* 1999, *274*, 1–7.

[25] Sebastian, K. L., *Phys. Rev. E* 2000, *61*, 3245–3248.

[26] Sebastian, K. L., Paul, A. K. R., *Phys. Rev. E* 2000, *62*, 927–939.

[27] Kumar, K. K., Sebastian, K. L., *Phys. Rev. E* 2000, *62*, 7536–7539.

[28] Chuang, J., Kantor, Y., Kardar, M., *Phys. Rev. E* 2001, *65*, 011802.

[29] Pernodet, N., Samuilov, V., Shin, K., Sokolov, J., Rafailovich, M. H., Gersappe, D., Chu, B., *Phys. Rev. Lett.* 2000, *85*, 5651–5654.

[30] Seo, Y., Samuilov, V., Sokolov, J., Rafailovich, M., Tinland, B., Kim, J., Chu, B., *Electrophoresis* 2002, *23*, 2618–2625.

[31] Luo, H., Gersappe, D., *Electrophoresis* 2002, *23*, in press.

[32] Grest, G., Kremer, K., *Phys. Rev. A* 1986, *33*, 3628–3631.

[33] Reimann, P., Hänggi, P., *Appl. Phys. A* 2002, *75*, 169–178.

[34] Griess, G. A., Serwer, P., *Appl. Phys. A* 2002, *75*, 223–228.

[35] Linke, H. (Ed.), *Appl. Phys. A* 2002, *75*, 167–352.

[36] Keller, C., Marquardt, F., Bruder, C., *Phys. Rev. E* 2002, *65*, 041927.

[37] Fistul, M. V., *Phys. Rev. E* 2002, *65*, 046621.

[38] Borromeo, M., *Phys. Rev. E* 2002, *65*, 041110.

[39] Eichhorn, R., Reimann, P., Hänggi, P., *Phys. Rev. Lett.* 2002, *88*, 190601.

[40] Reimann, P., Van den Broeck, C., Linke, H., Hänggi, P., Rubi, J. M., Pérez-Madrid, A., *Phys. Rev. Lett.* 2001, *87*, 010602.

[41] Popescu, M. N., Arizmendi, C. M., Salas-Brito, A. L., Family, F., *Phys. Rev. Lett.* 2000, *85*, 3321–3324.

[42] Porto, M., Urbakh, M., Klafter, J., *Phys. Rev. Lett.* 2000, *85*, 491–494.

[43] Cortés, E., *Physica A* 2000, *275*, 78–85.

[44] Landa, P. S., McClintock, P. V. E., *Physics Reports* 2000, *323*, 1–80.

[45] Austin, R. H., Darnton, N., Huang, R., Sturm, J., Bakajin, O., Duke, T., *Appl. Phys. A* 2002, *75*, 279–284.

[46] Chou, C. F., Austin, R. H., Bakajin, O., Tegenfeltd, J. O., Castelino, J. A., Chan, S. S, Cox, E. C., Craighead, H., Darnton, N., Duke, T., Han, J., Turner, S., *Electrophoresis* 2000, *21*, 81–90.

[47] Mercier, J.-F., Tessier, F., Slater, G. W., *Electrophoresis* 2001, *22*, 2631–2638.

[48] Marquet, C., Buguin, A., Talini, L., Silberzan, P., *Phys. Rev. Lett.* 2002, *88*, 168301.

[49] Bader, J. S., Deem, M. W., Hammond, R. W., Henck, S. A., Simpson, J. W., Rothberg, J. M., *Appl. Phys. A* 2002, *75*, 275–278.

[50] Hammond, R. W., Bader, J. S., Henck, S. A., Deem, M. W., McDermott, G. A., Bustillo, J. M., Rothberg, J. M., *Electrophoresis* 2000, *21*, 74–80.

[51] Bader, J. S., Hammond, R. W., Henck, S. A., Deem, M. W., McDermott, G. A., Bustillo, J. M., Simpson, J. W., Mulhern, G. T., Rothberg, J. M., *PNAS* 1999, *96*, 13165–13169.

[52] Griess, G. A., Rogers, E., Serwer, P., *Electrophoresis* 2001, *22*, 981–989.

[53] Griess, G. A., Rogers, E., Serwer, P., *Electrophoresis* 2001, *22*, 859–864.

[54] Han, J., Turner, S. W., Craighead, H. G., *Phys. Rev. Lett.* 1999, *83*, 1688–1691.

[55] Tessier, F., Slater, G. W., *Appl. Phys. A* 2002, *75*, 285–291.

[56] Ajdari, A., *Appl. Phys. A* 2002, *75*, 271–274.

[57] Ajdari, A., *Phys. Rev. E* 2000, *61*, R45-R48.

[58] Brown, A. B. D., Smith, C. G., Rennie, A. R., *Phys. Rev. E* 2001, *63*, 016305.

[59] Buguin, A., Talini, L., Silberzan, P., *Appl. Phys. A* 2002, *75*, 207–212.

[60] Kettner, C., Reimann, P., Hänggi, P., Müller, F., *Phys. Rev. E* 2000, *61*, 312–323.

[61] Gorre-Talini, L., Spatz, J. P., Silberzan, P., *Chaos* 1998, *8*, 650–656.

[62] Griess, G. A., Serwer, P., *Appl. Phys. A* 2002, *75*, 223–228.

[63] Baumgärtner, A., Muthukumar, *J. Chem. Phys.* 1987, *87*, 3082–3088.

[64] Baumgärtner, A., Muthukumar, M., *Macromolecules* 1989, *22*, 1937–1941.

[65] Muthukumar, M., Baumgärtner, A., *Macromolecules* 1989, *22*, 1941–1946.

[66] Arvanitidou, E., Hoagland, D., *Phys. Rev. Lett.* 1991, *67*, 1464–1466.

[67] Hoagland, D., Muthukumar, M., *Macromolecules* 1992, *25*, 6696–6698.

[68] Mayer, P., Slater, G. W., Drouin, G., *Appl. Theor. Electrophor.* 1993, *3*, 147–155.

[69] Slater, G. W., Wu, S. Y., *Phys. Rev. Lett.* 1995, *75*, 164–167.

[70] Nixon, G. I., Slater, G. W., *Phys. Rev. E* 1996, *53*, 4969–4980.

[71] Rousseau, J., Drouin, G., Slater, G. W., *Phys. Rev. Lett.* 1997, *79*, 1945–1948.

[72] Boileau, J., Slater, G. W., *Electrophoresis* 2001, *22*, 673–683.

[73] Liu, L., Li, P., Asher, S. A., *Nature* 1999, *397*, 141–144.

[74] Hoagland, D., *APS March Meeting Bulletin* 2002, D5.003.

[75] Turner, S. W. P., Cabodi, M., Craighead, H. G., *Phys. Rev. Lett.* 2002, *88*, 128103.

[76] Han, J., Craighead, H. G., *Anal. Chem.* 2002, *74*, 394–401.

[77] Tessier, F., Labrie, J., Slater, G. W., *Macromolecules* 2002, *35*, 4791–4800.

[78] Yaman, K., Pincus, P., Solis, F., Witten, T. A., *Macromolecules* 1997, *30*, 1173–1178.

[79] Ueda, M., Hayama, T., Takamura, Y., Horiike, Y., Baba, Y., *Electrophoresis* 2002, *23*, 2635–2641.

[80] Gardiner, C. W., *Handbook of Stochastic Methods for Physics, Chemistry, and the Natural Sciences*, Springer-Verlag, New York 1983.

[81] Park, P. J., Sung, W., *J. Chem. Phys.* 1999, *111*, 5259–5266.

[82] Lee, S., Sung, W., *Phys. Rev. E* 2001, *63*, 021115.

[83] Lee, K., Sung, W., *Phys. Rev. E* 2001, *64*, 041801.

[84] Reguera, D., Rubi, J. M., *Phys. Rev. E* 2001, *64*, 061106.

[85] Volkmuth, W. D., Austin, R. H., *Nature* 1992, *358*, 600.

[86] Doyle, P. S., Bibette, J., Bancaud, A., Viovy J.-L., *Science* 2002, *295*, 2237.

[87] Mayer, P., Bibette, J., Viovy, J.-L., *Mater. Res. Soc. Symp. Proc.* 1997, *463*, 57–66.

[88] André, P., Long D., Ajdari, A., *Euro. Phys. J. B.* 1998, *4*, 307–312.

[89] Nixon, G. I., Slater, G. W., *J. Chem. Phys.* 1994, *50*, 5033–5038.

[90] Sevick, E. M., Williams, D. R. M., *Euro. Phys. Lett. 2001, 56, 529–535.*

[91] Liu, J., Lawrence, E. M., Wu, A., Ivey, M. L., Flores, G. A., Javier, K., Bibette J., Richard, *J. Phys. Rev. Lett.* 1995, *74*, 2828–2831.

[92] Long, D., Dobrynin, A. V., Rubinstein, M., Ajdari, A., *J. Chem. Phys.* 1998, *3*, 108.

[93] Olivera, B. M., Baine, P., Davidson, N., *Biopolymers* 1964, *2*, 245.

[94] Desruisseaux, C., Long, D., Drouin, G., Slater, G. W., *Macromolecules* 2001, *34*, 44–52.

[95] Desruisseaux, C., Drouin, G., Slater, G. W., *Macromolecules* 2001, *34*, 5280–5286.

[96] Vreeland, W. N., Desruisseaux, C., Karger, A. E., Drouin, G., Slater, G. W., Barron, A. E., *Anal. Chem.* 2001, *73*, 1795–1803.

[97] Vreeland, W. N., Slater, G. W., Barron, A. E., *Bioconj. Chem.* 2002, *13*, 663–670.

[98] McCormick, L. M., Slater, G. W., Karger, A. E., Vreeland, W. N., Barron, A. E., Desruisseaux, C., Drouin, G., *J. Chromatogr. A* 2001, *924*, 43–52.

[99] Zhang, B., Hattori, T., Dubin, P. L., *Macromolecules* 2001, *34*, 6790–6794.

[100] Cottet, H., Gareil, P., Theodoly, O., Williams, C. E., *Electrophoresis* 2000, *21*, 3529–3540.

[101] Dovichi, N. J., Hu, S., *Anal. Chem.* 2002, *74*, 2833–2850.

[102] Stellwagen, N., Gelfi, C., Righetti, P. G., *Biopolymers* 1997, *42*, 687–703.

[103] Stellwagen, N. C., Stellwagen, E., *Electrophoresis* 2002, *23*, 1935–1941.

[104] Olson, W. I., Zhurkin, V. B. in: Sarma, R. L., Sarma, M. H. (Eds.), *Biological Structure and Dynamics*, Adenine Press, Schenectady, NY 1996, pp. 341–370.

[105] Righetti, P. G., Gelfi, C., D'Acunto, M. R., *Electrophoresis* 2002, *23*, 1361–1374.

[106] Mohanty, U., McLaughlin, L., *Annu. Rev. Phys. Chem.* 2001, *52*, 93–106.

[107] Allison, S. A., Li, Z., Reed, D., Stellwagen, N. C., *Electrophoresis* 2002, *23*, in press.

[108] Stellwagen, A., Stellwagen N. C., *Biopolymers* 1990, *30*, 309–324.

[109] Ekani Nkodo, A., Garnier, J. M., Tinland, B., Ren, H., Desruisseaux, C., McCormick, L. C., Drouin, G., Slater, G. W., *Electrophoresis* 2001, *22*, 2424–2432.

[110] Stellwagen, N. C., Magnusdottir, S., Gelfi, C., Righetti, P. G., *Biopolymers* 2001, *58*, 390–397.

[111] Barron, A. E., Blanch, H. W., Soane, D. S., *Electrophoresis* 1994, *15*, 597–615.

[112] Todorov, T. I., de Carmejane, O., Walter, N. G., Morris, M. D., *Electrophoresis* 2001, *22*, 2442–2447.

[113] Todorov, T. I., Morris, M. D., *Electrophoresis* 2002, *23*, 1033–1044.

[114] Wang, S-C., Morris, M. D., *Anal. Sci.* 2001, *17*, i173-i176.

[115] Starkweather, M. E., Muthukumar, M., Hoagland. D. A., *Macromolecules* 1998, *31*, 16, 5495–5501.

[116] Ekani Nkodo, A., Tinland, B., *Electrophoresis* 2001, *22*, 2424–2432.

[117] Ekani Nkodo, A., *PhD Thesis*, L'Universite Louis Pasteur, Strasbourg, France 2001.

[118] Hubert, S. J., Slater, G. W., Viovy, J.-L., *Macromolecules* 1996, *29*, 1006–1009.

[119] Starkweather, M. E., Muthukumar, M., Hoagland. D. A., *Macromolecules* 1999, *32*, 6837–6840.

[120] Starkweather, M. E., Muthukumar, M., Hoagland. D. A., *Macromolecules* 2000, *33*, 1245–1253.

[121] Noguchi, H., *J. Chem. Phys.* 2000, *112*, 9671–9678.

[122] Noguchi, H., Takasu, M., *J. Phys. Soc. Jpn.* 2000, *69*, 3762–3795.

[123] Noguchi, H., Takasu, M., *J. Chem. Phys.* 2001, *114*, 7260–7266.

[124] Jin, Y., Yang, B.-C., Fung, Y-S., *Fresenius' J. Anal. Chem.* 2001, *379*, 1015–1022.

[125] Viovy, J. L., *Rev. Mod. Phys.* 2000, *72*, 813–872.

[126] Doi, M., Edwards, S. F., *The Theory of Polymer Dynamics*, Oxford Science Publications, New York 1986.

[127] Slater, G. W. in: Heller, C. (Ed.), *Analysis of Nucleic Acids by Capillary Electrophoresis*, Vieweg & Sohn, Wiesbaden 1997, pp. 24–66.

[128] Meistermann, L., Tinland, B., *Phys. Rev. E* 1998, *58*, 4801–4806.

[129] Rousseau, J., Drouin, G., Slater, G. W., *Electrophoresis* 2000, *21*, 1464–1470.

[130] van Winkle, D. H., Beheshti, A., Rill, R. L., *Electrophoresis* 2002, *23*, 15–19.

[131] Rill, R. L., Beheshti, A., van Winkle, D. H., *Electrophoresis* 2002, *23*, 2710–2719.

[132] Slater, G. W., *Electrophoresis* 2002, *23*, 1410–1416.

[133] Chacron, M. J., Slater, G. W., *Phys. Rev. E* 1997, *56*, 3446–3450.

[134] Frumin, L. L., Peltek, S. E., Zilberstein, G. V., *Phys. Rev. E* 2001, *64*, 021902.

[135] Baskin, E. M., Zilberstein, G. V., *Electrophoresis* 2002, *23*, 1410–1416.

[136] Guillouzic, S., McCormick, L. C., Slater, G. W., *Electrophoresis* 2002, *23*, 1822–1832.

[137] Liang, D., Song, L., Quesada, M. A., Tian, Z., Studier, F. W., Chu, B., *Electrophoresis* 2000, *21*, 3600–3608.

[138] Slater, G. W., Noolandi, J., *Electrophoresis* 1988, *9*, 643–646.

[139] Izzo, V., Craxi, A., Barbieri, R., *Electrophoresis* 2001, *22*, 29–32.

[140] Kist, T. B. L., *Phys. Rev. Lett.* 1995, *6*, 1210–1213.

[141] Burmeister, M., Ulanovsky, L., *Pulsed-Field Gel Electrophoresis: Protocols, Methods, and Theories*, Humana Press, Totowa, NJ 1992.

[142] Schoffen, J. R., Mandaji, M., Termignoni, C., Grieneisen, H. P. H., Kist, T. B. L., *Electrophoresis* 2002, *23*, 2704–2709.

[143] Locke, B. R., Trinh, S. H., *Electrophoresis* 1999, *20*, 3331–3334.

[144] Tietz, D., *Electrophoresis* 1995, *16*, 460–461.

[145] Ogston, A. G., *Trans. Faraday Soc.* 1958, *54*, 1754–1757.

[146] Morris, C. J. O. R. in: Peeters, H. (Ed.), *Protides of the Biological Fluids, 14th Colloquium*, Elsevier, New York 1967, pp. 543–551.

[147] Rodbard, D., Chrambach, A., *Proc. Natl. Acad. Sci. USA* 1970, *65*, 970–977.

[148] Mercier, J.-F., Slater, G. W., Guo, H. L., *J. Chem. Phys.* 1999, *110*, 6050–6056.

[149] Slater, G. W., Guo, H. L., *Electrophoresis* 1996, *17*, 977–988.

[150] Slater, G. W., Guo, H. L., *Electrophoresis* 1996, *17*, 1407–1415.

[151] Slater, G. W., Treurniet, J. R., *J. Chromatogr. A* 1997, *772*, 41–48.

[152] Mercier, J.-F., Slater, G. W., *Electrophoresis* 1998, *19*, 1560–1565.

[153] Labrie, J., Mercier, J.-F., Slater, G. W., *Electrophoresis* 2000, *21*, 823–833.

[154] Mercier, J.-F., Slater, G. W., *Macromolecules* 2001, *34*, 3437–3445.

[155] Mercier, J.-F., Slater, G. W., *J. Chem. Phys.* 1999, *110*, 6057–6065.

[156] Mercier, J.-F., Slater, G. W., *J. Chem. Phys.* 2000, *20*, 9109–9112.

[157] Trinh, S., Arce, P., Locke, B. R., *Transport in Porous Media* 2000, *38*, 241–259.

[158] Schlicht, L., Ilgenfritz, G., *Physica A* 1996, *227*, 239–247.

[159] Tsai, D. S., Strieder, W., *Chem. Eng. Commun.* 1986, *40*, 207–204.

[160] Amsden, B., *Macromolecules* 1998, *31*, 8382–8395.

[161] Amsden, B., *Macromolecules* 1999, *32*, 874–879.

[162] Amsden, B., *Macromolecules* 2001, *34*, 1430–1435.

[163] Amsden, B., Grotheer, K., Angl, D., *Macromolecules* 2002, *35*, 3179–3183.

[164] Locke, B. R., *Electrophoresis* 2002, *23*, 2745–2754.

[165] Dorfman, K. D., Brenner H., *Phys. Rev. E* 2002, *65*, 021103.

[166] Edwards, D. A., *Trans. R. Soc. Lond. A* 1995, *353*, 205–242.

[167] Brenner H., Edwards, D. A., *Macrotransport Processes*, Butterworth-Heinemann, Boston 1993.

[168] Brenner H., *Phil. Trans. R. Soc. Lond. A* 1980, *297*, 81–133.

[169] de Gennes, P. G., *J. Chem. Phys.* 1971, *55*, 572–579.

[170] Carmesin, I., Kremer, K., *Macromolecules* 1988, *21*, 2819–2823.

[171] Evans, K. E., Edwards, S. F., *J. Chem. Soc. Faraday Trans. 2* 1981, *77*, 1929–1938.

[172] Rubinstein, M., *Phys. Rev. Lett.* 1987, *59*, 1946–1949.

[173] van Heukelum, A., Barkema, G. T., *Electrophoresis* 2002, *23*, in press.

[174] Doi, M., *J. Polymer Sci. B* 1983, *21*, 667–684.

[175] Klein, J., *Nature (London)* 1978, *271*, 143–145.

[176] Tinland, B., *Electrophoresis* 1996, *17*, 1519–1523.

[177] Pluen, A., Tinland, B., Sturm, J., Weill, G., *Electrophoresis* 1998, *19*, 1548–1559.

[178] Tinland, B., Meistermann, L., Weill, G., *Phys. Rev. E* 2000, *61*, 6993–6998.

[179] Deutsch, J. M., Madden, T. L., *J. Chem. Phys.* 1989, *91*, 3252–3257.

[180] Barkema, G. T., Krenzlin, H. M., *J. Chem. Phys.* 1998, *109*, 6486–6489.

[181] Barkema, G. T., Marko, J. F., Widom, B., *Phys. Rev. E* 1994, *49*, 5303–5309.

[182] Carlon, E., Drzewinski, A., van Leeuwen, J. M. J., *Phys. Rev. E* 2001, *64*, 010801(R).

[183] van Heukelum, A., Beljaars, H. R. W., *J. Chem. Phys.* 2000, *113*, 3909–3915.

[184] Azuma, R., Takayama, H., *Phys. Rev. E* 1999, *59*, 650–655.

[185] Newman, M. E. J., Barkema, G. T., *Monte Carlo Methods in Statistical Physics*, Clarendon Press, Oxford 1999.

[186] Slater, G. W., *Electrophoresis* 1993, *14*, 1–7.

[187] Lavery, R., Lebrun, A., Allemand, J.-F., Bensimon, D, Croquette, V., *J. Physics: Cond. Matter* 2002, *14*, R383–R414.

[188] Vreeland, W. N., Barron, A. E., *Curr. Opin. Biotech.* 2002, *13*, 287–294.

[189] Reyes, D. R., Iossifidis, D., Auroux, P.-A., Manz, A., *Anal. Chem.* 2002, *74*, 2623–2636.

[190] Auroux, P.-A., Reyes, D. R., Iossifidis, D., Manz, A., *Anal. Chem.* 2002, *74*, 2637–2652.

[191] Weinberger, R., *Am. Lab.* 2002, *34*, 32–40.

[192] Quesada, M. A., Menchen, S., in: Mitchelson, K. R., Cheng, J. (Eds.), *Capillary of Nucleic Acids, Volume 1*, Humana Press, Totowa, NJ 2001, pp. 139–166.

[193] Beebe, D. J., Mensing, G. A., Walker, G. M., *Annu. Rev. Biomed. Eng.* 2002, *4*, 261–286.

[194] Brahmasandra, S. N., Burke, D. T., Mastrangelo, C. H., Burns, M. A., *Electrophoresis* 2001, *22*, 1046–1062.

[195] Heller, C., *Electrophoresis* 2001, *22*, 629–643.

[196] Marziali, A., Akeson, M., *Annu. Rev. Biomed. Eng.* 2001, *3*, 195–223.

[197] Mitnik, L., Novotny, M., Felten, C., Buonocore, S., Koutny, L., Schmalzing, D., *Electrophoresis* 2001, *22*, 4104–4117.

[198] Chou, C.-F., Austin, R. H., Bakajin, O., Tegenfeldt, J. O., Castelino, J. A., Chan, S. S., Cox, E. C., Craighead, H., Darnton, N., Duke, T., Han, J., Turner, S., *Electrophoresis* 2000, *21*, 81–90.

[199] Buchholz, B. A., Shi, W., Barron, A. E., *Electrophoresis* 2002, *23*, 1398–1409.

[200] Figeys, D., Pinto, D., *Anal. Chem.* 2000, *72*, 330A–335A.

[201] Reimann, P., *Phys. Reports* 2002, *361*, 57–265.

[202] Bustamante, C., Smith, S. B., Liphardt, J., Smith, D., *Curr. Opin. Struct. Biol.* 2000, *10*, 279–285.

Index